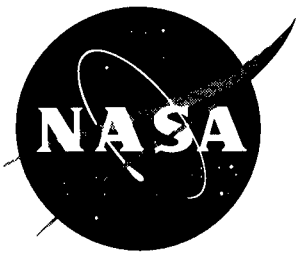


Catastrophic Failure Modes Assessment of the International Space Station *Alpha*

B.E.P. Lutz and C.J. Goodwin

Contract NAS8-37383
Prepared for Marshall Space Flight Center

February 1996



Catastrophic Failure Modes Assessment of the International Space Station *Alpha*

B.E.P. Lutz and C.J. Goodwin
Meyer Analytics, Inc.

National Aeronautics and Space Administration
Marshall Space Flight Center • MSFC, Alabama 35812

Prepared for Marshall Space Flight Center
under Contract NAS8-37383

February 1996

F O R E W O R D

In addition to the existing micrometeoroids, dead satellites, remains of rocket stages and a multitude of other pieces of man-made space debris speeding at a hypervelocity around the Earth could damage severely the planned International Space Station Alpha (ISSA).

This report presents the results of an additional work-study that supplement the ongoing engineering activities by The National Aeronautics and Space Administration (NASA), BOEING Aerospace Company and Contractors for the optimization of the survivability of ISSA when under micrometeoroids or orbital debris (M/OD) threats. Successfully mitigating the technical, schedule, and cost uncertainty associated with the development and integration for creating the catastrophic failure risk models, the failures' modes and procedures for estimating their likelihood and provides specific estimates for the ISSA design are a progressing multi-disciplinary technical and management challenge.

NASA/MSFC contracted Meyer Analytics, Incorporated (MA) through Science Applications International Corporation (SAIC) for supporting NASA for the development and verification of risks models for predicting the likelihood of catastrophic failure of selected components of the ISSA due to impact by M/OD. Catastrophic failure in this context means the occurrence of an event, like rapid depressurization and/or unzipping of an habitable module, resulting in the loss of a crew or the loss of the entire ISSA.

The performed work-study by MA for supporting NASA in the above activities, centralized into two major technical areas. The first one concerns the Critical Crack Length (CCL) of four ISSA manned Modules, which is described in Section A of the report. The second one, given in Section B, address the primary and secondary effects of M/OD penetration on the proposed Russian Functional Energy Block (FGB), or called sometimes the Space "TUG", propulsion module and propellant tanks arrayed in pairs around its exterior, and on the Gyrodynes module.

SECTION A

CRITICAL CRACK LENGTH of MANNED MODULES and Russian FGB Selected Auxiliary Tanks

(An Advanced Fracture Mechanics Study)

by

Dr. Bernard E.P. Lutz

A-i

MEYER ANALYTICS, INC.
WARRENTON, VA 22186-9212
USA

SECTION A

TABLE of CONTENTS

	Page
AI EXECUTIVE SUMMARY	A-1
AII INTRODUCTION	A-5
AIII FRACTURE MECHANICS	A-6
AIII-1 Prologue	A-6
AIII-2 Stress Intensity Factor (SIF) Determination at a Crack-Tip	A-6
AIII-3 Nonlinear Crack Bulging Effects on the SIF	A-15
AIII-4 Aluminum Alloy 2219-T87 Material Fracture Toughness Data	A-18
AIV CRITICAL CRACK LENGTHS	A-27
AIV-1 Prologue	A-27
AIV-2 UNITED STATES of AMERICA COMMON (i.e., HAB & LAB) MODULE	A-28
AIV-2.1 - Main Cylindrical Shell	A-28
AIV-2.2 - Shell End Cone	A-38
AIV-3 EUROPEAN SPACE AGENCY (ESA) MPLM COLUMBUS MODULE	A-46
AIV-3.1 - Main Cylindrical Shell	A-46
AIV-3.2 - Shell End Cone	A-54
AIV-4 JAPAN SPACE AGENCY (NASDA) JEM PM LAB MODULE	A-63
AIV-4.1 - Main Cylindrical Shell	A-63
AIV-5 RUSSIAN FGB (TUG) PROPULSION MODULE	A-74
AIV-5.1 - Main Cylindrical Shell	A-74
AIV-6 RUSSIAN FGB SELECTED AUXILIARY TANKS	A-84
AIV-7 RUSSIAN RESEARCH MODULE SPHERICAL END CONE	A-87
AV CONCLUSIONS and RECOMMENDATIONS	A-89
AVI REFERENCES	A-92
AVII ACKNOWLEDGMENTS	A-94

SECTION A

A P P E N D I C E S

	Page
APPENDIX	
A. ALUMINUM ALLOY 2219-T87 MATERIAL PROPERTIES DATA	A-95
B. NOTES on FRACTURE MECHANICS of THROUGH-CRACKED CYLINDERS	A-103

NOTATION

A	area
AFM	advanced fracture mechanics
a	half-crack length
a_o	initial half-crack length
a_c	critical half-crack length
B	compact tension (CT) fracture test specimen thickness
B_{unc}	uncertainties on fracture parameters
CCL	critical crack length
CG	center of gravity
CL	center-line
CMOD	crack-mouth opening displacement
CT	implying compact tension
CTIP	crack-tip
CTOA	crack-tip opening angle
CTOD	crack-tip opening displacement
CCT	center cracked tension (fracture type of test specimen)
c	subscript denoting critical value
D	shell diameter
d	hole diameter
e	subscript for energy
E	material modulus of elasticity (Young's Modulus)
EFM	elastic fracture mechanics
EPFM	elastic-plastic fracture mechanics
ESIF	elastic stress intensity factor (also, SIF)
F	force vector
F_{ty}	material tensile yield strength
F_{tu}	material ultimate tensile strength
FEA	finite element analysis
FEM	finite element method; finite element modeling
G	material shear modulus (also denoted by μ); Griffith strain energy release rate.
H	height (i.e., for a compact tension specimen)
h	thickness (used in lieu of t, for time)
i	subscript

A-v

NOTATION, Continued

j	subscript
J	path-independent contour integral (<i>J</i> - Rice integral)
K_I	mode one (I) fracture toughness or stress intensity factor
K_{II}	mode two (II) fracture toughness or stress intensity factor
K_{Ic}	critical fracture toughness at crack-initiation, quasi-static (stable crack growth)
K_{I_{ns}}	critical fracture toughness at crack instability, quasi-static (unstable crack growth)
K_p	plastic stress intensity factor
L	length (i.e., tip-to-tip crack length)
LSY	subscript implying large scale yielding
n	material strain hardening exponent (Ramberg-Osgood Law)
NCM	nonlinear computational mechanics
o	subscript implying initial conditions (i.e., initial crack-length)
PE	potential energy
r,θ	polar coordinates
r_o	radius
r_p	crack-tip plastic zone in plane stress
R	radius; reliability (Weibull); R-curve
R_m	membrane shell radius
S	arc length
SE	strain energy
SED	strain energy density
SERR	strain energy release rate
SHE	strain hardening exponent
SIF	stress intensity factor
SSY	subscript implying small scale yielding
t	time
T	traction
u_x,u_y,u_z	displacement components in the x, y, and z coordinate directions respectively
V	volume
VCC	virtual crack closure
W	width of a compact tension (CT) fracture test specimen; external work; SED
x,y,z	Cartesian Coordinates
X,Y,Z	Cartesian Coordinates

NOTATION, Continued

α	crack angle
β	bulging factor
Γ	closed contour about a crack-tip
δ	displacement
ε	strain
σ	stress
ν	elastic Poisson's ratio
ζ	energy release rate (see also G)
θ	hoop coordinate; angle
λ	shell geometry parameter; crack length parameter
μ	shear modulus (G also used in solid mechanics)
η	dimensionless constant (elastic-plastic fracture mechanics)
ρ	mass density

LIST OF FIGURES

<u>No.</u>	<u>TITLE</u>	<u>Page</u>
1	INTERNATIONAL SPACE STATION ALPHA (ISSA)	2
2	Through-the-Wall Longitudinal (axial) Cracks in a Typical ISSA Pressurized Manned Module	3
3	Segment of Crack Opening	9
4	Calculation of Energy Release Rate by Finite Element Method	9
5	Two Generally Used Positions for Measuring CTOD	11
6	Energy Computation for Crack Advance	11
7	Estimation of CTOD from 90° Intercept	11
8	Predicted J-CTOD Relationships for Plane Stress	14
9	Crack Bulging Typical Scenario	16
10	Weibull Fracture Toughness Distribution for 2219-T87 Aluminum Alloy	19
11	J-R Curves for 2219-T87 Aluminum Alloy	21
12	R-Curves for 2219-T87 Aluminum Alloy, L-T Direction (Martin Marietta)	22
13	J-R Curves for the Quasi-Static CCT Specimen (SwRI, 1993)	23
14	Comparison of the Weibull Fracture Toughness Distribution for three published data bank for 2219-T87 Aluminum Alloy	24
15	Derived J-R Curves for two CCT Test Specimen made of Al/Al 2219-T87	25
16	US Common Module Shell and Waffle-Skin Design Details	29
17	US Common Module Shell 3D Finite Element 1/4 (90°) Model -Overall Arrangement	30
18	US Common Module Shell 3D FEA 1/4 (90°) Model - Principal Stress (psi) Distribution	31
19	CCT Flat Plate Analytical Specimen Overall Configuration for the US Module Shell Waffle-Skin	32
20	CCT Flat Plate Analytical Specimen for the US Module Waffle-Skin Prior to Finite Element Meshing	33
21	CCT Flat Plate Analytical Specimen for the US Module Waffle-Skin - Plane Stress Elasto-Plastic Finite Element Model	34

LIST of FIGURES (Cont'd)

<u>No.</u>	<u>TITLE</u>	<u>Page</u>
22	CCT Flat Plate Analytical Specimen for the US Module Waffle-Skin - 2D Plane Stress Elasto-Plastic FEA Results - Crack Opening Displacement vs. Crack Length	35
23	CCT Flat Plate Analytical Specimen for the US Module Waffle-Skin - 2D Plane Stress Elasto-Plastic FEA Results - Stress Intensity Factors vs. Crack Length	36
24	US Common Module End Cone Overall Arrangement	39
25	US Common Module End Cone 3D FEA 1/4 (90°) Model with an Axial Crack (Lo = 8 inch) within the Region of Minimum Thickness (0.188")	40
26	US Common Module End Cone 3D FEA 1/4 (90°) Model with an Axial Crack, Lo = 8 inches - Maximum Principal Stress (psi) Distribution around the Cracked Region	42
27	US Common Module End Cone - CTIP-A (North) SIF for Crack Lengths between 4 and 8 inches	43
28	US Common Module End Cone - Interpolated CTIP-A (North) SIF vs. Crack Length	44
29	US Common Module End Cone - CTIP-B (South) SIF vs. Crack Length	45
30	ESA MPLM "COLUMBUS" Module General Arrangement	47
31	ESA MPLM Cylindrical Shell 3D FEA 1/4 (90°) Model - Top View	48
32	ESA MPLM Cylindrical Shell 3D FEA 1/4 (90°) Model - Details of the Isogrid Pressure Wall	49
33	ESA MPLM Cylindrical Shell 3D FEA 1/4 (90°) Model - Side View	50
34	ESA MPLM Cylindrical Shell 3D FEA 1/4 (90°) Model - Crack Displacement and Bulging Details	51
35	ESA MPLM Cylindrical Shell with an Isogrid Reinforced Skin - CCT Flat Plate Analytical Specimen	52
36	ESA MPLM Cylindrical Shell with an Isogrid Reinforced Skin - CCT Elasto-Plastic 2D Plane Stress Finite Element Model	53
37	ESA MPLM Cylindrical Shell with an Isogrid Reinforced Skin - SIF vs. Crack length for Five SIF Criterion	55
38	ESA MPLM Module End Cone Design Details	56
39	ESA MPLM Module End Cone 3D FEA 1/4 (90°) Model - Overall Arrangement Without an Artificial Crack (Internal Pressure + Blow Out Load Vectors at 14.9 psia)	57

LIST of FIGURES (Cont'd)

<u>No.</u>	<u>TITLE</u>	<u>Page</u>
40	ESA MPLM Module End Cone 3D FEA 1/4 (90°) Model with an Artificial Crack within a Waffle Grid Cell (Inside View)	58
41	ESA MPLM Module End Cone 3D FEA 1/4 (90°) Model - Principal Stress (psi) Distribution Around the Cracked Region (at 14.9 psia internal pressure loading)	59
42	ESA MPLM End Cone with an Axial Crack within a Waffle-Grid Cell - Crack Tips (A & B) SIF vs. Crack Length	60
43	ESA MPLM End Cone with an Axial Crack within a Waffle-Grid Cell - Crack-Tip "A" SIF Comparison vs. Crack Length for Three Different Analytical Methods	62
44	NASDA JEM PM Structure General Arrangement	64
45	NASDA JEM PM Cylindrical Shell 3D FEA 1/4 (90°) Model - Model Perspective View	65
46	NASDA JEM PM Cylindrical Shell 3D FEA 1/4 (90°) Model - Model Top View	66
47	NASDA JEM PM Cylindrical Shell 3D FEA 1/4 (90°) Model - Model Without a Crack - Principal Stress (psi) Distribution	67
48	NASDA JEM PM Cylindrical Shell Isogrid Stiffened Skin - CCT Flat Plate Analytical Specimen	68
49	NASDA JEM PM Cylindrical Shell Isogrid Stiffened Skin - CCT Flat Plate 1/4 Analytical Model (Reduced Size due to Symmetry and Prior to Finite Element Meshing)	69
50	NASDA JEM PM Cylindrical Shell Isogrid Stiffened Skin - CCT Flat Plate Plane Stress Elasto -Plastic Finite Element Model	70
51	NASDA JEM PM Cylindrical Shell Isogrid Stiffened Skin - CCT Plane Stress Elasto - Plastic Finite Element Analysis Results - Crack Opening Displacements (COD) vs. Half-Crack Length	71
52	NASDA JEM PM Cylindrical Shell Isogrid Stiffened Skin - CCT Plane Stress Elasto - Plastic Finite Element Analysis Results - Stress Intensity Factors vs. Half-Crack Length	72
53	NASDA JEM PM Cylindrical Shell Isogrid Stiffened Skin - CCT Plane Stress Elasto-Plastic Finite Element Analysis - COD and Crack-Tip Critical Locations	73
54	RUSSIAN FGB (Space Tug) Cylindrical Shell - 3D Finite Element 1/4 (90°) Model of a Section of the Waffle-Grid Reinforced Skin	75
55	RUSSIAN FGB (Space Tug) Cylindrical Shell - Waffle-Grid Reinforced Skin Design Details	76

A-x

LIST of FIGURES (Cont'd)

<u>No.</u>	<u>TITLE</u>	<u>Page</u>
56	RUSSIAN FGB (Space Tug) Cylindrical Shell - 3D FEA Model with Internal Pressure Loading	77
57	RUSSIAN FGB (Space Tug) Cylindrical Shell without a Crack - Principal Stress (psi) Distribution at 14.9 psia Internal Pressure	78
58	RUSSIAN FGB (Space Tug) Cylindrical Shell Waffle-Grid Reinforced Skin - CCT Flat Plate Analytical Specimen	79
59	RUSSIAN FGB (Space Tug) Cylindrical Shell Waffle-Grid Reinforced Skin - CCT Plane Stress Elasto-Plastic FEA Model	80
60	RUSSIAN FGB (Space Tug) Cylindrical Shell Waffle-Grid Reinforced Skin - CCT Plane Stress Elasto-Plastic FEA Results - COD vs. Half-Crack Length	81
61	RUSSIAN FGB (Space Tug) Cylindrical Shell Waffle-Grid Reinforced Skin - CCT Plane Stress Elasto-Plastic FEA Results - SIF vs. Half-Crack Length	82
62	RUSSIAN FGB (Space Tug) Cylindrical Shell Waffle-Grid Reinforced Skin - CCT Plane Stress Elasto-Plastic FEA Model - SIF and Crack-Tip (CTIP) Critical Locations	83
63	RUSSIAN FGB (Space Tug) Auxiliary Tanks - Propellant Tank Critical Crack Length	85
64	RUSSIAN FGB (Space Tug) Auxiliary Tanks - GN2 Spherical Bottle Critical Crack Length	86
65	Russian Research Module Spherical Enc Cone - SIF vs. Crack Length at 14.7 psia Internal Pressure Loading	88
66	Pressure Measurements in a Test Chamber Under Ballistic Impact Loading	91

AI - EXECUTIVE SUMMARY

The effects of micrometeoroids and orbital debris (M/OD) on the station equipment can result from a local damage problem to a possible catastrophic system failure, followed by either crew loss or station loss. Diverse failure mechanisms were identified, which are the result of M/OD hits. Three of these are directly applicable to the habitable modules: 1) crew injury from debris or decompression; 2) uncontrollable station attitude due to venting pulse; 3) station principal structure overloading due to venting forces. All these mechanisms have a common denominator: the station pressurized elements wall penetration by M/OD cloud particles. The prevalent factor affecting each failure mechanisms is the probability of a penetration inducing, in addition to a perforation, unstable crack lengths which could "unzip" a pressurized element. The term "unzip" is the uncontrolled propagation of a crack from the point of penetration to otherwise undamaged structure.

Section A of this report summarizes the conducted analytical study and the obtained results for determining the critical crack length (CCL) of the ISSA Manned Modules which includes the United States of America (US) HAB or LAB Module, the Russian FGB (TUG) Module, the European Space Agency (ESA) MPLM COLUMBUS Module, and the Japan's National Space Development Agency (NASDA) JEM PM LAB Module, as depicted in Figure 1, while pressurized. Additionally, selected highly pressurized auxiliary tanks of the Russian FGB Propulsion Unit are also addressed.

Classical engineering structural mechanics, and advanced fracture mechanics concepts coupled with numerical solution techniques were used to predict the strength of these pressure vessels in which cracks had completely penetrated the vessel wall, as shown pictorially in Figure 2. The principal component investigated of these habitable modules was the orthotropic shell comprising the main body. For two modules, where complete structural design details could be made available, their end-cones CCL were also evaluated. These are only for the US and the ESA modules.

A summary on the respective ISSA Modules critical crack length (CCL) is displayed in Table I. The CCL shown are for the CCL at initiation and stable growth, and at unstable growth or the CCL level for which 'unzipping' of a particular structure could occur.

INTERNATIONAL SPACE STATION ALPHA

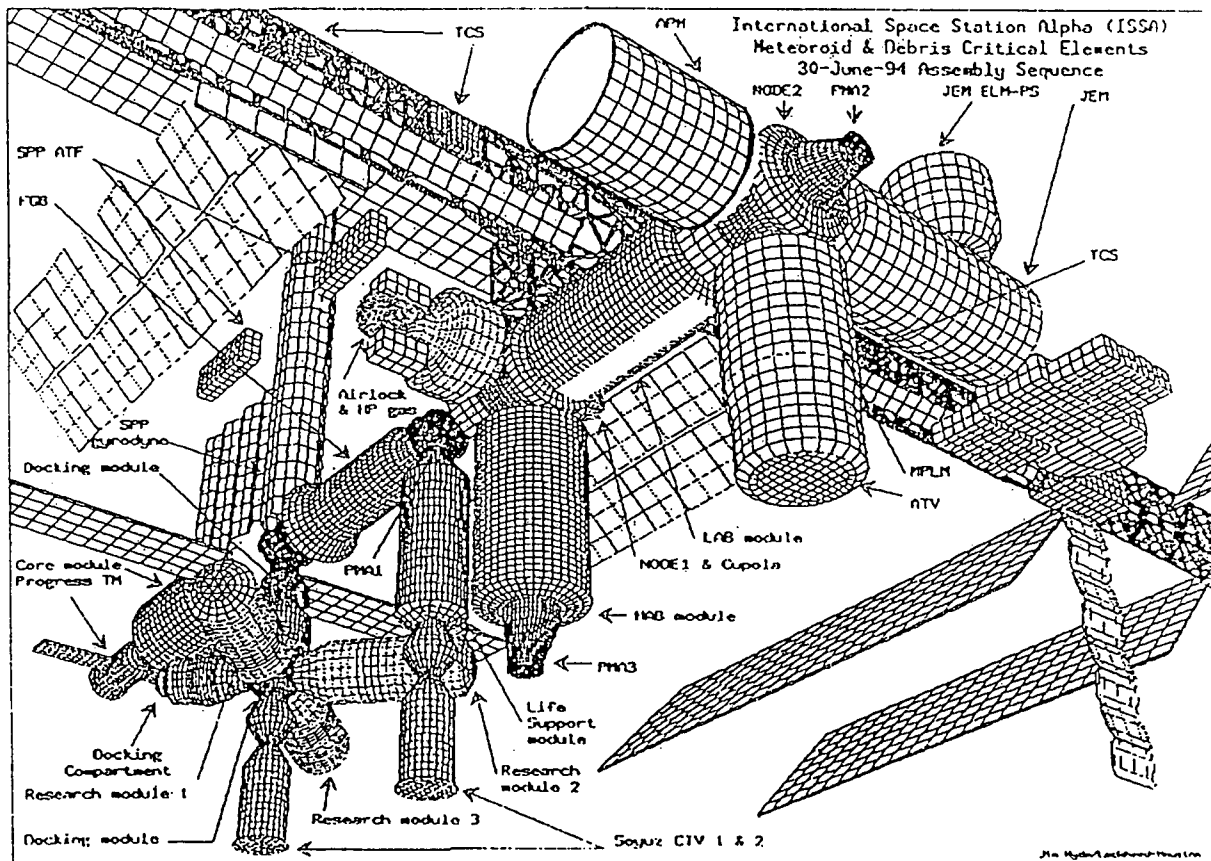
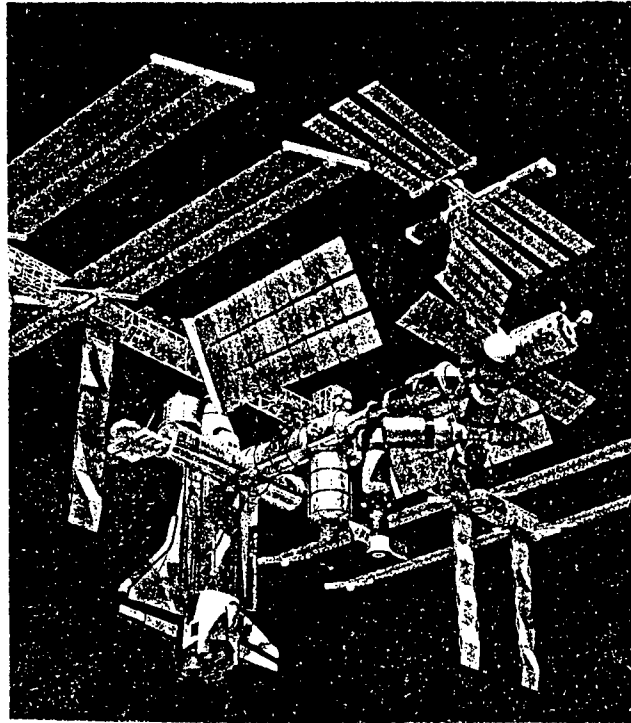


Figure 1 - INTERNATIONAL SPACE STATION ALPHA (ISSA)
Meteoroid & Orbital Debris Critical Elements
(Courtesy of NASA & Lockheed, Houston, TX)

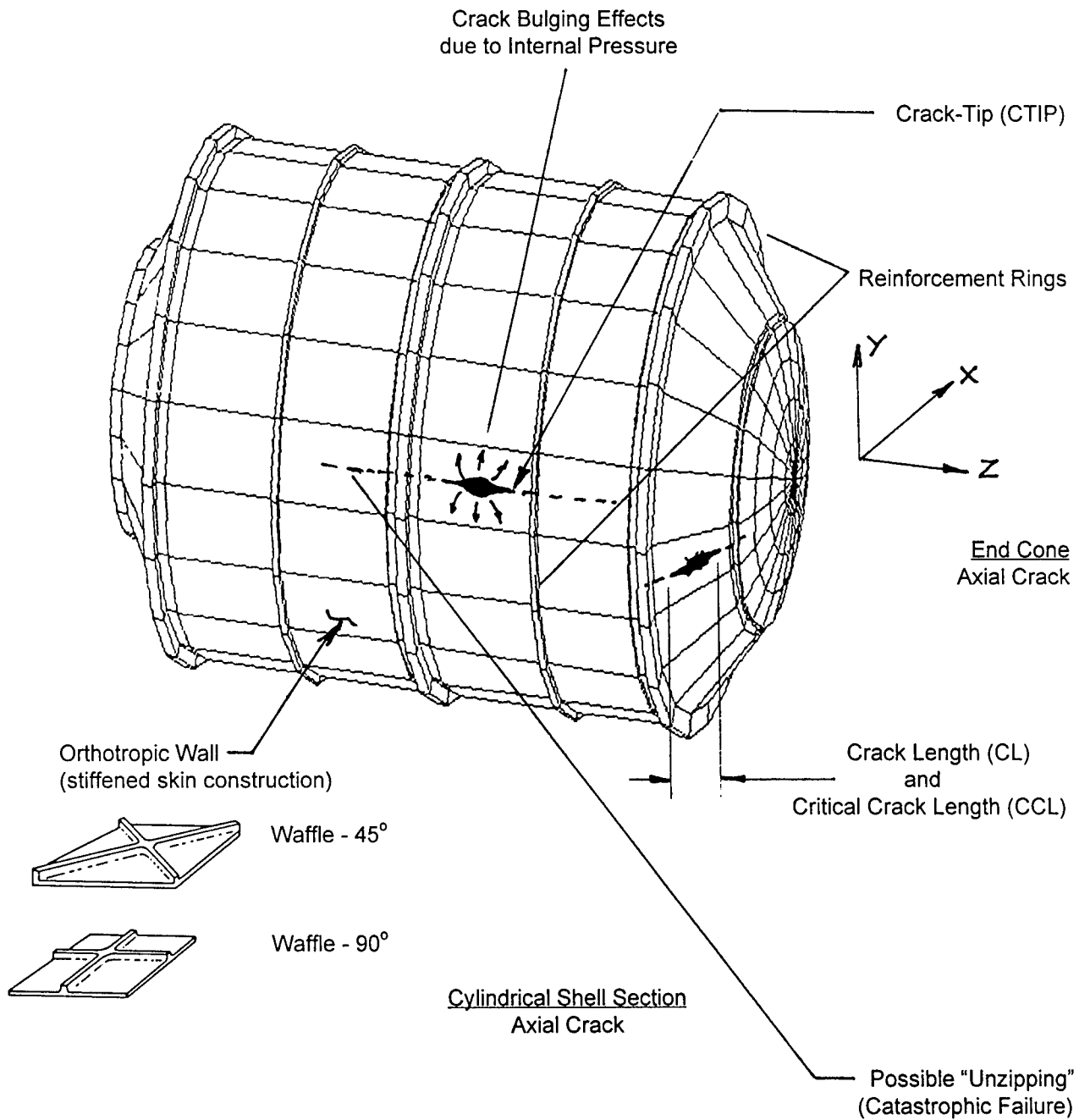


Figure 2 - THROUGH THE WALL LONGITUDINAL (axial) CRACKS
in a TYPICAL ISSA PRESSURIZED MANNED MODULE

TABLE I - SUMMARY ON THE ISSA MANNED MODULES CRITICAL CRACK LENGTH

MODULE	CRACK PROPAGATION CONDITIONS	CRACK LENGTH (inch)	
		AROUND the MEAN VALUE	MINUS ONE STANDARD DEVIATION
US HAB/LAB SHELL	1	12.8	10.7
	2	N/A	17.5
US END CONE	1	5.7	4.4
	2	12.5	10.4
ESA MPLM SHELL	1	9.8	9.2
	2	15.2	13.6
ESA END CONE	1	5.3	3.7
	2	7.0	4.2
JEM PM SHELL	1	12.0	10.0
	2	N/A	15.3
FGB SHELL (see notes)	1	N/A	N/A
	2	N/A	N/A

Notes: 1 = Stable Initiation and Growth
 2 = Unstable (Critical)
 N/A = not applicable

* For the Russian FGB Propulsion Module, it will be very difficult to propagate a crack within the waffle-skin under 14.9 psia pressure loading alone. Other damage conditions must prevail in order to "unzip" the shell.

AII - INTRODUCTION

The purpose of this report is to describe the analytical and modeling efforts performed for assessing the risk level of the ISSA pressurized modules structure under Micrometeoroid and Orbital Debris (M/OD) cloud threat. These modules will team-up with the cluster of other modules used in the International Space Station Alpha (ISSA), as shown in Figure 1.

The risk level here is defined as the criticality for these modules to "unzip" catastrophically if they are subjected to orbital debris cloud impact and subsequent pressure wall penetration.

There is no simple solution to the catastrophic rupture problem of an orthotropic cylindrical shell structure. Tension load carried in the shell pressure wall can cause an existing crack (or crack emanating from a perforation) to grow in an abrupt and unbounded fashion (unzipping), if the initial crack length exceeds a certain length called the Critical Crack Length (CCL). The probability of unzipping has been demonstrated by previous research work performed by several organizations, including by NASA laboratory experiments with pressure vessels impacted by hypervelocity projectiles. A catastrophic rupture of a pressurized element, in particular high pressurized elements as the propulsion tanks will be, by itself, a debris-inducing event, posing the greatest threat to crew survival and the station. This catastrophic scenario imposed the need to determine, among other variables, the CCL of ISSA pressurized vessels .

However, to minimize risks of penetration, the pressurized ISSA elements possess a structural arrangement as a defense against M/OD threat, called a double-walled M/OD bumper system, or "Whipple Shield". If the standoff shield is penetrated by a projectile, the debris from the projectile and the shield will travel across the distance between bumper and the shell pressure wall, and strike the pressure wall. The induced damage on the vessel wall by the debris cloud loading may result in a penetration, petaling, and cracks.

To assess the **damage tolerance** of these habitable modules (and other pressurized elements) to M/OD strikes, we have used the technology of **fracture mechanics** principles in addition to classical numerical methods, like the Finite Element Method.

AIII - FRACTURE MECHANICS

AIII-1 PROLOGUE

Essentially, the fracture strength of pressure vessels with through the wall cracks (Figure 2), is related to the vessel radius and thickness, the crack geometry (crack tip and crack length), the material elastic modulus, yield, and ultimate tensile strengths, the material fracture toughness, and the loading conditions (i.e., pressure, temperature, time effects). The problem has been to define a suitable expression that takes into account all known variables affecting the crack driving force, or Stress Intensity Factor (SIF), at the crack tip.

The use of classical Linear Elastic Fracture Mechanics (LEFM = quasi-static assumptions, i.e., brittle) versus Advanced Fracture Mechanics (AFM = nonlinear and dynamic effects, i.e., ductile) for estimating the SIF, introduces another type of constraint. The former, being much more simpler, is usually the preferred method; and it gives usually conservative estimates for the SIF. However, the AFM techniques, which are inherently more sophisticated, permits a better and more realistic evaluation of the SIF. Both methods were used in this study. A brief overview on the methodology of how to estimate the SIF in cracked structures is given in this section. Only the problem of thin pressure vessels and flat panels with through cracks in a state of plane stress is addressed.

Once the SIF is assessed, the rupture strength of the vessel is estimated by comparing the SIF against the material resistance to fracturing, i.e., the fracture toughness, K_{IC} .

AIII-2 STRESS INTENSITY FACTOR (SIF) DETERMINATION AT A CRACK TIP

Nowadays, several techniques exists to undertake stress intensity factor (SIF) evaluation at a crack tip. The following methods, among others, are used extensively:

- a) closed form solution for simple structural systems;
- b) displacement extrapolation;
- c) strain-energy release rate approach;
- d) virtual crack extension technique;
- e) virtual crack closure method, via FEM;

- f) strip yield model (Crack Opening Displacement, COD);
- g) path independent J - integral (RICE-integral).

In our study, we have adopted at first, the available closed form solutions for a quick SIF assessment. Then, we have utilized a combination of c, e, f, and g techniques.

a) Closed Form Solutions:

For isotropic cylindrical shells with through the thickness longitudinal cracks, closed form solution for the SIF calculation were developed by Folias [1] and Newman [2] some time ago and are here exhibited by Equation 1.0 and Equation 2.0, respectively. However, they are somewhat limited to low shell geometric ratio R/h (membrane radius to wall thickness ratio), and small crack lengths. They were used in this work-study for comparative purpose only.

FOLIAS (Through-Wall Axial Crack, Monocoque Shells, valid range: $5 < R/h < 50$)

$$\text{SIF}(\text{Mode I}) = \frac{p \cdot R_m}{h} \cdot \sqrt{\pi \cdot a_o} \cdot \sqrt{1 + 3.22 \left[\frac{(a_o)^2}{2 \cdot R_m \cdot h} \right]} \quad \text{Eq. 1.0}$$

p = internal pressure

a_o = half-crack length

R_m = shell membrane radius

h = shell wall thickness

NEWMAN (Axial Through Wall Crack, Monocoque Shells)

$$\text{SIF}(\text{Mode I}) = \frac{p \cdot R_m}{h} \cdot \sqrt{\pi \cdot a_o} \cdot F_N \quad \text{Eq. 2.0}$$

F_N = shell-curvature correction factor for an axial through-wall crack

$$= \left[1.0 + \left[0.52 \cdot \lambda_h + 1.29 \cdot (\lambda_h)^2 - 0.074 \cdot (\lambda_h)^3 \right] \right]^{0.50}$$

$$\lambda_h = a_o \cdot (\sqrt{R_m \cdot h})^{-1}$$

c) Strain-Energy Release Rate (SERR) Approach:

No formal derivations for the SERR will be presented in what follows as the approach is well established and readily found in the references cited by the bracketed numbers.

The energy rate **G** (Griffith energy criterion) can be regarded as the force tending to open the crack, and its evaluation requires only a knowledge of the stresses and displacements near the crack-tip. This approach was conceived also in a closed-form [3]. Following Griffith [4], and Irwin [5], the strain energy released is the work done in the process of advancing the half-crack length, a_0 , by an amount Δa by the stresses acting through the COD displacement (u_y) provided that Δa is small enough such that in the limit as $\Delta a \rightarrow 0$, the conditions $COD(a_0) \rightarrow COD(a_0 + \Delta a)$, and $X_a \rightarrow X_b$ are fulfilled (see Figure 3).

The work done (crack closure as derived by Irwin) at both ends for a two-dimensional crack is,

$$G_I = 2 \cdot \lim_{\Delta a \rightarrow 0} \delta \cdot \frac{1}{\Delta a} \int_0^{\Delta a} \frac{\sigma_y}{2} (\Delta a - X_a, 0) \cdot u_y(X_a, \pi) dX_a \quad \text{Eq. 3.0}$$

and,

$$\text{SIF (Mode I)} = \sqrt{G_I \cdot E \cdot \eta} \quad (\text{plane stress}) \quad \text{Eq. 4.0}$$

E = material elastic modulus of elasticity

η = dimensionless constant that depends on the material strain hardening exponent n , yield strength, and elastic modulus (elastic-plastic fracture mechanics). This constant is described later on this section.

e) Virtual Crack Closure Method via Finite Element Method:

One can employ the concept of virtual crack closure, as described previously, which measures the work required to close an increment of crack length Δa . The crack closure method allows, using Finite Element Analysis, to calculate the strain energy release rate by calculating the strain energy at single crack length. That is, only one Finite Element run with a fixed crack length is required, with the condition that the nodal pattern in front and behind the crack-tip (CTIP) are identical. In a two-dimensional, mode I situation, the strain energy release rate can be rewritten as

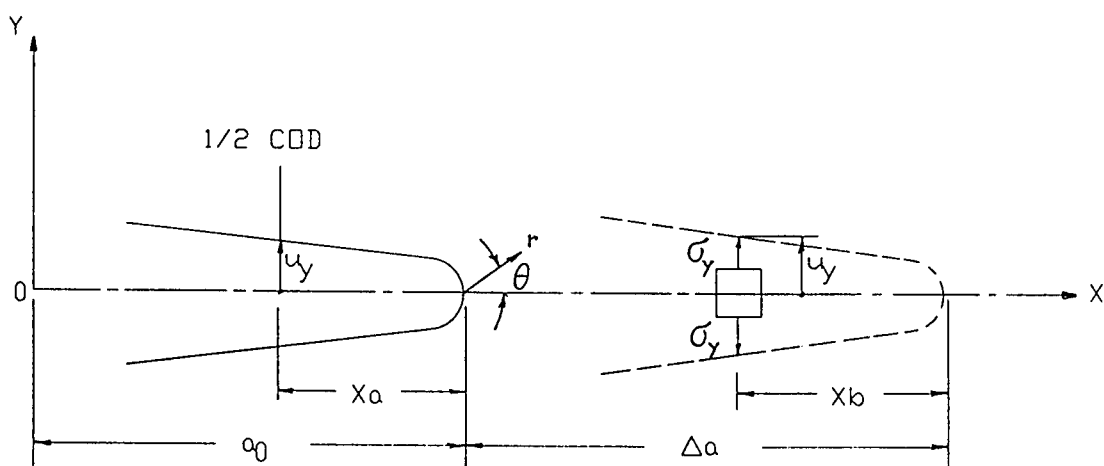


Figure 3 - SEGMENT OF CRACK OPENING

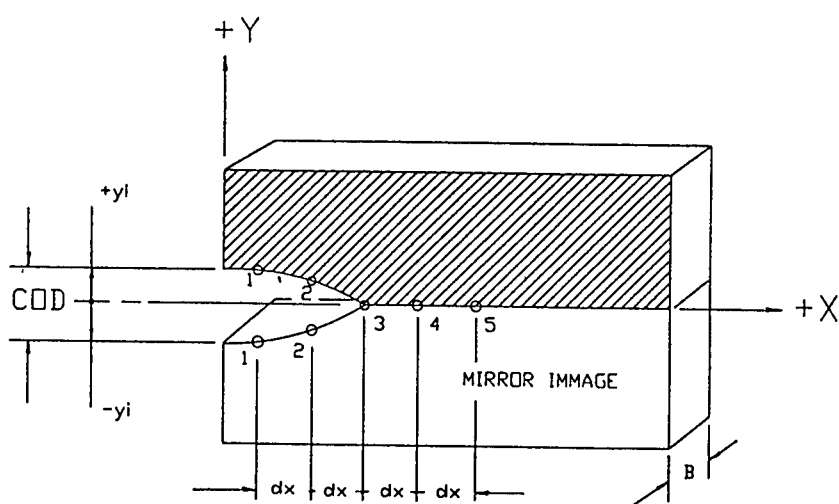


Figure 4 - CALCULATION OF ENERGY RELEASE RATE BY FINITE ELEMENT METHOD

$$G_I = \frac{1}{B \cdot 2 \cdot dx} \cdot \left(\sum_{i=1}^n Fy_i \cdot uy_j \right) \quad \text{Eq. 5.0}$$

where

Fy_i = normal component of the nodal forces ahead of the crack-tip

uy_j = net crack opening displacement = $(uy_i)_{upper} - (uy_i)_{lower}$

dx = nodes spacing (element length)

B = shell wall thickness or plate thickness

i = node number

j = $i - 2$ (according to the system shown in Fig. 4)

For a three-nodes spacing (two elements) configuration as shown in Figure 4, Equation 5.0 becomes:

$$G_I = \frac{1}{2 \cdot B \cdot dx} \cdot ((Fy_3 \cdot uy_1) + (Fy_4 \cdot uy_2)) \quad \text{Eq. 5.1}$$

Then, the SIF is obtained using Equation 4.0.

f) Strip Yield Model (COD):

Several techniques, both theoretical and experimental, have been taken to establish the relationship of the crack-tip opening displacement, which is variously called COD, CTOD and δ_T to K, J or SIF. In general, the reported relationships are of the form,

$$\delta_T = \lambda \cdot \left(\frac{K^2}{F_{ty} \cdot E} \right) \quad \text{Eq. 6.0}$$

The coefficient λ takes into account for the variations in the position at which δ_T is measured. Its value ranges from 0.25 to 1.0 [6]. Two common positions are shown in Figure 5. The crack-tip opening displacement (CTOD) at position II is frequently used, and a fairly representative value for λ is 0.60.

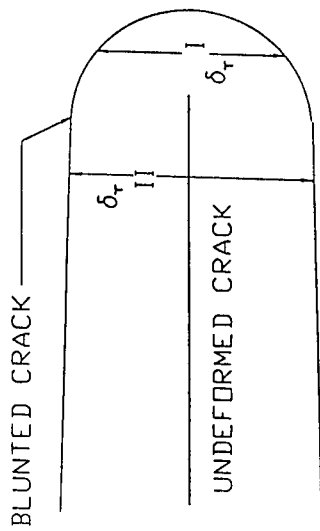


Figure 5 - TWO GENERALLY USED POSITIONS FOR MEASURING CTOD

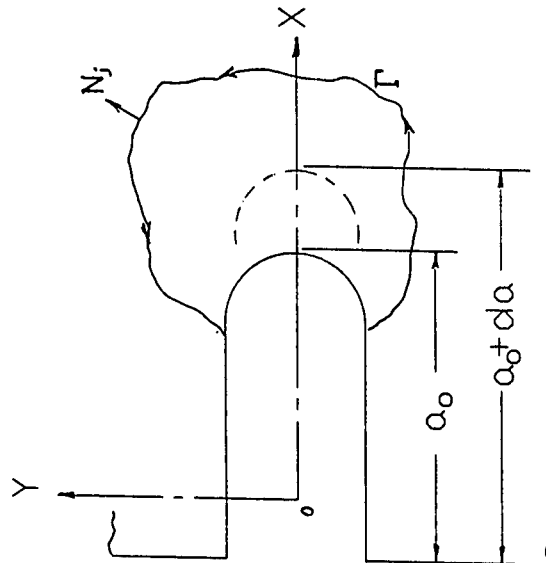


Figure 6 - ENERGY COMPUTATION FOR CRACK ADVANCE

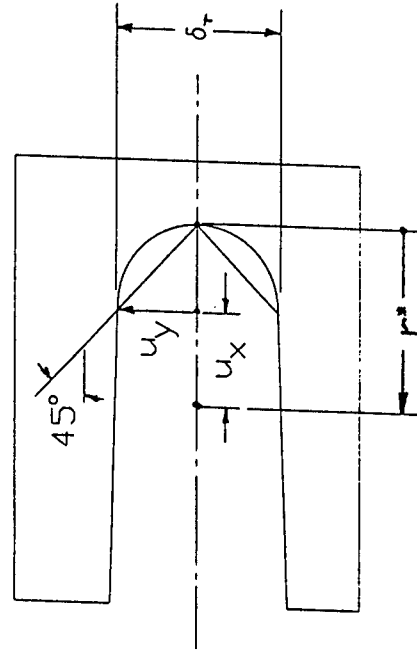


Figure 7 - ESTIMATION OF CTOD FROM 90° INTERCEPT

g) Path-Independent J - integral (RICE-integral)

James R. Rice [7,8] represented the energy rate as a path-independent line integral taken around the crack-tip for an homogeneous material as

$$J = \int_{\Gamma} W du_y - T \cdot \left[\left(\frac{d}{dx} u \right) \cdot ds \right] \quad \text{Eq. 7.0}$$

Here, Γ is a curve which surround the crack-tip, starting from the lower flat notch surface and ending on the upper flat notch surface, as shown in Figure 6. The curve is traversed in the counterclockwise sense, s is arc length, and $T = \sigma \cdot N$ is the traction vector on Γ according to an outward unit vector N normal to the curve. W is the strain energy density (SED), and u_y is the displacement in the y -direction.

Kishimoto *et al.* [9,10], and Aoki *et al.* [11], redefined Rice-Integral which consists of a line integral for the elastic strain energy and four additional area integrals to consider contributions of plastic strains, thermal strains, inertia forces and body forces, as follows:

$$J_j = \int_{\Gamma} \left(W_e \cdot N_j - T_i \cdot \frac{d}{dx_j} U_i \right) d\Gamma$$

$$+ \int \int_A \left[\sigma_{ij} \cdot \frac{d}{dx_j} \vec{\epsilon}_{ij} + \left[\rho \cdot \left(\vec{U}_i \right) - F_i \right] \cdot \frac{d}{dx_j} U_i \right] dA \quad \text{Eq. 7.1}$$

where, A is the area inside the contour Γ , W_e is the elastic strain energy density, U_i the displacement vector, \vec{U}_i the acceleration vector, σ_{ij} the stress tensor, T_i the traction vector which is defined by $T_i = \sigma_{ij} \cdot N_j$ and $\vec{\epsilon}_{ij}$ is the eigen strain tensor, ρ the mass density, and F_i the body force vector.

This eigen strain tensor can be regarded as the sum of the plastic and thermal strains.

Obviously, in cases without inertia force, body force, pressure loading on cracked surface or where eigen strains are neglected, Eq. 7.1 is reduced to Eq.7.0.

The elastic strain energy density (SED) is defined as $W_e = 1/2 \times \sigma_{ij} \times \epsilon_{ij}$; using Finite Element Method, SED can be derived directly from nodal principal stresses ($\sigma_1, \sigma_2, \sigma_3$), that is,

$$W_e = 2/E (\sigma_x^2 + \sigma_y^2 + \sigma_z^2) - \{ \nu/E (\sigma_x \sigma_y + \sigma_y \sigma_z + \sigma_x \sigma_z) \} \quad \text{Eq. 8.0}$$

if the crack faces are traction free, Eq. 7.0 reduces to $J_f = \int W_e dy$

On the Dimensionless Constant Eta (η)

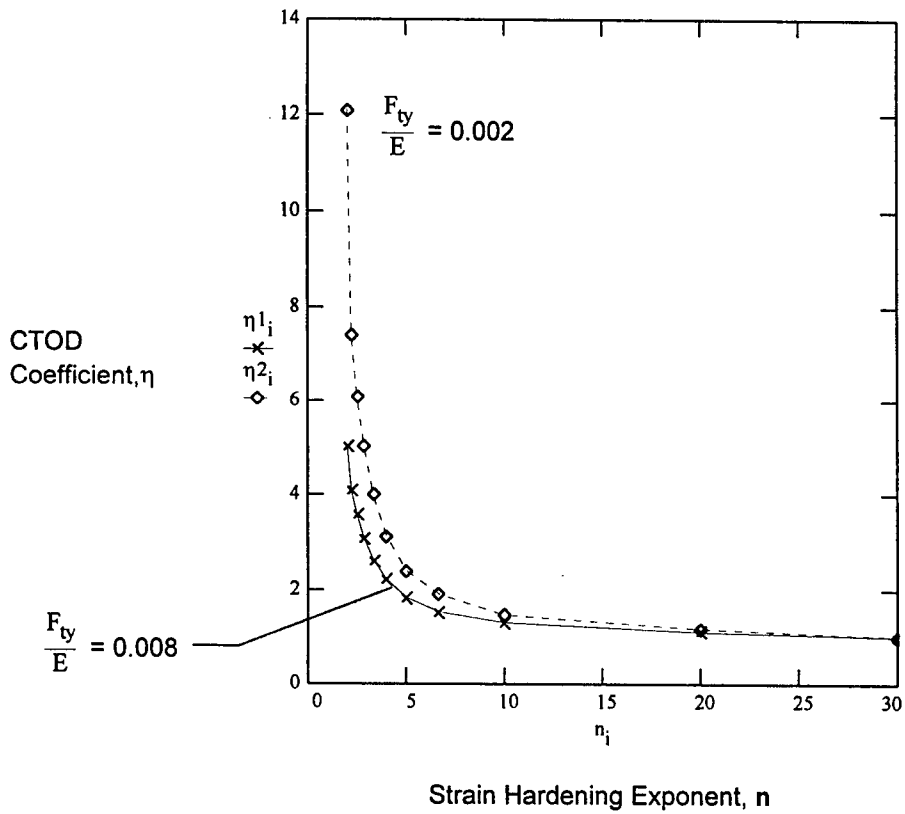
The dimensional constant η used in Eq. 4.0 is used when one performs an elastic-plastic fracture mechanics analysis of a cracked structure employing the crack-tip opening displacement (CTOD) technique (Figure 7) for determining the SIF. This constant exhibits a strong dependence on the material strain hardening exponent (n) and a mild dependence on the yield strength to elastic modulus ratio, as shown in Figure 8. Generally, in the fracture mechanics literature, the reciprocal of this constant ($dn = 1 / \eta$) function of the reciprocal of the strain hardening exponent ($1 / n$) is plotted [12, 13]. For nonhardening material ($n = \infty$) in plane stress, this constant is equal to unity.

SUMMARY ON THE SIF

For simple structure and for Mode I loading, the SIF can be assessed using the following expression,

$$\text{SIF} = C \sigma (\pi a_o)^{0.50} \quad \text{Eq. 9.0}$$

where C is a dimensionless geometry correction factor, and σ is a characteristic stress. Thus, fracture analysis (EFM) of a linear structure is relatively easy to perform, once a SIF solution is obtained for a particular crack geometry. Refer to Appendix B for additional known closed form solutions toward estimating the SIF in through-cracked monolithic cylinders.



The CTOD Coefficient η is used in the following expressions:

$$1) \text{ SIF} = \sqrt{J \cdot E} = \sqrt{\delta_T \cdot \sigma_0 \cdot \eta \cdot E}$$

$$2) \quad J = \delta_T \cdot \sigma_0 \cdot \eta \quad (J\text{-integral})$$

where

σ_0 = Material Tensile Yield Strength = F_{ty}

δ_T = Crack Tip Opening Displacement (CTOD)

E = Material Modulus of Elasticity

Figure 8 - PREDICTED J-CTOD RELATIONSHIPS FOR PLANE STRESS
(CTOD Coefficient η versus Material Strain Hardening Exponent n)

However, for complex structures and loading conditions, as reinforced-skin pressure vessels, one as to rely on more sophisticated techniques, as described above and like the ones used in advanced fracture mechanics (AFM) and nonlinear computational mechanics (NCM). For instance, in cracked pressure vessels, in addition to the classical Mode I (opening mode) loading, one has to consider the effect of local crack bulging due to the internal pressure. This problem is addressed next.

AIII-3 NONLINEAR CRACK BULGING EFFECT on the SIF

David Y. Jeong and Pin Tong [14] summarized very well the problem of bulging effect on the SIF of a cracked pressure vessel. Bulging refers to the rotation and deflection of the edges of a longitudinal crack in a pressurized thin shell as shown in Figure 9. Its main effect is to introduce local bending at the crack-tip and therefore affecting the value of the SIF calculated using only the hoop (or normal) stress to the crack length. However, the bulging factor (β) is employed only when one uses closed form solution for determining the SIF in curved and unreinforced panels. That is, its applicability is restricted, somewhat, to simple monocoque isotropic shells.

Bulging factors have been earlier developed empirically by Kuhn [19] and analytically by Folias [1] as displayed by Eq. 10.0 and Eq. 11.0 respectively.

$$\beta = 1 + 10 \cdot \left(\frac{a_o}{R} \right) \quad \frac{R}{h} \geq 100 \quad \text{Eq. 10.0}$$

$$\beta = \sqrt{1 + 0.317 \cdot \lambda^2} \quad \lambda = \frac{a_o}{\sqrt{R \cdot h}} \cdot \sqrt{12 \cdot (1 - \nu^2)} \quad \text{Eq. 11.0}$$

where, R = shell radius, h = shell wall thickness, a_o = half-crack length,
 ν = Poisson's ratio

A better derivation of this factor using a strain energy approach combined with dimensional analysis, was proposed by Jeong and Ping [14] as follows:

$$\beta = \sqrt{1 + \alpha \cdot \left[\left(\frac{E}{\sigma_o} \right) \cdot \left(\frac{a_o}{R} \right)^2 \right]^{\frac{2}{3}}} \quad \text{Eq. 12.0}$$

here, E = material Young's modulus, σ_o = material tensile yield strength

INTERNATIONAL SPACE STATION ALPHA

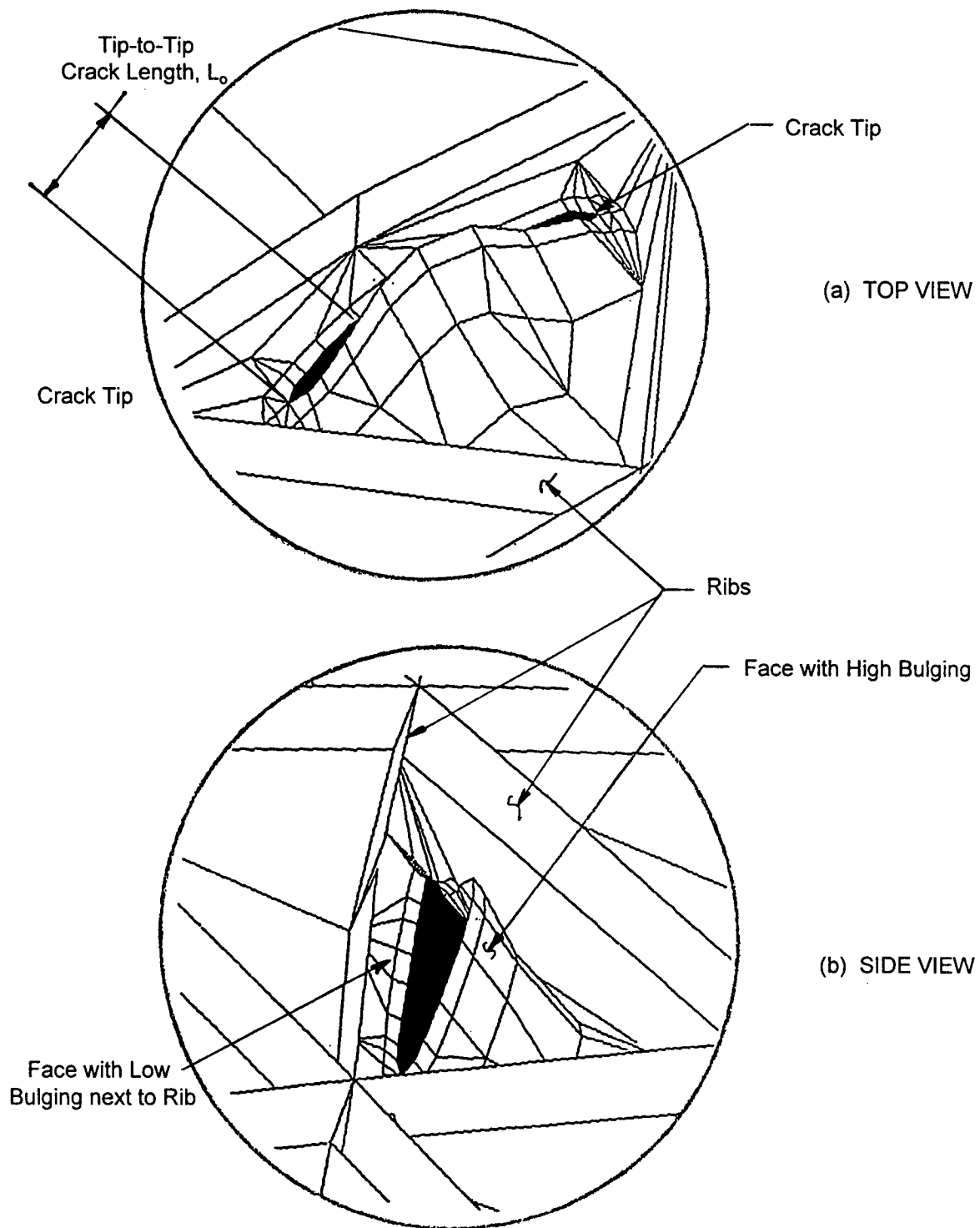


Figure 9 - CRACK BULGING TYPICAL SCENARIO

Shown Here is a FEM of the ESA MPLM Shell with a Longitudinal Crack Between Ribs
(Note the Uneven Bulging of the Crack Faces due to the Presence of Ribs)

Thus, for curved panels, the crack resistance in terms of SIF rely on β and Eq. 9.0 is rewritten as follows,

$$\text{SIF} = C \beta \sigma (\pi a_o)^{0.50} \quad \text{Eq. 9.1}$$

AIII-4 ALUMINUM ALLOY 2219-T87 MATERIAL FRACTURE TOUGHNESS DATA

As indicated earlier, once one has determined the SIF of a particular cracked body, the assessment of the level of criticality for catastrophic failure is done by comparing the fracture capability, or fracture toughness (K) of the material that the body is made of, with the SIF. The difficulty arises on obtaining and selecting the appropriate K . Most fracture mechanics work are deterministic; i.e., a single value of fracture toughness is used to estimate failure loads or critical crack length (CCL). However, as we know, much of what happens in the real world is not predictable per se. Other factors may also introduce uncertainty into fracture analyses. It is well known that, the intrinsic problem in designing large structures involves the extrapolation of strength and reliability data obtained from small coupon test specimens to values appropriate to the large structure in consideration. Due to these complexities, fracture should be viewed probabilistically rather than deterministically.

We have researched and reviewed the pertinent literature and test data furnished by NASA (R. Foreman, JSC [17]) and other sources (Dr. N. Elfer, Martin Marietta [16], and Dr. J. Gallagher, UDRI/US Air Force [15]) on the fracture toughness of the Aluminum Alloy 2219-T87 that the ESA MPLM shell structure is made of. Some of the material property data on the Al/Al 2219-T87 is attached in this report as Appendix A. The gathered data indicated much more scatter in fracture toughness than anticipated. Therefore, a statistical evaluation of the various parameters affecting the toughness values was in order. We have used the extreme value (or Weibull) statistical distribution function, which has been widely applied in materials science and engineering, to the available data. Of relevance here, is the data published by Gallagher [15], which was reduced as shown in Figure 10. We have classified two main levels of fracture toughness function of the Weibull reliability R namely: A and B which represent a lower shelf and upper shelf, respectively, of the data. The performed statistical analysis indicated a lower shelf mean value of $83.5 \text{ KSI-in}^{0.5}$ and an upper shelf mean value of $93.8 \text{ KSI-in}^{0.5}$ for the fracture toughness. These values, of course, are applicable to the type of center cracked tension (CTT) type specimen used for testing with a thickness of 0.100 inch (thin sheet) and under the state of plane stress conditions; i.e., thicker test specimen (state of plain strain) will yield much lower values for the fracture toughness.

Next, one has to consider the fracture mode and the type of material utilized. The fracture mode is one of either brittle cleavage or ductile tearing. For aluminum alloy type of materials, the fracture mode (at room temperature) is mostly ductile tearing. In addition, one also to take into consideration the effects of the strain hardening exponent n (discussed previously) on the fracture parameters.

INTERNATIONAL SPACE STATION ALPHA

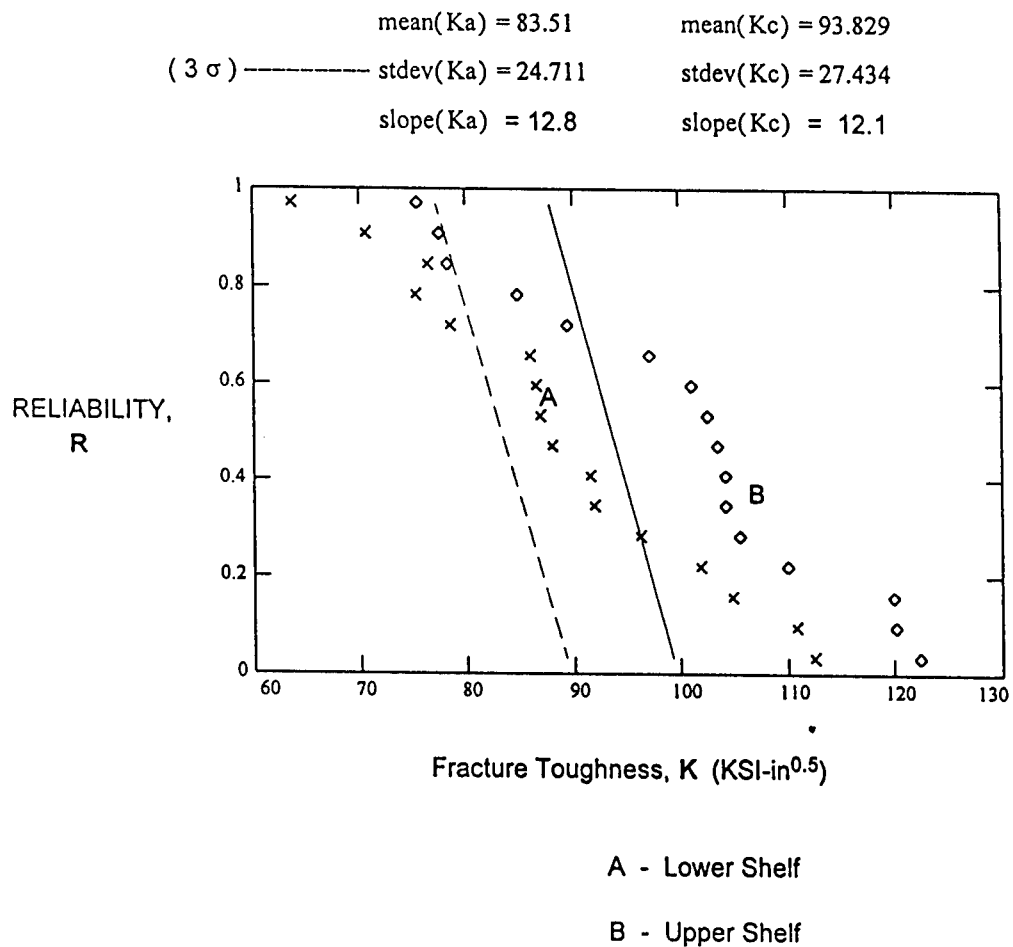


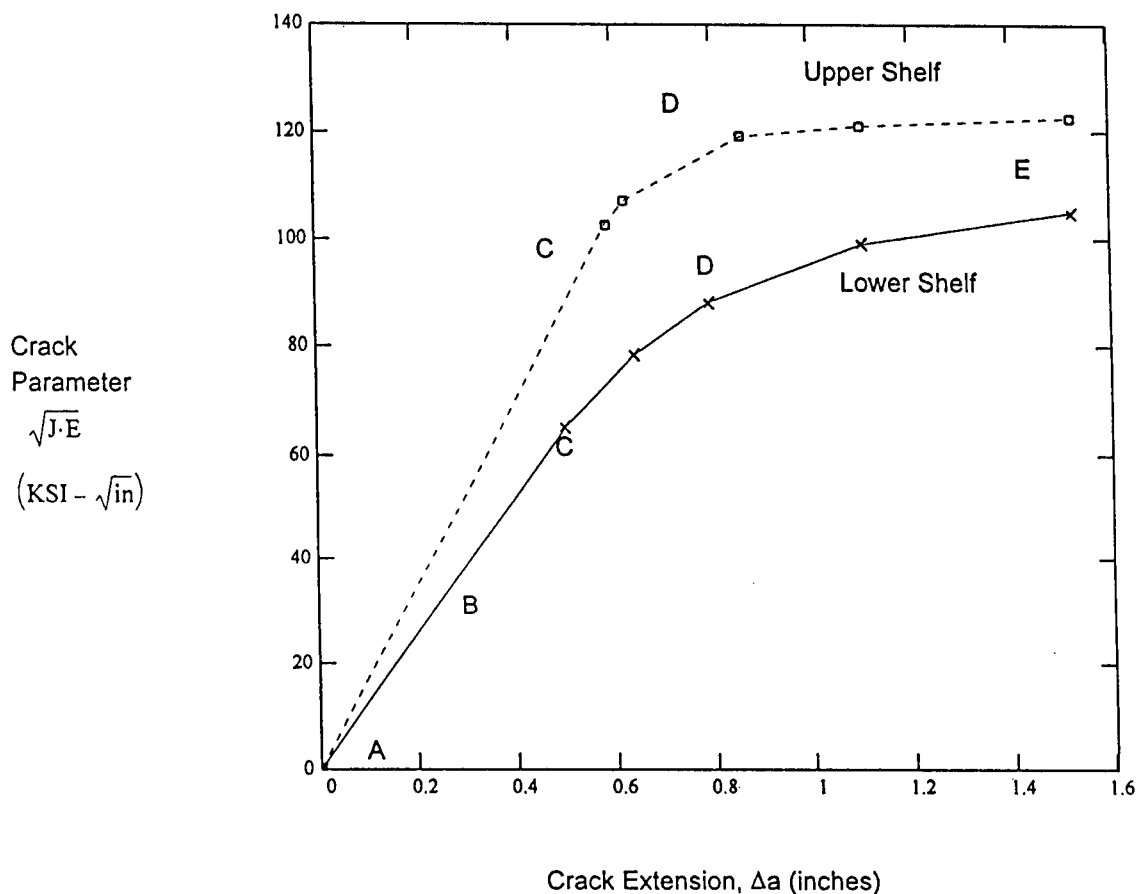
Figure 10 - WEIBULL FRACTURE TOUGHNESS DISTRIBUTION
 for 2219-T87 Aluminum Alloy
 (Re.: J. Gallager [15], UDRI, 1983; CCT specimen thickness = 0.100 inch,
 width = 48 inch, L-T grain direction)

Most often, ductile fracture is characterized by a plot of **K** for **EFM** or **J** for **EPFM** versus ductile crack extension called the fracture resistance curve or R-curve. Based on the Gallager data, we have generated the **J-R** curves for the lower and upper shelves of the 2219-T87 aluminum alloy as illustrated in Figure 11.

Fracture toughness tests were also performed in 1986-1987 on Center Cracked Tension (CCT) specimens with a thickness of 0.128 inch and with a width of 24.0 inches of 2219-T87 aluminum alloys by Dr. Elfer[16]. Based on the test results, R-curves were generated as shown in Figure 12. Finally, in 1993 Southwest Research Institute (SwRI), San Antonio, Texas, conducted limited fracture tests on the same material [18]. Quasi-static and dynamic fracture toughness values were obtained. The objective of the SwRI program study was to obtain dynamic toughness and compare it to the quasi-static one. It was concluded that the quasi-static plane stress toughness **J-R** curve is lower than the dynamic plane stress toughness **J-R** curve. The SwRI **J-R** curve for the quasi-static regime is shown in Figure 13.

From the published data by Elfer, and Foreman, we have generated the corresponding Weibull reliability versus the fracture toughness. A comparison of the **K** distribution for the three data banks is shown in Figure 14. One can readily realize the large data scatter for **K** function of its reliability. At this point, which data set one will choose for conducting a failure tolerance analysis of a particular structure made of 2219-T87 aluminum alloy? The answer is that the data scatter is due to test specimen geometry (width, height and thickness) for one, and secondly on how the **K** (or SIF) was derived. Gallager test data was generated with a somewhat large CCT specimen (width = 48.0 inches). Whereas, Elfer test specimen were 24.0 inches in width by 44.0 inches in height with a thickness of 0.128 inch. Therefore, one can conclude that the size effects are extremely important and should be taken into account for determining the fracture parameters of a particular material, as depicted in Figure 15. Note that, all data shown are at room temperature conditions.

Based on the available data for 2219-T87 and on the 5456 series Aluminum Alloys, we have grouped the fracture toughness and other pertinent data for the ISSA Manned Modules as shown in Table II. Note that, here, we have selected two values for the fracture toughness, as a function of the module's wall thickness, at crack initiation & stable growth, and at crack unstable propagation (critical plateau), respectively. One standard deviation ($\pm 1 \sigma$) on the toughness is also listed.



- A - Start: Sharp Crack, No Loading
- B - Step 1: Crack Tip Blunting
- C - Step 2: Initiation of Stable Crack Growth
- D - Step 3: Stable Crack Growth
- E - Step 4: Ductile Instability

Figure 11 - J-R CURVES FOR 2219-T87 ALUMINUM ALLOY
 - *representation of the ductile fracture process* -
 (Adapted from test data published by J. Gallager [15], UDRI, 1983;
 panel thickness = 0.100", panel width = 48.0", L-T grain direction)

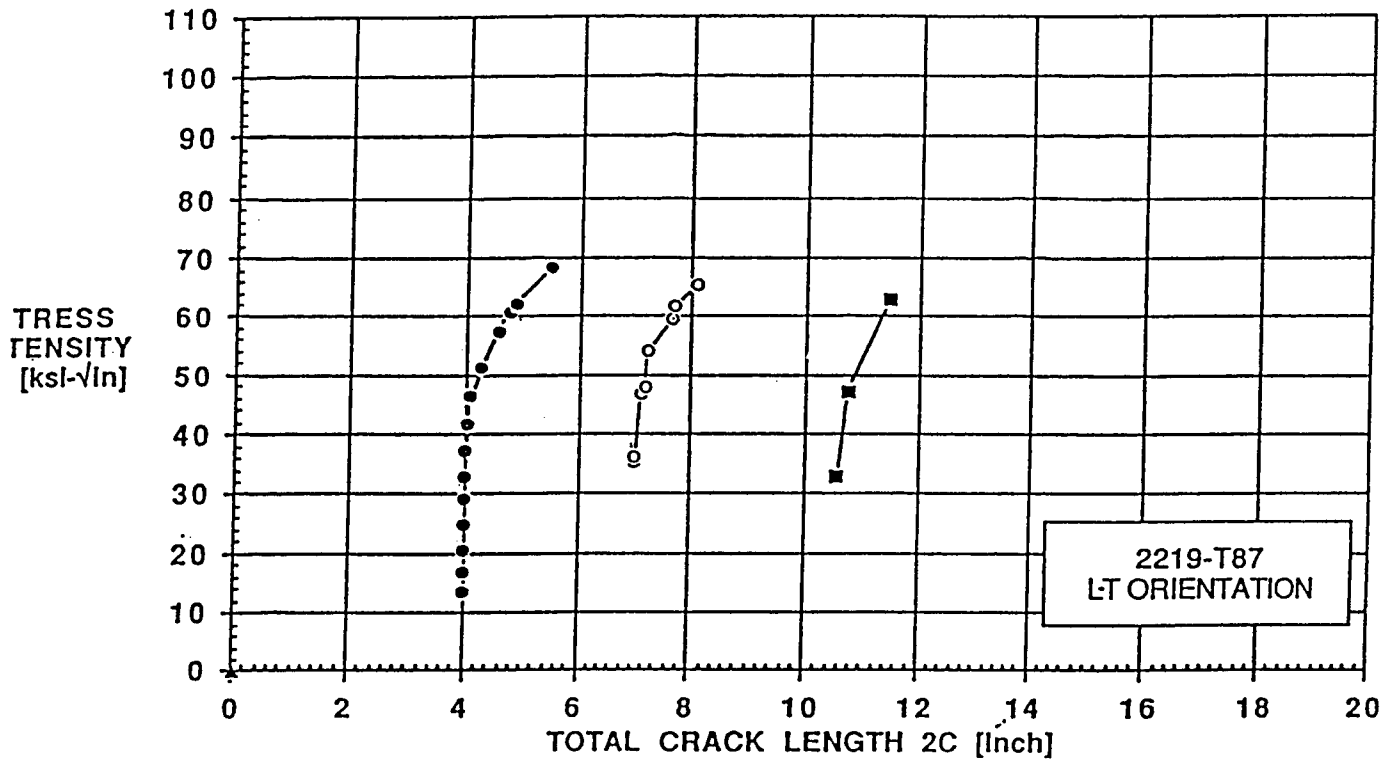


Figure 12 - **R-CURVES** for 2219-T87 Aluminum Alloy, L-T Orientation
(Ref.: Dr. N. Elfer, Martin Marietta Manned Space Systems,
Michoud Assembly Facility, New Orleans, LA 70189,
IR&D Report No. S87-47501-001, July 1987)

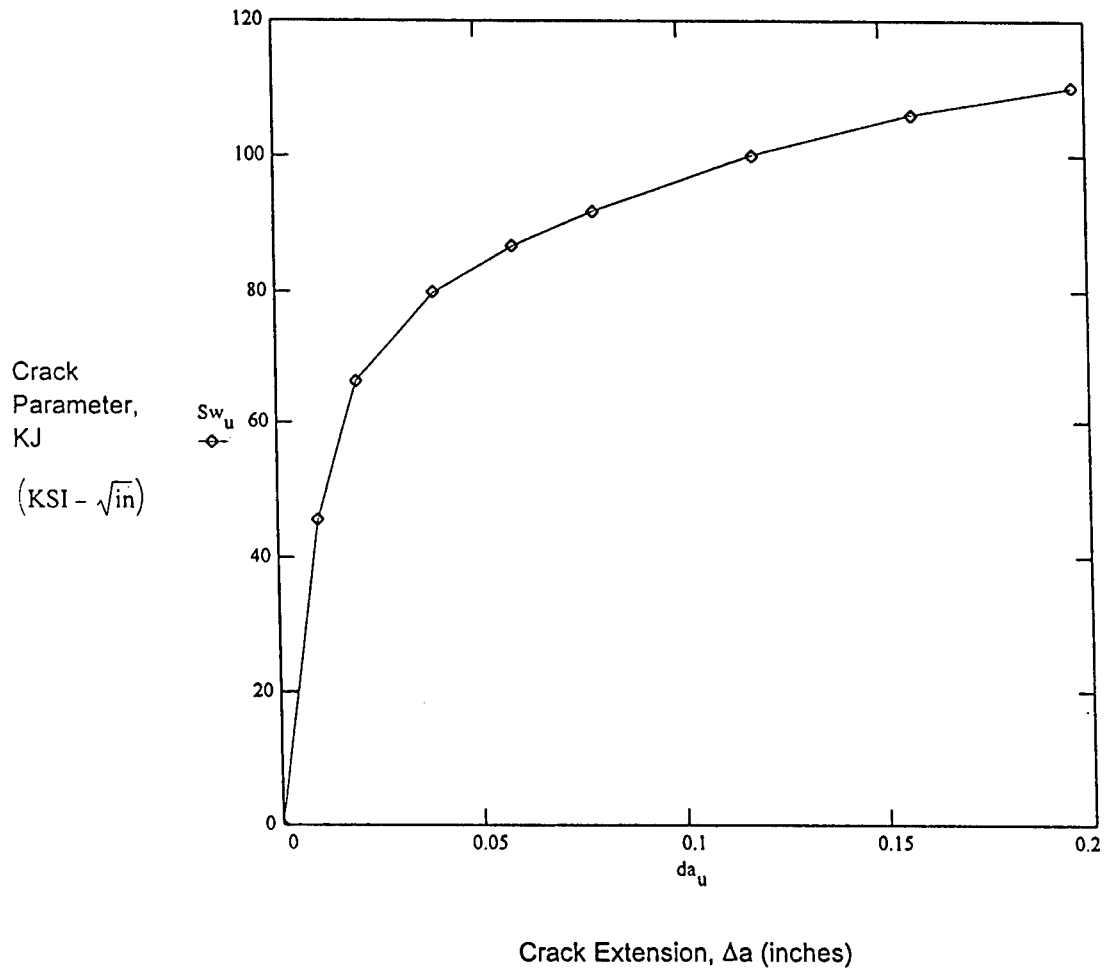


Figure 13 - J-R CURVE for the QUASI-STATIC CCT SPECIMEN
(Adapted from SwRI work-study [18] performed in 1993 with
CCT test specimen of 0.125 inch thick)

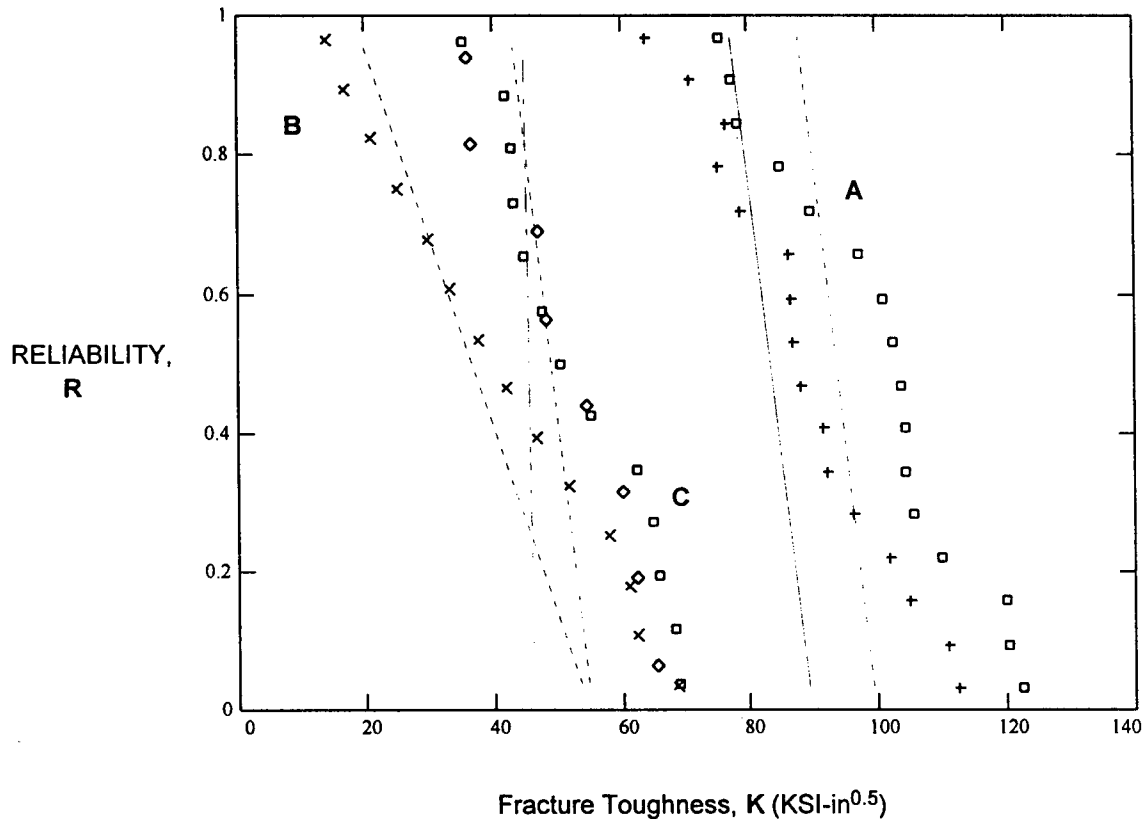
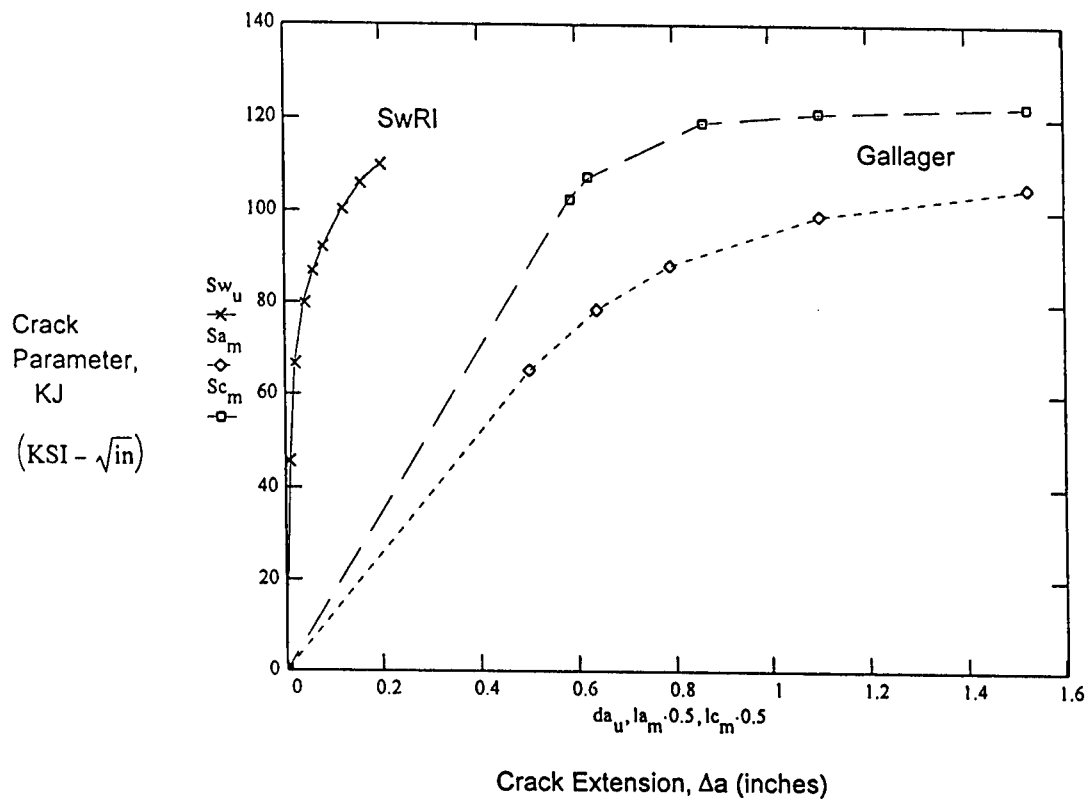


Figure 14 - COMPARISON of the WEIBULL FRACTURE TOUGHNESS DISTRIBUTION for Three Published Data Bank for 2219-T87 Aluminum Alloy



SwRI - CCT width = 3.0" x height = 4.0" x thickness = 0.125"

Gallager - CCT width = 48.0" x height = 36.0" x thickness = 0.100"

Figure 15 - DERIVED J-R CURVES for two CCT TEST SPECIMEN
made of
Aluminum Alloy 2219-T87

TABLE II - MATERIAL FRACTURE TOUGHNESS ESTIMATES for THE ISSA MANNED MODULES

MODULE TYPE	DESIGN DATA		FRACTURE TOUGHNESS K (KSI-in ^{0.5})				
	MAT'L (Al / Al)	WALL minimum thickness (in)	TEST Conditions	One Standard Deviation (+/- 1σ)	Stable Initiation & Growth	Unstable Propagation or Unzip (critical)	Strain Hardening Exponent (n)
US Hab & Lab	2219-T87	0.188	Static	6.7	62.0	87.0	14
ESA MPLM	2219-T87	0.098 0.118	Dynamic	N/A	79.0	101.0	N/A
NASDA JEM PM	2219-T87	0.126	Static	8.2 7.9	83.5 79.0	113.0 107.0	14 14
RUSSIAN FGB	5456-0	0.063	Static	7.8	77.0	105.0	14
				N/A	80.0	N/A	50

Note: 1) Fracture Toughness Data for the Russian Module was not made available during this study.

The mean was conservatively estimated from 5456-H117 and H321 US AIAI test Data.

2) The listed Fracture Toughness' for all other Modules were extrapolated as explained in the body of this report.

3) Dynamic Fracture Toughness Data for 0.188 inch thickness test specimen was provided by SwRI (1993).

4) N/A = Not Available (also, not applicable)

AIV - CRITICAL CRACK LENGTHS

AIV-1 PROLOGUE

This section presents a summary on the analytical study performed and the results obtained on assessing the Stress Intensity Factor (SIF) function of Crack-Length (CL) for the respective ISSA habitable modules, and selected high pressure tanks of the Russian FGB module. A combination of numerical methods, like the Finite Element Method (FEM) and closed form solutions outlined in Section III, were employed in the study.

For comparative purposes and to determine the spread of the pertinent results, several fracture criterion were utilized for deriving the SIF. In general, more accurate results on the SIF are obtained by employing numerical techniques as the FEM by modeling the particular shell of interest with all its geometric and construction details, in contrast of published closed form solutions which are applicable only to unreinforced-skin cylindrical shell structures. We have used essentially two finite element codes: 1) ALGOR 3D Linear Stress Solution, and 2) ELASTO 2D Elasto-Plastic Plane Stress Solver. ALGOR is a well-know FEM package, being commercially available for quite some time. The ELASTO 2D FEM computer program was developed, for the stress analysis of plane structure in the elastic-plastic regime, during the Space Station Freedom Program [20].

Once the stresses at the crack-tip and the crack opening displacements (CTOD, and CMOD) were obtained for a particular crack length and shell geometry, the SIF was estimated using selected closed form solutions listed in Section III-B and Section III-C. For this purpose, we have utilized the MathCad software package that runs under Windows environment. MathCad is a powerful spreadsheets computer program, and work with formulas, numbers, text, and graphs. Then, the SIF was compared to the material fracture toughness (K) as outlined in Section III-D, function of the shell minimum thickness and the type of aluminum alloy material that the shell is constructed with, to assess the SIF in question.

Note that, all analyses were performed under quasi-static (time independent) loading conditions. That is, the principal driver for crack opening and crack extension is the hoop (circumferential) stress, due to the internal pressure (14.9 psia) loading.

AIV-2 UNITED STATES of AMERICA COMMON MODULE (i.e., HAB & LAB)

For the US module we have assessed the SIF for two particular regions of the structure that was considered critical, namely the main shell with a waffle-skin (orthotropic) design, and one of the End-Cone's. The employed analytical procedure and pertinent results obtained for the cylindrical shell are outlined in Section AIV-2.1. Similarly, Section AIV-2.2, address the SIF for the end-cone.

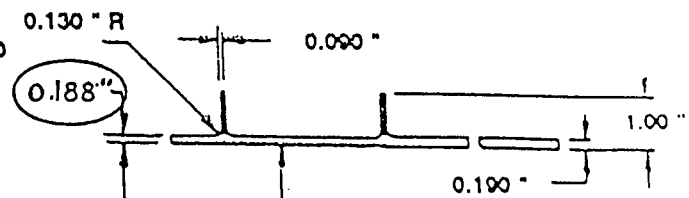
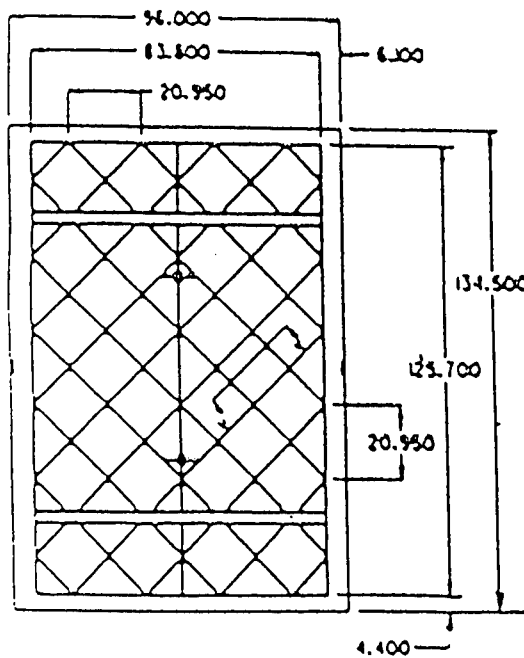
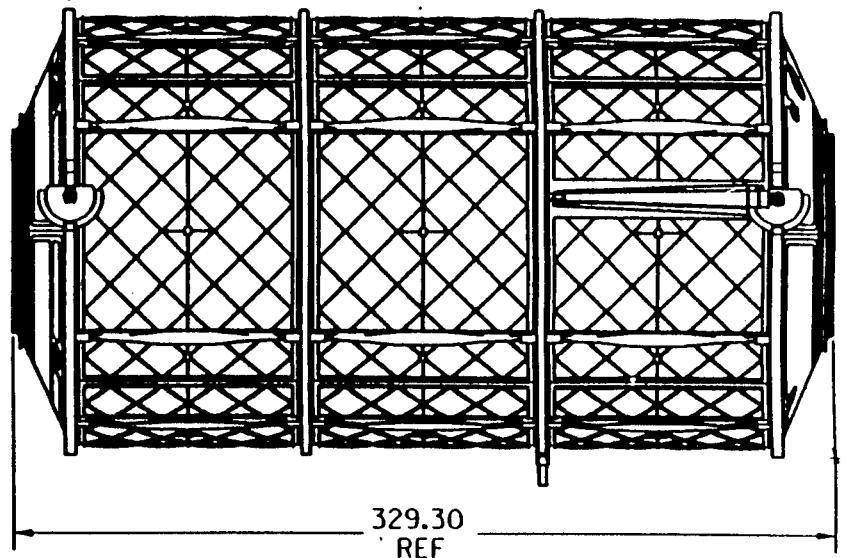
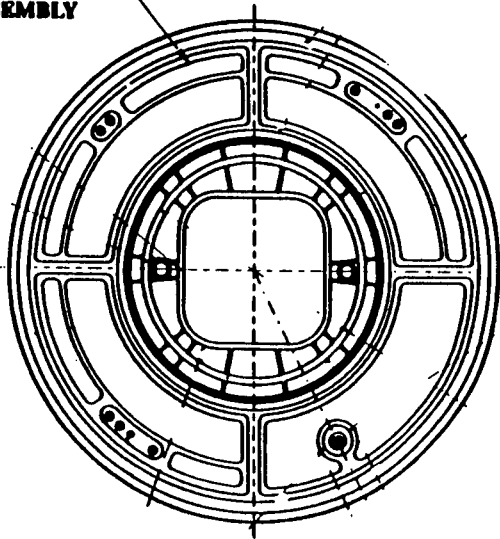
AIV-2.1 MAIN CYLINDRICAL SHELL

The US Common Module Shell overall arrangement with its waffle-skin Design Details are shown in Figure 16.

We have performed at first, a 3D elastic finite element analysis (FEA) using the ALGOR computer program of a segment of the module shell wall to determine the stress distribution within the Waffle-Skin, without cracks, under a 14.9 psia internal pressure loading. Figure 17 illustrates the 3D FEA model. Figure 18 displays the principal stress distribution within the wall. Then, we have conducted a plane stress nonlinear elasto-plastic finite element analysis, using our ELASTO code, of a discrete section of the waffle-skin using a center cracked tension (CCT) analytical specimen as shown in Figure 19 through Figure 21. This CCT model possess all the features of the Waffle-Skin design, including the reinforcement at the joints and the fillet radius at the rib to skin intersection. The loading conditions consisted of the hoop stress and axial stress (biaxial loading conditions) that were obtained from the 3D FEA. We have performed several computer runs, whereby the crack length was extended progressively (crack growth by unzipping of nodes), from the waffle-skin cell center-line to the rib joint. The resulting crack-tip (CTIP) opening displacements (CTOD) and crack mouth opening displacements (CMOD), as illustrated in Figure 22, were recorded and catalogued as functions of the crack length. The data was then stored in a file that can be retrieved and used with the MathCad program.

We have here, utilized three fracture criterion for assessing the SIF, two of which are applicable to through the wall cracks in pressure vessels. They are displayed in Figure 23 and have all in common the crack bulging factor (β) due to internal pressure. However, Folias and Jeong & Tong criterion uses Linear Elastic Fracture Mechanics (LEFM) principles, and applies to monolithic and isotropic shells only, whereas MA-1 parameter uses the CTOD and J contour integral developed by Rice.

GORE PANEL
ASSEMBLY

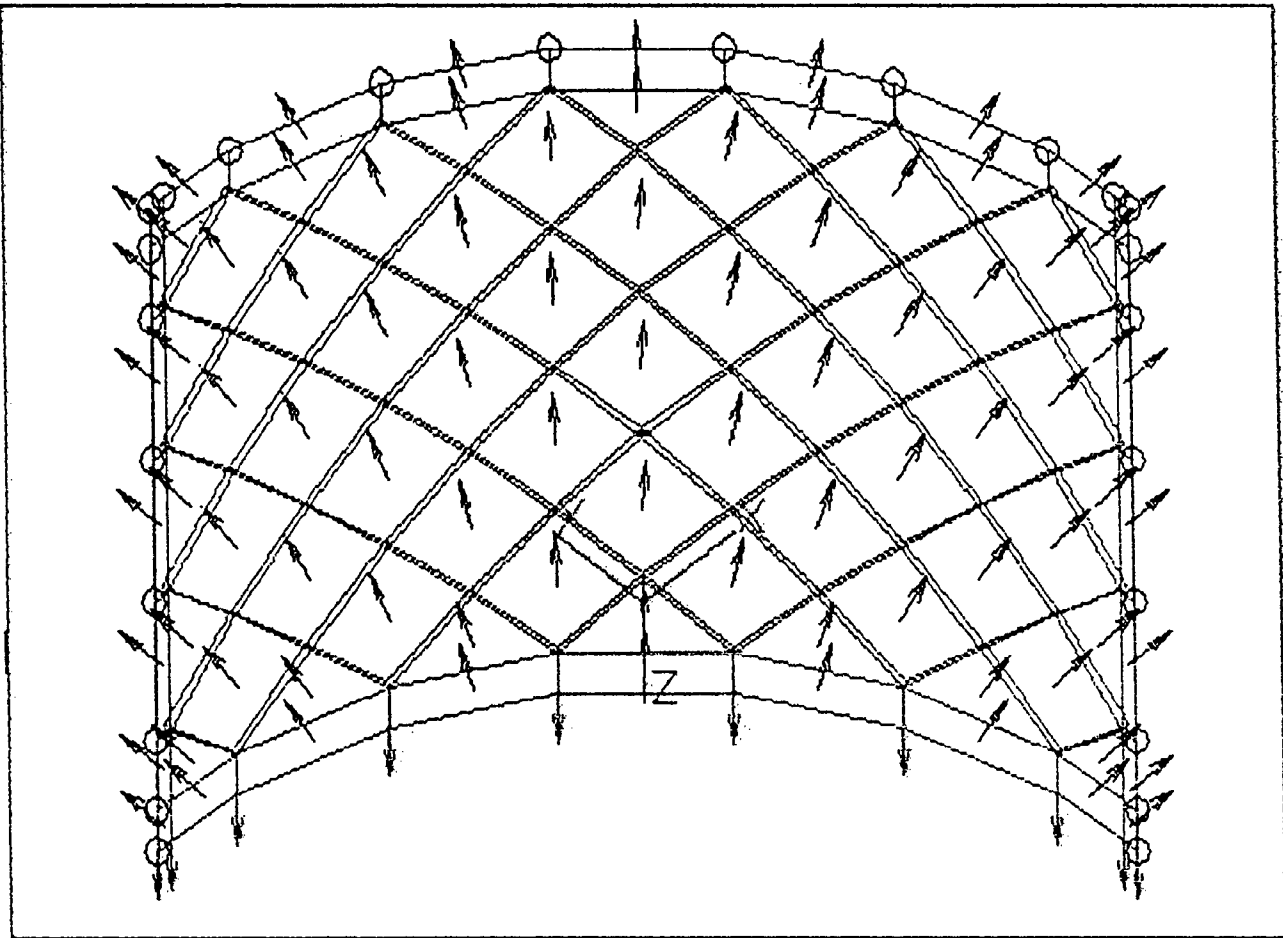


SECTION U-U

INTERNAL DIAMETER = 168. inch

TYPICAL WAFFLE
SKIN PANEL

Figure 16 - US COMMON MODULE SHELL and WAFFLE-SKIN DESIGN DETAILS



Shell with a Stiffened Waffle-Skin Construction

Internal Radius = 83.0 inch

Pressure Wall Minimum Thickness, $h = 0.188$ inch

Waffle-Grid Pitch Spacing = 20.95 inch (axial & circumferential)

Rib Height and Thickness = 1.00 x 0.90 inch

Material: Aluminum Alloy 2219-T87

Figure 17 - US COMMON MODULE SHELL 3D FINITE ELEMENT 1/4 (90°) MODEL
OVERALL ARRANGEMENT - TOP VIEW

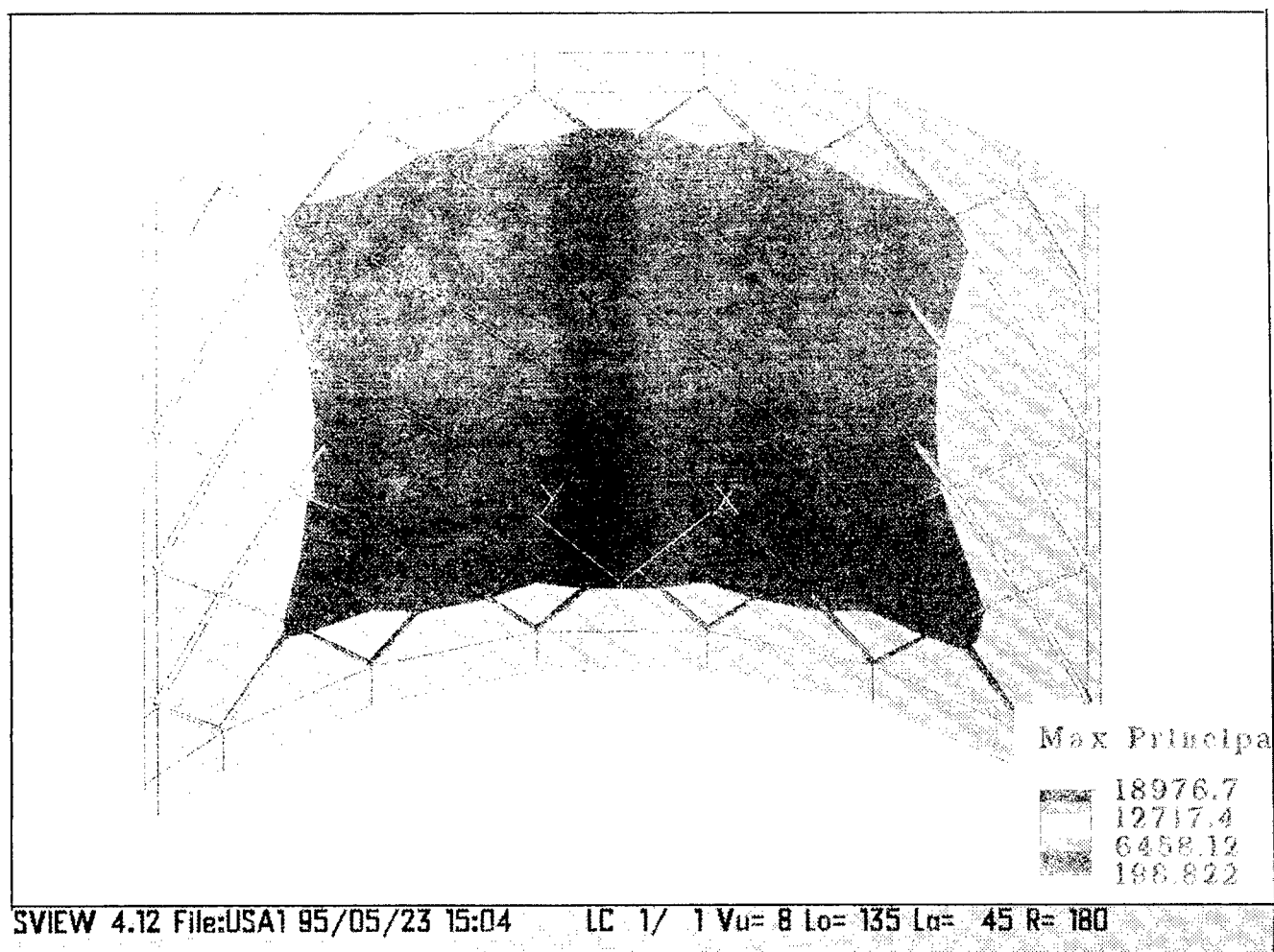


Figure 18 - US COMMON MODULE SHELL 3D FEA 1/4 (90°) MODEL
PRINCIPAL STRESS (psi) DISTRIBUTION
 (At an Internal Pressure of 14.9 psia and Axial Blow Out Load)

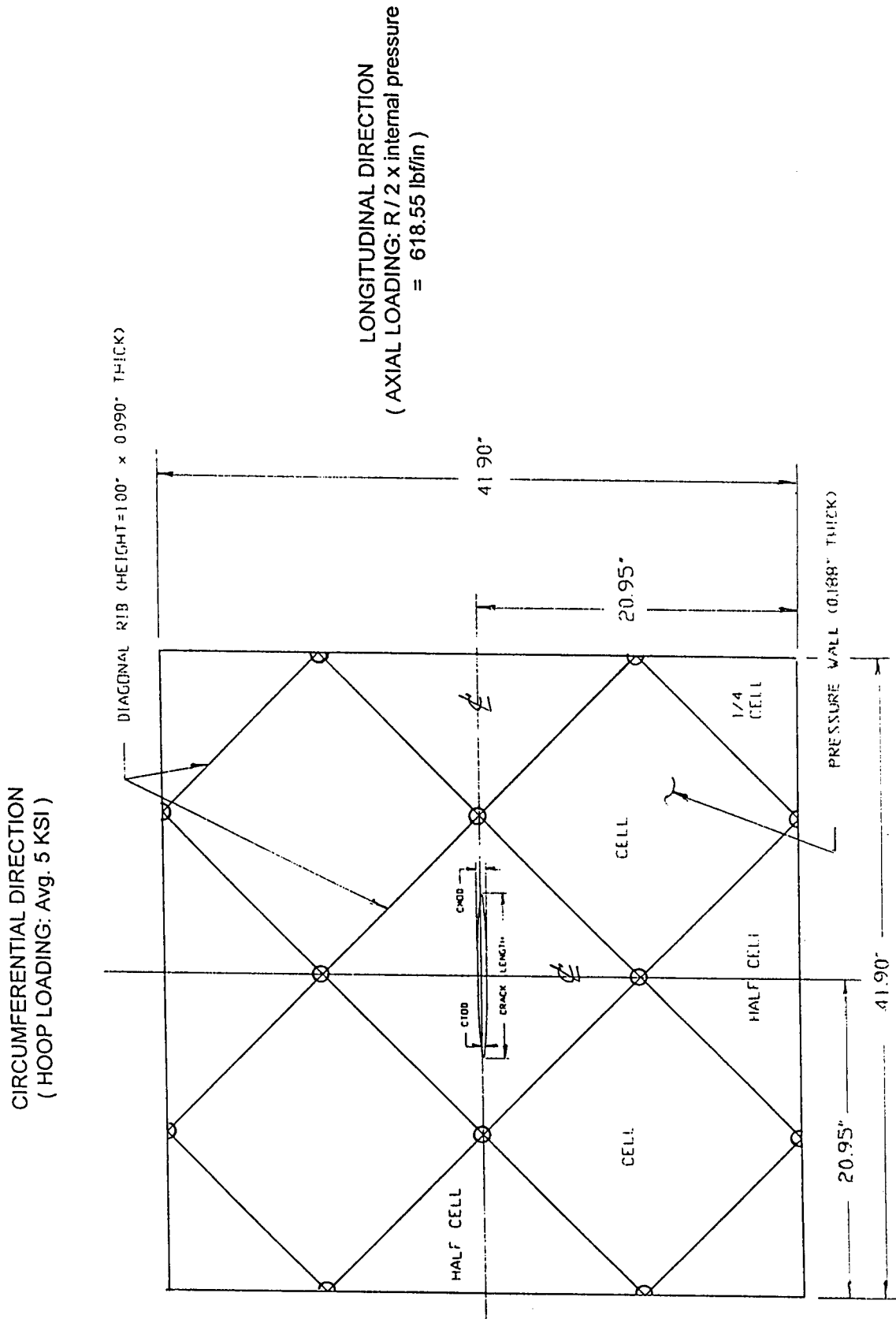


Figure 19 - CCT FLAT PLATE ANALYTICAL SPECIMEN OVERALL CONFIGURATION
for the US MODULE SHELL WAFFLE-SKIN

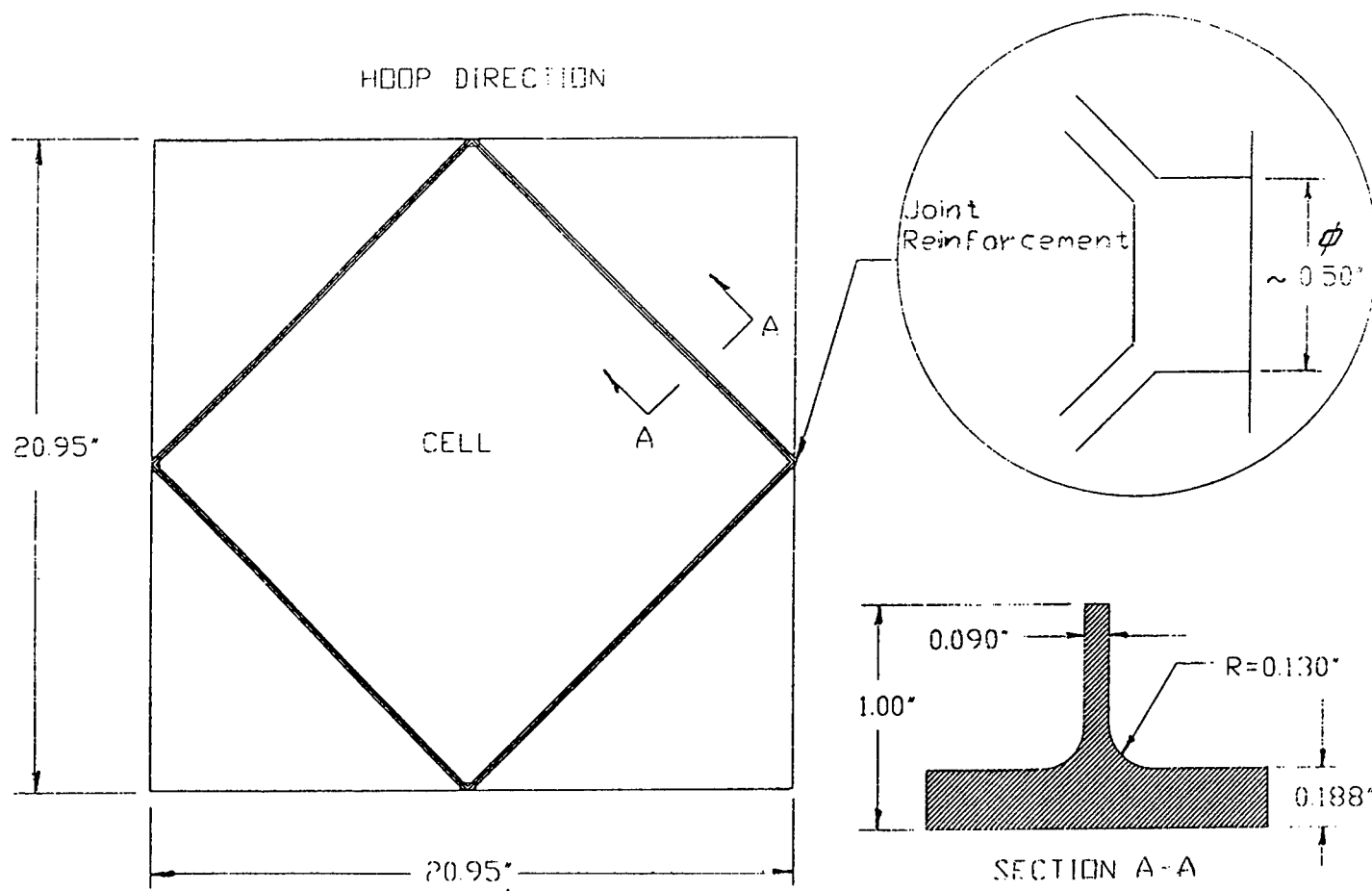


Figure 20 - CCT FLAT PLATE ANALYTICAL SPECIMEN for the US MODULE WAFFLE-SKIN
PRIOR TO FINITE ELEMENT MESHING
(A Quarter Model was only necessary due to symmetry)

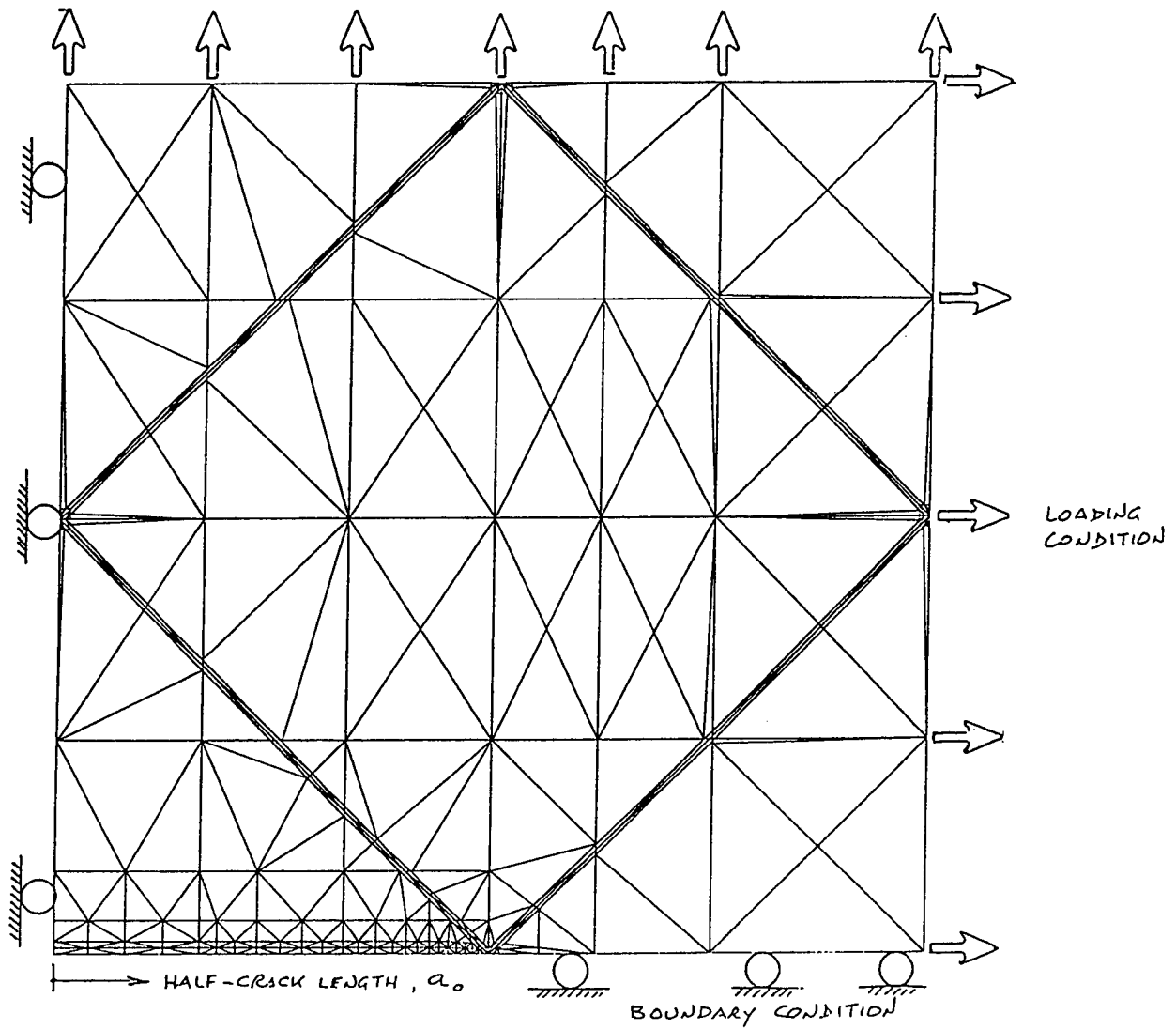
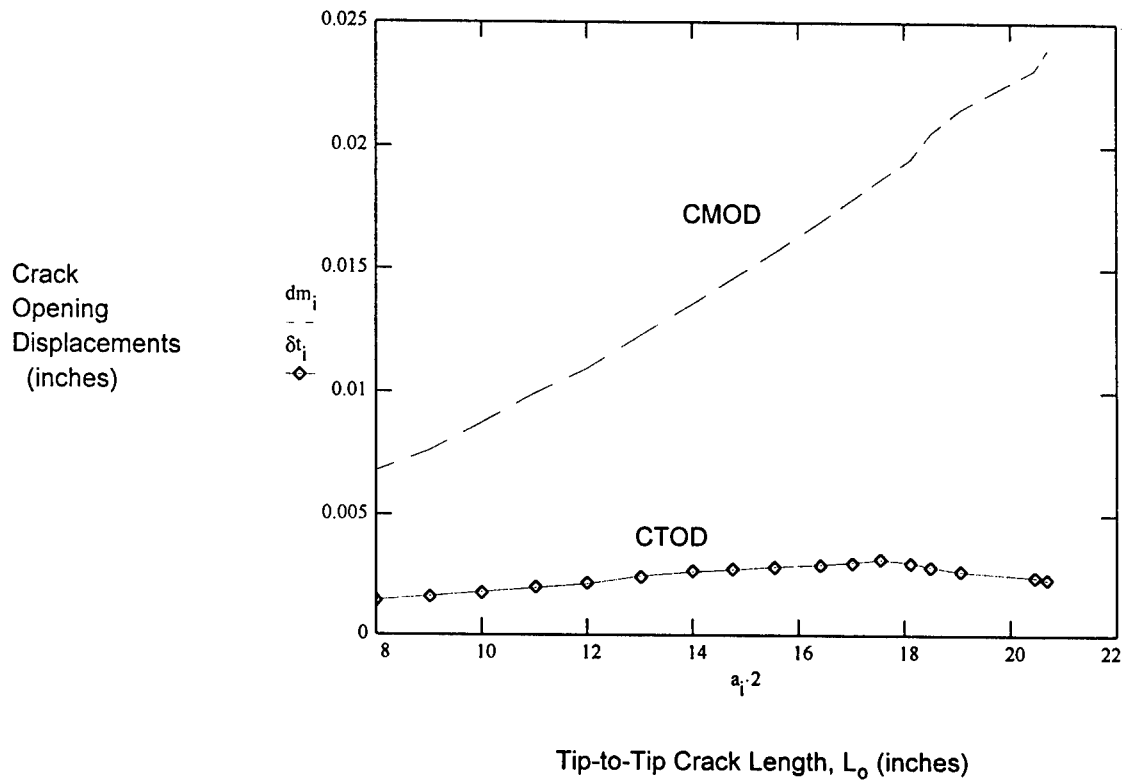
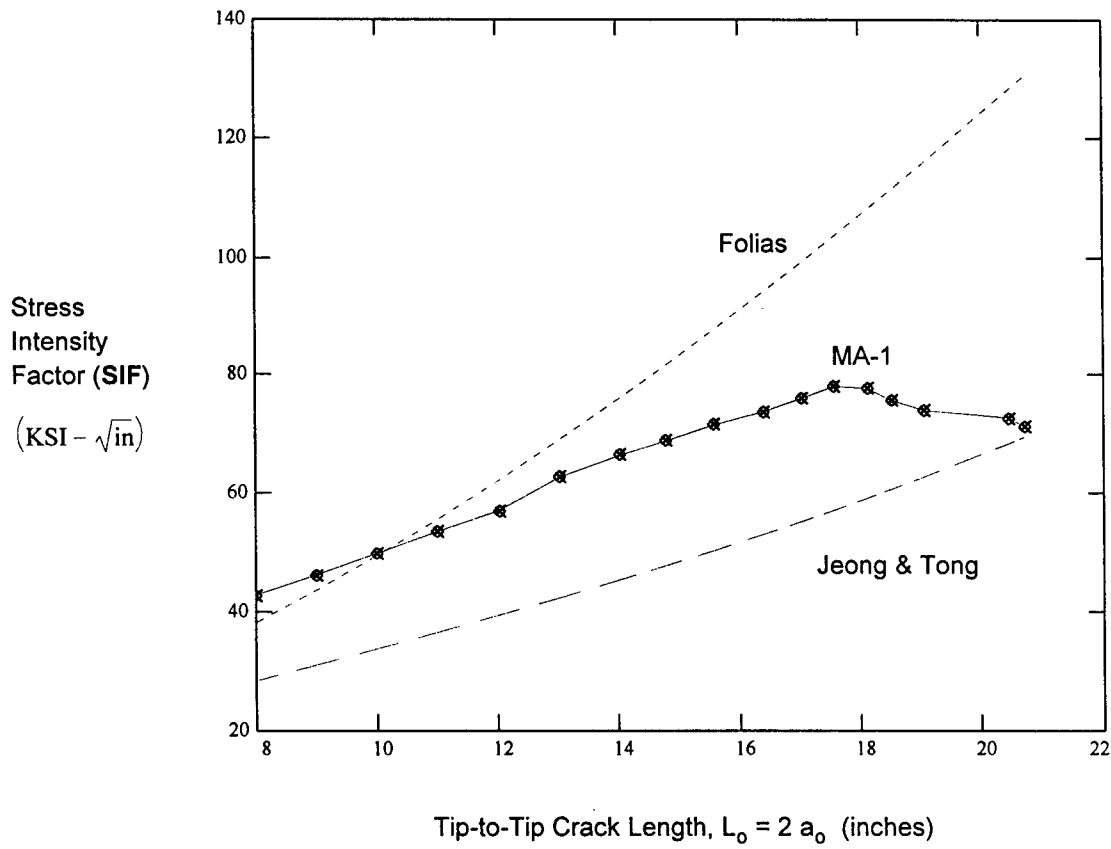


Figure 21 - CCT FLAT PLATE ANALYTICAL SPECIMEN for the US MODULE WAFFLE-SKIN
PLANE STRESS ELASTO-PLASTIC FINITE ELEMENT MODEL



CTOD = Crack Tip Opening Displacement
 CMOD = Crack Mouth Opening Displacement

Figure 22 - CCT FLAT PLATE ANALYTICAL SPECIMEN for the US MODULE WAFFLE-SKIN
 2D PLANE STRESS ELASTO-PLASTIC FEA RESULTS
 CRACK OPENING DISPLACEMENT vs. CRACK LENGTH



$$\text{Folia's, SIF} = \frac{p \cdot R}{h} \cdot \sqrt{\pi \cdot a} \cdot \sqrt{1 + \left[3.22 \cdot \left(\frac{a^2}{2 \cdot R \cdot h} \right) \right]}$$

$$\text{Jeong \& Tong, SIF} = \frac{p \cdot R}{h} \cdot \sqrt{\pi \cdot a} \cdot \sqrt{1 + \alpha \cdot \left[\left(\frac{E}{\sigma_y} \right) \cdot \left(\frac{a}{R} \right)^2 \right]^{\frac{2}{3}}}$$

$$\text{MA-1, SIF} = \sqrt{\frac{E}{0.60} \cdot \int_0^{\delta_T} \sigma_y d\delta_t} \cdot \sqrt{1 + \alpha \cdot \left[\left(\frac{E}{\sigma_y} \right) \cdot \left(\frac{a}{R} \right)^2 \right]^{\frac{2}{3}}}$$

Figure 23 - CCT FLAT PLATE ANALYTICAL SPECIMEN for the US MODULE WAFFLE-SKIN
2D PLANE STRESS ELASTO-PLASTIC FEA RESULTS
STRESS INTENSITY FACTORS vs. CRACK LENGTH

It is worth to reiterate here, that LEFM is valid only as long as nonlinear material deformation is confined to a small region surrounding the CTIP ([12] and [13]). The COD and J -integral parameters describe CTIP conditions in elastic-plastic materials, and each can be used as a fracture criterion (See Section AIII-2). Critical values of CTOD or J , employing elastic-plastic fracture (EPFM), give nearly size-independent assessment of the SIF, even for large amounts of CTIP plasticity. EPFM applies to materials that exhibit time-independent, nonlinear behavior (i.e., plastic deformation).

Also note that, using FEM for modeling a particular cracked structure (i.e., as shown in Figure 22), the CTIP is a stress concentration in a mesh and strain and stress gradients can be very large as the CTIP is approached. This means that the FEM mesh must be refined as the CTIP is approached. However, the CTOD and/or the J -integral is an energy measure and with "surprisingly" coarse meshes accurate J values can be obtained, even though the local stress and strain fields are not quite accurate.

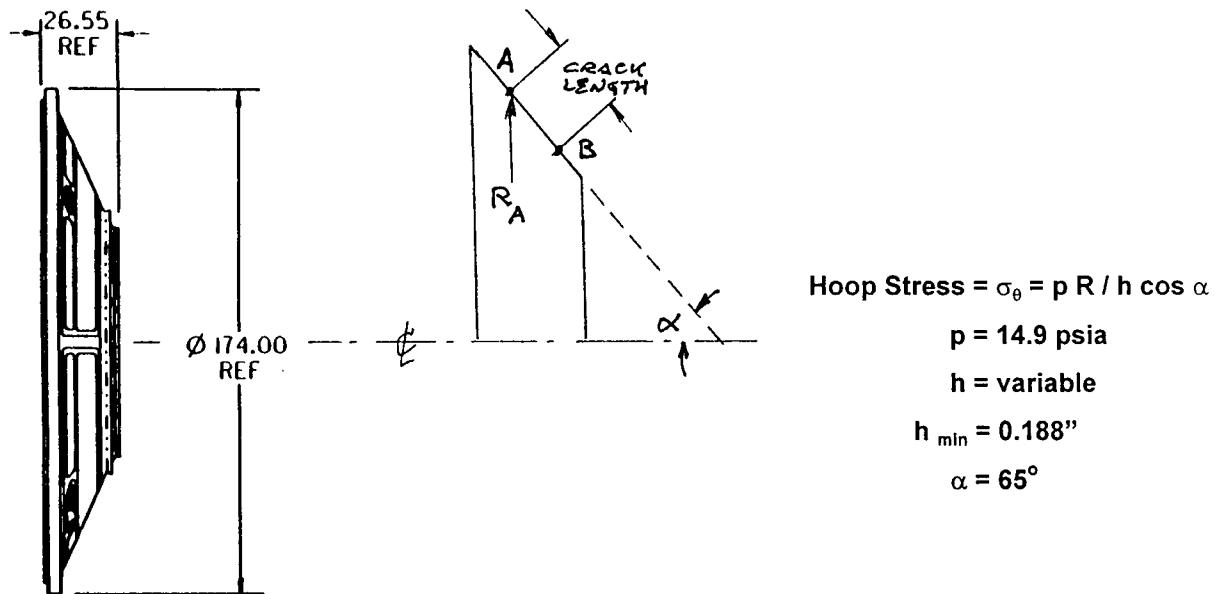
Having assessed the SIF function of CL for the US module cylindrical shell waffle-skin, the CCL can be evaluated by comparing the material that the shell is made off (Aluminum Alloy 2219-T87) fracture toughness (K) to the SIF. The estimated values for K for the material and specific minimum thickness (0.188 inch) and under quasi-static conditions, were tabulated in Table II, Section AIII-4. At crack initiation and stable crack growth, $K = 62 \text{ KSI-in}^{0.5}$, and at the unstable crack propagation, $K = 87 \text{ KSI-in}^{0.5}$, with a standard deviation ($\pm 1 \sigma$) of $6.7 \text{ KSI-in}^{0.5}$.

Using the CCT analytical specimen, the maximum estimated SIF for the MA-1 criterion, was near $80 \text{ KSI-in}^{0.5}$ for a tip-to-tip crack length of 17.5 inch, as shown in Figure 23. A slight decay on the SIF can be observed as the CTIP approaches the ribs joint. In essence, the waffle-grid joints (with their added stiffness), and the fillet radius at the rib root, tends to act as crack-stoppers. Based on the above, the respective CCL for the US common module cylindrical shell waffle-skin were estimated to be:

CRACK PROPAGATION CONDITIONS	AROUND the MEAN VALUE	MINUS ONE STANDARD DEVIATION
Stable Initiation & Growth	12.8 inch	10.7 inch
Unstable (Critical)	N/A	17.5 inch

AIV-2.2 SHELL END CONE

For a conical shell under internal pressure, the driver for the SIF at the CTIP is, as per the cylindrical shell, the hoop loading. However, here, the hoop stress is proportional to the local radius and skin thickness (both variable), and the cone half-angle (a constant) as illustrated by the accompanying sketch. Consequently, this driver continuously changes, likewise the corresponding SIF at the CTIP, as the CTIP progress from the cone smaller diameter (near the cone apex) toward the larger diameter at the base of the cone. Thus, one has to assess the CCL for this particular structure, by considering two CTIP function of the CL and its particular location along the cone wall. We have designated CTIP-A for the upper-most crack tip (North), and CTIP-B for the lower one (South).



We have performed a 3D FEA of a segment of the US module end cone (quarter segment = 90°) shown in Figure 24, having an axial through-the-wall crack, under a 14.9 psia internal pressure loading. Note that, the end cone FEM includes the reinforcing North and South rings (see sketch above) and gussets, in addition to the variable thickness within the gore panel. Figure 25 depicts the global 3D FEM with the crack located within the cone pressure wall minimum thickness of 0.188 inch, and the ensuing principal stress (psi) distribution for a chosen crack length.

INTERNATIONAL SPACE STATION ALPHA

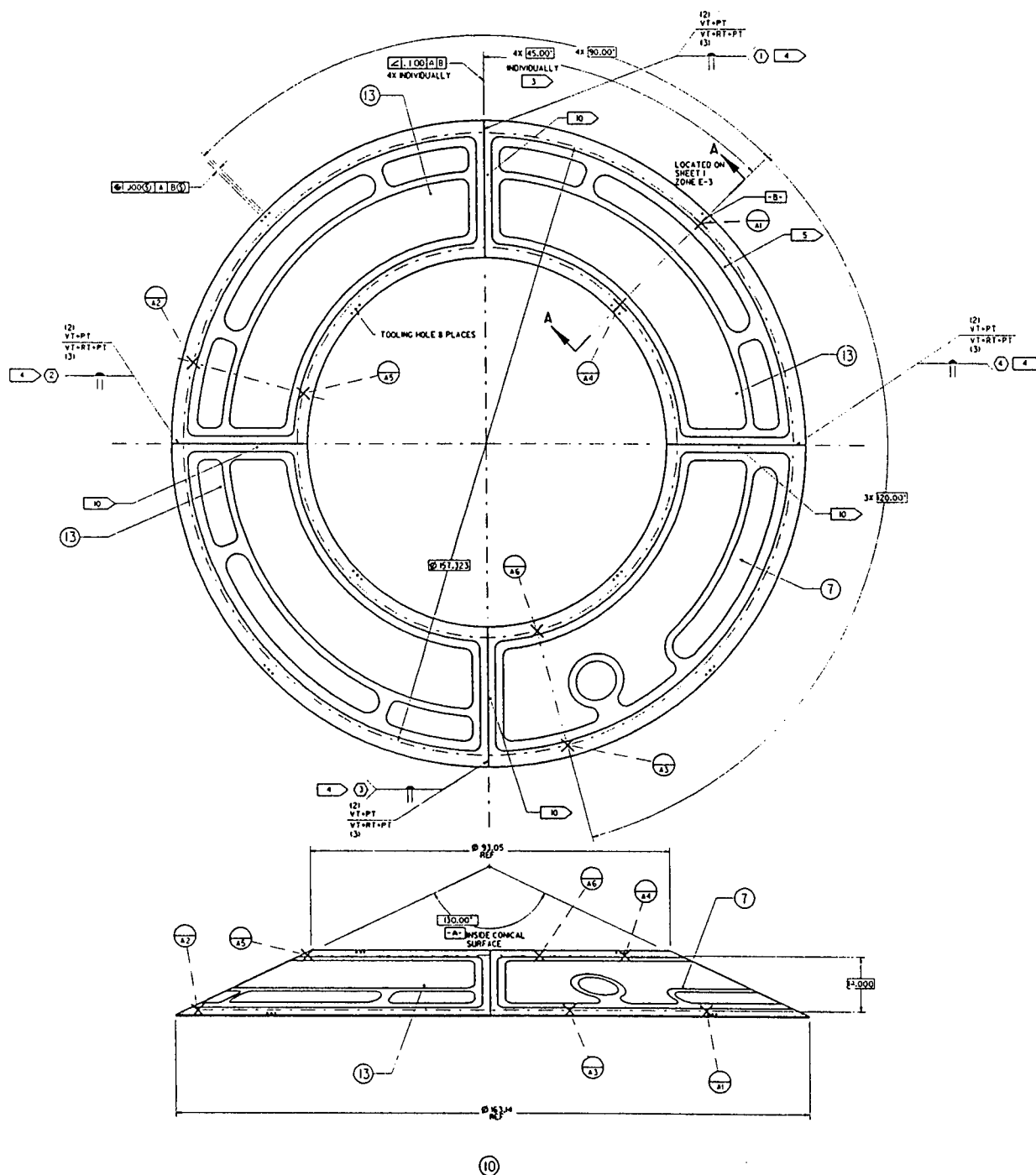


Figure 24 - US COMMON MODULE END CONE OVERALL ARRANGEMENT
(Ref.: BOEING, Seattle, WA 98124 - DWG. No.. 683-11211, Rev B, 94-03-21)

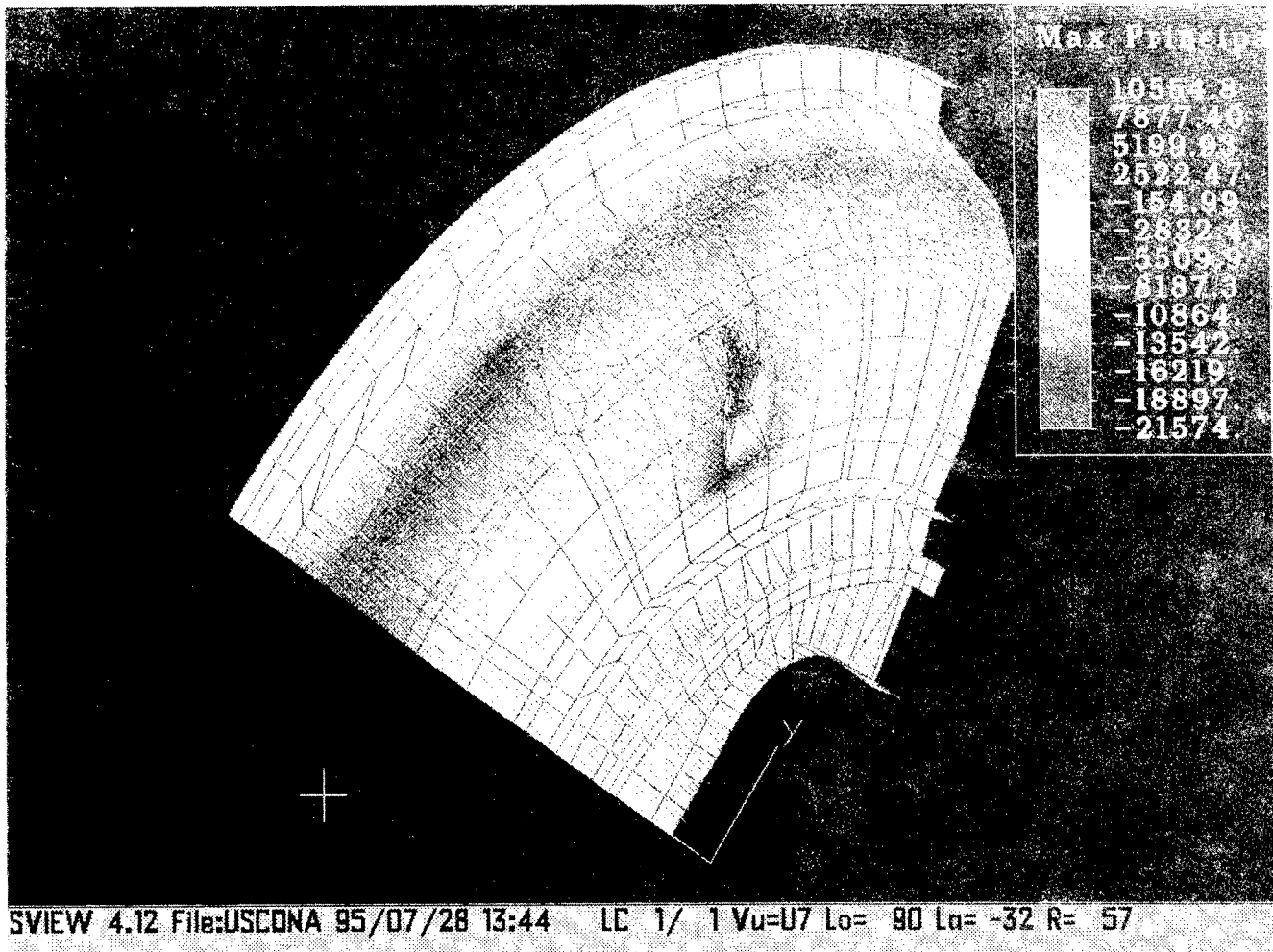


Figure 25 - US COMMON MODULE END CONE 3D FEA 1/4 (90°) MODEL
with an Axial Crack ($L_o = 8$ inch) within the Region of Minimum Thickness (0.188")
Shown are the Maximum Bending Principal Stress (psi) Distribution and
Overall displacement (magnified 30 time) at 14.9 psia pressure loading

From the resulting crack opening displacements, and principal stress (as shown in Figure 26 for a particular CL) at the crack tips **A** and **B**, we have utilized five (5) fracture criterion to assess the corresponding SIF. They are displayed graphically in Figure 27 and Figure 28, for the North CTIP and in Figure 29 for the South CTIP, respectively. They have all in common the crack bulging effects due to the internal pressure. The significant results here is that the CTIP-A is the most stressed one. However, as the CTIP-A approaches the end of the 0.188" thick zone of the wall, and encounters another zone with a higher thickness (0.230"), the SIF will be reduced, therefore limiting further crack extension. Thus, the maximum possible CCL (local unzipping) will be confined to the gore panel (see Figure 16) with a span of 18.3 inch.

The conservative CCL's, based on the CTIP-A SIF and on the fracture toughness for 0.188 inch thick 2219-T87 Aluminum Alloy, were assessed, under quasi-static loading conditions, to be:

CRACK PROPAGATION CONDITIONS	AROUND the MEAN VALUE	MINUS ONE STANDARD DEVIATION
Stable Initiation & Growth	5.7 inch	4.4 inch
Unstable (Critical)	12.5 inch	10.4 inch

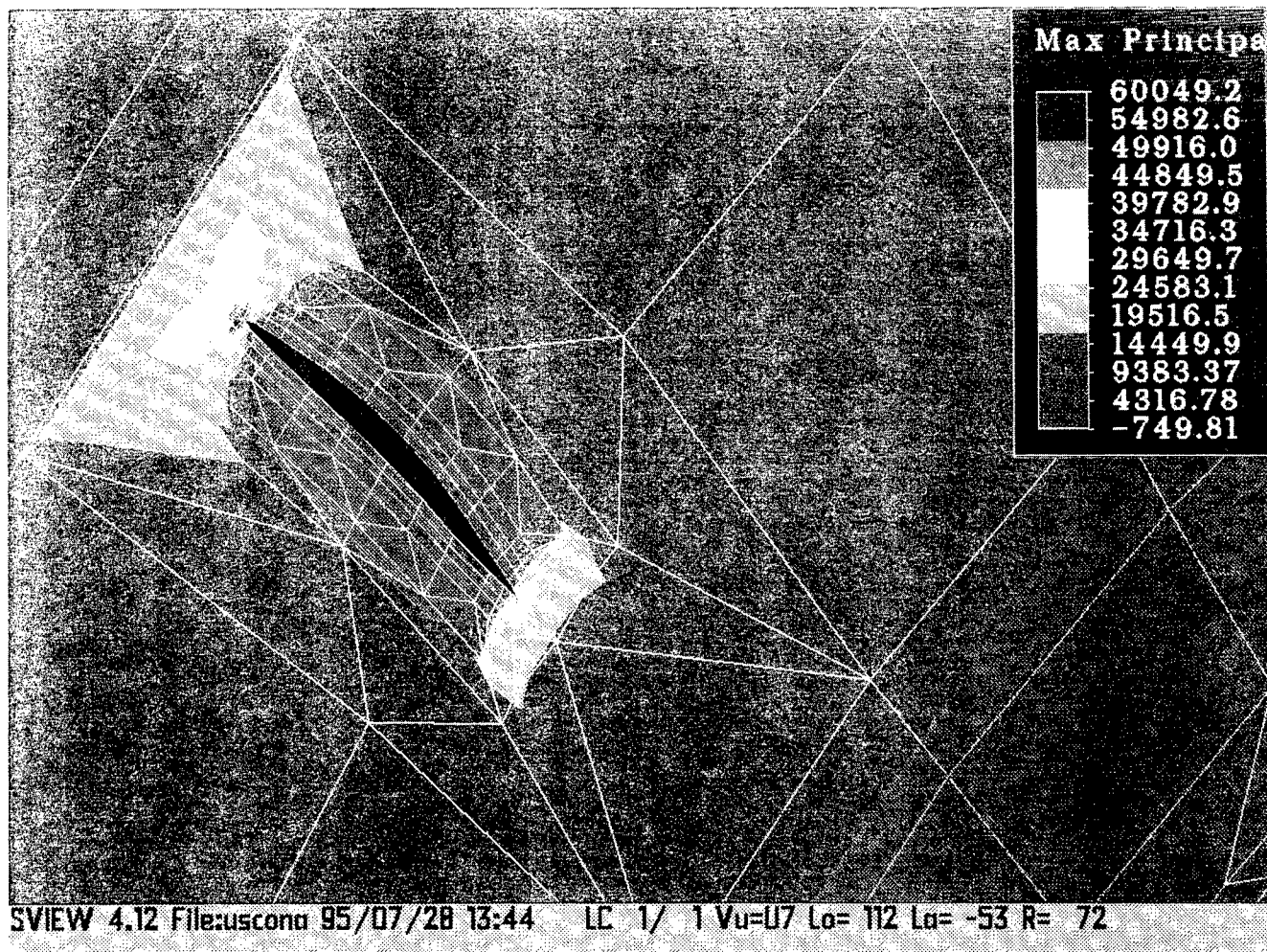


Figure 26 - US COMMON MODULE END CONE 3D FEA 1/4 (90°) MODEL
with an Axial Crack ($L_o = 8$ inch) within the Region of Minimum Thickness (0.188")
Shown are The Maximum Stress Distribution around the Cracked Region and
Overall displacement (magnified 30 time) at 14.9 psia pressure loading

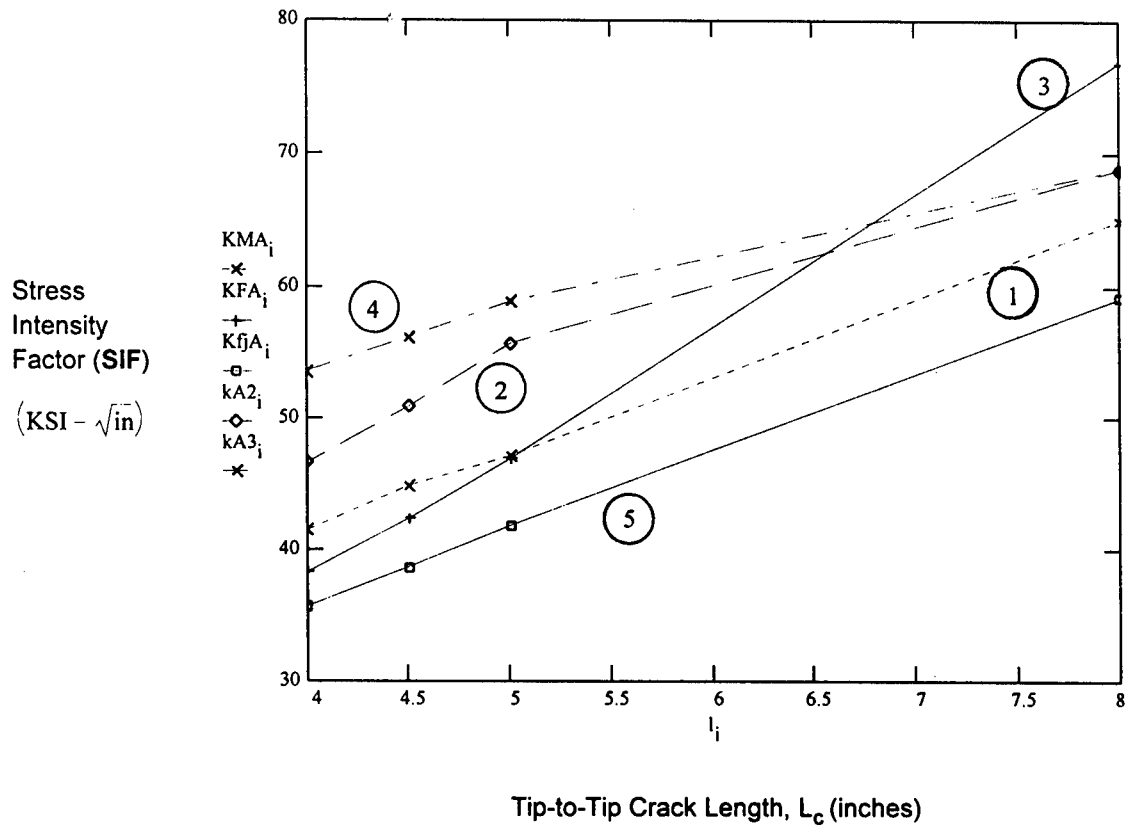
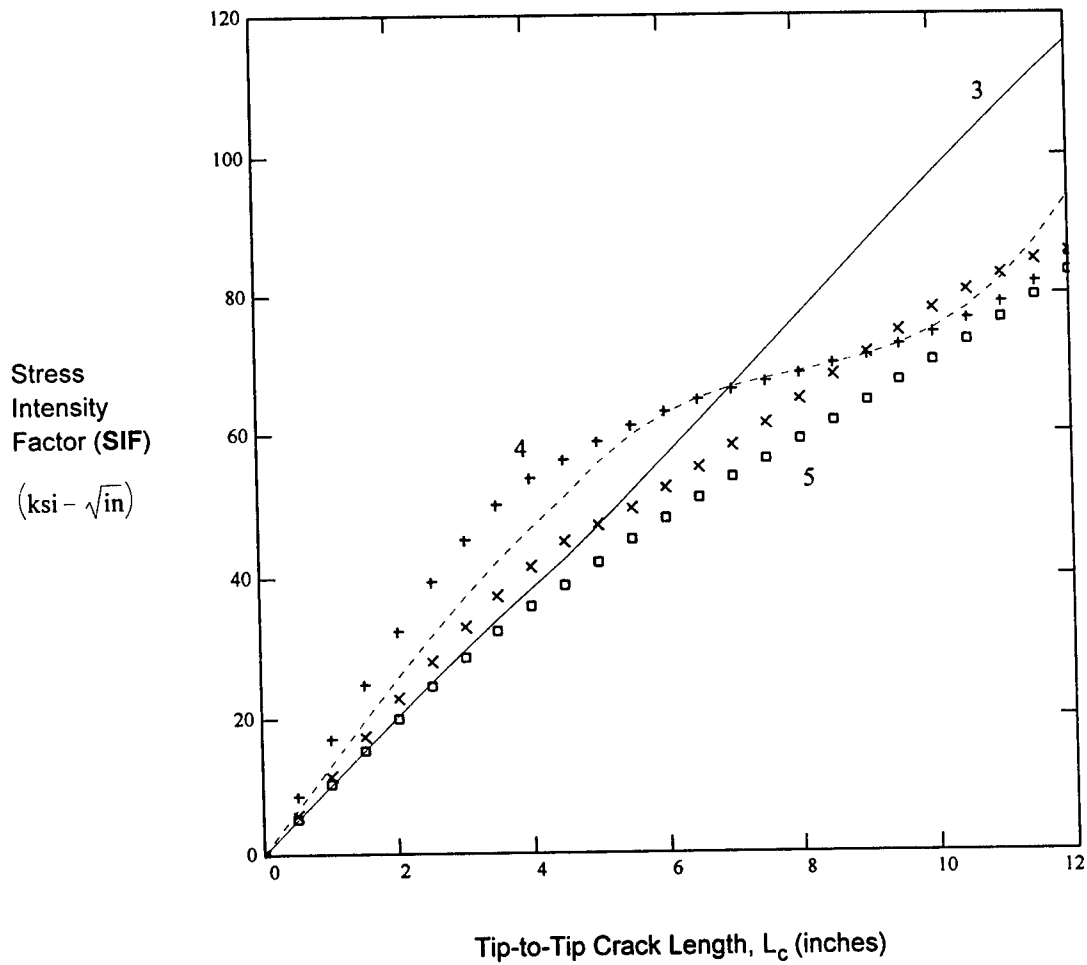
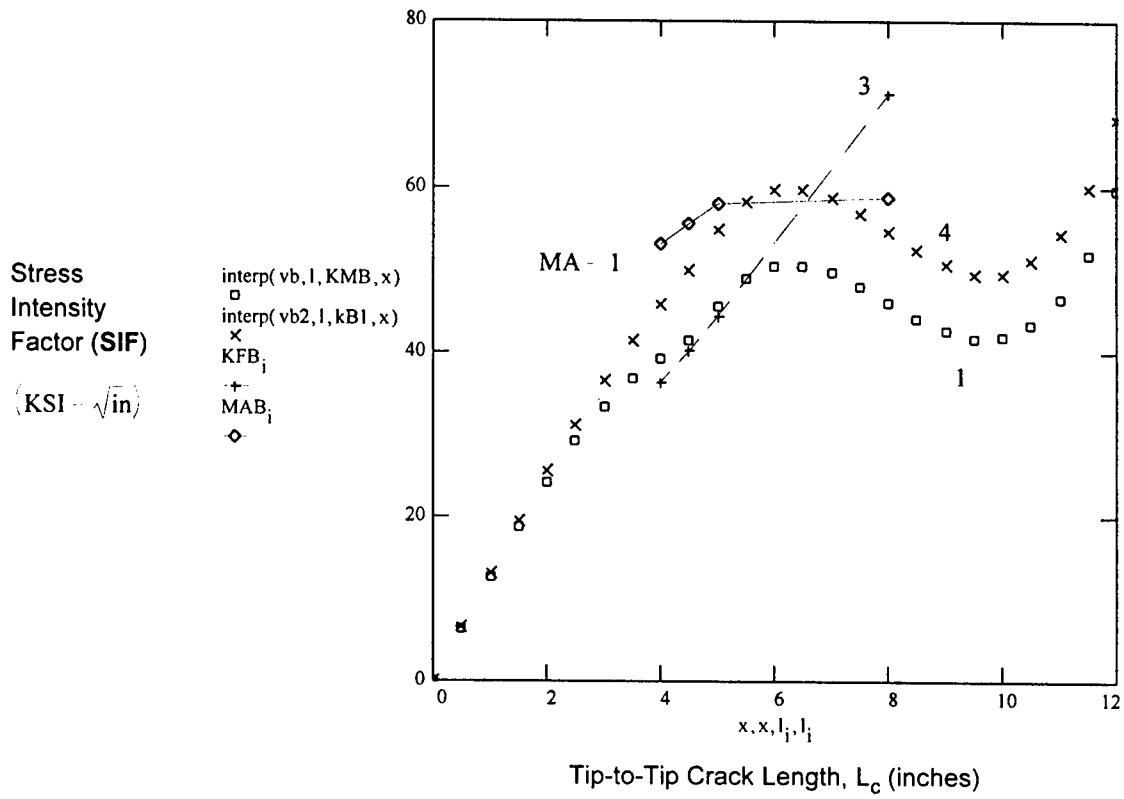


Figure 27 - US COMMON MODULE END CONE
CTIP-A (North) Stress Intensity Factor (SIF) for Crack Length between 4 and 8 inches



LEGEND: see Figure 27

Figure 28 - US COMMON MODULE END CONE
Interpolated CTIP-A (North) Stress Intensity Factor vs. Crack Length



LEGEND: see Figure 23 and Figure 27

Figure 29 - US COMMON MODULE END CONE
Interpolated CTIP-B (South) Stress Intensity Factor (SIF) for Crack Length

AIV-3 EUROPEAN SPACE AGENCY (ESA) MPLM COLUMBUS MODULE

We have adopted the similar analytical procedure, for the ESA module, as per the one employed for the US module. We have assessed the SIF's for two main regions of the structure. Section AIV-3.1 summarizes the work done for evaluating the SIF within the MPLM cylindrical shell Isogrid reinforced pressure wall. Section AIV-3.2 treats the SIF for one of the module end cone.

AIV-3.1 MAIN CYLINDRICAL SHELL

The ESA MPLM Module Structure general arrangement is exhibited in Figure 30.

A 3D FEA model of a quarter segment of the Isogrid shell was developed with a longitudinal crack within one cell region, as shown from Figure 31 through Figure 33. Several computer runs were performed, whereby the crack length was progressively extended, under internal pressure of 14.9 psia loading. A typically resulting crack opening displacement and local crack length bulging effects are displayed in Figure 34. Note here, the non-uniformity of the COD along the crack length. Reduced COD can be seen at the boundary of the cracked-edge near the longitudinal rib. Essentially, this particular analysis was done in order to determine the bulging effects within the cracked region because of the internal pressure.

Subsequently, we have conducted a plane stress nonlinear elasto-plastic FEA, using the ELASTO program, of a local region of the Isogrid reinforced skin, using a CCT analytical model as depicted in Figure 35 and Figure 36. This CCT model has all the design details of the Isogrid skin cells and ribs. The main loading conditions consisted of the hoop stress and the axial blow-out load. Basically, the biaxial loading conditions, usually encountered in a pressure vessel. Several computer runs were done, in which the crack length was extended progressively, from the cell centerline toward the end of the CCT edge (see Figure 36). For each crack length, the resulting CMOD, CTOD, and CTIP stresses were tabulated. The data was then stored in a file that can be retrieved and used by the MathCad software.

Technical drawing of a large industrial machine, likely a centrifugal pump or fan, showing a side elevation and a top-down view. The side elevation (top) shows a rectangular frame with a diamond-patterned mesh. The top-down view (bottom) shows a circular structure with a radial grid pattern. Dimensions are provided in millimeters.

A-47

MA-TR-101-95
SECTION A

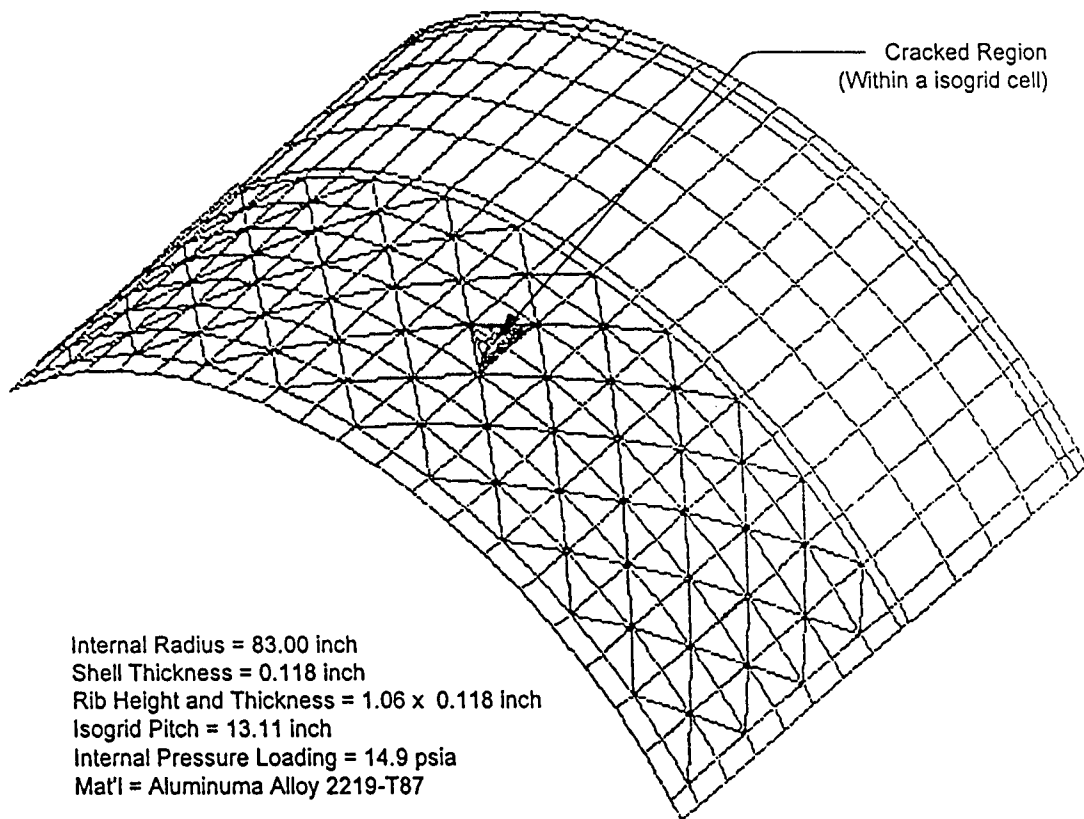


Figure 31 - ESA MPLM CYLINDRICAL SHELL 3D FEA 1/4 (90°) MODEL
TOP VIEW

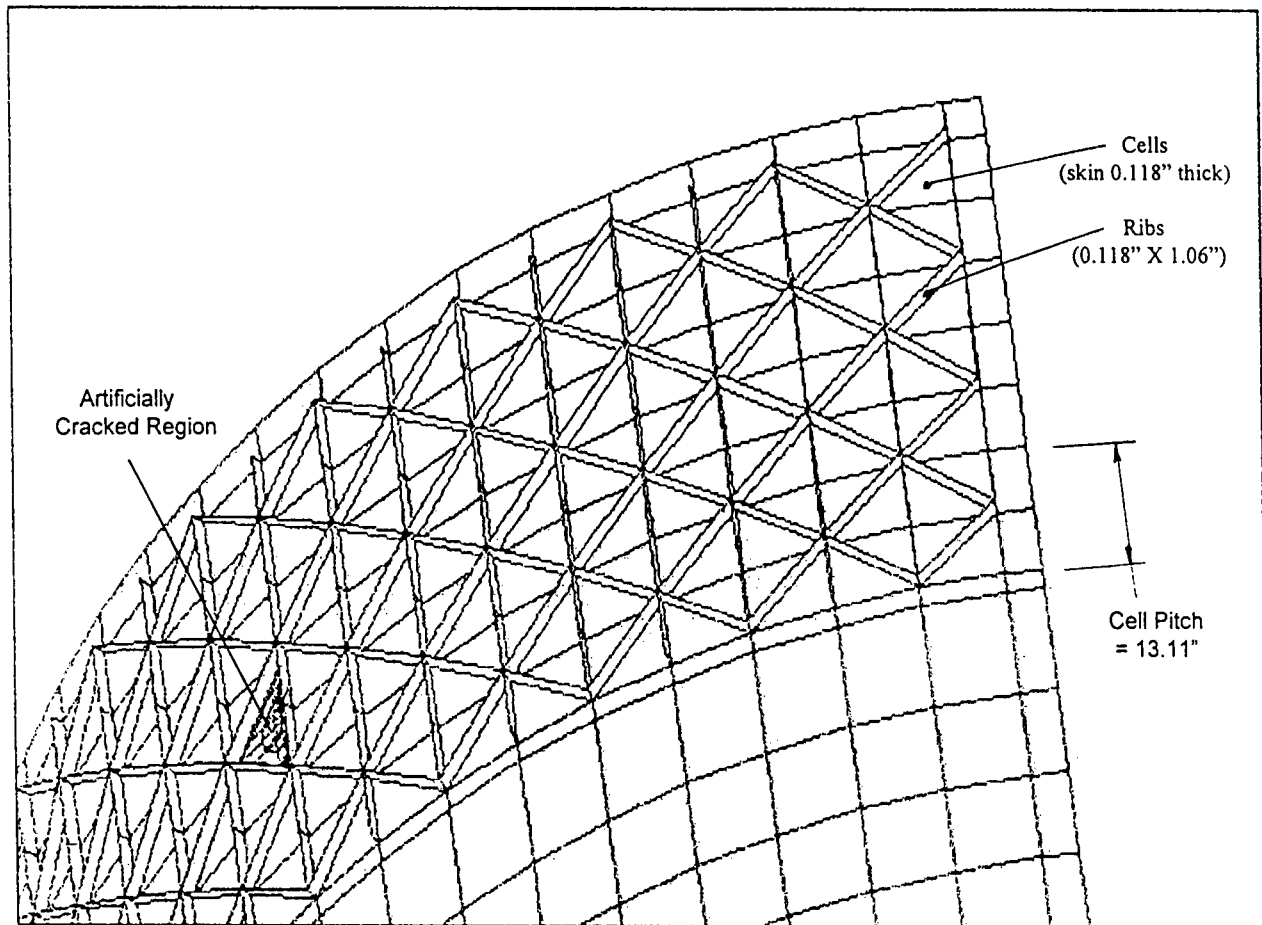


Figure 32 - ESA MPLM CYLINDRICAL SHELL 3D FEA 1/4 (90°) MODEL
DETAILS of the ISOGRID PRESSURE WALL

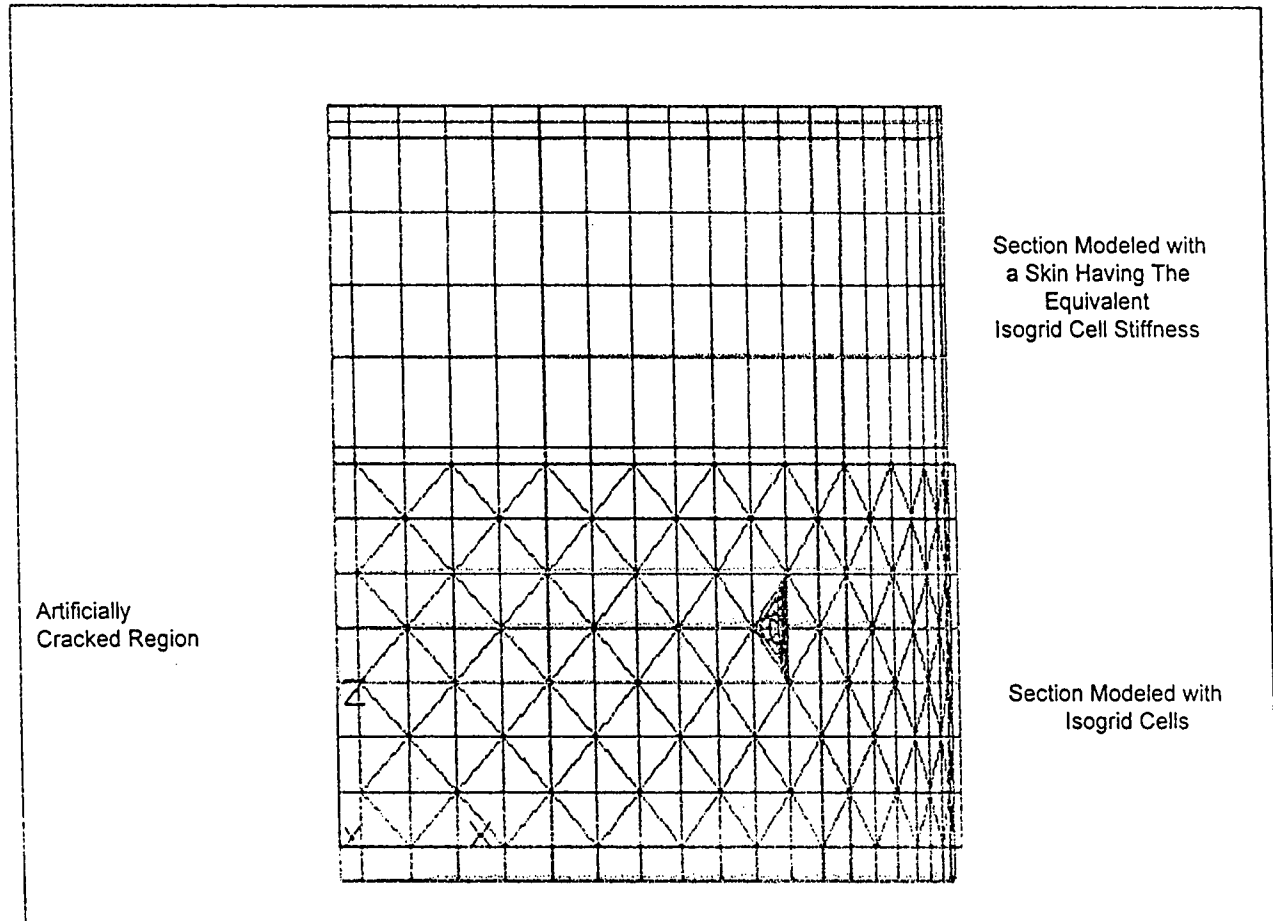


Figure 33 - ESA MPLM CYLINDRICAL SHELL 3D FEA 1/4 (90°) MODEL
SIDE VIEW

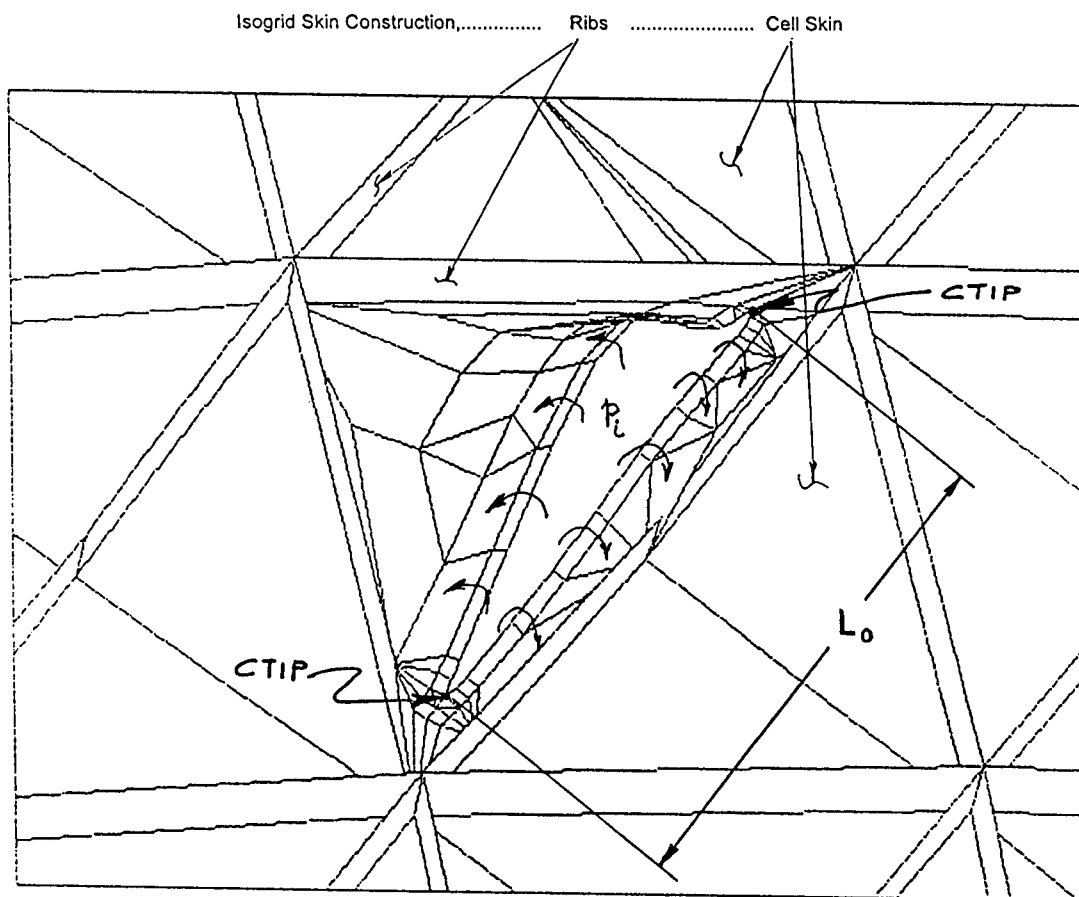


Figure 34 - ESA MPLM CYLINDRICAL SHELL 3D FEA 1/4 (90°) MODEL
 CRACK DISPLACEMENT and BULGING DETAILS
 (magnified 50 times for clarity; crack length, $L_0 = 9.5"$)

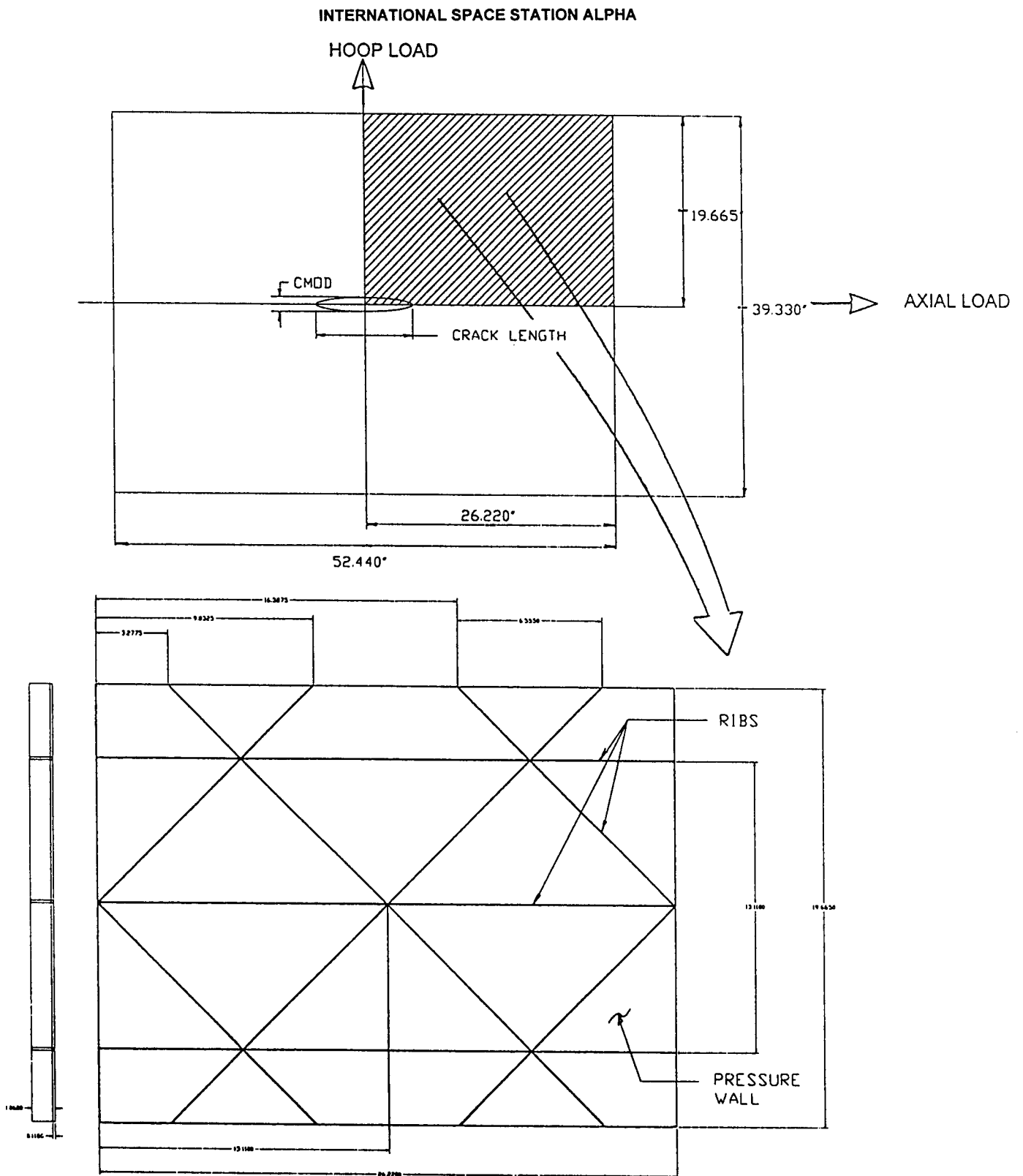


Figure 35 - ESA MPLM CYLINDRICAL SHELL with an ISOGRID REINFORCED SKIN
CCT FLAT PLATE ANALYTICAL SPECIMEN

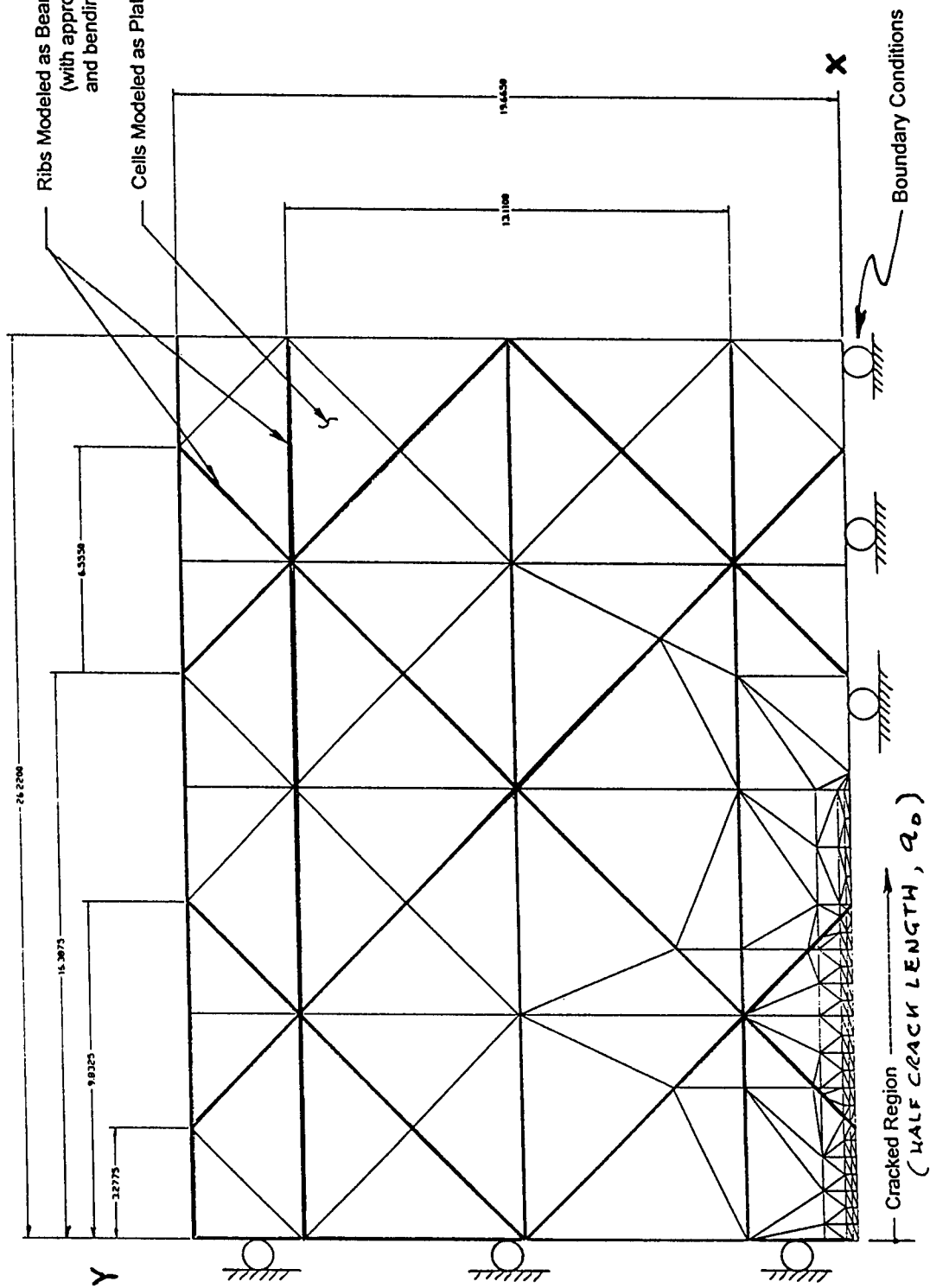


Figure 36 - ESA MPLM CYLINDRICAL SHELL with an ISOGRID REINFORCED SKIN
CCT ELASTO-PLASTIC 2D PLANE STRESS FINITE ELEMENT MODEL

Using the relevant data, we have employed five (5) fracture criterion for estimating the SIF's. The results are displayed in Figure 37, along with the respective SIF parameter. Folias and Jeong & Tong parameters are for unreinforced CCT specimen. MA-3 criterion uses the CMOD, and it is considered to be conservative. MA-1 & MA-2 parameters are identical, and uses the *J*-integral principle developed by Rice. All five criterion includes the bulging effects. Note that, from Figure 36 and Figure 37, the resulting SIF's above a crack length of approximately 7.0 inch, assumes that the ribs around one cell have been precracked by other means other than the biaxial loading condition. Based on the results shown in Figure 37, the CCL will be confined within one cell, obviously, only if the initial damage done by M/OD impact is confined locally within the cell and not damaging in the process the adjacent ribs.

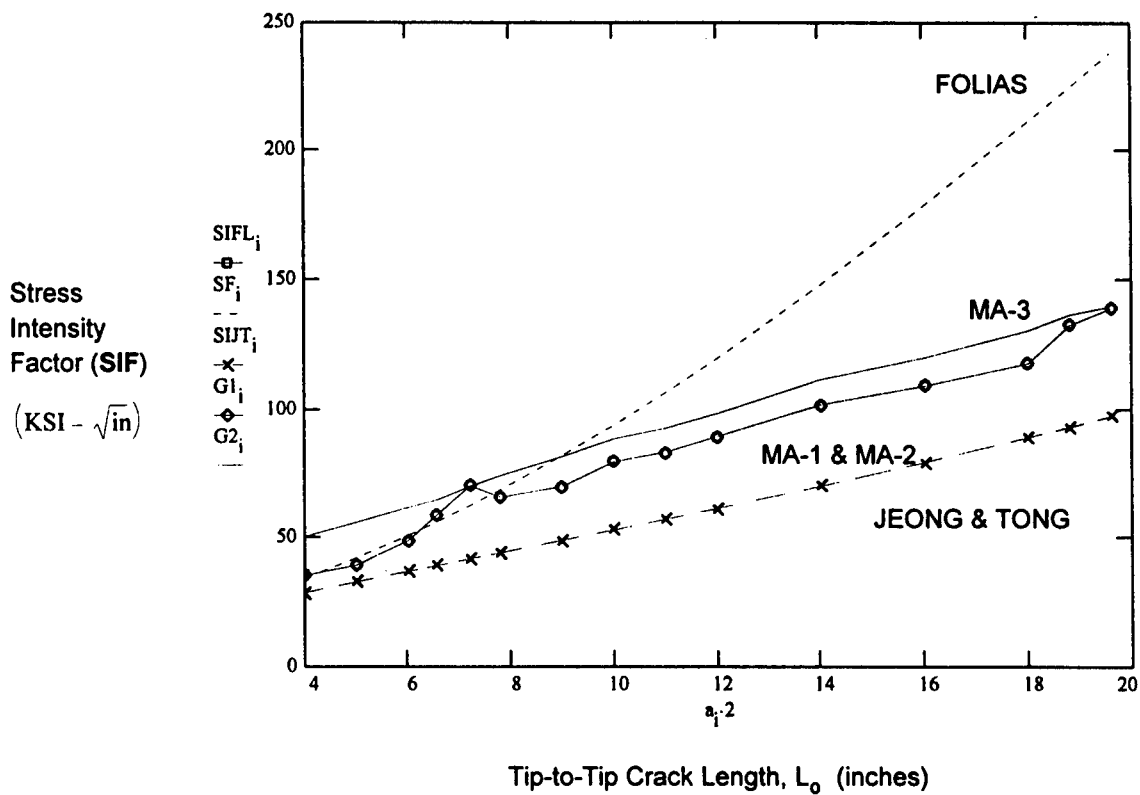
In summary, the estimated CCL for the ESA MPLM module cylindrical shell with an Isogrid reinforced skin, and under the 14.9 psia internal pressure loading are shown below.

CRACK PROPAGATION CONDITIONS	AROUND the MEAN	MINUS ONE STANDARD DEVIATION
Stable Initiation & Growth	9.8 inch	9.2 inch
Unstable (Critical)	15.2 inch	13.6 inch

AIV-3.2 SHELL END CONE

The ESA MPLM end cone overall design is shown in Figure 38. The main pressure wall is reinforced with integral ribs located inside to the cone. A 3D FEA model of the cone and its inner and outer rings was developed as depicted in Figure 39. Then, we have introduced an axial crack within the region of maximum hoop stress, as displayed in Figure 40. Several computer runs were performed, whereby the crack length was progressively extended. For each FEA run with a particular crack length, we have recorded the crack-tips (A and B, or North Side and South Side respectively) principal stresses σ_x , σ_y , σ_z . A typical maximum stress distribution around the crack-tips is shown in Figure 41. From the FEA results we have computed the Strain Energy Density (SED) directly from nodal (CTIP) principal stresses, and the relevant CTOD and CMOD. By using nodal strain energy densities, the expectation is that the energies will be more accurate than the element-based energies. Having defined the SED, we have used the *J*-integral to derive the SIF for the respective CTIP and CL. The results are displayed in Figure 42.

INTERNATIONAL SPACE STATION ALPHA



FOLIAS:
$$SIF = \frac{p \cdot R}{h} \cdot \sqrt{\pi \cdot a} \cdot \sqrt{1 + \left[3.22 \cdot \left(\frac{a^2}{2 \cdot \pi \cdot R} \right) \right]}$$

JEONG & TONG:
$$SIF = \frac{p \cdot R}{h} \cdot \sqrt{\pi \cdot a} \cdot \sqrt{\sec\left(\frac{\pi \cdot a}{W}\right)} \cdot \sqrt{1 + \left[\alpha \cdot \left(\frac{E}{\sigma_y} \right) \cdot \left(\frac{a}{R} \right)^2 \right]^{\frac{2}{3}}}$$

MA-1:
$$SIF = \sqrt{\frac{E}{0.60} \cdot \text{fact} \cdot \int_0^{\delta T} \sigma_{TIP} d\delta T} \cdot \sqrt{1 + \left[\alpha \cdot \left(\frac{E}{\sigma_y} \right) \cdot \left(\frac{a}{R} \right)^2 \right]^{\frac{2}{3}}}$$

MA-2:
$$SIF = \left(E \cdot \text{fact} \cdot \frac{2}{a} \cdot \int_0^a \frac{\sigma_{TIP}}{2} \cdot \delta da \right)^{0.5} \cdot \sqrt{1 + \left[\alpha \cdot \left(\frac{E}{\sigma_y} \right) \cdot \left(\frac{a}{R} \right)^2 \right]^{\frac{2}{3}}}$$

MA-3:
$$SIF = \sqrt{\frac{E}{0.6} \cdot \sigma_y \cdot \delta T \cdot \text{fact}} \quad \text{"fact function of mat'l SHE"}$$

Figure 37 - ESA MPLM CYLINDRICAL SHELL with an ISOGRID REINFORCED SKIN
SIF vs. CRACK LENGTH for FIVE SIF CRITERION

INTERNATIONAL SPACE STATION ALPHA

SECTION A-A
SCALE 1:2

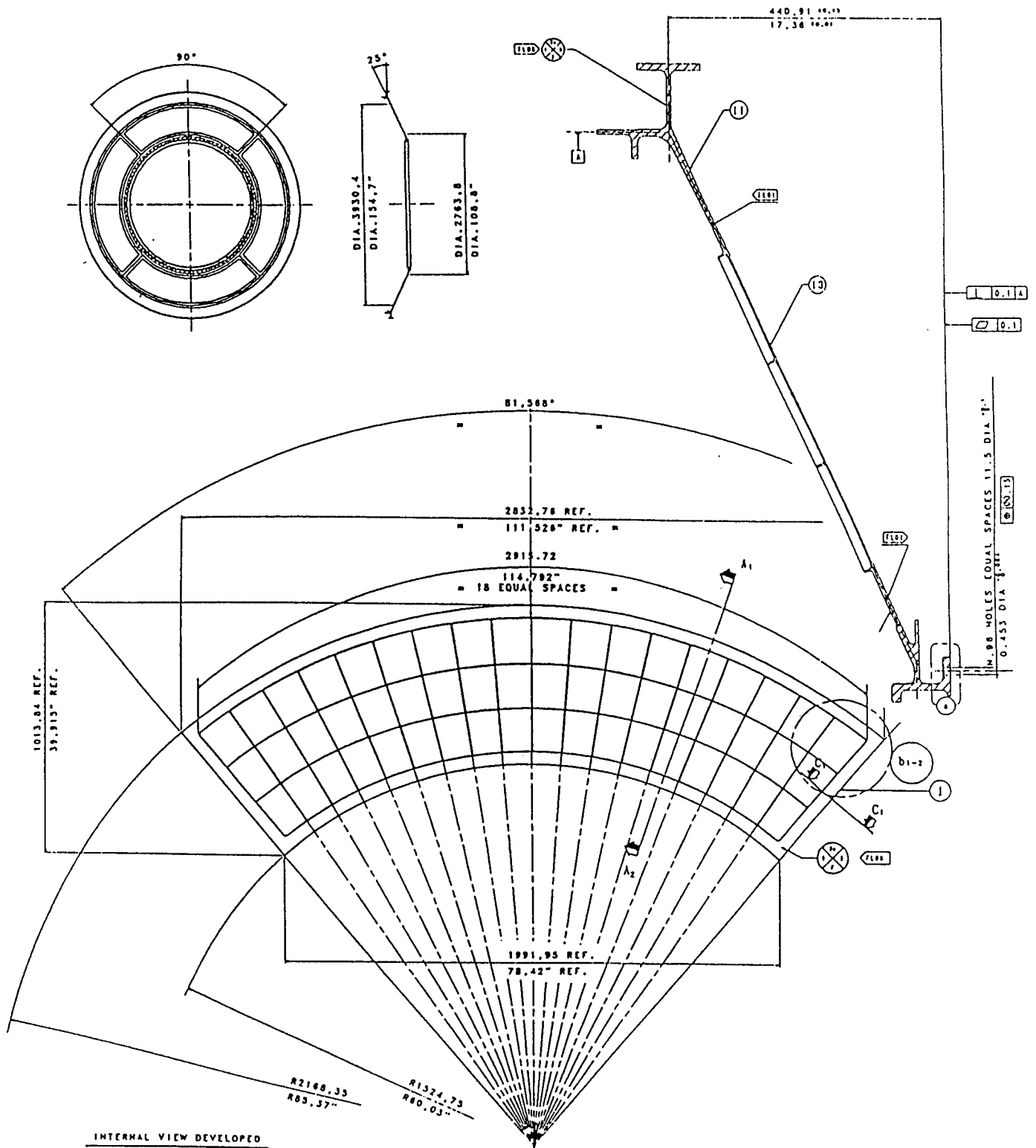
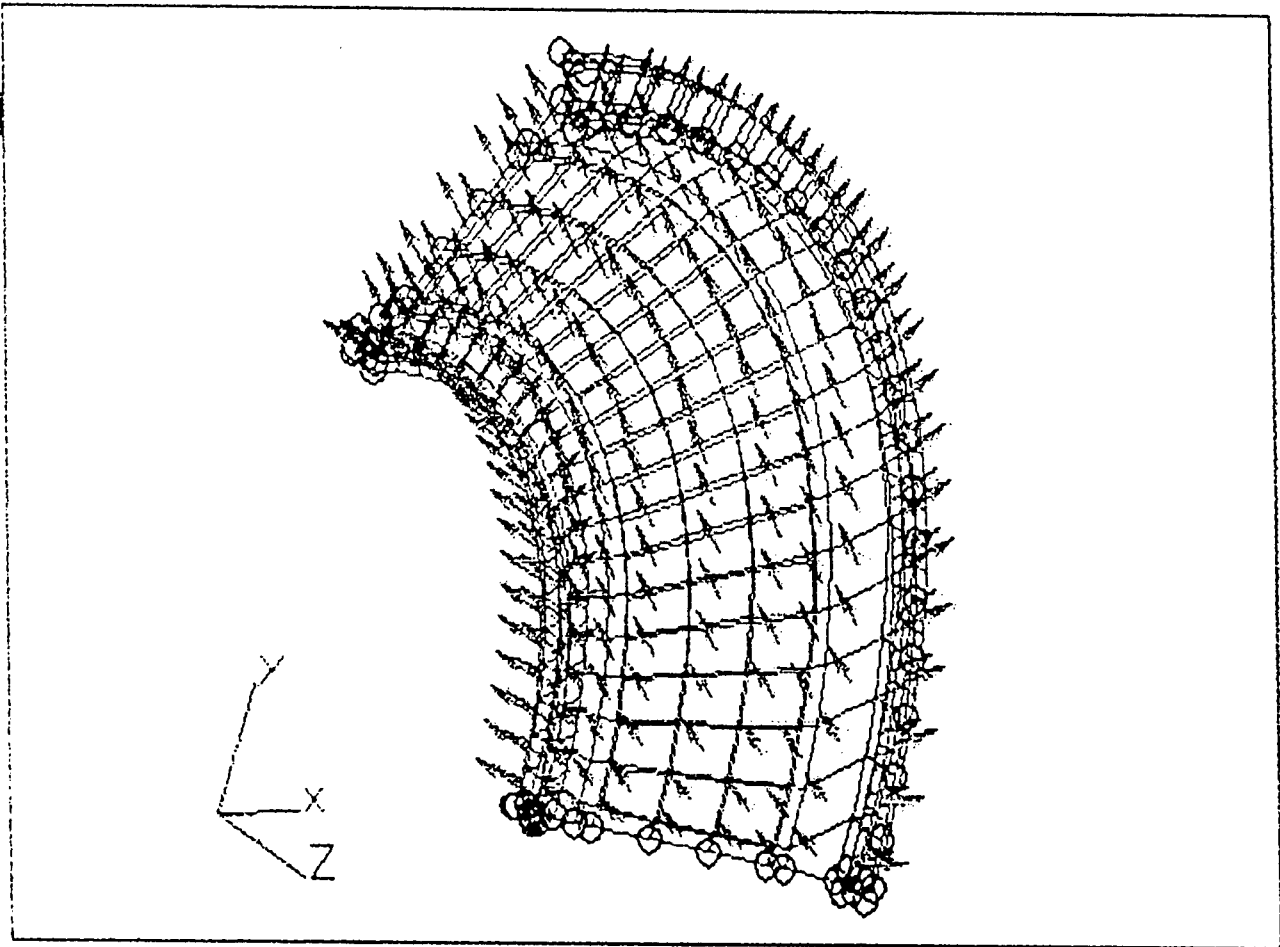


Figure 38 - ESA MPLM MODULE END CONE DESIGN DETAILS

A-56

MA-TR-101-95
SECTION A



Cone Design Details:

Height: 17.36" (Outer to Inner Rings)
 Outer Radius: 83.07"
 Inner Radius: 48.00"
 Minimum Pressure Wall Thickness: 0.098"
 Internal Ribs Height and Thickness: 0.748" x 0.098"
 Half Cone Angle: 65°
 Material: Aluminum Alloy 2219-T87

Figure 39 - ESA MPLM MODULE END CONE 3D FEA 1/4 (90°) MODEL
 OVERALL ARRANGEMENT WITHOUT AN ARTIFICIAL CRACK
 (Internal Pressure + Blow Out Load Vectors at 14.9 psia)

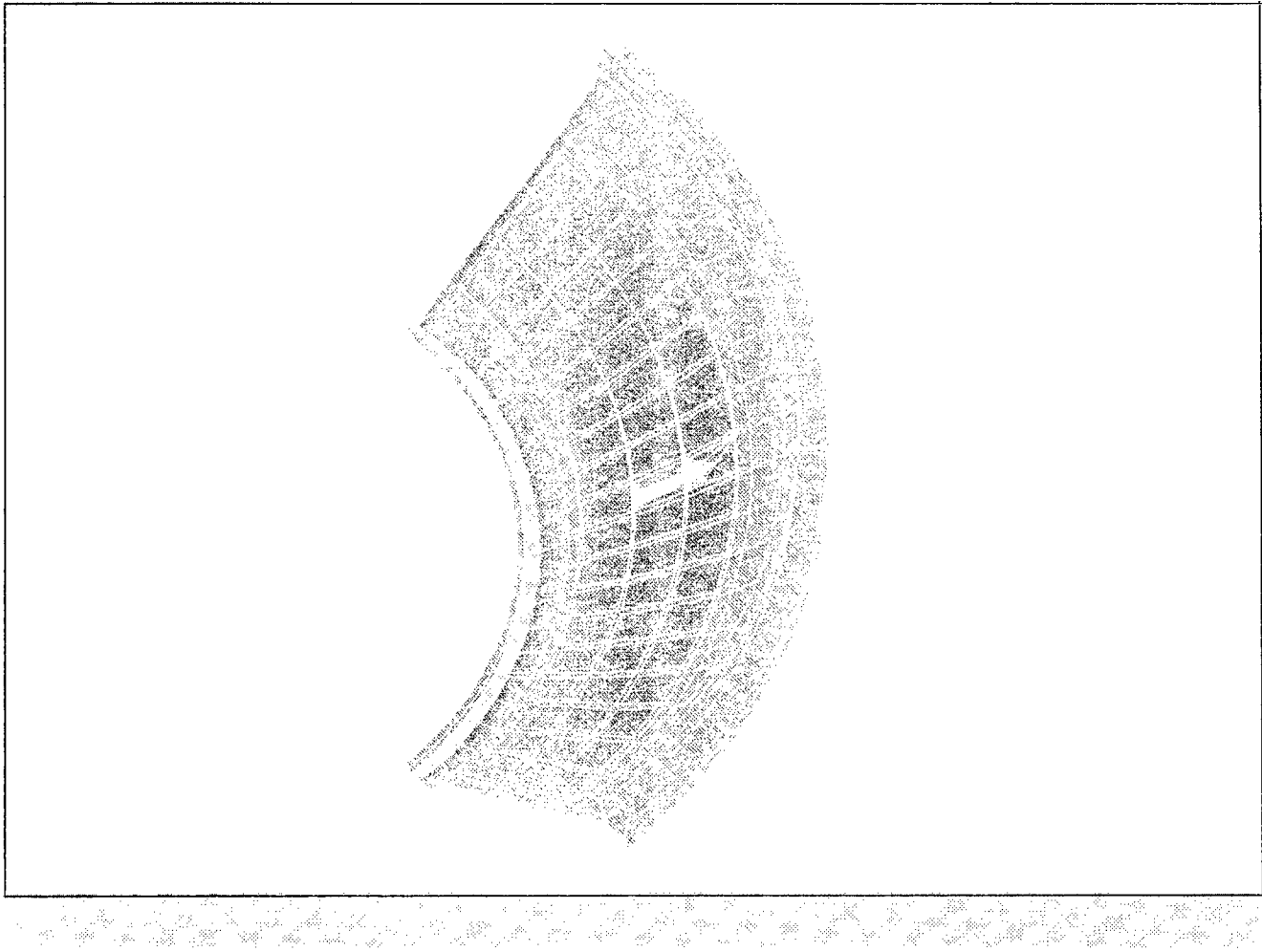
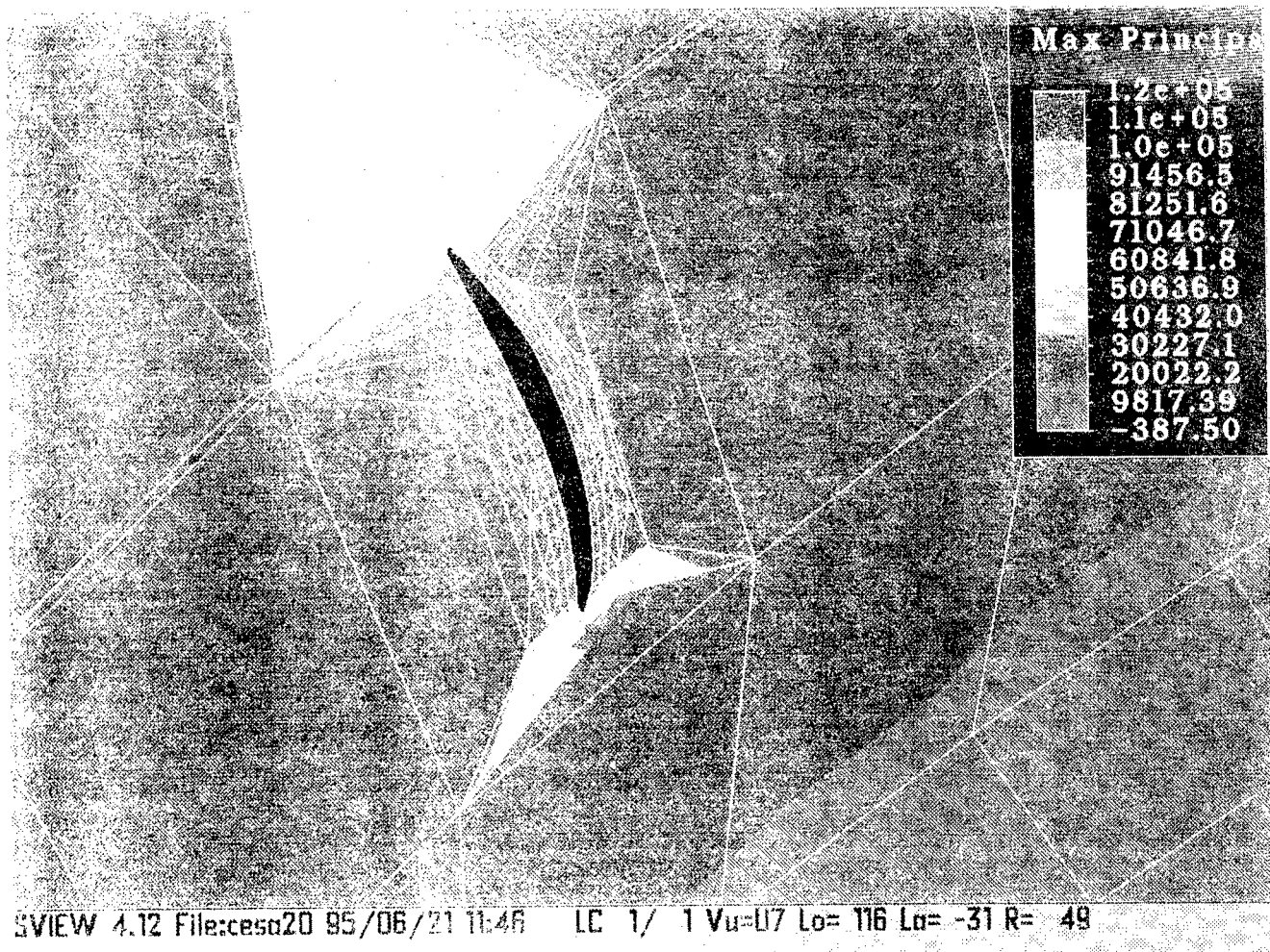
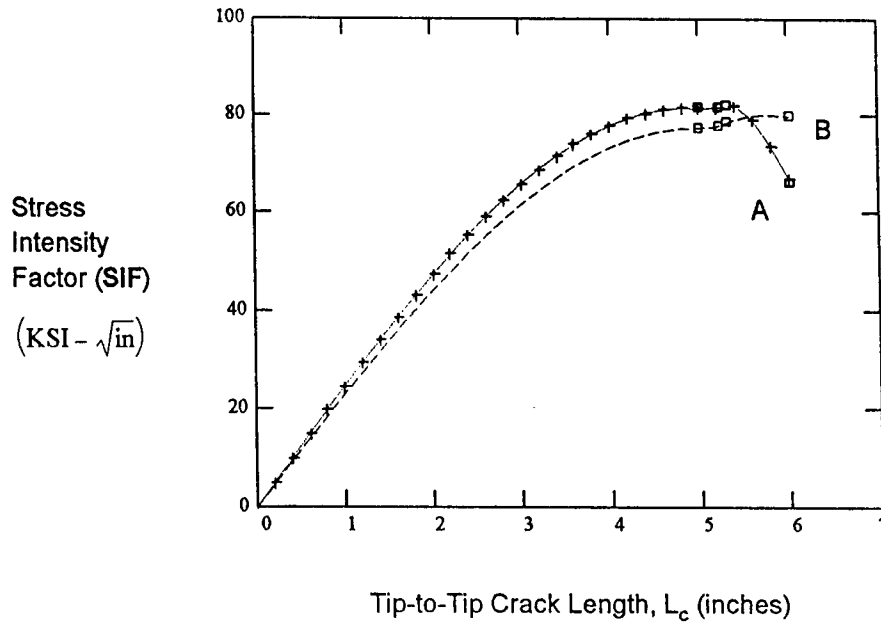


Figure 40 - ESA MPLM MODULE END CONE 3D FEA 1/4 (90o) MODEL
with an ARTIFICIAL CRACK within a WAFFLE-GRID CELL
(Inside View)



Left Hand CTIP = Upper (or North) CTIP-A
 Right Hand CTIP = Lower (or South) CTIP-B
 (Crack Length, L_o = 6.0 inches)

Figure 41 - ESA MPLM MODULE END CONE 3D FEA 1/4 (90°) MODEL
 PRINCIPAL STRESS DISTRIBUTION (psi) around the CRACKED REGION
 (at 14.9 psia internal pressure loading)



from crack-tip principal stresses: $\text{SIF} = \sqrt{E \cdot \zeta \cdot C}$

ζ = Strain Energy Density

C = a constant (may include n , the SHE)

$$\zeta = \left[\frac{1}{2 \cdot E} \cdot (\sigma_1^2 + \sigma_2^2 + \sigma_3^2) - \frac{\nu}{E} \cdot (\sigma_1 \cdot \sigma_2 + \sigma_2 \cdot \sigma_3 + \sigma_1 \cdot \sigma_3) \right]$$

A = Upper Crack-Tip Located **at the** Pressure Wall and Rib Intersection

B = Lower Crack-Tip Located **before** Pressure Wall and Rib Intersection

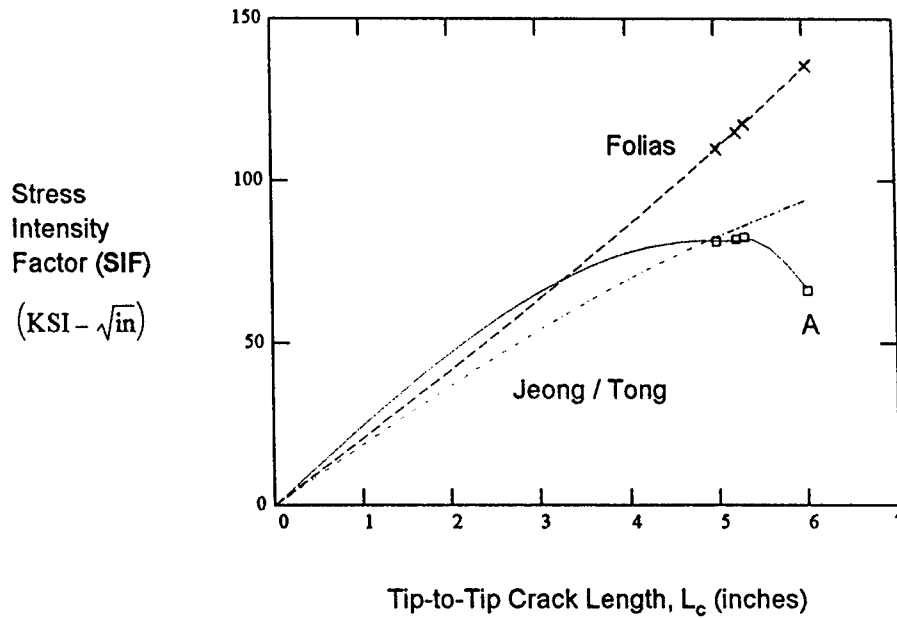
Figure 42 - ESA MPLM END CONE with an AXIAL CRACK within a WAFFLE-GRID CELL
 CRACK TIPS (A & B) STRESS INTENSITY FACTORS (SIF) vs. CRACK LENGTH
 (at 14.9 psia internal pressure loading)

For comparative purposes, we have also utilized two additional fracture parameters, developed by Folias and Jeong & Tong, for through the wall cracks in pressure vessels. Figure 43 shows the results of this comparison. Note that, the fracture criterion by Folias and Jeong & Tong are applicable to isotropic shells only. Nevertheless, they were employed so that to verify the order of magnitude of our calculated SIF's.

From the estimated values of fracture toughness of 2219-T87 Aluminum Alloy with a minimum thickness of 0.098 inch (see Section AIII-4, TABLE II), and from the results of the SIF shown in Figure 42, we have assessed the corresponding CCL for the ESA MPLM under quasi-static loading conditions, as summarized below.

CRACK PROPAGATION CONDITIONS	CRACK-TIP	AROUND the MEAN	MINUS ONE STANDARD DEVIATION
Stable Initiation & Growth	A	5.3 inch	3.7 inch
	B	7.0 inch	4.2 inch
Unstable (Critical)	A	N/A	N/A
	B	7.7 inch	7.5 inch
N/A = Not Applicable			

The significant results of this study for the ESA MPLM end cone structure criticality to fracture indicated that the CCL is confined to one cell spacing only. As shown in Figure 42, a pronounced decay on the SIF is observed as the CTIP-A (North Crack) approaches an internal rib. The ribs acts essentially as crack-stoppers. In brief, the CCL here is irrelevant, as far as the unzipping issue is concerned, if one confines the CL within one cell only.



$$\text{Folias SIF} = \frac{p \cdot R}{h \cdot \cos(\alpha)} \cdot \sqrt{\pi \cdot a} \cdot \sqrt{1 + \left[3.22 \cdot \left(\frac{a^2}{2 \cdot R \cdot h} \right) \right]}$$

$$\text{Jeong \& Tong SIF} = \frac{p \cdot R}{h \cdot \cos(\alpha)} \cdot \sqrt{\pi \cdot a} \cdot \sqrt{1 + \left[0.67 \cdot \left[\frac{E}{F_{ty}} \cdot \left(\frac{a}{R} \right)^2 \right]^{\frac{2}{3}} \right]}$$

$$\text{A SIF} = \sqrt{E \cdot \zeta \cdot C} \quad \zeta = \text{Strain Energy Density at the Crack-Tip}$$

C = a constant (may include n, the SHE)

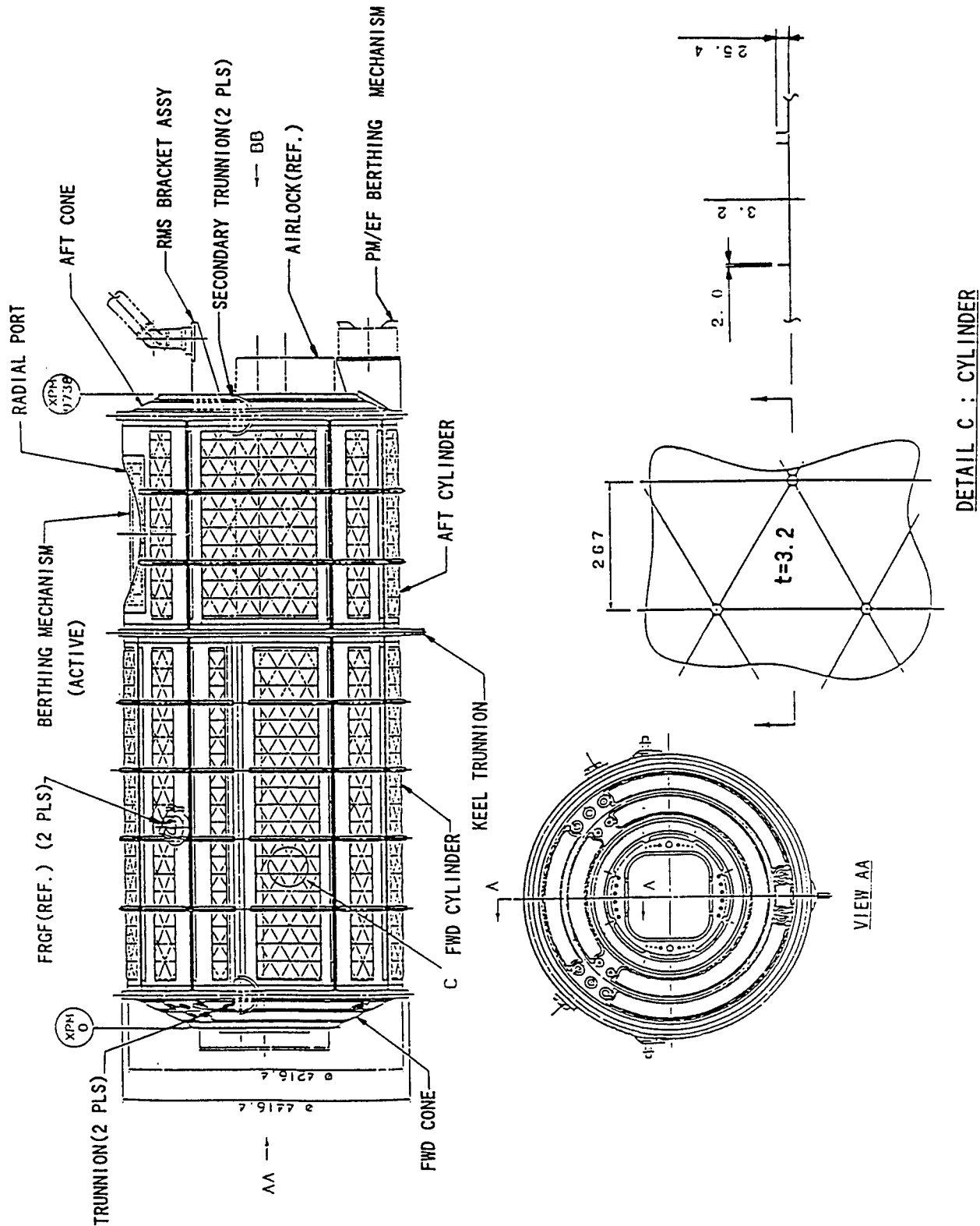
Figure 43- ESA MPLM END CONE with an AXIAL CRACK within a WAFFLE-GRID CELL
CRACK-TIP "A" SIF COMPARISON vs. CRACK LENGTH
for THREE DIFFERENT ANALYTICAL METHODS
(at 14.9 psia internal pressure loading)

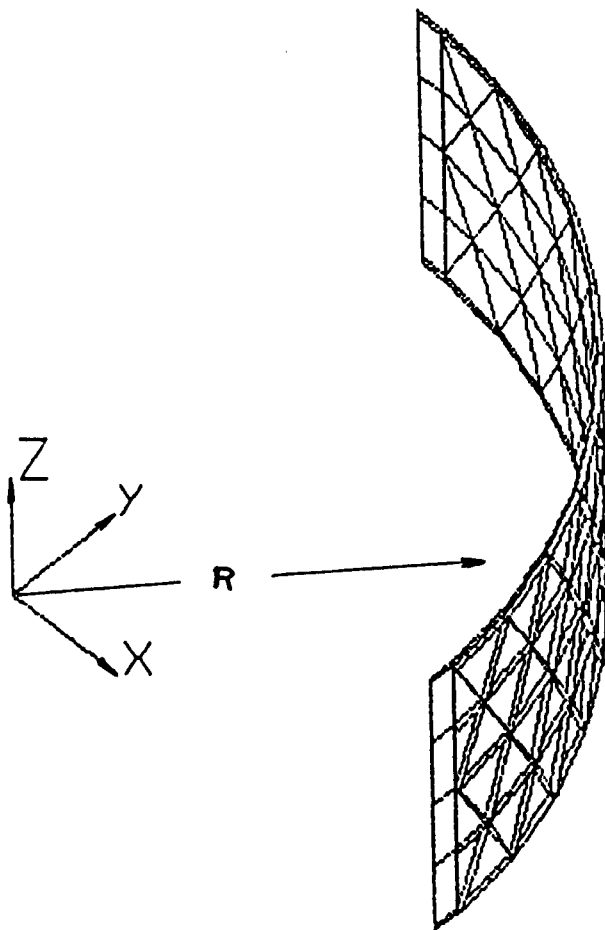
AIV-4 JAPAN SPACE AGENCY (NASDA) JEM PM LAB MODULE

The JEM LAB module overall design arrangement is displayed in Figure 44. At first, a 3D finite element model of a 1/4 segment of the shell Isogrid stiffened pressure wall (without any cracks) of the shell was developed as shown in Figure 45. The model was run with the ALGOR code for an elastic solution to determine the stress distribution within the Isogrid skin under a 14.9 psia internal pressure loading, as illustrated in Figure 46. The resulting principal stress distribution throughout the system is shown in Figure 47. Next, we have conducted a plane stress nonlinear elasto-plastic finite element analysis, using the ELASTO FEA code, of a discrete section of the Isogrid wall using a center cracked tension (CCT) analytical specimen as depicted in Figure 48 through Figure 50. This CCT model possess all the features of the Isogrid stiffened skin design, in particular the reinforcement at the ribs joint. The CCT loading conditions consisted of the hoop and axial average principal stresses (biaxial loading) obtained from the 3D FEA model. Several iterations were made, whereby the crack length (here, half-crack length, a_0) by finite increments. The resulting crack-tip (CTIP) opening displacements (CTOD), and crack mouth opening displacements (CMOD), as shown in Figure 51, were catalogued and saved in a file that can be used by the MathCad software. For this structure, we have utilized three fracture criterion to assess the stress intensity factor at the CTIP. They are graphically displayed in Figure 52, with the respective criteria listed. They have all in common the crack bulging effects due to the internal pressure. However, Folias and Jeong & Tong criterion are for monolithic and isotropic type of shell, whereas MA-1 criterion uses the J -integral principle along with the corresponding pertinent results obtained from the CCT specimen. The SIF function of the crack length indicated a maximum SIF of about 100 KSI-in^{0.5} for a 16 inch tip-to-tip crack length. A slight decay on the SIF can be observed in Figure 52 (see also Figure 53, point B) when the CTIP approaches a joint. In essence, the joints, with they added stiffness, tends to act as crack-stoppers.

The significant results of this study on the JEM PM module criticality to fracture suggest that the CCL is approximately 16 inches, if one assumes that one hoop-rib is ruptured by an M/OD impact. Otherwise, the CCL is irrelevant if one confines the CL within one cell only. Based on the above findings and on the allowable 2219-T87 fracture toughness with a thickness of 0.126 inch (see TABLE II, Section AIII-4), the estimated CCL for this module are as follows:

<u>CRACK PROPAGATION CONDITIONS</u>	<u>AROUND the MEAN VALUE</u>	<u>MINUS ONE STD. DEVIATION</u>
Stable Initiation & Growth	12.0 inches	10.0 inches
Unstable (Critical)	N/A	15.3 inches





Reinforced Skin with a Isogrid
Construction

Internal Radius = 83.0 inch
 Shell Thickness within Cells = 0.126 inch
 Isogrid Spacing: axial = 10.51 inch
 hoop = 12.136 inch
 Rib Height & Thickness = 1.0 x 0.079 inch
 Internal Pressure = 14.9 psia
 Material: Aluminum Alloy 2219-T87

Figure 45 - NASDA JEM PM CYLINDRICAL SHELL 3D FEA 1/4 (90°) SEGMENT
 MODEL PERSPECTIVE VIEW

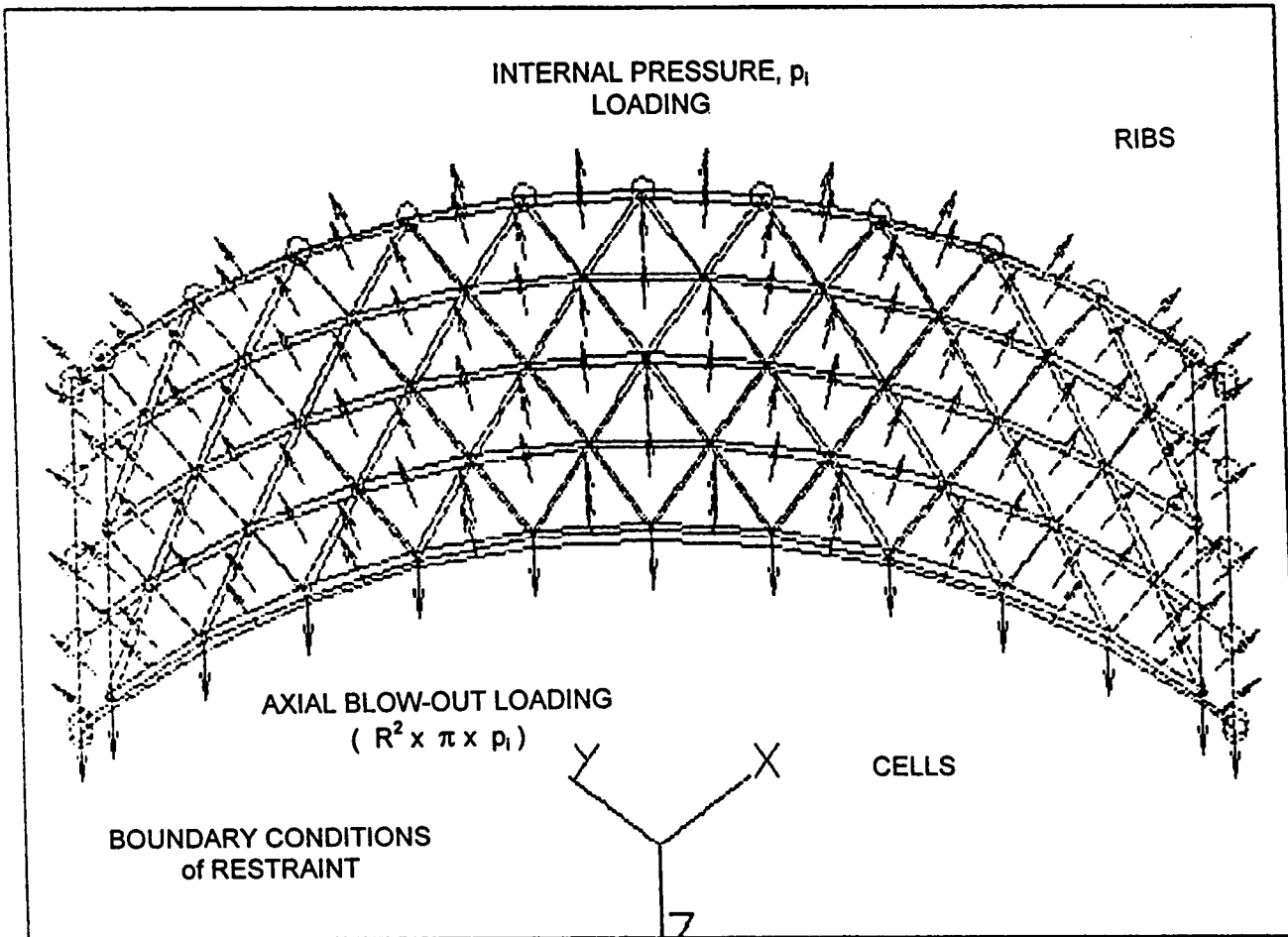


Figure 46 - NASDA JEM PM CYLINDRICAL SHELL 3D FEA 1/4 (90°) SEGMENT
MODEL TOP VIEW
(Internal Pressure and Axial Blow Out Loading)

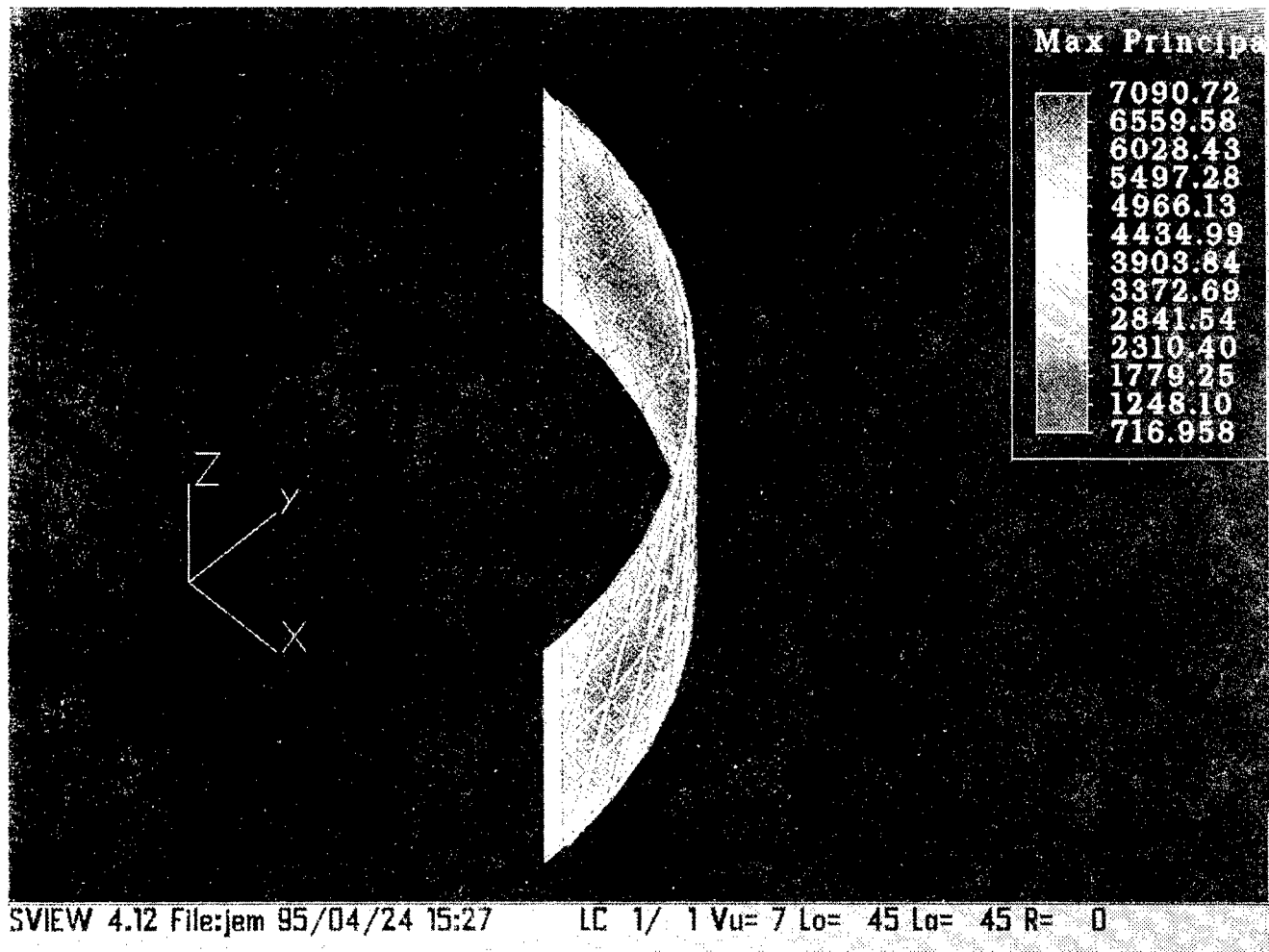


Figure 47 - NASDA JEM PM CYLINDRICAL SHELL 3D FEA 1/4 (90°) SEGMENT
MODEL WITHOUT a CRACK - PRINCIPAL STRESS (psi) DISTRIBUTION
(Internal Pressure and Axial Blow Out Load (biaxial loading) at 14.9 psia)

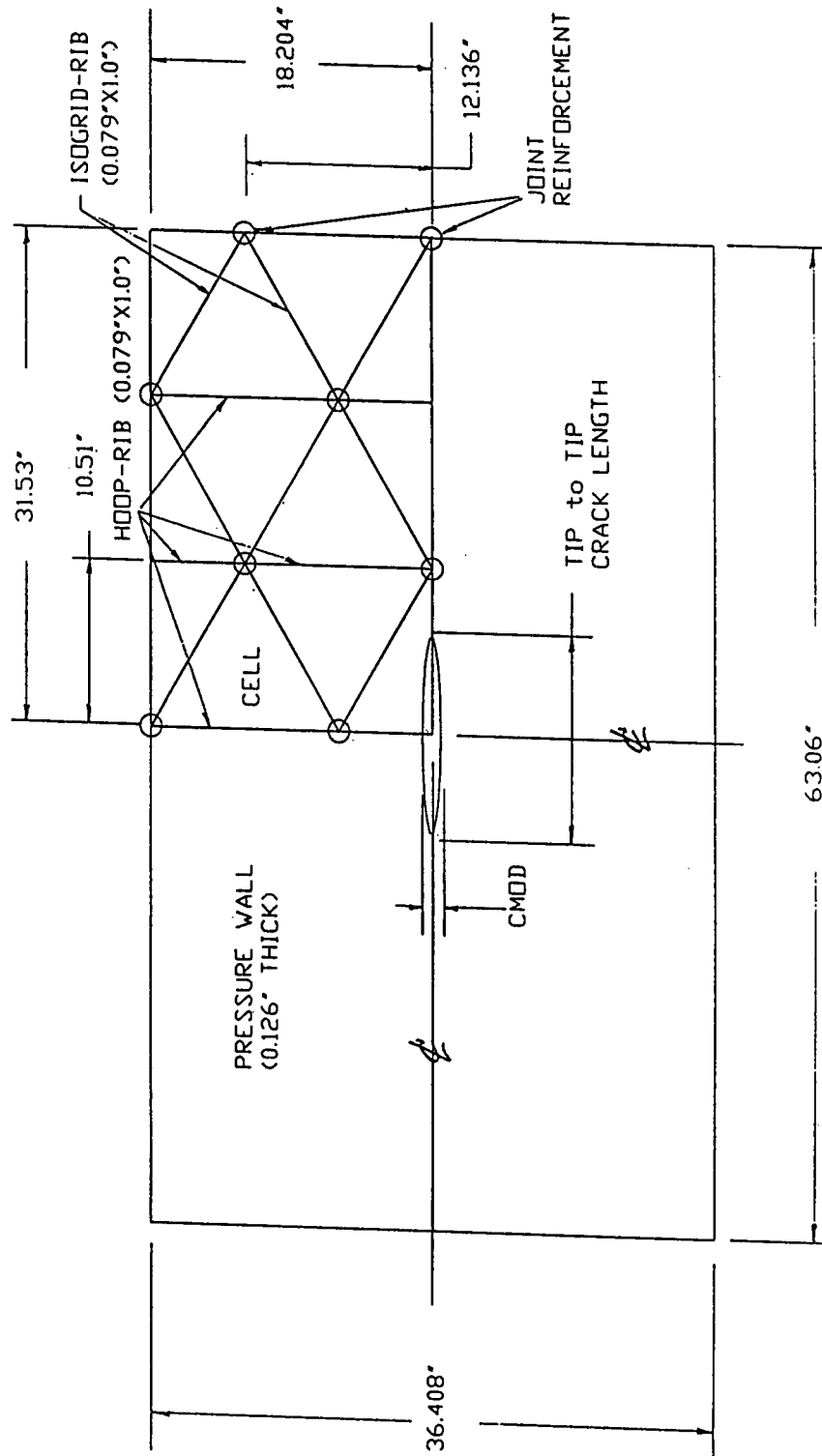


Figure 48 - NASDA JEM PM CYLINDRICAL SHELL ISOGRID STIFENED SKIN
CCT FLAT PLATE ANALYTICAL SPECIMEN

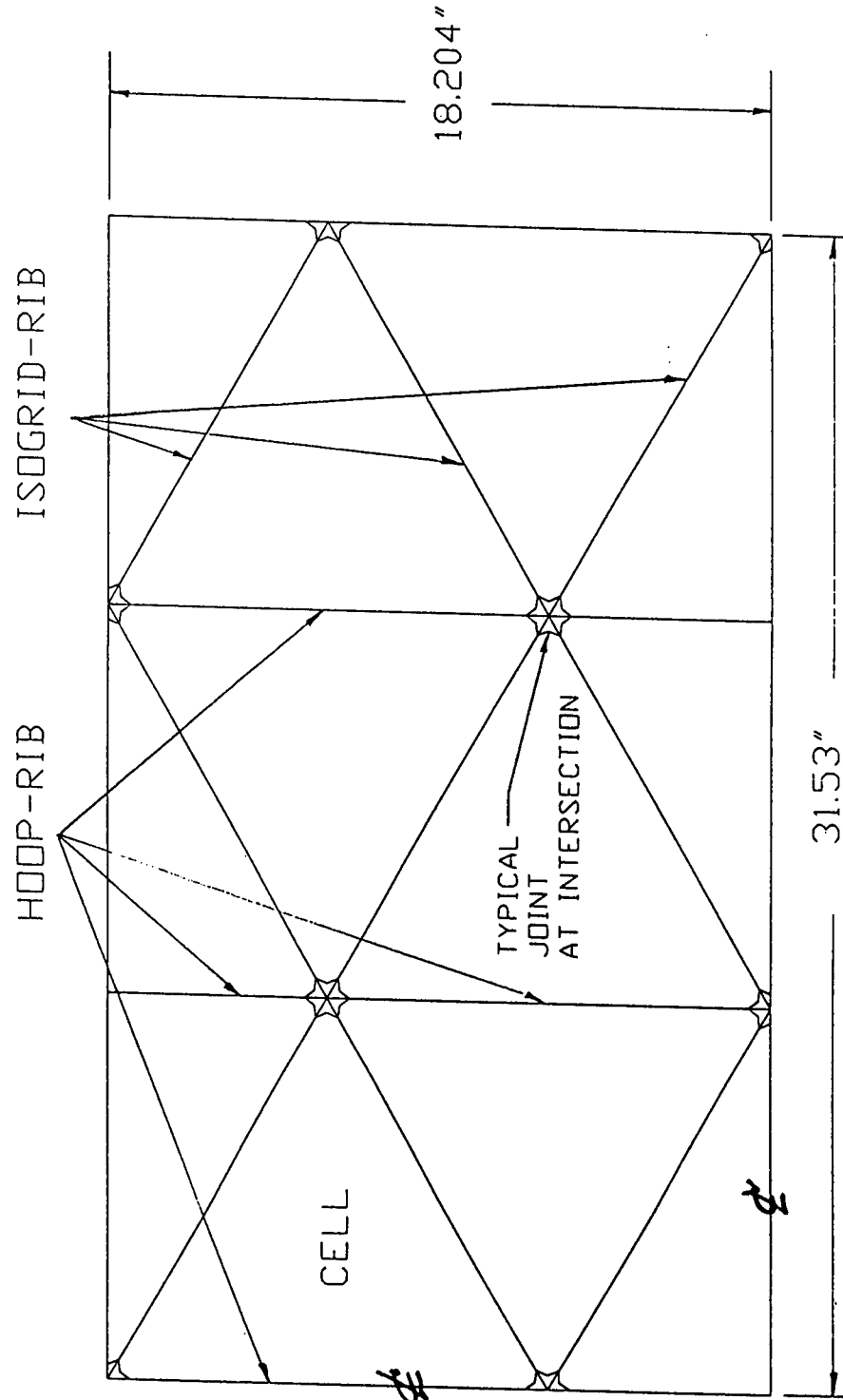


Figure 49 - NASDA JEM PM CYLINDRICAL SHELL ISOGRID STIFENED SKIN
CCT FLAT PLATE 1/4 ANALYTICAL MODEL
(Reduced Size due to Symmetry and Prior to Finite Elements Meshing)

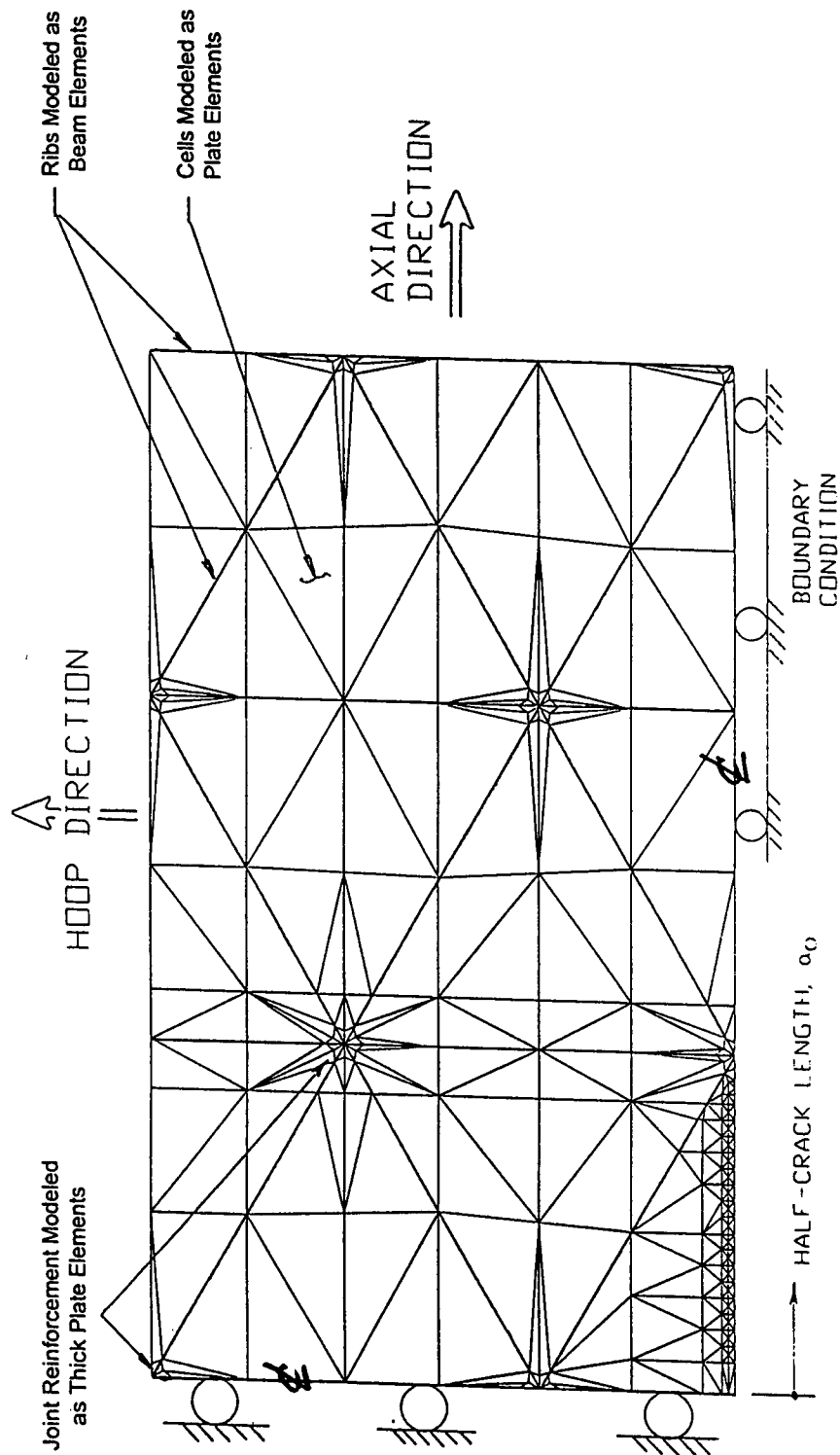


Figure 50 - NASDA JEM PM CYLINDRICAL SHELL ISOGRID STIFENED SKIN
CCT FLAT PLATE
PLANE STRESS ELASTO-PLASTIC FINITE ELEMENT MODEL

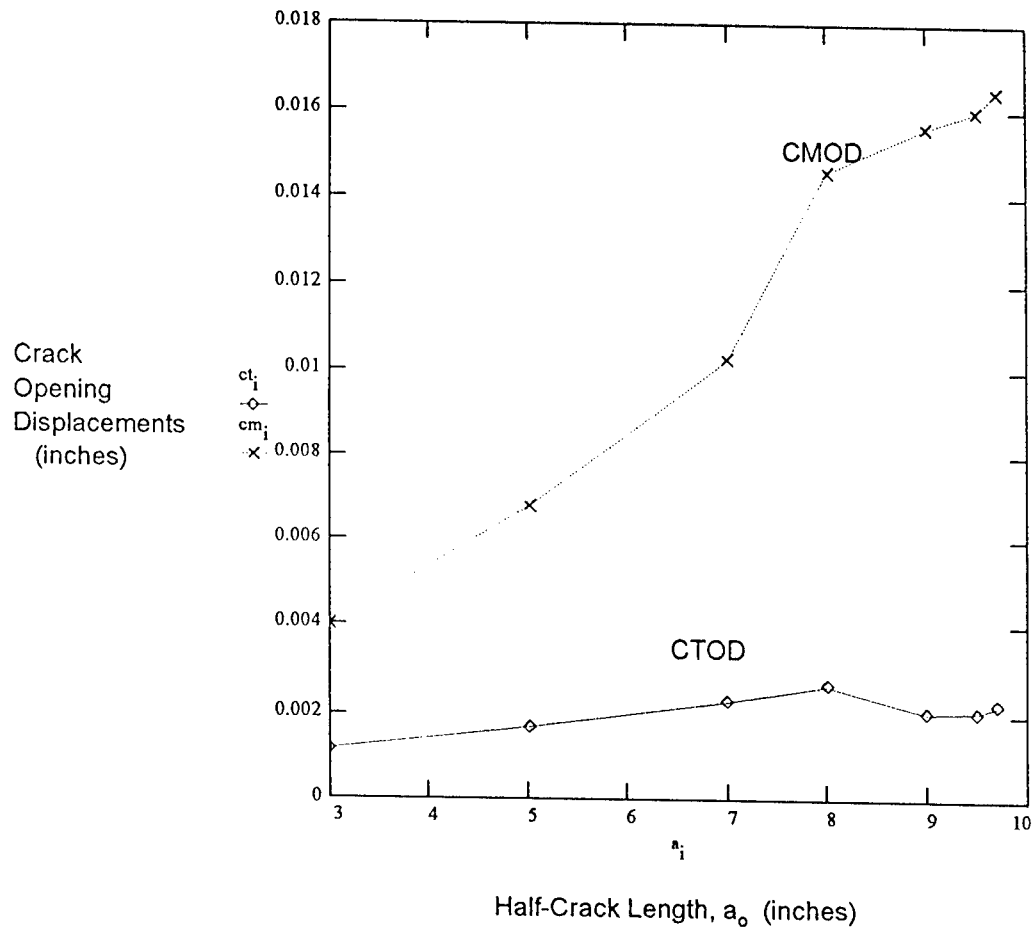
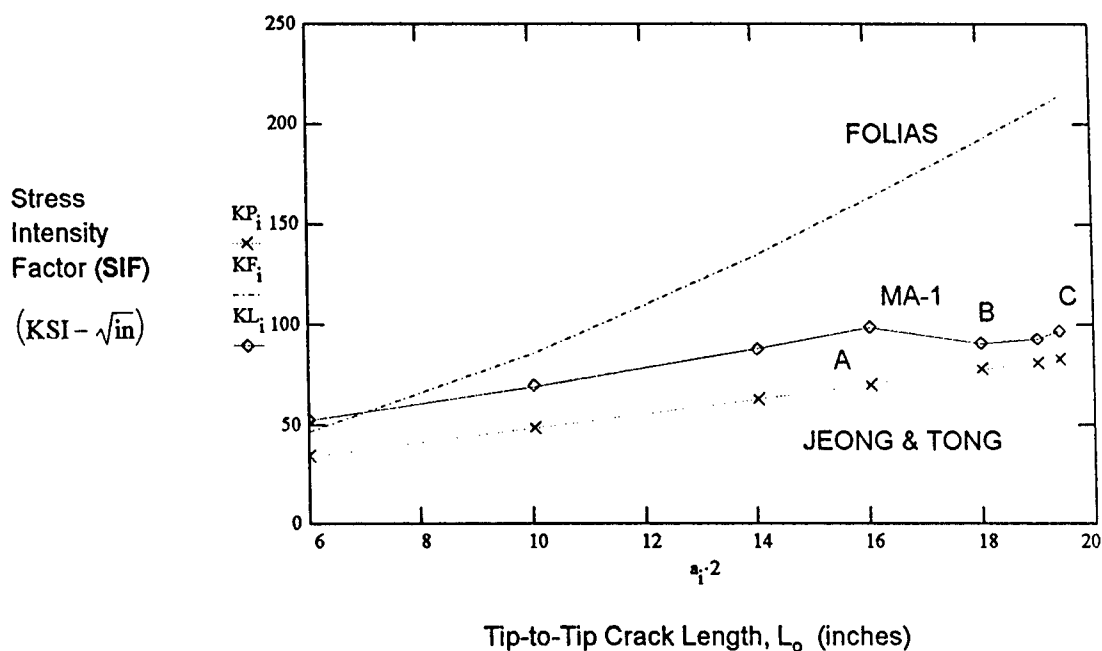


Figure 51 - NASDA JEM PM CYLINDRICAL SHELL ISOGRID STIFENED SKIN
CCT PLANE STRESS ELASTO-PLASTIC FINITE ELEMENT ANALYSIS RESULTS
CRACK OPENING DISPLACEMENTS (COD) vs. HALF-CRACK LENGTH (a_o)



$$\text{FOLIAS: SIF} = \frac{p \cdot R}{h} \cdot \sqrt{\pi \cdot a} \cdot \sqrt{1 + \left[3.22 \cdot \left(\frac{a^2}{2.0 \cdot R \cdot h} \right) \right]}$$

$$\text{JEONG/TONG: SIF} = \frac{p \cdot R}{h} \cdot \sqrt{\pi \cdot a} \cdot \sqrt{1 + \alpha \cdot \left[\left(\frac{E}{\sigma_y} \right) \cdot \left(\frac{a}{R} \right)^2 \right]^{\frac{2}{3}}}$$

$$\text{MA-1: SIF} = \sqrt{\frac{E}{0.6} \int_0^{\delta_T} \sigma_y d\delta_T} \cdot \sqrt{1 + \alpha \cdot \left[\left(\frac{E}{\sigma_y} \right) \cdot \left(\frac{a}{R} \right)^2 \right]^{\frac{2}{3}}}$$

δ_T = Crack Tip Opening Displacement

α = Empirical Constant

σ_y = Material Yield Strength

Figure 52 - NASDA JEM PM CYLINDRICAL SHELL ISOGRID STIFENED SKIN
CCT PLANE STRESS ELASTO-PLASTIC FINITE ELEMENT ANALYSIS RESULTS
STRESS INTENSITY FACTORS (SIF) vs. HALF-CRACK LENGTH (a_0)

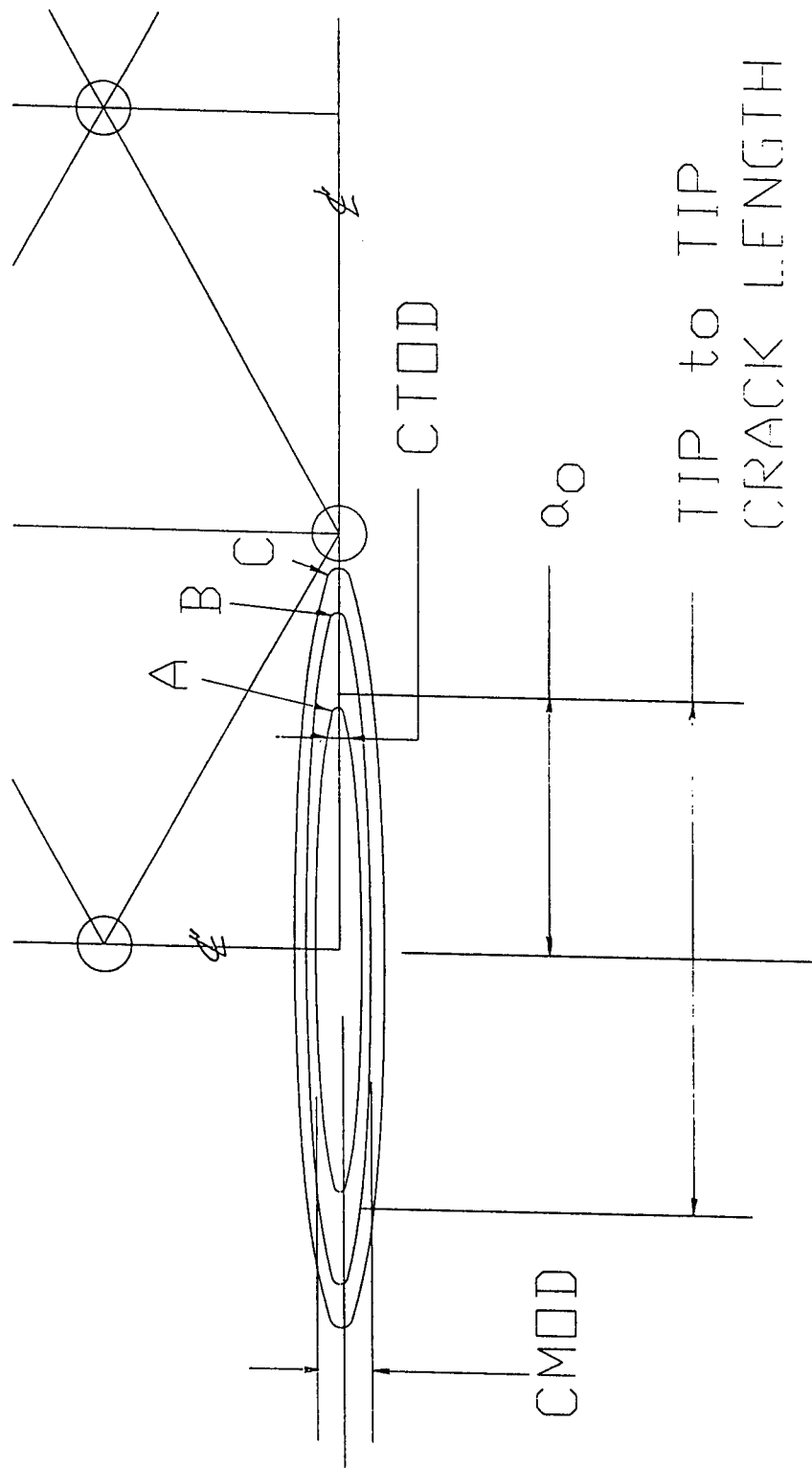


Figure 53 - NASDA JEM PM CYLINDRICAL SHELL ISOGRID STIFFENED SKIN
CCT PLANE STRESS ELASTO-PLASTIC FINITE ELEMENT ANALYSIS
COD and CRACK-TIP CRITICAL LOCATIONS (see Figure 52)

AIV-5 RUSSIAN FGB (SPACE TUG) PROPULSION MODULE

Initially, a 3D elastic finite element analysis of a segment of the shell without any cracked region within the pressure wall, was performed to determine the stress distribution within the waffle-skin, under an internal pressure loading of 14.9 psia. The overall FEA model is shown in Figure 54 along with pertinent design details, also illustrated in Figure 55, with the pressure loading shown in Figure 56. The resulting principal stress distribution within the shell is displayed Figure 57. Then, we have conducted a plane stress nonlinear elastic-plastic finite element analysis of a discrete section of the shell wall with a center cracked tension (CCT) specimen shown in Figure 58. The FEA model is displayed in Figure 59, which consists only of a quarter of the CTT, due to geometric symmetry. The CCT model has all the features and characteristics of the waffle-skin design; that is, fillet radius adjacent to the rib root at the pressure wall, and rib equivalent stiffness were incorporated in the FEA model. Several iterations were made, using the computer code ELASTO, in which the crack length was extended by finite increments. The ensuing crack displacements (CTOD and CMOD), as displayed in Figure 60, were recorded and inputted into the MathCad software program for post processing. We have mainly selected four fracture criterion for assessing the SIF of interest. They are displayed graphically in Figure 61 with the corresponding criterion listed. They have all in common the crack bulging effects due to the internal pressure. However, Folias and Jeong & Tong parameters are for isotropic cylindrical shell and plate, respectively, whereas MA-1 and MA-2 uses the FEA results along with the J -integral criterion. In Figure 61, we have designated three points, whereby the CTIP SIF display a discontinuity. In point A, as the CTIP approaches a rib, the SIF decreases substantially. In point B, we have artificially precracked two ribs, so that the crack length could be extended. Here, the SIF jump to a higher level. As the CTIP progresses toward another rib, again the SIF drops dramatically. This event is illustrated by point C, in Figure 61. This crack growth scenario is illustrated in Figure 62. Essentially, the integrally machined ribs of the waffle-skin tends to act as crack-stoppers. Moreover, limited test data indicated the unit propagation energy of the Aluminum Alloy 5456-0 used for the shell construction is in the order of 1000 in-lbf/in^2 which is, for example, about three times higher than the 2219-T87 Al/Al. The unit propagation energy, is the energy required to extend the crack to specimen fracture divided by the net cross section. Based on the confined data, we have chosen a fracture toughness of $80 \text{ KSI-in}^{0.5}$ as the median value for the 5456-0 Al/Al (see Figure 61).

The important results of this assessment on the criticality for the Russian TUG shell to unzip, indicated it will be very difficult to propagate a through-the-wall axial crack within the waffle-skin under 14.9 psia pressure loading alone, and for this particular shell design and selected material. Other damage conditions must prevail in order to "unzip" the shell catastrophically.

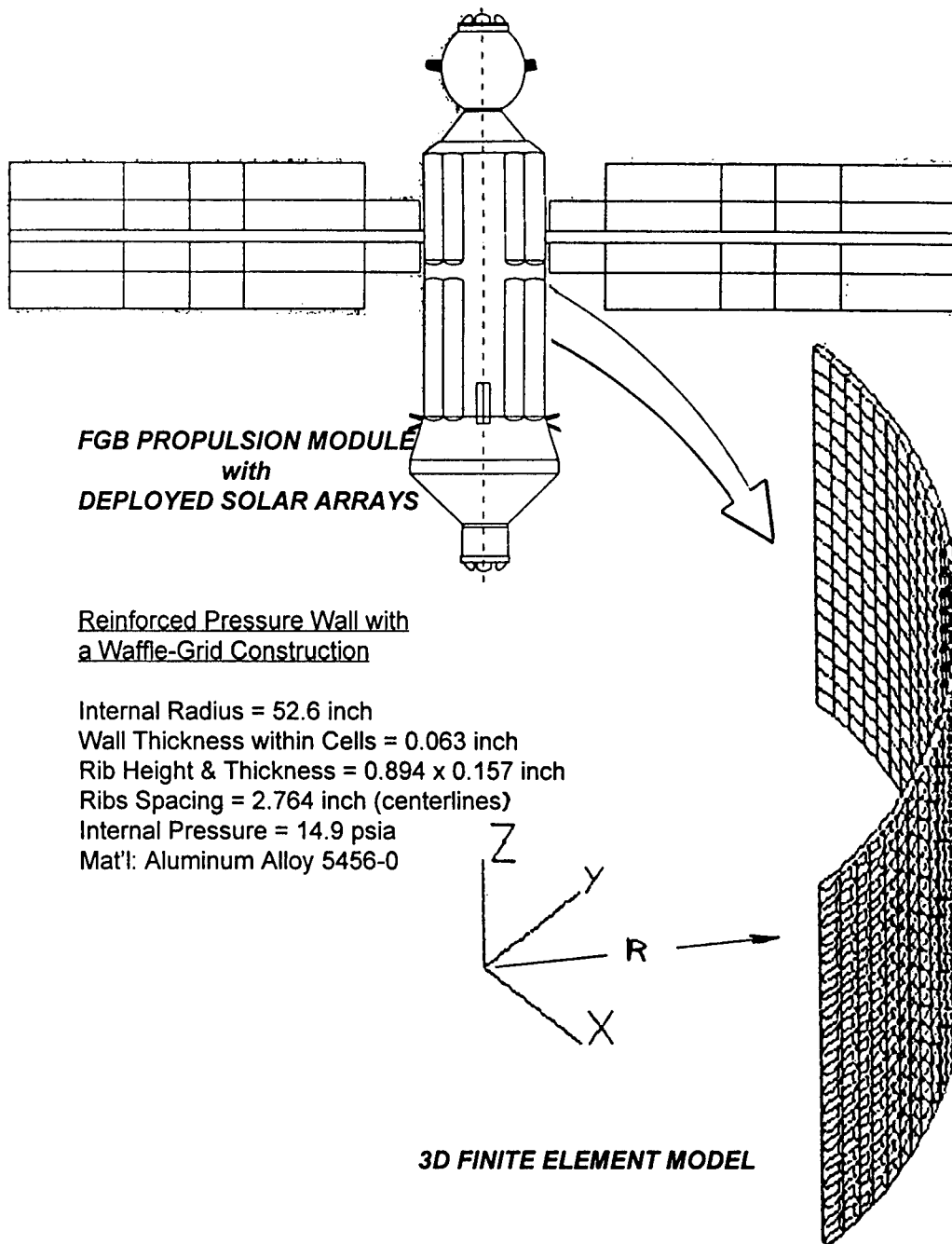


Figure 54 - RUSSIAN FGB (SPACE TUG) CYLINDRICAL SHELL
 3D FINITE ELEMENT 1/4 (90°) MODEL of a SECTION of the WAFFLE GRID REINFORCED SKIN

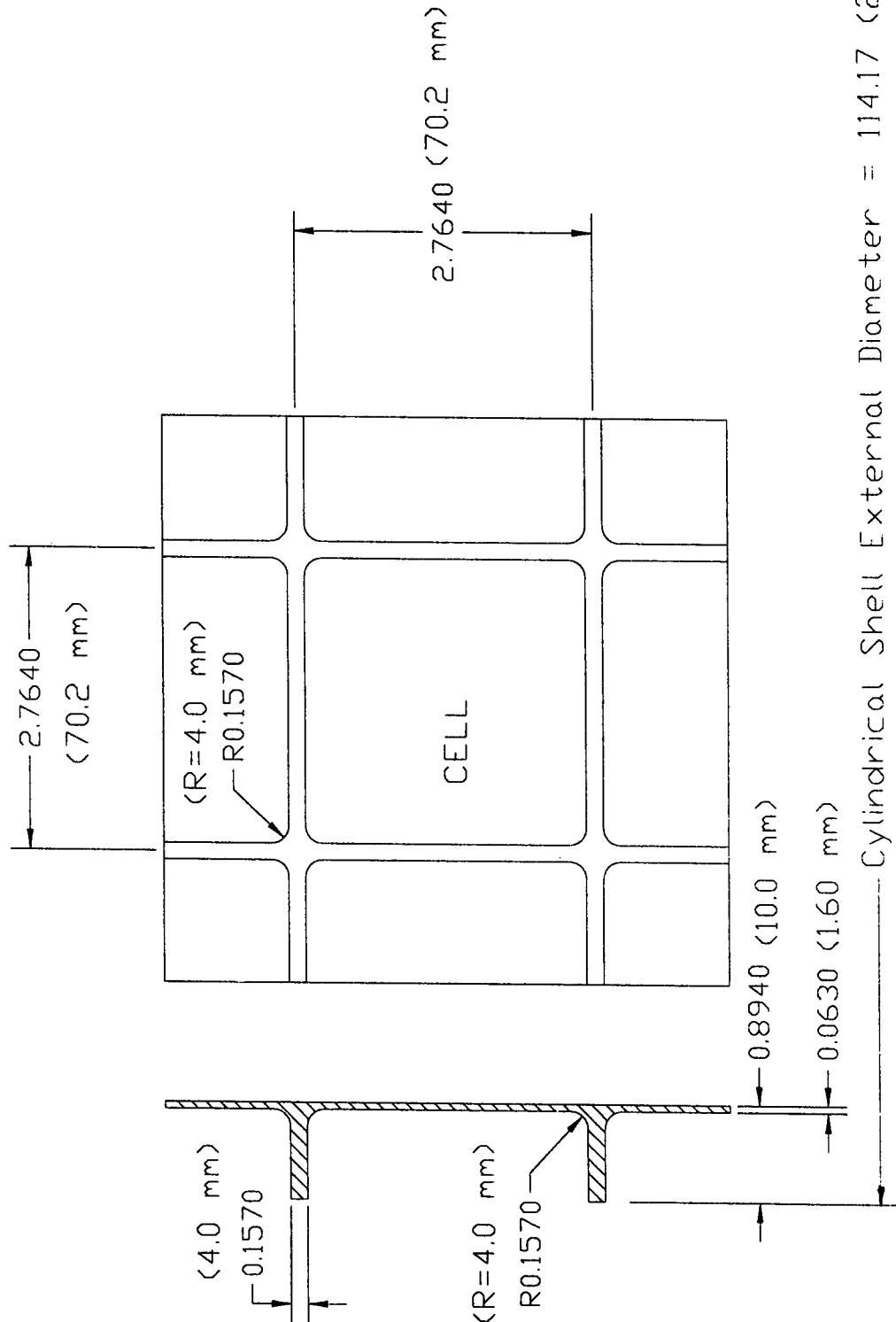


Figure 55 - RUSSIAN FGB (SPACE TUG) CYLINDRICAL SHELL
WAFFLE GRID REINFORCED SKIN DESIGN DETAILS

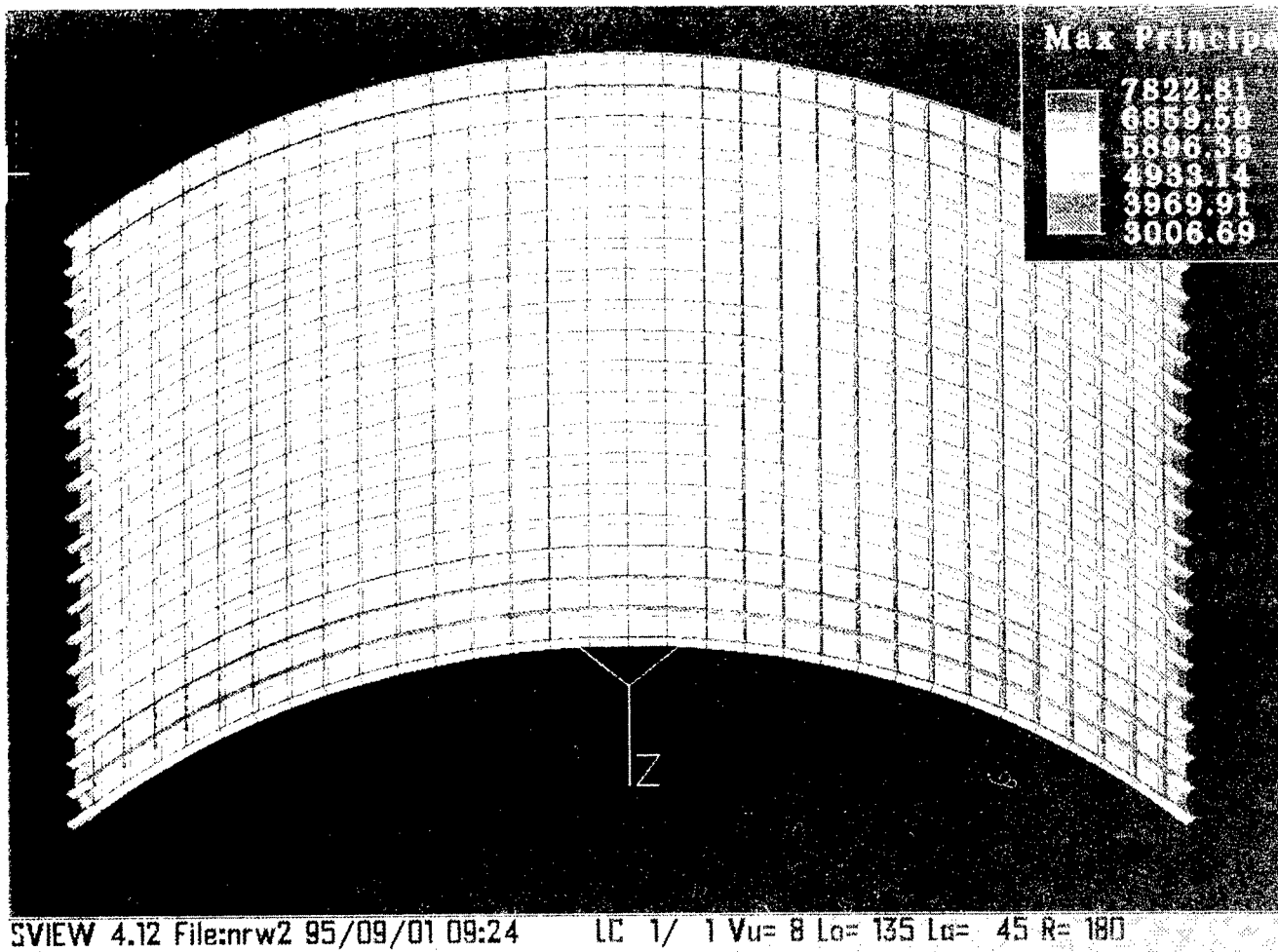


Figure 56 - RUSSIAN FGB (SPACE TUG) CYLINDRICAL SHELL
3D FEA MODEL with INTERNAL PRESSURE LOADING
(Note Ribs are External to the Shell Pressure Wall)

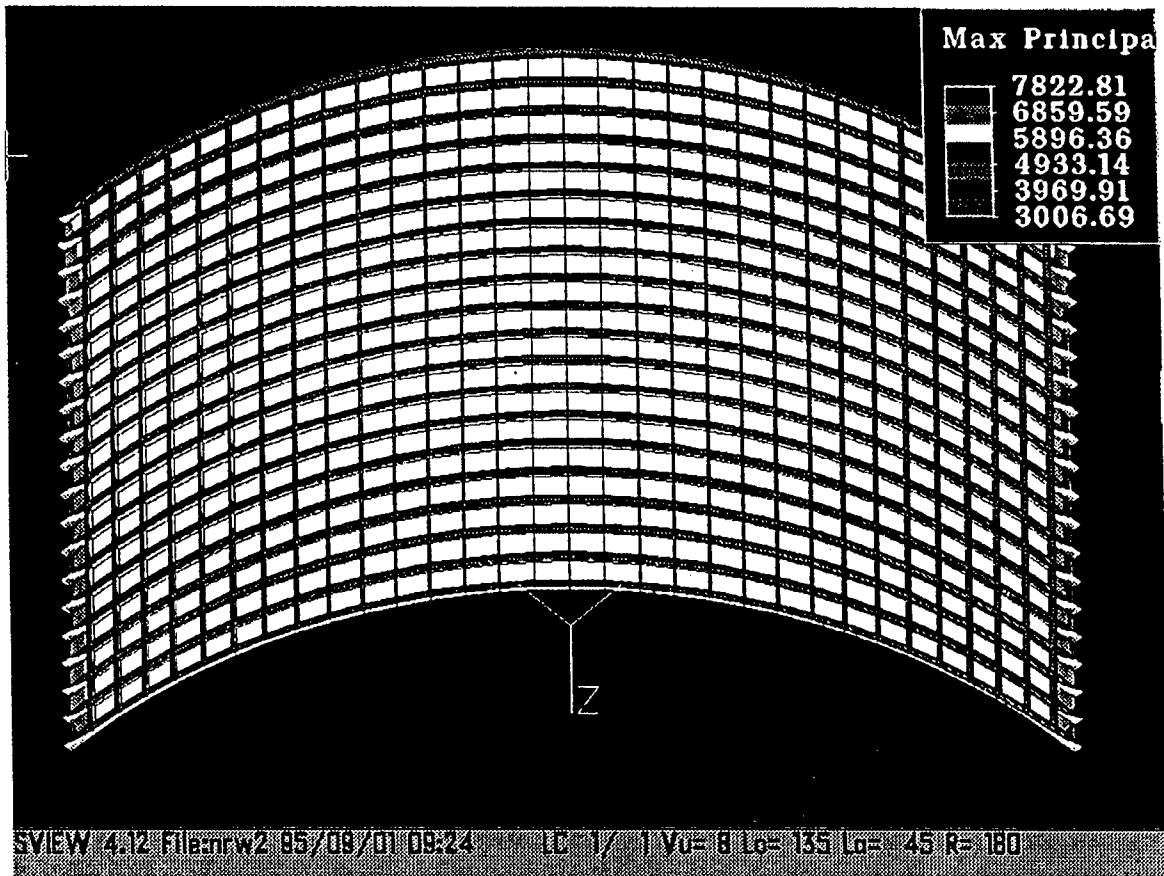


Figure 57 - RUSSIAN FGB (SPACE TUG) CYLINDRICAL SHELL WITHOUT A CRACK
PRINCIPAL STRESS (psi) DISTRIBUTION at 14.9 psia INTERNAL PRESSURE

INTERNATIONAL SPACE STATION ALPHA

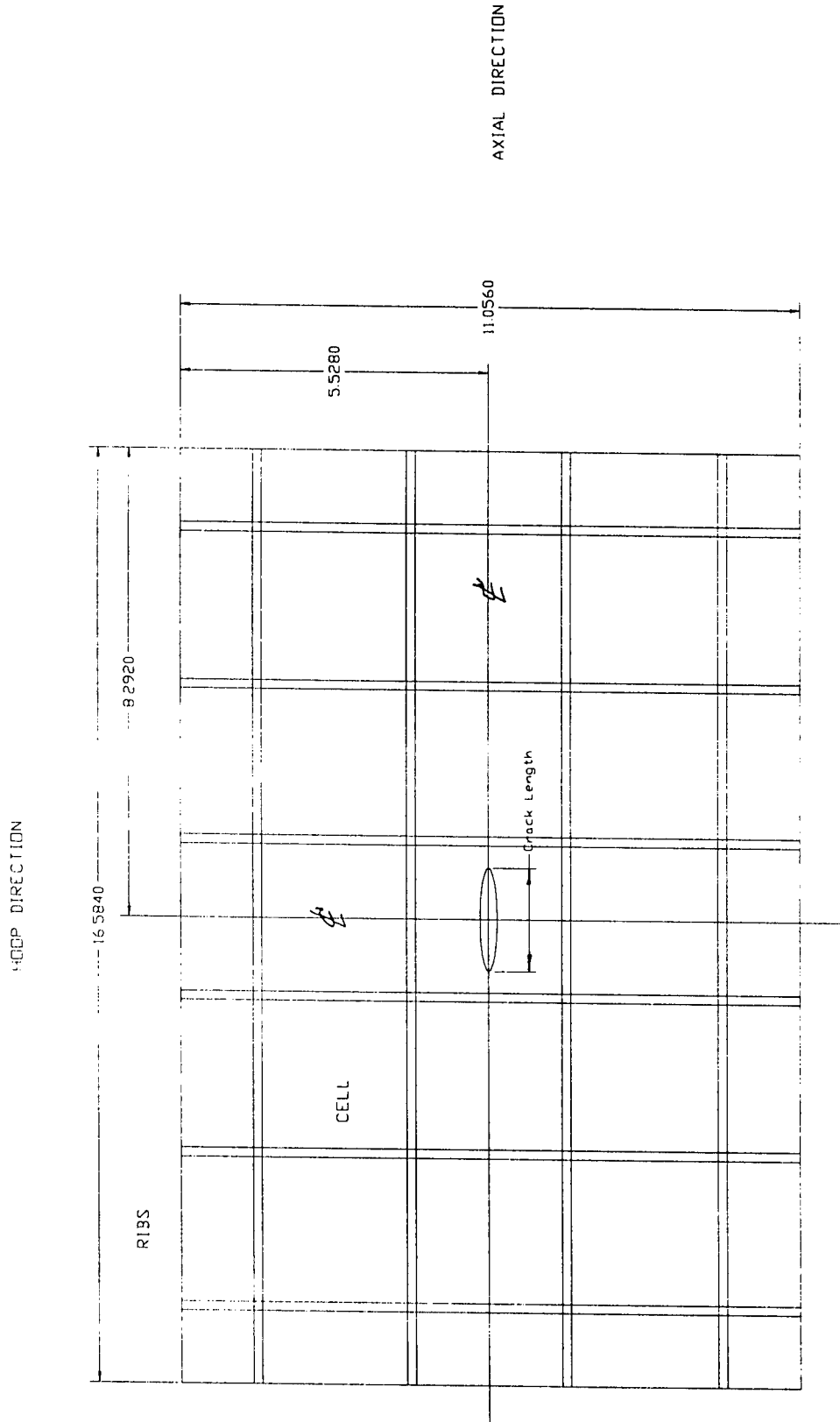


Figure 58 - RUSSIAN FGB CYLINDRICAL SHELL WAFFLE-GRID REINFORCED SKIN
CCT FLAT PLATE ANALYTICAL SPECIMEN

A-79

MA-TR-101-95
SECTION A

INTERNATIONAL SPACE STATION ALPHA

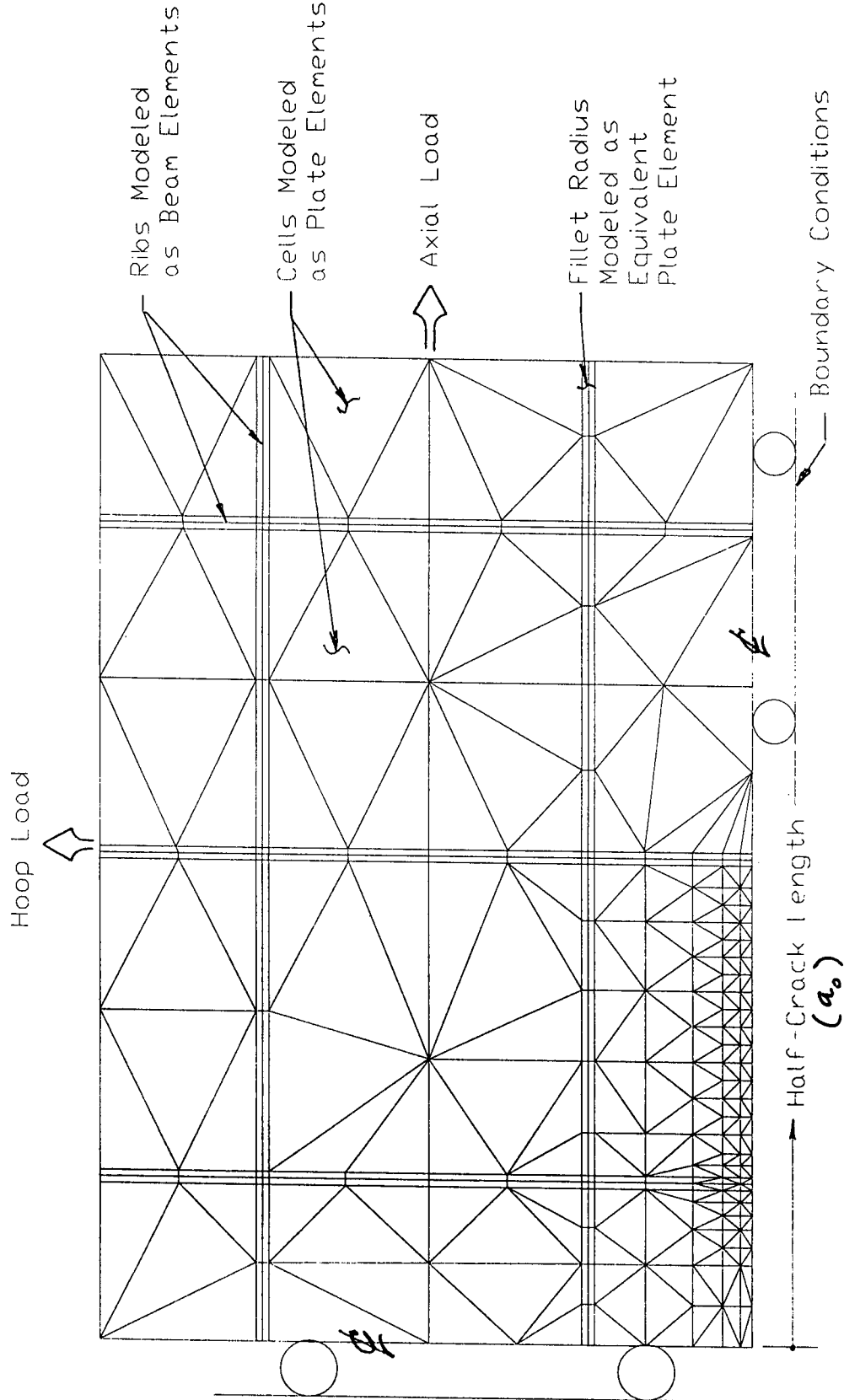
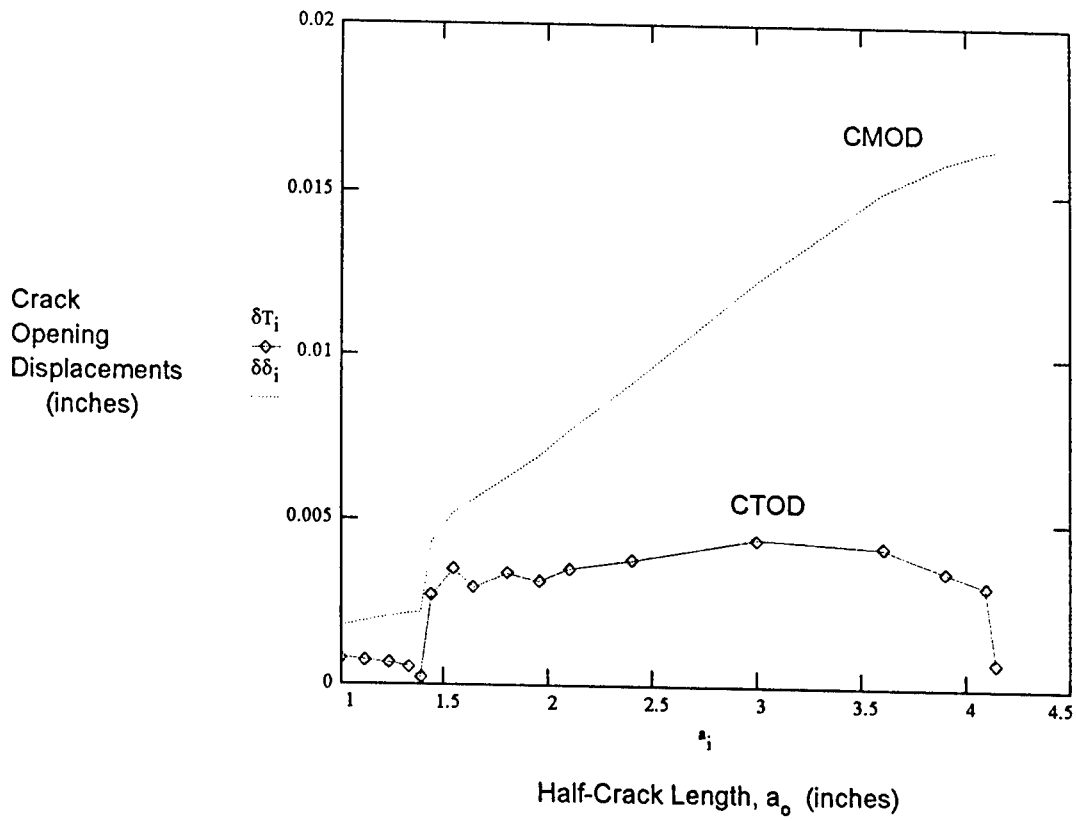


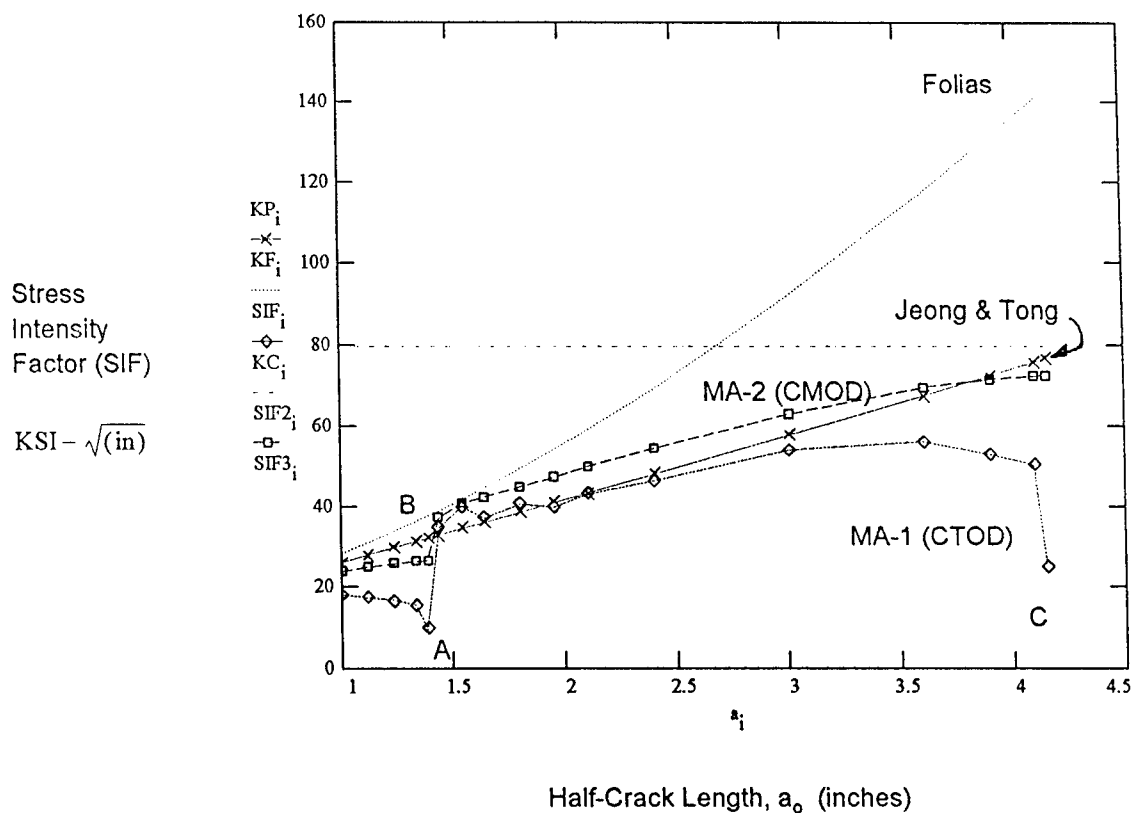
Figure 59 - RUSSIAN FGB CYLINDRICAL SHELL WAFFLE-GRID REINFORCED SKIN CCT FLAT PLATE PLANE STRESS ELASTO-PLASTIC FEA MODEL



CTOD = Crack Tip Opening Displacement

CMOD = Crack Mouth Opening Displacement

Figure 60 - RUSSIAN FGB CYLINDRICAL SHELL WAFFLE-GRID REINFORCED SKIN
CCT FLAT PLATE PLANE STRESS ELASTO-PLASTIC FEA RESULTS
CRACK OPENING DISPLACEMENTS (COD) vs. HALF-CRACK LENGTH



$$\text{FOLIAS: } \text{SIF} = \frac{p \cdot R}{h} \cdot \sqrt{\pi \cdot a} \cdot \sqrt{1 + \left[3.22 \cdot \left(\frac{a^2}{2.0 \cdot R \cdot h} \right) \right]}$$

$$\text{JEONG \& TONG: } \text{SIF} = \frac{p \cdot R}{h} \cdot \sqrt{\pi \cdot a} \cdot \sqrt{1 + \left[\left(\frac{E}{\sigma_y} \right) \cdot \left(\frac{a}{R} \right)^2 \right]^{\frac{2}{3}}}$$

$$\text{MA-1: } \text{SIF} = \sqrt{\frac{E}{0.6} \int_0^{\delta_T} \sigma_y d\delta_T} \cdot \sqrt{1 + \left[\left(\frac{E}{\sigma_y} \right) \cdot \left(\frac{a}{R} \right)^2 \right]^{\frac{2}{3}}}$$

$$\text{MA-2: } \text{SIF} = \sqrt{\frac{E}{0.6} \cdot \sigma_y \cdot \delta_{\text{cmo}} \cdot} \cdot \sqrt{1 + \left[\left(\frac{E}{\sigma_y} \right) \cdot \left(\frac{a}{R} \right)^2 \right]^{\frac{2}{3}}}$$

Figure 61 - RUSSIAN FGB CYLINDRICAL SHELL WAFFLE-GRID REINFORCED SKIN
CCT FLAT PLATE PLANE STRESS ELASTO-PLASTIC FEA RESULTS
STRESS INTENSITY FACTORS (SIF) vs. HALF-CRACK LENGTH

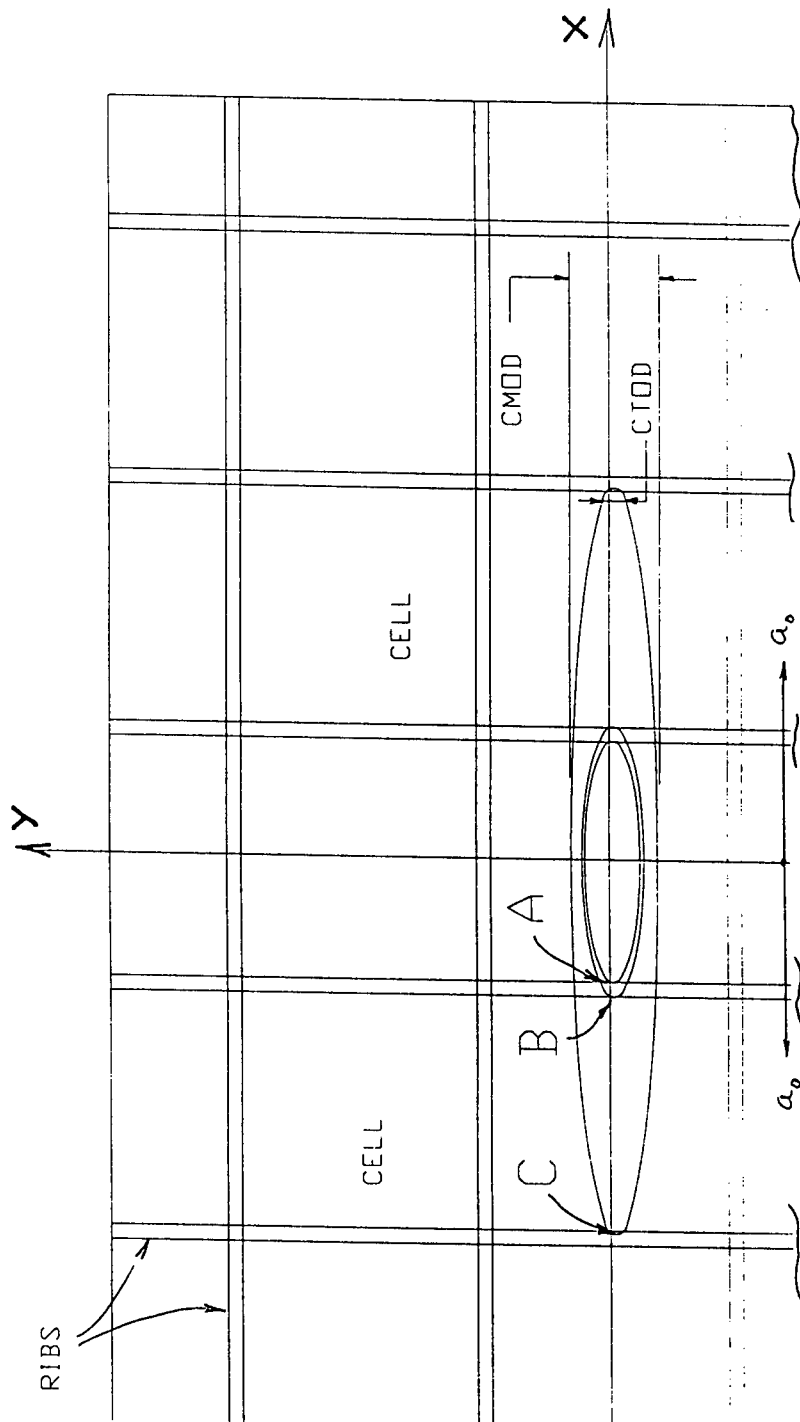


Figure 62 - RUSSIAN FGB CYLINDRICAL SHELL WAFFLE-GRID REINFORCED SKIN
CCT PLANE STRESS ELASTO-PLASTIC FEA MODEL
SIF and CRACK-TIP (CTIP) CRITICAL LOCATIONS

AIV-6 RUSSIAN FGB SPACE TUG AUXILIARY TANKS

A rapid assessment of the critical crack length (CCL) of two FGB propulsion module auxiliary tanks was performed to determine the criticality to fracture under internal quasi-static pressure. The pressure vessels considered were the propellant tank and the GN2 spherical bottle.

Here, we have used mainly two fracture criterion, namely: 1) Folias closed form solution [1], and 2) Jeong & Tong [14] modified parameter by Lutz. Both includes bulging effects due to the internal pressure.

The pertinent results are shown in Figure 63 for the propellant tank, and in Figure 64 for the GN2 bottle. Conservative values (lower shelf) were used for the fracture toughness at crack instability, for the respective material employed for these vessels construction.

Russian FGB auxiliary tanks, critical crack lengths**1) propellant tank - Material = Alu/Magnesium, 5XXX series**

$$p_1 := 233.0 \quad h_1 := 0.098 \quad D_1 := 18.9 \quad E_1 := 10200000.0 \quad \alpha_1 := 0.67 \quad i := 1..6$$

$$K_{I_1} := 80.0 \quad \sigma_{ly} := 42000.0 \quad n := 50 \quad \sigma_{ly} \cdot E_1^{-1} = 0.004 \quad \eta_1 := 1.01$$

$$a_{l_i} :=$$

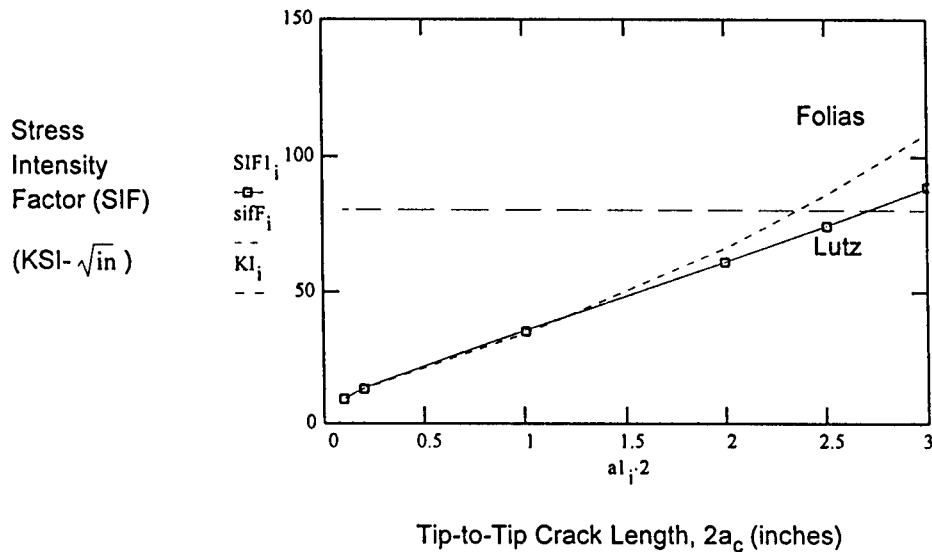
.05
.1
.5
1.
1.25
1.5

$$\beta_{l_i} := \sqrt{1 + \left[\alpha_1 \cdot \left(\frac{E_1}{\sigma_{ly}} \right) \cdot \left(\frac{a_{l_i}}{0.5 \cdot D_1} \right)^2 \right]^{\frac{2}{3}}}$$

$$SIF_{l_i} := \frac{p_1 \cdot D_1}{2 \cdot h_1} \cdot \beta_{l_i} \cdot \sqrt{\pi \cdot a_{l_i} \cdot \eta_1} \cdot 1000^{-1}$$

$$sifF_i := \frac{p_1 \cdot D_1}{2 \cdot h_1} \cdot \sqrt{\pi \cdot a_{l_i}} \cdot \left[1 + \left[3.22 \cdot \frac{(a_{l_i})^2}{D_1 \cdot h_1} \right] \right]^{0.5} \cdot 1000^{-1} \quad \frac{0.5 \cdot D_1}{h_1} = 96.429$$

Note: SIF results shown includes crack bulging effects due to internal pressure



Significant Results: the critical crack-length at 233 psia pressure loading for this tank is:

$$L_c (\text{Lutz}) = 2.7 \text{ inches for a Material Fracture Toughness of } 80 \text{ KSI-in}^{0.5}$$

(conservative lower shelf for crack instability)

Figure 63 - RUSSIAN FGB (SPACE TUG) AUXILIARY TANKS
PROPELLANT TANK CRITICAL CRACK LENGTH

Russian FGB auxiliary tanks, critical crack lengths

2) G N2 Spherical Bottle - Material = Ti-6Al-4Va $j := 1..6$

$h2 := 0.217$ $D2 := 16.535$ $p2 := 3343.0$ $K2_j := 120.$ $\sigma_{2y} := 130000.0$

$E2 := 16000000.0$ $\sigma_{2y} \cdot E1^{-1} = 0.013$ $n := 33$ (RT) $\frac{1}{n} = 0.03$ $\eta2 := 1.0$

$a2_j :=$

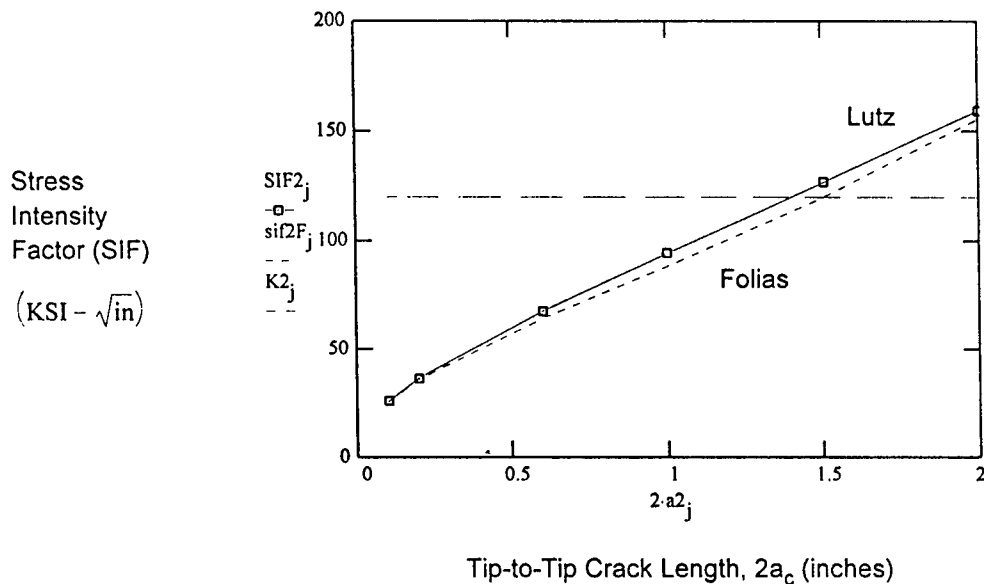
.05
.1
.3
.5
.75
1.

$$\beta_{2j} := \sqrt{1 + \left[\alpha_1 \cdot \left(\frac{E2}{\sigma_{2y}} \right) \cdot \left(\frac{a2_j}{0.5 \cdot D2} \right)^2 \right]^{\frac{2}{3}}}$$

$$SIF2_j := \frac{p2 \cdot D2}{4 \cdot h2} \cdot \beta_{2j} \cdot \sqrt{\pi \cdot a2_j} \cdot \eta2 \cdot 1000^{-1}$$

$$sif2F_j := \frac{p2 \cdot D2}{4 \cdot h2} \cdot \sqrt{\pi \cdot a2_j} \cdot \left[1 + \left[3.22 \cdot \frac{(a2_j)^2}{D2 \cdot h2} \right] \right]^{0.5} \cdot 1000^{-1} \quad \frac{0.5 \cdot D2}{h2} = 38.099$$

Note: SIF results shown includes crack bulging effects due to internal pressure



Significant Results: the critical crack-length at 3343 psia pressure loading for this tank is;

L_c (Lutz) = 1.4 inches for a Material Fracture Toughness of $120 \text{ KSI-in}^{0.5}$

(conservative lower shelf for crack instability)

Figure 64 - RUSSIAN FGB (SPACE TUG) AUXILIARY TANKS
GN2 SPHERICAL BOTTLE CRITICAL CRACK LENGTH

AIV-7 RUSSIAN RESEARCH MODULE SPHERICAL END CONE

As per the FGB auxiliary tanks, an estimate of the CCL of the Russian Research Module Spherical End Cone was performed, employing closed form solutions.

Figure 65 shows the Stress Intensity Factor (SIF) versus the tip-to-tip crack length for the structure when subjected to an internal pressure of 14.7 psia. Two fracture criterion were used, namely the Folias and the Newman parameters, as indicated in the Figure.

The thickness of the spherical end cone is approximately 0.256 inch. For this thickness, one as to consider the plain strain fracture toughness (fracture resistance capability) of the material, rather than the state of plain stress. We do not have any data for the Aluminum Alloy 5456-0 for this condition. However, based on other types of Aluminum Alloys, we can assume a conservative level of 50 KSI-in^{0.50}, for which yields a CCL of approximately 22 to 23 inches.

INTERNATIONAL SPACE STATION ALPHA

Spherical Cone Dimensions: Internal Radius (R_i) = 2.6 m (102.36 inch)

Thickness (h) = 6.6 mm (0.256 inch)

Mat'l: Aluminum Alloy 5456-0 (assumed)

$$SIF = \frac{p \cdot R_m}{2.0 \cdot h} \cdot \sqrt{\pi \cdot a} \cdot \left[1.0 + 3.22 \cdot \left(\frac{a^2}{2.0 \cdot R_m \cdot h} \right) \right]^{\frac{1}{2}} \quad (\text{Folias})$$

$$SIF = \frac{p \cdot R_m}{2.0 \cdot h} \cdot \sqrt{\pi \cdot a} \cdot F \quad (\text{Newman})$$

$$R_m = R_i + h/2 \quad (\text{inch})$$

$$a = \text{half-crack length (inch)}$$

$$p = \text{internal pressure (psia)}$$

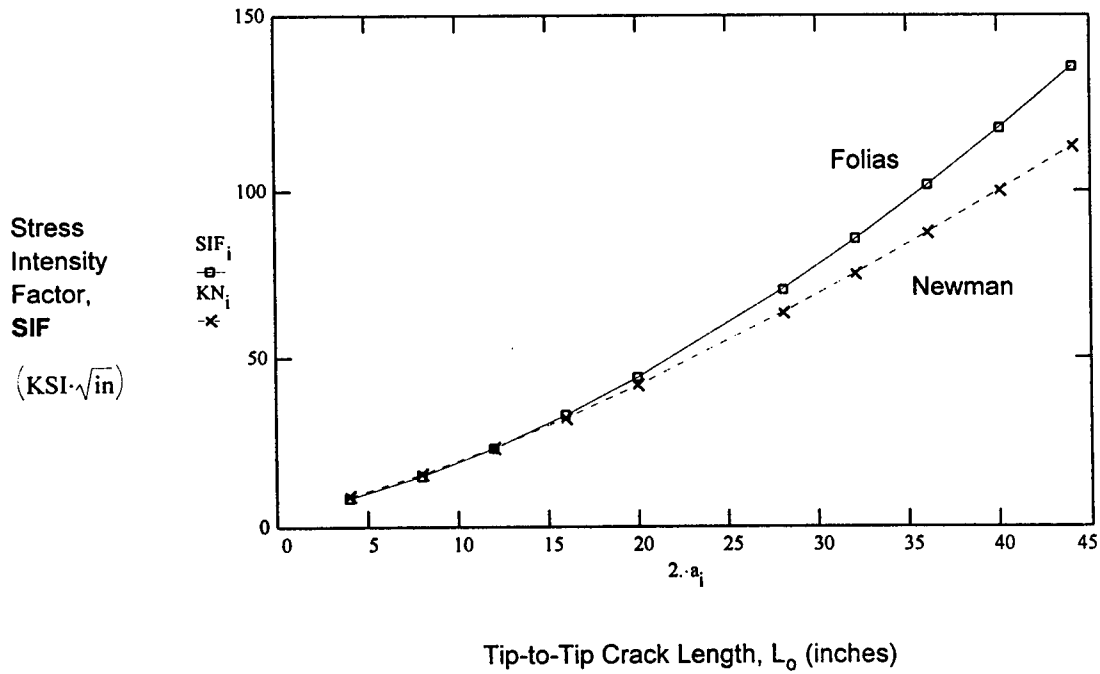


Figure 65 - RUSSIAN RESEARCH MODULE SPHERICAL END CONE
SIF vs. CRACK LENGTH at 14.7 psia INTERNAL PRESSURE LOADING

AV - CONCLUSIONS and RECOMMENDATIONS

AV-1 CONCLUSIONS

The principal goal and objectives, of this limited effort summarized in this section, were to determine with a certain degree of confidence, the criticality for the International Space Station Alpha (ISSA) selected habitable modules to "unzip" catastrophically if they are subjected to Micrometeoroids and Orbital Debris (M/OD) cloud impact and subsequent module wall penetration.

As indicated in the body of this report, the primary loading condition for assessing the criticality to fracture, is the tensile loading carried in the skin of a pressurized module, which can cause an existing or induced through-the-skin crack to grow in an abrupt fashion (i.e., "unzipping"), if the initial flaw length exceeds a certain length called the critical crack length (CCL).

The analytical methods employed in this study were based on advanced fracture mechanics (AFM) principles (i.e., nonlinear elastic-plastic, and pressure effects), and numerical methods such as the finite element. Several fracture criterion were considered during this work, to ensure compatibility and relative accuracy of the analytical procedure for assessing the CCL for the respective ISSA modules. However, the available closed-form solutions for determining the stress intensity factor (SIF) at a crack tip (CTIP) have some shortcomings, in particular when applied to reinforced pressure wall (orthotropic) design. Although, these solutions includes sometime effects of geometric nonlinearity and crack bulging due to the internal pressure, they are not quite applicable to complex pressure wall design, as the ones for example, used for the ISSA habitable modules. Nevertheless, they were used in the study (as indicated above) for comparative purposes only. The most applicable fracture criterion for these type of vessels is the J -integral coupled with the finite element analysis (FEA) of the pressure wall design in consideration.

The analysis concentrated mainly on two principal stages of the CCL: 1) the quasi-static stable (no dynamic effects, i.e., due to inertia and/or time dependent loading effects) crack growth (crack starter & arrest), and 2) quasi-static, unstable crack growth. The first stage is the prediction of the crack length (CL) at initiation. Such a crack is expected to arrest itself. The second stage, called the critical stage, is the predicted CL required before unbounded growth, or "unzipping", occurs.

Basically, the respective CCL were determined using the well established R-curves (crack growth resistance curves) technique, whereby the J-integral and crack-tip-opening-displacement (CTOD) increase with crack growth. Instability occurs when the driving force curve is tangent to the R-curve pertaining to a chosen material.

AV-2 RECOMMENDATIONS

As in all engineering disciplines, the utilization of selected analytical techniques requires a thorough understanding of their limitations.

One should recognize the shortcomings for using quasi-static load (internal pressure) driver for determining the SIF and crack extension or no extension, and using limited data on the fracture toughness of the selected material used for the construction of the vessel.

Consider, at first, the dynamic effects on fracture mechanics problems. Here, time is an important variable. At high loading rates, for instance, inertia effects and material rate dependence can be crucial. There are two types of dynamic fracture situations that are directly related to the ISSA pressurized elements: 1) fracture initiation as a result of rapid loading of the M/OD cloud pressure pulse, and 2) rapid propagation of a crack. As an example, Figure 66 illustrates a typical load-time response during impact loading of a pressurized vessel. The pressure loading (due to projectile impact) rises with time, but oscillates at a particular frequency which is in function of the geometry and materials properties of the structure. The amplitude of the oscillations decrease with time, as kinetic energy is absorbed by the structure. Thus, inertia effects are most significant at short loading times. Because the scope of this work-study was very limited, the investigation of the dynamic effects on the SIF was not conducted.

Additionally, the scatter in the material fracture toughness data for the 2219-T87 Aluminum Alloy, mainly employed for the construction of the ISSA modules, is another uncertainty factor in determining the CCL. Finally, the CCL for the FGB and JEM modules end cones should be also addressed.

It is highly recommended to conduct an analytical (and perhaps experimental) program for assessing the dynamic effects on the SIF, so that to remove or to add of conservatism in the CCL predictions. This program could show that the dynamic, state immediately following the impact event due to M/OD, actually governs the potential for unzipping.

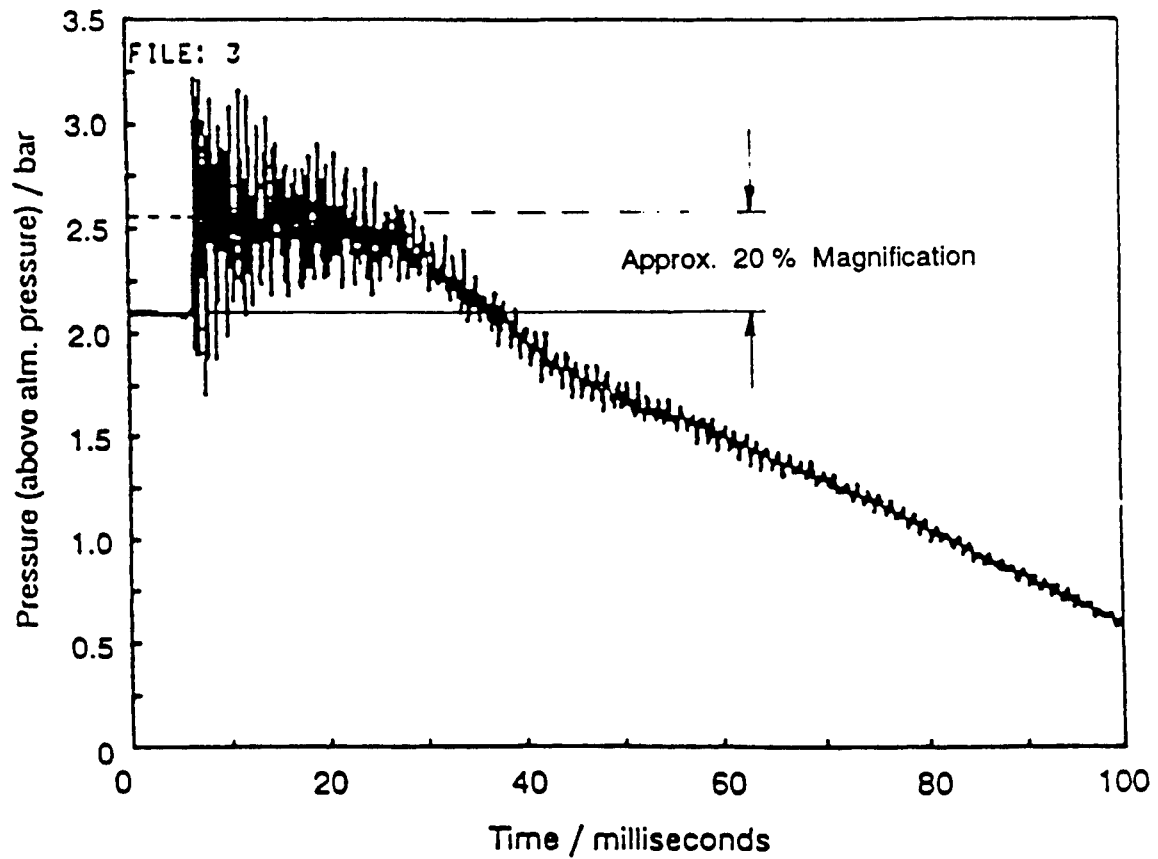


Figure 66 - PRESSURE MEASUREMENTS in a TEST CHAMBER
UNDER BALLISTIC IMPACT LOADING
(Ref.: MBB / ERNO, Columbus Program, 1992)

AVI REFERENCES

- [1] Folias, E.S.: An Axial Crack in a Pressurized Cylindrical Shell, *International Journal of Fracture Mechanics* 1, 104-113, 1965.
- [2] Newman, Jr., J.C.: Fracture Analysis of Surface and Through Cracks in Cylindrical Pressure Vessels, NASA TN D-8325, 1976.
- [3] FRACTURE, An Advanced Treatise, Volume 2, Mathematical Fundamentals, *Academic Press*, N.Y., 1968, Edited by Harold Liebowitz.
- [4] Griffith, A.A., The Phenomena of Rupture and Flow in Solids, *The Philosophical Society Transactions of The Royal Society of London*, Vol. 221(A), 1920.
- [5] Irwin, G.R., Analysis of Stresses and Strains Near the End of a Crack Traversing a Plate, *Journal of Applied Mechanics*, Vol. 24, 1957.
- [6] Nair, S.V., Tien, J.K., Bates, R.C., and Buck, O., FRACTURE MECHANICS: microstructure and Micromechanisms, *ASM INTERNATIONAL*, Ohio, 1987.
- [7] Rice, J.R., A Path Independent Integral and the Approximate Analysis of Strain Concentration at Notches and Cracks, *Tans. ASME, J. appl. Mech.* 35, 379-386, 1968.
- [8] Rice, J.R., Mathematical Analysis in the Mechanics of Fracture, Ref. [3] above, Chapter 3.
- [9] Kishimoto, K., Aoki, S., and Sakata, M., On the Fracture Mechanical Parameter Described the Crack Extension, *Trans. Japan Soc. Mech. Eng.* 46-110, A. 1049-1061, 1980.
- [10] Kishimoto, K., Aoki, S., Ohsato, T., and Sakata, M., The Finite Element Analysis of the Dynamic Stress Intensity Factor Using J-Integral. *Trans. Japan Soc. Mech. Eng.* 46-406, A. 584-589, 1980.
- [11] Aoki, S., Kishimoto, K., Matsumoto, I., Tachiara, M., and Sakata, M., J-Integral in Thermal Field. *Tans. Japan Soc. Mech. Eng.* 47-415, A. 304-312, 1981.
- [12] Kanninen, M.F., and Popelar, C.H., Advanced Fracture Mechanics, *Oxford Engineering Science Series* 15, 1985.
- [13] Anderson, T.L., FRACTURE MECHANICS, Fundamentals and Applications, *CRC Press*, Boston, 1991.
- [14] Jeong, D.Y., and Pin Tong, Nonlinear Bulging Factor Based on R-Curve Data, *NASA Conference Publication* 3274, Part 1, 1994.
- [15] Gallager, J.: Damage Tolerance Handbook, MCIC-HB-01R, *University of Dayton Research Institute*, Dayton, Ohio, 1983. (see Appendix A)

INTERNATIONAL SPACE STATION ALPHA

- [16] Elfer, N.: Space Debris and Meteoroid Protection, APPENDIX G - FRACTURE TOUGHNESS COMPARISON: 2219 vs. 5456 Aluminum, *Martin Marietta Manned Systems*, N.O., LA, IR&D Report No. S87-47501-001, 1987.
- [17] Foreman, R. G.: *Fifth Meeting of the Advanced Fracture Mechanics Group*, December 1-2, 1992, Houston, Texas.
- [18] Investigation of Crack Initiation and Unstable Propagation due to Meteoroid or Orbital Debris Impact Into Space Station Freedom Pressure Vessels, *Southwest Research Institute*, S.A., TX, Project Number 06-5537, 1993.
- [19] Kuhn, P.: Notch Effects on Fatigue and Static Strength, *Symposium of the International Committee on Aeronautical Fatigue* (ICAF), Rome, Italy, 1963.
- [20] Lutz, B.E.P.: Common Module Shell Unzipping due to Meteoroid / Orbital Debris Strikes, Space Station Freedom Program, Report No. GSS-40.05-RPT-6-001, *GRUMMAN Space Station Engineering and Integration Contractor* (SSEIC), Reston, VA, 1994.

VII ACKNOWLEDGMENTS

The work-study summarized by this report was performed by Meyer Analytics, Inc. (Joseph Goodwin and Dr. B. Lutz), during the period from early November 1994 through the end of September 1995. NASA/MSFC contracted MA, through Science Applications International Corporation (SAIC) for supporting NASA and BOEING Aerospace Company, the main International Space Station Alpha (ISSA) contractor, for the development and verification of risks models applicable to ISSA.

MA would like to take this opportunity for acknowledging the support and contributions made by several institutions and many individuals, prior to the program having taken place, and during the duration of the program itself. In particular, MA its grateful to:

- * Mrs. Katy Jones, Dr. J. E. Williamsen and Greg Olsen, from NASA/MSFC, Code ED-52.
- * Russell Graves, from Boeing Space Station Integration, Houston, TX.
- * Mrs. Janice K. Schuckman, and Mrs. Carol Johnson, both from SAIC, Huntsville, AL.
- * Phil Bogert, from NASA HQ., Washington, DC.
- * Dr. N. Elfer, from Martin Marietta Manned Systems, LA.

Mr. Graves, Mr. Bogert, and Dr. Williamsen were specially instrumental in helping MA obtaining the contract for this program.

Our sincere thanks to you all.

APPENDIX A

ALUMINUM ALLOY 2219-T87 MATERIAL PROPERTY DATA

1 June 1987

TABLE 3.2.6.0(b). Design Mechanical Properties of 2219 Aluminum Alloy Sheet and Plate

Specification Form	9Q-A-250/10 Sheet and plate																							
	T62						T81						T851						T87					
	0.020- 2.000		0.020- 0.249		0.250- 1.000		0.020- 0.249		0.250- 1.000		0.020- 0.249		0.250- 1.000		0.020- 0.249		0.250- 1.000		0.020- 0.249		0.250- 1.000		0.020- 0.249	
	A	B	A	B	A	B	A	B	A	B	A	B	A	B	A	B	A	B	A	B	A	B	A	B
Thickness, in.	54	55	54	55	54	55	54	55	54	55	54	55	54	55	54	55	54	55	54	55	54	55	54	55
Basis	L	LT	L	LT	L	LT	L	LT	L	LT	L	LT	L	LT	L	LT	L	LT	L	LT	L	LT	L	LT
Mechanical properties:																								
F_{tu} , ksi:																								
L	54	55	54	55	54	55	54	55	54	55	54	55	54	55	54	55	54	55	54	55	54	55	54	55
LT	54	55	54	55	54	55	54	55	54	55	54	55	54	55	54	55	54	55	54	55	54	55	54	55
F_{ty} , ksi:																								
L	36	37	36	37	36	37	36	37	36	37	36	37	36	37	36	37	36	37	36	37	36	37	36	37
LT	36	37	36	37	36	37	36	37	36	37	36	37	36	37	36	37	36	37	36	37	36	37	36	37
F_{cy} , ksi:																								
L	38	39	38	39	38	39	38	39	38	39	38	39	38	39	38	39	38	39	38	39	38	39	38	39
LT	38	39	38	39	38	39	38	39	38	39	38	39	38	39	38	39	38	39	38	39	38	39	38	39
F_{su} , ksi:																								
L	32	32	32	32	32	32	32	32	32	32	32	32	32	32	32	32	32	32	32	32	32	32	32	32
F_{bu} , ksi:																								
(e/D=1.5)	84	86	84	86	84	86	84	86	84	86	84	86	84	86	84	86	84	86	84	86	84	86	84	86
(e/D=2.0)	109	111	109	111	109	111	109	111	109	111	109	111	109	111	109	111	109	111	109	111	109	111	109	111
F_{br} , ksi:																								
(e/D=1.5)	63	65	63	65	63	65	63	65	63	65	63	65	63	65	63	65	63	65	63	65	63	65	63	65
(e/D=2.0)	79	82	79	82	79	82	79	82	79	82	79	82	79	82	79	82	79	82	79	82	79	82	79	82
e, percent (S Basis):																								
L
LT
E, 10 ³ ksi																								
E _c , 10 ³ ksi																								
G, 10 ³ ksi																								
μ																								
Physical properties:																								
ω , lb/in. ³																								
C, Btu/(lb)(F)																								
K, Btu/(hr)(ft ²)(F/ft)																								
α , 10 ⁻⁶ in./in./F																								

aSee Table 3.1.2.1.1. Bearing values are "dry pin" values per Section 1.4.7.1.

bT62 and T81: 0.020-0.039 in., 6 percent; 0.040-0.249 in., 7 percent; T62: 0.250-1.000 in., 8 percent; 1.00-2.000 in., 7 percent.

cThese allowables apply when samples of material supplied in the O or F temper are heat treated to demonstrate response to heat treatment. Properties obtained by the user however, may be lower than those listed if the material has been formed or otherwise cold or hot worked, particularly in the annealed temper, prior to solution heat treatment.

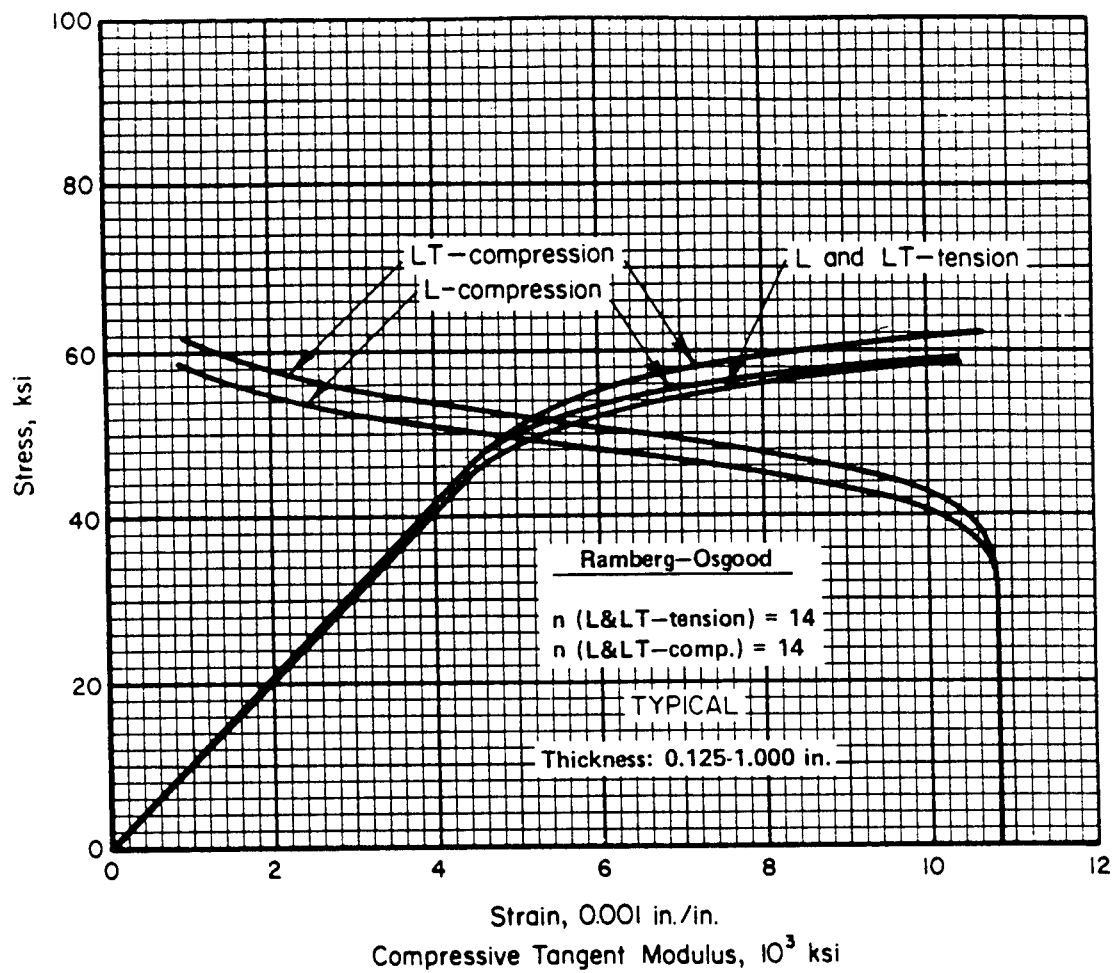


FIGURE 3.2.6.4.6(a). Typical tensile and compressive stress-strain and compressive tangent-modulus curves for 2219-T87 aluminum alloy sheet and plate at room temperature.

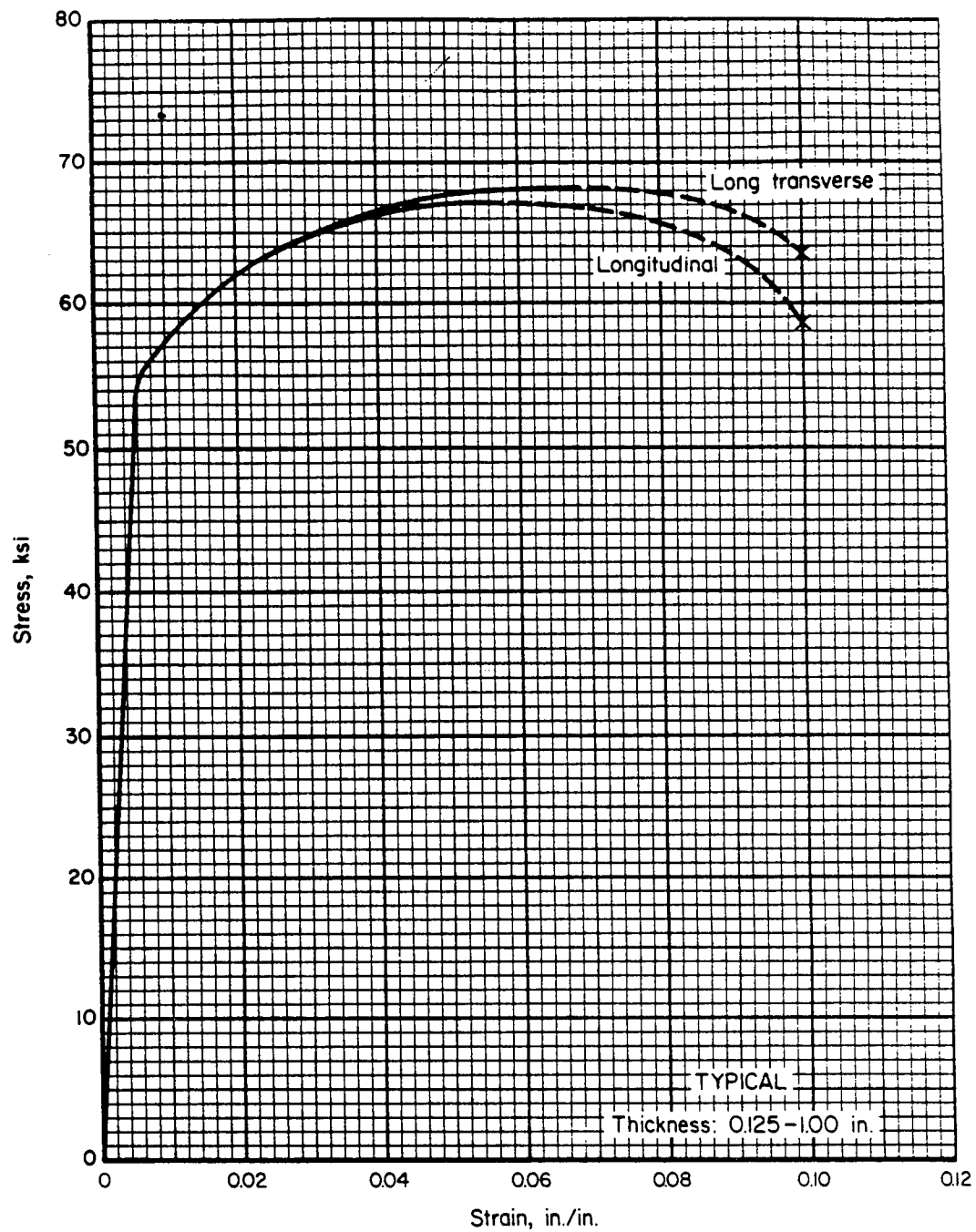


FIGURE 3.2.6.4.6(b). Typical tensile stress-strain curves (full range) for 2219-T87 aluminum alloy sheet and plate at room temperature.

Volume 3

Damage Tolerant Design Handbook

A Compilation of Fracture and Crack Growth
Data for High-Strength Alloys

Compiled by
J. Gallagher
Program Manager
University of Dayton Research Institute
Dayton, Ohio

Sponsored by

Materials Laboratory
Air Force Wright Aeronautical Laboratories
Wright-Patterson Air Force Base, Ohio 45433

December 1983

Metals and Ceramics Information Center
BATTELLE
Columbus Laboratories
505 King Avenue
Columbus, Ohio 43201

Approved for public release; distribution unlimited

Post-It™ brand fax transmittal memo 7671		# of pages ▶ 3
To	Dr. Herman Nield	From
Co.	GE R&D CTR	Co.
Dept.	518-387-5463	Univ of Dayton
		Phone #
		513-229-4447
		Fax #
		513-229-4251

Table 7.10.2.2 (Con't)

CONDITION	--PRODUCT-- FORM THICK (IN)	TEST SPEC OR TEMP (F)	YIELD STR (KSI)	ALUMINUM				2219				K(C)					
				SPECIMEN				CRACK LENGTH CROSS STRESS				K(C)					
				WIDTH (IN)	THICK (IN)	INIT (IN)	FINAL (IN)	UNDET (KSI)	MAX (KSI)	K(APP) (KSI+80RT IN)	STAN DEV	K(C) (KSI+80RT IN)	MEAN DEV	K(C) STAN DEV	DATE	REFER	
				W	B	2A(0)	2A(F)	S(0)	S(MAX)								
BUCKLING OF CRACK EDGES RESTRAINED																	
T87	B	0.06 - 423 L-T	70.7	6.700	0.068	0.820	---	---	58.20	66.67*	---	---	---	---	1971	80104	
		0.06	70.7	6.700	0.069	1.030	---	---	59.70	71.90*	---	---	---	---	1971	80104	
		0.06	70.7	6.700	0.068	1.180	---	---	53.60	74.40*	---	---	---	---	1971	80104	
		0.06	70.7	6.700	0.068	0.890	---	---	57.50	68.74*	---	---	---	---	1971	80104	
T87	B	0.06 - 423 L-T	73.8	18.930	0.062	5.060	6.410	---	26.30	79.13	92.91	1966	69759				
		0.06	73.8	15.990	0.061	5.000	5.980	---	26.30	78.49	88.35	90.6/	3.2	1966	69759		
T87	B	0.06 - 320 L-T	64.5	5.500	0.068	0.420	---	---	57.10	56.80*	---	---	---	---	1971	80104	
		0.06	64.5	5.500	0.069	0.420	---	---	61.50	50.13*	---	---	---	---	1971	80104	
		0.06	64.5	5.500	0.068	0.480	---	---	60.20	52.82*	---	---	---	---	1971	80104	
		0.06	64.5	5.500	0.068	0.330	---	---	63.20	45.60*	---	---	---	---	1971	80104	
T87	B	0.06 - 320 L-T	64.5	6.700	0.069	1.200	---	---	51.10	71.58*	---	---	---	---	1971	80104	
		0.06	64.5	6.700	0.067	0.880	---	---	53.90	64.43*	---	---	---	---	1971	80104	
		0.06	64.5	6.700	0.068	1.000	---	---	54.60	67.39*	---	---	---	---	1971	80104	
T87	B	0.06 R.T. L-T	55.0	5.500	0.068	0.420	---	---	47.90	47.64*	---	---	---	---	1971	80104	
		0.06	55.0	5.500	0.067	0.400	---	---	51.30	40.80*	---	---	---	---	1971	80104	
		0.06	55.0	5.500	0.067	0.520	---	---	49.80	45.26*	---	---	---	---	1971	80104	
		0.06	55.0	5.500	0.068	0.330	---	---	52.50	37.88*	---	---	---	---	1971	80104	
T87	B	0.06 R.T. L-T	55.0	6.700	0.067	0.910	---	---	47.30	57.20*	---	---	---	---	1971	80104	
		0.06	55.0	6.700	0.068	1.000	---	---	46.10	58.58*	---	---	---	---	1971	80104	
		0.06	55.0	6.700	0.068	1.190	---	---	43.40	60.52*	---	---	---	---	1971	80104	
T87	B	0.10 R.T. L-T	58.5	3.500	0.100	0.750	0.980	---	46.40	51.84*	60.52*	1962	62306				
T87	B	0.10 R.T. L-T	58.5	6.000	0.100	2.000	2.460	---	34.60	65.90*	76.06*	1962	62306				
T87	B	0.10 R.T. L-T	58.5	12.000	0.100	2.000	2.480	---	41.30	74.48*	87.44*	1962	62306				
		0.10	58.5	12.000	0.100	4.000	4.770	---	27.90	75.15	84.79	1962	62306				
T87	B	0.10 R.T. L-T	58.5	24.000	0.100	20.000	20.650	---	6.40	70.51	78.16	1962	62306				
		0.10	58.5	24.000	0.100	4.000	5.730	---	33.90	86.46	109.43	1962	62306				

*NOTE- NET SECTION STRESS EXCEEDS 80% OF YIELD STRENGTH. VALUE NOT INCLUDED IN MEAN OR STD. DEV.

Table 2.2 (Con't)

CONDITION	ALUMINUM		2219		K(C)											
	--PRODUCT--		SPECIMEN--		CRACK LENGTH ORDS		STRESS									
	FORM	THICK (IN)	TEST SPEC OR (F)	YIELD (KSI)	W	B	WIDTH (IN)	THICK (IN)	INIT (IN)	FINAL (IN)	ONSET (KSI)	MAX (KSI)	K (APP) (KSI=80RT IN)	K (APP) MEAN DEV (KSI=80RT IN)	STAN DEV (K(C) MEAN DEV (KSI=80RT IN)	K(C) STAN DEV DATE REFER
BUCKLING OF CRACK EDGES RESTRAINED																
187	8	0.10	R. T.	L-T	58.5	24.000	0.100	8.000	7.580	---	24.00	91.42	103.46	1962	62306	
		0.10			58.5	24.000	0.100	18.000	19.430	---	7.40	63.61	75.31	1962	62306	
		0.10			58.5	24.000	0.100	18.000	18.420	---	8.40	72.20	77.36	1962	62306	
		0.10			58.5	24.000	0.100	12.000	13.450	---	17.80	91.90	104.11	1962	62306	
		0.10			58.5	24.000	0.100	2.000	2.590	---	42.40	78.48	86.14	1962	62306	
		0.10			58.5	24.000	0.100	1.000	1.400	---	48.40	60.73	71.73	1962	62306	
		0.10			58.5	24.000	0.100	0.500	0.770	---	54.40	48.22	59.87	90.6/15.0	1962	62306
187	8	0.10	R. T.	L-T	58.5	30.000	0.100	18.000	19.700	---	12.50	86.70	97.03	1962	62306	
187	8	0.10	R. T.	L-T	58.5	34.000	0.100	4.000	8.450	---	34.00	83.88	100.91	1962	62306	
187	8	0.10	R. T.	L-T	58.5	48.000	0.100	4.000	5.580	---	34.90	87.84	104.19	1962	62306	
		0.10			58.5	48.000	0.100	12.000	15.050	---	23.20	104.79	120.17	1962	62306	
		0.10			58.5	48.000	0.100	36.000	37.170	---	7.90	96.03	102.47	1962	62306	
		0.10			58.5	48.000	0.100	41.900	43.180	---	4.30	78.34	89.39	1962	62306	
		0.10			58.5	48.000	0.100	24.000	25.720	---	15.40	112.45	119.93	1962	62306	
		0.10			58.5	48.000	0.100	8.000	9.250	---	28.20	101.71	110.02	1962	62306	
		0.10			58.5	48.000	0.100	12.000	14.200	---	24.50	110.66	122.38	107.8/12.1	1962	62306

BUCKLING OF CRACK EDGES NOT RESTRAINED

187	8	0.03	- 423	L-T	74.0	12.000	0.032	1.210	2.020	---	48.10	66.73	87.21	1966 66103
187	8	0.03	- 423	L-T	74.0	16.000	0.032	4.240	7.030	---	27.80	75.02	103.20	1966 66103
187	8	0.12	- 423	L-T	74.0	12.000	0.125	1.230	1.940	---	46.20	64.64	81.97	1966 66103
187	8	0.12	- 423	L-T	74.0	16.000	0.125	4.830	6.310	---	26.90	78.55	93.86	1966 66103
187	8	0.06	R. T.	L-T	59.2	2.000	0.063	0.623	1.110	---	38.10	40.16	62.72	1973 86213
		0.06			59.2	2.000	0.064	0.622	0.810	---	38.10	40.08	47.92	1973 86213

*NOTE- NET SECTION STRESS EXCEEDS 80% OF YIELD STRENGTH VALUE NOT INCLUDED IN MEAN OR STD. DEV.

APPENDIX B

NOTES
on
FRACTURE MECHANICS
of
THROUGH-CRACKED CYLINDERS

FRACTURE MECHANICS OF THROUGH-CRACKED CYLINDERS**FOLIAS** (Through-Wall, Axial Crack, Monocoque Shells)**valid range: $5 < R/t_s < 50$**

$$\sigma_{\theta} = \frac{KI_c}{\sqrt{\pi \cdot a}} \left[1 + 3.22 \cdot \left(\frac{a^2}{D \cdot t_s} \right) \right]^{-\frac{1}{2}}$$

 σ_{θ} = Hoop Stress KI_c = material fracture toughness a = half crack length D = shell diameter = $2 R$ t_s = shell wall thickness**SIMPLE CRACK-TIP PLASTICITY MODEL**

$$K_{TPM} = \sigma_{\theta} \cdot \sqrt{\pi \cdot a} \cdot \left[1 - \left[0.5 \cdot \left(\frac{\sigma_{\theta}}{\sigma_f} \right)^2 \right] \right]^{-0.50}$$

 K_{TPM} = stress intensity factor σ_f = shell material equivalent yield (or flow) stress $\sigma_f = (\sigma_y + \sigma_u) \cdot 0.50$ σ_u = shell material ultimate tensile strength σ_y = shell material yield tensile strength**COD (Crack Opening Displacement)**

$$K_{COD} = \sqrt{\delta \cdot E \cdot \sigma_y \cdot \left[1 + \frac{\pi^2}{24} \cdot \frac{(\sigma_{\theta})^2}{\sigma_y} \right]^{-1}}$$

 δ = crack opening displacement E = elastic modulus of the shell material

VERY THIN PRESSURE VESSEL**valid range: $100 < R/t_s < 2500$**

(Monocoque Shells)

$$\sigma_{\theta c} = \frac{KI_c}{\sqrt{\pi \cdot a \cdot \phi_3}} \left[1 + 1.61 \cdot \left(\frac{a}{R} \right)^2 \cdot \left(50 \cdot \tanh \left(\frac{R}{50 \cdot t_s} \right) \right) \right]^{-0.50} = \frac{KI_c}{\sqrt{\pi \cdot a \cdot \phi_3}} \cdot \frac{1}{M}$$

ϕ_3 = plasticity correction factor (Hahn, Sarrate, and Rosenfield, 1969, Battelle Memorial Institute, Columbus, Ohio)

$$= \left(\frac{\pi \cdot M \cdot \sigma_{\theta}}{2 \cdot \sigma} \right)^{-2} \cdot \ln \left(\sec \left(\frac{\pi \cdot M \cdot \sigma_{\theta}}{2 \cdot \sigma} \right) \right)^2$$

σ = average flow stress acting in the plastic zone (= yield or 0.5 (yield+ult))

M = function of the crack length

$$= \left[1 + 1.61 \cdot \left(\frac{a^2}{R^2} \right) \cdot \left(50 \cdot \tanh \left(\frac{R}{50 \cdot t_s} \right) \right) \right]^{\frac{1}{2}}$$

= for very thin wall, low and medium toughness vessels with relatively long **through-wall** cracks.

J-INTEGRAL and CRACK-GROWTH (via Finite Element Method)

$$J = \frac{1}{\Delta a_c} \left[\int_{V_1}^{V_2} V \, d \left(\sigma_{ij} \cdot \frac{d}{d x_k} u_j - W \cdot \delta_{ik} \right) \cdot \frac{d}{d x_i} \Delta x_k - f_i \cdot \left[\left(\frac{d}{d x_j} u_i \right) \cdot \Delta x_j \right] \right. \\ \left. - \frac{1}{\Delta a_c} \cdot \int_{S_1}^{S_2} t_i \cdot \left[\left(\frac{d}{d x_j} u_i \right) \cdot \Delta x_j \right] dS \right]$$

V = volume; S = body surface

σ_{ij} = stress tensor

u_i = displacement vector

W = strain energy density

x_i = cartesian coordinate

Δa_c = virtual crack extension due to Δx_k

f_i = body forces = $-\rho \cdot \frac{d}{dt} u_i$

A-106

STRAIN ENERGY DENSITY (via Finite Element Method)

From Nodal Principal Stresses (σ_1 σ_2 σ_3)

$$W = \frac{1}{2 \cdot E} \cdot \left[(\sigma_1)^2 + (\sigma_2)^2 + (\sigma_3)^2 \right] - \frac{\nu}{E} \cdot (\sigma_1 \cdot \sigma_2 + \sigma_2 \cdot \sigma_3 + \sigma_1 \cdot \sigma_3)$$

ERDOGAN (Through-Wall, Axial Crack, Monocoque Shells - Initial Work)

$K_m = A_m \cdot K_p$ = membrane stress intensity factor

$$K_p = \sigma_\theta \sqrt{\pi \cdot a}$$

$$A_m = 0.481 \cdot \lambda + 0.614 + 0.386 \cdot e^{-1.25 \cdot \lambda}$$

$$\lambda = \frac{\left[12 \cdot (1 - \nu^2) \right]^{\frac{1}{4}} \cdot a}{\sqrt{R \cdot t_s}}$$

ν = Poisson's ratio

ERDOGAN/RATWANI (Through-Wall Axial Crack, Thin Monocoque Shells - 1972)

$$K_{er} = \sigma_\theta \sqrt{\pi \cdot a_p} \quad (A_m \text{ +/- } A_b)$$

a_p = half crack length with plane stress plastic zone correction factor at the crack-tip

$$= a \cdot \cos \left[\sigma_\theta \cdot \frac{\pi}{2} \cdot (\sigma_f)^{-1} \right]^{-1}$$

A_m & A_b = membrane and bending components of the stress intensity ratio
(curvature correction factors)

+/- = (+) for outer surface and (-) for inner surface

NEWMAN, Jr., J.C. (NASA Langley Research Center, 1976)

Axial Through Crack Monocoque Shells

$$K_{Ie} = \sigma_{\theta} \sqrt{\pi \cdot a} \cdot F$$

F = shell-curvature correction factor for an axial through crack

$$= \left[1.0 + 0.52 \cdot \lambda_t + 1.29 \cdot (\lambda_t)^2 - 0.074 \cdot (\lambda_t)^3 \right]^{0.50}$$

$$\lambda_t = \frac{a}{\sqrt{R \cdot t_s}}$$

ANDERSON and SULLIVAN (NASA Lewis R.C., 1966)

Axial Though-Cracked Monocoque Cylindrical Pressure Vessels

$$\sigma_{\theta c} = \frac{K_c}{\sqrt{\pi \cdot a_c + \frac{1}{2} \cdot \frac{(K_c)^2}{(\sigma_y)^2} \cdot \left(1 + C \cdot \frac{a_c}{R} \right)}} = \text{critical hoop stress}$$

C = bulge coefficient

LUTZ, B.E.P. (Grumman, Reston, VA, 1993)

Axial Through-Cracked Waffle-Skin Construction Cylindrical Pressure Vessels

$$Kl_i = K_{er} \times B_{waffle} \times B_{biax} \times B_{nl} \times B_D \times B_{unc}$$

K_{er} = Erdogan/Ratwani predictive equation (see above)

B_{waffle} = waffle-skin correction factor function of crack length/location

B_{biax} = load biaxiality effects coefficient

B_{nl} = nonlinear (geometric & material) effects coefficient

B_D = dynamic effects coefficient

B_{unc} = uncertainties on the parameters coefficient

JEONG & TONG 1994 - (Through-Wall Axial Cracks for Curved Panels)

$$K_R = \sigma_\theta \cdot \beta_B \cdot \sqrt{\pi \cdot (a_o + \Delta a)} \cdot \sqrt{\sec \left[\frac{\pi \cdot (a_o + \Delta a)}{W} \right]}$$

W = panel width Δa = crack extension σ_θ = hoop stress

$$\beta_B = \text{nonlinear bulging factor} = \sqrt{1 + \alpha \cdot \left[\left(\frac{E}{\sigma_\theta} \right) \cdot \left(\frac{a_o + \Delta a}{R} \right)^2 \right]^{\frac{2}{3}}}$$

α = empirical constant = 0.67

STRAIN ENERGY RELEASE RATE (SERR) via Crack-Tip-Opening-Displacement (CTOD)

$$\text{SIF} = \left(\frac{2 \cdot E \cdot m}{a_o} \cdot \int_0^{a_o} \sigma_{\text{tip}} \cdot \frac{\delta_{\text{tip}}}{2} da \right)^{\frac{1}{2}} = \sqrt{J \cdot E \cdot m} = \sqrt{E \cdot \sigma_y \cdot \delta_{\text{tip}} \cdot m}$$

J = Rice J-integral m = empirical constant function of crack geometry & material strain hardening exponent.

δ_{tip} = crack-tip-opening displacement (CTOD)

STRAIN ENERGY RELEASE RATE (SERR) by Virtual Crack Closure using FEM

$$\text{SIF} = \sqrt{\frac{E}{2 \cdot B \cdot L} (F_1 \cdot \delta_2 + F_2 \cdot \delta_1)} \quad \text{"state of plane stress"}$$

F₁ = crack-tip normal force (node 1) = principal stress x thickness (B) x L/2

F₂ = node 2 force ahead of the crack-tip at a distance L/2

δ₁ = crack opening displacement behind the crack-tip at a distance L/2

δ₂ = crack opening displacement behind the crack-tip at a distance L

SECTION B

STORED ENERGY RISKS
of
FGB PROPULSION and
GYRODYNES MODULE

by

Charles J. Goodwin

B-i

MEYER ANALYTICS, INC.
WARRENTON, VA 22186-9212
USA

SECTION B

TABLE of CONTENTS

		Page
	LIST OF FIGURES	B-iv
	LIST OF TABLES	B-v
BI	INTRODUCTION	B-1
BII	SCOPE AND OBJECTIVES	B-2
BII	FGB PROPULSION RISKS	B-3
	BIII-1 FGB MODULE DESCRIPTION	B-3
	BIII-2 FGB FAULT MECHANISMS	B-4
	BIII-3 UNZIPPING as a GENERATOR of HOLES of LARGE AREA	B-8
	BIII-4 FGB BALLISTIC LIMITS and DAMAGE CONTOURS	B-9
	BIII-5 FGB FAULT TREES	B-11
BIV	GYRODYNE MODULE RISKS	B-8
	BIV-1 GYRODYNE MODULE DESCRIPTION	B-28
	BIV-2 GYRODYNE FAULT MECHANISMS	B-29
	BIV-3 GYRODYNE MODULE FAULT TREE	B-32
BV	FINDINGS and RECOMMENDATIONS	B-44
BVI	REFERENCES	B-48

A P P E N D I C E S

APPENDIX

BI	FGB Module Propellant Tanks
BII	UDMH Detonation Threshold
BIII	Overall Station Prime Structure / SARJ
BIV	Debris Cloud / Wall Energies - SSEIC Method
BV	Debris Flux
BVI	Gyrodyne Module and Units

SECTION B LIST OF FIGURES

- Figure B-1 Side View of Station
- Figure B-2 FGB General Arrangement
- Figure B-3 Assumed FGB Propellant Tank Dimensions
- Figure B-4 Geometric Probability of BL (or greater) Hits on Bumper, going on to penetrate Tanks etc.
- Figure B-5 Specific FGB Targets & Failure Mechanisms
- Figure B-6 Concept of Crack Length / Equivalent Hole Dia.
- Figure B-7 Field of UDMH Detonation
- Figure B-8 Field of GN2 Venting from Propellant Tanks
- Figure B-9 Field of High Pressure GN2 Bottle Venting
- Figure B-10 Fault Tree Numbering Conventions
- Figure B-11 FGB Propellant Tank Fault Tree
- Figure B-12 FGB High Pressure GN2 Fault Tree

- Figure B-13 Gyrodyne Module with internal Gyrodyne Unit Locations / Allignments
- Figure B-14 Gyrodyne Unit Arrangement & Assumptions
- Figure B-15 Apertures
- Figure B-16 Probability of a Gyrodyne Hit following Penetration of the Module in its Aperture
- Figure B-17 Typical Fratricide Geometry--Cain-to-Abel
- Figure B-18 Module End View showing Gyrodyne Unit Geometry
- Figure B-19 Probability of Propagation of Rotor Rupture
- Figure B-20 Gyrodyne Module Fault Tree

- Figure B-21 Study Findings Summary

SECTION B LIST OF TABLES

- Table B-1 Proportion of Ballistic Limit (or greater) Hits that Penetrate Combinations of Tanks, and Reach GN2 or GN2 plus Propellant
- Table B-2 Venting Force / Hole Size to generate Limit Loads in SARJ
- Table B-3 'd' Ratio Values for FGB Propulsion Elements
- Table B-4 Probability of a Gyrodyne Hit following Penetration anywhere on a Main Module
- Table B-5 Feasible Cain / Abel Pairs and their Single Fragment Risks

B 1 INTRODUCTION

The primary purpose of this report is to describe the analytic and modelling work done to assess the risks posed, to the space station and its crew, by the stored energy associated with two, Russian supplied, modules. They are: the FGB (a tug ,that is the heart of stage #1 - the first launch), and the Gyrodyne Module (which brings the station to stage 9). Figure B-1 shows where these two are located on the completed station.(Stage 44).

On the FGB there are two types of stored energy, UDMH propellant (chemical) and gaseous nitrogen at pressure (potential). Both these fluids are in multiple, robust, tanks or pressure bottles on the outside of the FGB, protected by bumper shields. In the pressurized Gyrodyne module the stored energy is resident in six flywheels (kinetic), one in each of the six gyrodyne units located within the module. The module itself has a bumper shield. In each case, the impact of sufficiently heavy and fast orbital debris is the mechanism that threatens to release the stored energy.

This is quite a wide field of inquiry and our resources have been necessarily spread out in developing preliminary values for these risks. Consequently, the secondary purpose of the report is to identify where a deeper, more narrow, look should be taken where the risks, or their associated uncertainties, appear greatest.

B II Scope and Objectives

The subject of the work reported on here is stored energy (close to the crew modules, or inside crew modules) and its possible damaging release. It is only incidental that the modules involved are Russian supplied, and that their engineering details are less familiar than those of other contributors. Our purpose was to quantify the risks in a preliminary fashion, and identify either where the risks were high, or the uncertainties were too great.

There are three main steps in assessing orbital debris risk at a given orbit inclination, orbit altitude, over a given time span:

- 1) Calculate the probability of a component / module being penetrated (Bumper program output).
- 2) Given the penetration, which is in general above the Ballistic Limit rather than just on it, calculate the likelihood that the proximate result will be serious (eg Propellant detonation, Flywheel rupture, venting violent enough to overload structure).
- 3) Given a serious proximate result, assess the outcome (eg. crew hypoxia, repair of the damaged station, etc.) .

Because step #1 is an ongoing activity by others, and step #3 has been studied at some length in the past, we have concentrated our resources on step #2.

Our approach to performing step #2 has been to build, for each main fault mechanism, a relatively simple Fault Tree, starting with the last node of step #1 and ending with the first node of step #3. The nodes that comprise the full span of step #2 fall into two categories: 'Geometric' and 'Damage'. Geometric nodes deal with whether a Ballistic Limit hit on the bumper will go on to hit the inner target object. These Geometric probabilities are less than unity mainly because the target is smaller than the bumper, or shadowed. Damage nodes deal with whether the penetration is severe enough to cause a catastrophic failure. For example, not just any impulse on a propellant tank but one violent enough to trigger propellant detonation.

The building of the fault trees, and the analysis that underpins their node probabilities, provide the foundation for our objectives: to identify the failure mechanisms that appear significant, and to see how deeper analysis or remedial action might resolve them.

B III FGB Propulsion Risks

B III-I FGB Module Description. (See also Appendix BI-1 through 7)

The Russian supplied FGB module, as shown in Figure B-1, is located on the centerline of the ISSA, pointing along the line of flight. When the station is complete the module centroid lies about 366 inches behind the station c.g. The module itself, see Figure B-2, consists of a central pressurised vessel, occupied at times by the crew, with propulsion system tanks mounted on the outside of the central crew vessel. We are concerned here with risks arising from hypervelocity penetration of these external stored energy propulsion tanks. There are 32 of them: eight cylinders for UDMH, eight for N2O4 (arranged in pairs--see the cross section in Figure B-2) and 16 spherical storage bottles holding GN2 at relatively high pressure. The eight forward cylindrical tanks are 2923 mm long, the eight aft tanks are 3528 mm long. (Ref. B1)

Figure B-3, which gives dimensions for both tank lengths, shows that each 480 mm dia. aluminum tank, long or short, contains propellant, either UDMH or N2O4, together with GN2. The gaseous Nitrogen at a pressure as high as 300 psia. provides positive displacement feed for the propellant, from which it is separated by a sliding piston and stainless steel bellows. The piston is shown in the " all propellant used " position. Since the tanks are assembled with their gas feed end forward, any projectile penetrating the outer cylinder of the tank will have to penetrate the bellows and/or piston before coming into contact with the propellant. It should also be noted that the probability of a tank penetration reaching the propellant is influenced by the fore and aft location of the strike (see Appendix BI-3). Based on this, and assuming that the debris half cone angle is 30 deg, and that the direction of attack is 45 deg from the direction of flight in plan form, the probabilities, are:

	Forward, Short Tank	Aft, Long Tank
1) Penetrate to GN2 portion of tank only	0.575	0.590
2) Penetrate to GN2 and Propellant portion	0.245	0.254
3) No Tank penetration	0.180	0.156

Figure B-4, showing the bumper shield on the forward tanks, was scaled from preliminary Russian Layouts; then, using a 30 deg. debris half-cone angle, a graphic analysis was performed to determine what proportion of Ballistic Limit (or greater) strikes hitting the 'strike height band' would go on to hit: the outboard tank, the inboard tank, both tanks, or no tank. A similar analysis was done for the aft tanks, which have a slightly different geometry (see Appendix B 1-4), and the results are summarized in Table B-1. When, in this Table, the strike-height driven probability is combined with the strike-fore-and-aft driven probability, and the results for long and short tanks averaged, the following may be seen. Given what would normally be a Ballistic Limit (or greater) hit on the propellant tank bumper shield, the likelihood of:

- | | |
|--|-------|
| 1) Penetration to GN2 portion of the tank only, is | 0.466 |
| 2) Penetration to GN2 followed by Propellant. is | 0.202 |
| 3) No tank penetration, is | 0.332 |

Furthermore, because only half of the propellant tanks contain UDMH, the probability of this liquid being hit is about 10%,

Figure B-4 also shows how the high pressure GN2 bottles are well shadowed by the propellant tanks against lateral attack. It is not straightforward to analyse their exposure in exactly the same way as the propellant tanks because they occupy much less length and do not have anything analogous to the piston and bellows. However, when it comes to the GN2 Bottle Fault Tree, we use a conservative figure of 0.1 for the probability of a Ballistic Limit (or greater) hit on the bumper reaching the GN2 bottles. A more detailed analysis based on a firmer definition of the bumper might well halve this figure. These geometric analyses are carried forward to the Fault Trees for Propellant Tanks and GN2 Bottles.

B III-2 FGB Fault Mechanisms

We have identified three general risks to the crew and the station that may arise from hypervelocity penetration of FGB propulsion elements if the strike is severe

enough. They are:

- 1) Detonation of UDMH propellant.
- 2) Damage to the station prime structure due to violent venting of the gaseous N₂, either from the propellant tanks or the high pressure GN₂ supply bottles.
- 3) Overpowering of the attitude control system due to generally lesser, but longer-lasting, venting forces which, when brought under control, may find the station outside its attitude control limits.

A description of these fault mechanisms and our estimates of the severity of damage that can be tolerated before these faults occur are given in the following paragraphs.

UDMH Detonation (See also Appendix BII-1 through 6). In the FGB tanks we have already seen that, to reach the propellant itself, incoming debris would have to penetrate a three wall defense system; the bumper, the main wall, the bellows. In the absence of directly applicable test data establishing a numerical detonation threshold, we have come up with two possible measuring methods. For both methods, if a 'detonating attack' on the propellant is to succeed, the debris must, as a minimum, penetrate the main wall--meet or exceed Ballistic Limit 2. For the first method, the severity of the attack is measured in terms of the debris energy beyond the main wall, which strikes the bellows -- the third wall--. On the other hand, it may be that only the debris penetrating the third wall --exceeding BL3-- counts. Then for the second method, attack severity becomes the debris energy beyond the third wall. The truth probably lies somewhere between these two extremes, in part because the liquid propellant is in contact with the third wall and 'experiences' some of the impulse usually thought of as being absorbed in the third wall in a vacuum set-up. In this study we have adopted the first of these two measuring methods, calculating the total energy in the debris cloud behind the second, tank, wall; which is also the energy striking the third wall. This choice is partially self-compensating because the energy associated with tests is also subject to the same method of analysis.

We needed a numeric value of the attack energy --attack energy impacting the third wall (bellows) -- to be used as a detonation threshold. A search of the literature and enquiries within the propellant and test communities yielded two useable test sets.

The first test set was carried out at NASA Lewis Research Center in the 60's (Ref. 2). A tank containing UDMH, was penetrated by a projectile with impacting energy of 805 foot-pounds. There was no evidence of chemical interaction, combustion, or burning. This test was also performed with Hydrazine in the tank, with the same projectile energy and with the same negative result. We are taking this as a pessimistic, lower bound, of the detonation threshold; ie. any more vigorous attack might trigger a detonation. The second pair of tests were carried out at Wright Laboratory, Armament Directorate, in 1989 (Ref. 3) A small target tank containing Hydrazine was attacked by a fabricated projectile, which penetrated a bumper before penetrating the tank. The first test went according to plan, the whole projectile hit the bumper and broke up, the debris penetrated the tank with an impacting energy we calculate at 700,000 foot-pounds; and the Hydrazine detonated. The second test did not go according to plan; only the projectile cap hit the bumper, broke up, and penetrated the tank, this time with an impacting energy of about 103,000 foot-pounds. Again the Hydrazine detonated. For our purposes the first Wright Lab test is overkill; we are taking the second Wright Lab test energy, of 103,000 ft lb, as the optimistic, upper, bound of the detonation threshold (see Appendix BII-3,4,5,6,).

This gap of two orders of magnitude between our upper and lower detonation thresholds is probably a fair reflection of how 'thin' the test data is in this area. This also provides some justification for our use of Hydrazine data instead of UDMH data in establishing a provisional upper bound. There seems to be a measure of agreement that these two propellants are similar ; the NASA Lewis tests provide some support for this assumption.

Station Prime Structure Damage due to Venting (see also Appendix BIII-1 through 6).

NASA has analysed the station structure and identified the Solar Array Rotary Joint (SARJ), where the Solar Power elements attach to the port and starboard extremities of the main truss, as being generally weaker than other joints in the prime structure. We are limiting our study of the damage that venting can cause to this designated joint.

Our approach has been to 1) calculate from the SARJ specification the limit loadings in various planes that this joint can carry, 2) determine how large the FGB venting forces would have to be to generate these limit loads, 3) calculate the diameters of venting holes -- the penetrations of the propellant tanks or high pressure GN2 bottles-- that

could produce these forces, and 4) estimate the probability of such holes occurring. Summarizing our results:

In normal operation the SARJ completes one revolution for each station orbit of the Earth. Its torque limit strength, ie. it's ability to resist unwanted turning in this same sense, is about 230,000 inch-pounds. It's overhang limit strength, in a station yaw or roll sense, is about 180,000 inch-pounds. There is approximately a 5% fluctuation in this overhang strength as the joint rotates; we have used a mean value.

For purposes of gaining insight, we consider four venting force directions; all starting from the centroid of the FGB. Values associated with them are shown in Table B-2. The first force is up or down in the plane of symmetry, --z direction-- and pitches the station. This symmetric venting force loads the six fittings that comprise the moving parts of the SARJ, in both shear and tension. If the venting force rises to 4,080 lb. one of the six fittings reaches it's limit tension load of 731 lb. (a 22,600 lb. venting force is needed to bring one of the fittings to it's shear limit). With the GN2 in the cylindrical propellant tanks at an upper bound pressure of about 300 psia, and using a discharge coefficient of unity, the vent hole diameter to produce this 4,080 lb. force comes to 4.2 inches. Venting from the high pressure GN2 bottles at a pressure of 3,300 psia, the minimum vent hole diameter works out to 1.25 inches.

The second venting force is still vertical but its application point is displaced sideways out of the plane of symmetry and causes roll as well as pitch. The third force is purely lateral --y direction-- and is, by definition, at the same height as the station cg. - it causes yaw. The fourth remains lateral, but-- displaced up or down-- it adds some roll to the station's yaw.

Several points can be made. The geometry of the station and the FGB, and its tanks, make a venting-induced pure roll of the station virtually impossible; we have not treated it. Again, geometry suggests that a pure pitch or a pure yaw producing venting force, though just possible, is unlikely. Conservatively, we consider pitch-with-roll and yaw-with-roll to be the central cases. Of these two, pitch-with-roll requires a smaller hole to bring one of the fittings to it's limit load, and as such is the more likely to occur. Table B-2 also shows that, under these loading conditions, the weakest aspect of the joint fittings is their tension--not their shear--limit. At first blush it might seem attractive

to improve their tension capability (731 lb. force is a very modest fitting strength that might be increased a lot for very little weight or effort) but this calls for consideration of pressure vessel unzipping (see Section B III-3).

The assumptions made in the foregoing venting analysis are generally conservative. For instance, the load analysis used is quasi-static; a dynamic analysis would give a lower peak load at the SARJ which is about 100 ft from the venting load application point. The venting vectors will usually point a bit forward, which will reduce the station disturbing moments. There will probably be some break-up of the venting plume due to the torn bumper and stuffing, the discharge coefficient will be lower, and the GN2 pressures will, on a time average, be lower than the upper bound values used in Table B-2. This is particularly so in the case of the high pressure bottles. The SARJ itself may not be designed right down to its specification, and it may tolerate loading above the limit level on a one-time basis. At each place where we have simplified the analysis, we have made a conservative choice. One less conservative subset of the venting scenario, has a propellant tank or GN2 bottle breaking free of the station. We have not treated this.

Overpowering of Control. Detail investigation of this failure is not a part of this study, but previous work on Freedom shows that, with venting forces too low to damage the structure, but high enough to overpower the attitude control, and lasting long enough, the station may be driven outside its normal guidance, star tracking and crew environment limits. Some study, simulation, and training to deal with this, may be a wise investment.

To conclude this section, Figure B-5 summarises the specific hypervelocity targets within the FGB envelope, which we will be dealing with, and the failure mechanisms associated with each. 'Unzip' shows up in this figure and it is timely to discuss unzipping as it affects the venting forces.

B III-3 Unzipping as a generator of Holes of Large Area

Venting damage to the prime structure is caused by GN2 escaping from a hole with a certain minimum area. In the case of the propellant tanks an area of 13.6 square inches or an equivalent diameter of 4.2 in. This size hole can be made by

orbital debris within the range we are considering. But a smaller projectile can penetrate and make a crack, initially shorter than the 4.2 in. diameter, which can unzip; resulting within milliseconds in a hole many times larger than the 13.6 sq.in. above. The preliminary estimate of critical crack length (ccl) for the FGB propellant tanks - with their thickness, radius, pressure, and material- is 2.7 in. Calculating this length is a first step; the second, estimating what combination of attack and defense will result in a crack of this initial length, is less well understood. For the time being, we note that if a plain crack (like view a) in Figure B-6, with little or no holes or lateral cracks), is of critical length L; then a largish hole with short radial cracks (like view b), will be equally critical, in an unzipping sense, when the crack-tip to crack-tip length is a little longer than L. Essentially, the presence of the largish center hole, in a cylinder with hoop and axial tensions, reduces the stress concentration at the crack tips. For this study we are using the approximation that making an estimated hole diameter of 3.0 in. in the propellant tank main wall is equivalent to forming a critical crack length of 2.7 inches, from the unzipping point of view.

For the high pressure GN2 bottles the logic is the same, but the absolute values are:

Minimum hole to cause venting damage	1.0 sq.in. or 1.13 in. dia.
Critical crack length.	1.4 in.
Equivalent critical hole diameter	1.5 in.

For both targets, as projectile diameter is systematically increased, venting through a hole that unzips damages the structure before venting through a plain hole, -- unzipping is the dominant threat. Moderate increases in the SARJ fitting tension strength would not appear to improve this situation because a critical crack in the propellant tank, once unzipped, presents too large a hole area.

B III-4 FGB Ballistic Limits and Damage Contours

On a field of Projectile Diameter vs Projectile Initial Relative Velocity, we show the estimated Ballistic Limit together with appropriate Damage Contours above it. Damage Contour (a new term) reflects the fact that not all hits above the Ballistic Limit are catastrophic. Penetration hole size is zero below the Ballistic Limit, jumps to some positive value at it, and grows bigger as the projectile size increases above it. In the case of a crew module main wall, for instance, the effective penetration size just above

the Ballistic Limit is not, in general, large enough to cause crew hypoxia. A Damage Contour for this failure would be an estimated line on the field showing how much above the Ballistic Limit a hit would have to be to subject crew to this catastrophe. A specific Damage Contour is drawn for each of the targets/failure mechanism combinations named in Figure B-5, and discussed in the following paragraphs.

Inner UDMH Volume The risk here is detonation of the UDMH. This is triggered by the debris cloud behind the main tank wall (2) impacting the bellows (3). The triggering metric is the debris cloud energy. We have three exploratory values: an upper, optimistic, threshold of 103,000ft lb; a lower, pessimistic, threshold of 800 ft lb; and an arbitrary mid-way threshold of 10,000 ft lb. Figure B-7 shows the Field for UDMH. The attack is by Aluminum spheres of varying velocity, varying size, and an obliquity of 0 deg. The defense is all of aluminum, with a bumper (1) .04 in thick, a gap of 4.0 in, and a main wall 0.10 in thick.

The Field is divided, more or less vertically, into three phases that differentiate between the state of the incoming debris behind the bumper (1), and influence the position and slope of the BL within each phase. In phase A (low initial relative velocity, with the projectile passing substantially unbroken through the bumper) for the BL, we use the E. L. Christiansen Oct. '92 equations (Ref.4) verifying that the Fatepen2 (Ref. 5) values and some SSEIC calculations agree fairly closely. For phase B (intermediate initial relative velocity, with the projectile breaking into solid -not molten- fragments on encountering the bumper), for the BL, we compared Christiansen; G, T, Burtch Hole-Out (Ref. 6), and Fatepen2; and used the Christiansen estimates. In phase C (high initial relative velocity, with the projectile breaking into a mostly molten cloud on encountering the bumper, and with no fragments large enough to penetrate the main wall individually) for the BL, we again used the Christiansen equations, checking that they agreed fairly well with some SSEIC estimates.

To draw the Damage Contours for UDMH detonation, we need knowledge of the energy in the debris cloud behind the main wall. Up to an initial relative velocity of 5 km/s, Fatepen2 gives a direct read-out of this quantity; at higher speeds Fatepen2's applicability is open to some question. In phase C we use a SSEIC derived method of calculating cloud energy (See Appendix BIV-1 and 2). The gap between 5km/s and

most real life cases the three dimensional, vulnerable, main-wall target is smaller than the bumper that shields it. So 'r' can never be greater than 'd' and is often less. Table B-3 shows the 'd' values. (See also Appendix BV-1 through 6).

B III-5 FGB Fault Trees

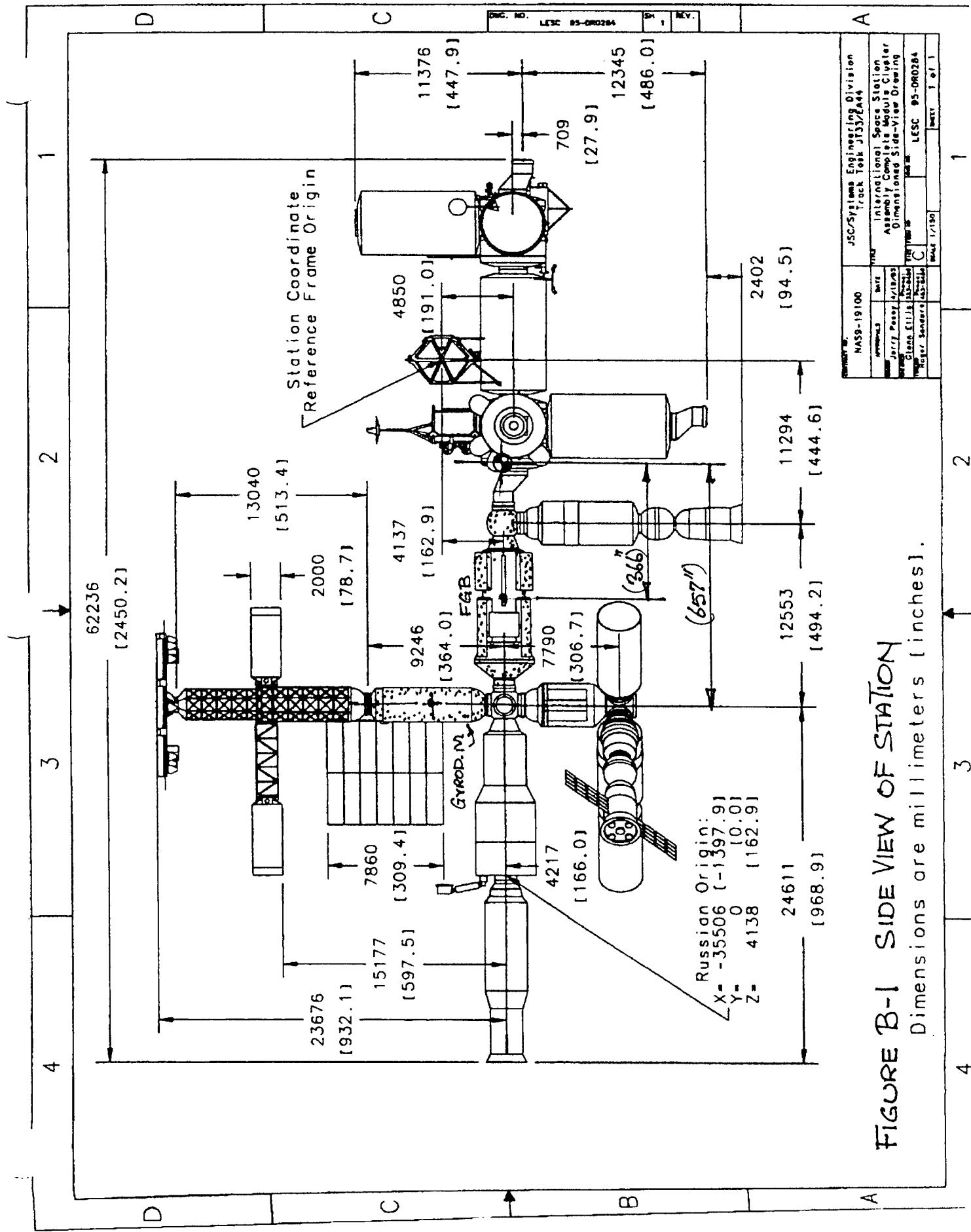
There are three Fault Trees in this report, two in this FGB section and one in the Gyrodyne section. All three use the sign conventions illustrated for a typical Node in Figure B-10. Each Node on a tree has a reference number, starting on the left with '0'; the 'yes' and 'no' branch probabilities always add up to one; each tree starts at Node #0 with an absolute population of 1,000, which flows across the tree indicating the cumulative effect of all upstream Nodes on the 'traffic' in each branch. The starting population number of 1,000 was chosen to make an easy distinction between traffic (using integers) and branch probabilities (using decimals).

FGB Propellant Tank Fault Tree (Figure B-11). Node #0 takes as a given that the FGB module has been hit in the propellant tank shield zone with a projectile having the wherewithal to achieve BL2 or above. Nodes #1 through #5 show on a purely internal geometry basis what is hit and what is not. These numbers are derived from Table B-1. The populations of Nodes #1 and #2 are combined, bringing all the potential UDMH detonation candidates together in Node #7. where we have used the most pessimistic detonation 'yes' probability from Table B-3. All the GN2 venting that has not been involved in a detonation is now gathered in node #7, and the SARJ damage 'yes' factor, from Table B-3 again ,is applied. Finally , the remaining GN2 venting is put through Node #8 where the 'yes' probability is just a low level placeholder, which if it were addressed would probably shrink.

Summarising, the populations (in the individual branches reaching the right of the page) when divided by the arbitrary 1,000, are the traditional 'r' values. UDMH detonation is almost certainly catastrophic but, with an 'r' value of 0.047, very unlikely. Going all the way from low detonation threshold to high, reduces the 'r' value to 0.015. Overloading the SARJ is probably not catastrophic, just expensive. At 0.30 the 'r' value is significant and some of the simplifying assumptions made in this study may be worth another look.

FGB High Pressure GN2 Fault Tree (Figure B-12). This Fault Tree is a simple version of the previous one, with Node #0 starting with all the hits on the high pressure bottle shielding zone that have BL 2 or above capability, Node #1 asks and answers the geometric question "What proportion of penetrations of the zone bumper go on to hit the high pressure bottles? " The proportion used (0.1) is conservative, and comes from the discussion in Section B III-1. Node #2 gets its 'yes' proportion from Table B-3; and Node #3, at 0.1, copies the corresponding Node in the previous Tree.

Summarising, with a lowish 'r' value just below 0.1, each Node along the top branch could be reexamined briefly. Node #0 for its underlying Bumper Ballistic Limit (2) penetration rate; #1 for a better definition of the shield-to-pressure-bottle geometry; #2 for a closer look at the reduced likelihood of unzipping as the storage pressure falls. On the general subject of reduced risk, are the storage bottles emptied starting from the front to exploit within-the-group shadowing, or could they be?



NASA-19100		JSC/Systems Engineering Division	
Track Task 3133/EA44		Track Task 3133/EA44	
Author	Drawn	Checked	Reviewed
Jerry Papp	1/19/93	1/19/93	1/19/93
Gregory E. H. H. H.	1/19/93	1/19/93	1/19/93
1/19/93	1/19/93	1/19/93	1/19/93
LSC 95-060284		LSC 95-060284	
Sheet 1 of 1		Sheet 1 of 1	

FIGURE B-1 SIDE VIEW OF STATION

Dimensions are millimeters [inches].

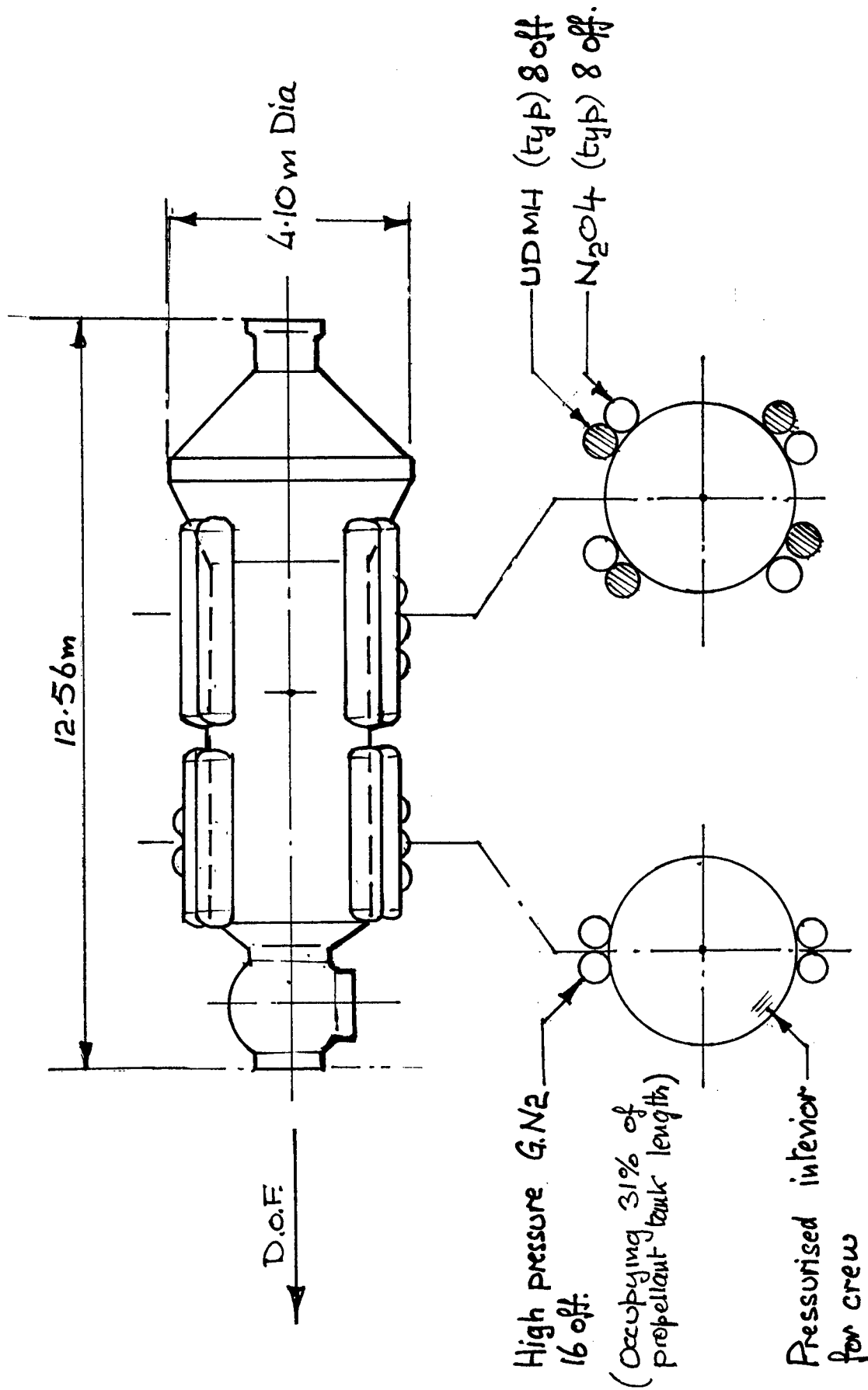


FIGURE B-2 FGB GENERAL ARRANGEMENT.

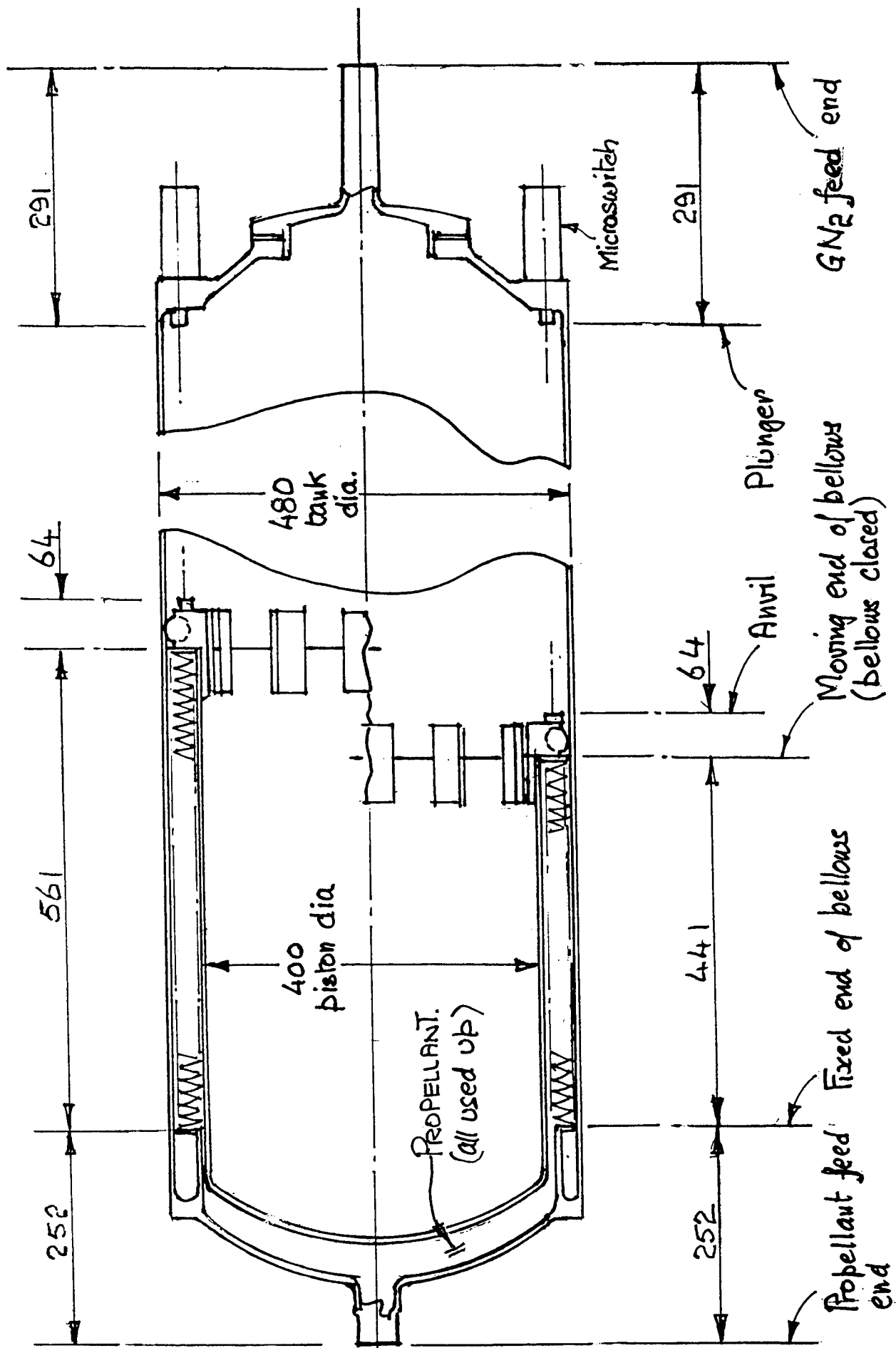


FIGURE B-3 ASSUMED FGB PROPELLANT TANK DIMENSIONS (mm)

LONG TANK ABOVE 3528 mm O'ALL L.
SHORT TANK BELOW 2923 mm O'ALL L.

Penetration vulnerability vs. Strike Height

- All debris assumed to come from flank
- half cone angle - 30°

Outboard tank 60%
Inboard tank 31%
GN₂ bottle 11%

- Note shadowing by outboard tank
- avg outboard tank gap 12 mm.
- " inboard " " 18 mm.

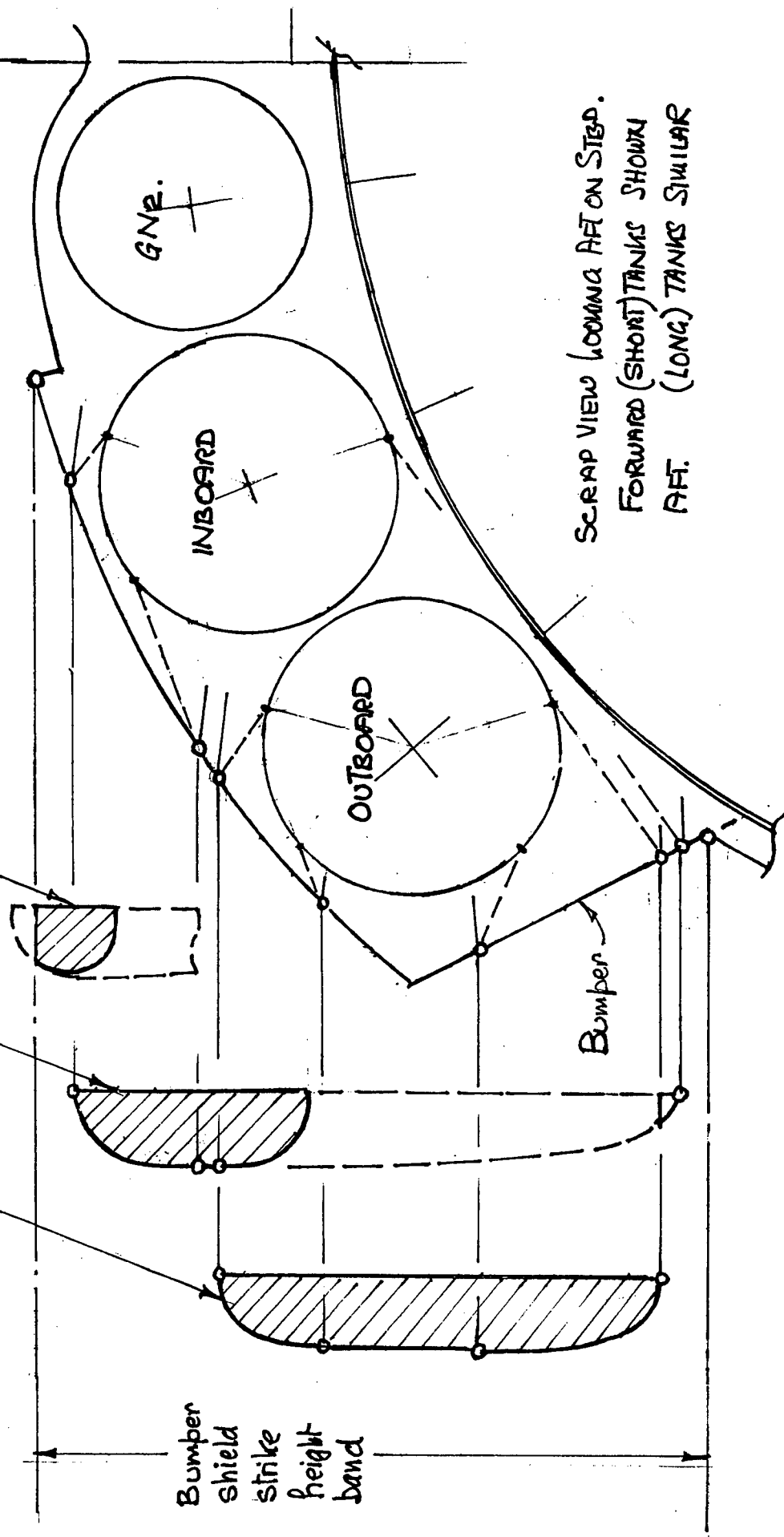


FIGURE B-4. GEOMETRIC PROBABILITY OF B.L. (OR GREATER) HITS ON BUMPER GOING ON TO PENETRATE TANKS ETC.

AFT. LONG TANKS	Probability driven by strike height	Probability driven by strike f & a. location			See Appendix BI-2
		No tank pen .156	GN ₂ only. .590	GN ₂ + propellant .254	
Outbd. tank	.451	.070	.268	.115	←
Inbd. tank	.230	.036	.136	.058	
Outbd & Inbd. t.	.106	.017	.062	.027	
No tank hit	.213	.213	—	—	
		.336	.464	.200	

FOR'D, SHORT TANKS					See Appendix BI-2
		.180	.575	.245	←
Outbd. tank	.506	.091	.288	.127	
Inbd. tank	.217	.039	.124	.054	
Outbd. & Inbd. t.	.096	.017	.055	.024	
No tank hit	.181	.181	—	—	
		.328	.467	.205	

ALL TANKS AVG.	.332	.466	.202
----------------	------	------	------

- Notes
- plan obliquity ~ 45° from DOF
 - tanks half full
 - GN₂ feed-end forward.
 - 1/2 cone angle = 30°

8 tanks contain UDMH
8 " " N₂O₄

TABLE B-1 PROPORTION OF BL (OR GREATER) HITS THAT PENETRATE COMBINATIONS OF TANKS, AND REACH GN₂ OR GN₂ + PROPELLANT.

		Station Response To Venting			
		Pitch	Pitch + roll	Yaw	Yaw + roll
Heaviest shear load on a joint fitting	lb	0239V	0272V	0089V	0122V
V for fitting shear load of 540 lb.	lb	22 600	19 900	60 700	44 300
Heaviest tension load on a joint fitting	lb	1791V	2223V	1411V	1843V
V for fitting tension load of 731 lb	lb	4080	3290	5180	3970
Smallest V load that will load a fitting to its limit ~ shear or tension	lb	4080	3290	5180	3970
Propellant Tank ~ GN ₂ at 300 psia					
• Vent hole area to produce V	in ²	13.6	11.3	17.3	13.2
• Equivalent hole dia	in	4.2	3.7	4.7	4.1
GN ₂ Bottle ~ GN ₂ at 3300 psia					
• Vent hole area to produce V	in ²	1.24	1.00	1.57	1.20
• Equivalent hole dia	in	1.25	1.13	1.41	1.24

- V = venting force
- Allowable shear load on any joint fitting - 540 lb limit
- " tension " " " " " - 731 lb "

TABLE B-2 VENTING FORCE/HOLE SIZE TO GENERATE LIMIT LOADS IN SARJ.

FAILURE MECHANISM	UDMH Detonation Debris impact on third 'wet' tank wall	Prime Structure Breackage Violent Venting Vector from escaping GN ₂
8 of 16 Propellant Tanks strike reaches inner UDMH	Upper threshold. 103,000 (4.1 lb) Mid " 10,000 Lower " 800	
16 Propellant Tanks strike reaches GN ₂ only, at 300 psia		<p>Initial 2.7 l. crit. crack or > 2.7 dia hole</p> <p>Unzip</p> <p>pitch → 11.3 in² area + roll → 3.7 dia</p> <p>Yaw + roll → 4.1 dia 13.2 in² area</p>
16 G.N ₂ Bottles 3300 psia.		<p>Initial 1.4 l. crit. crack or > 1.4 dia. hole</p> <p>Unzip</p> <p>pitch → 1.0 in² area + roll → 1.13 dia</p> <p>Yaw + roll → 1.24 dia 1.2 in² area</p>

FIGURE B-5 SPECIFIC FGB TARGETS & FAILURE MECHANISMS

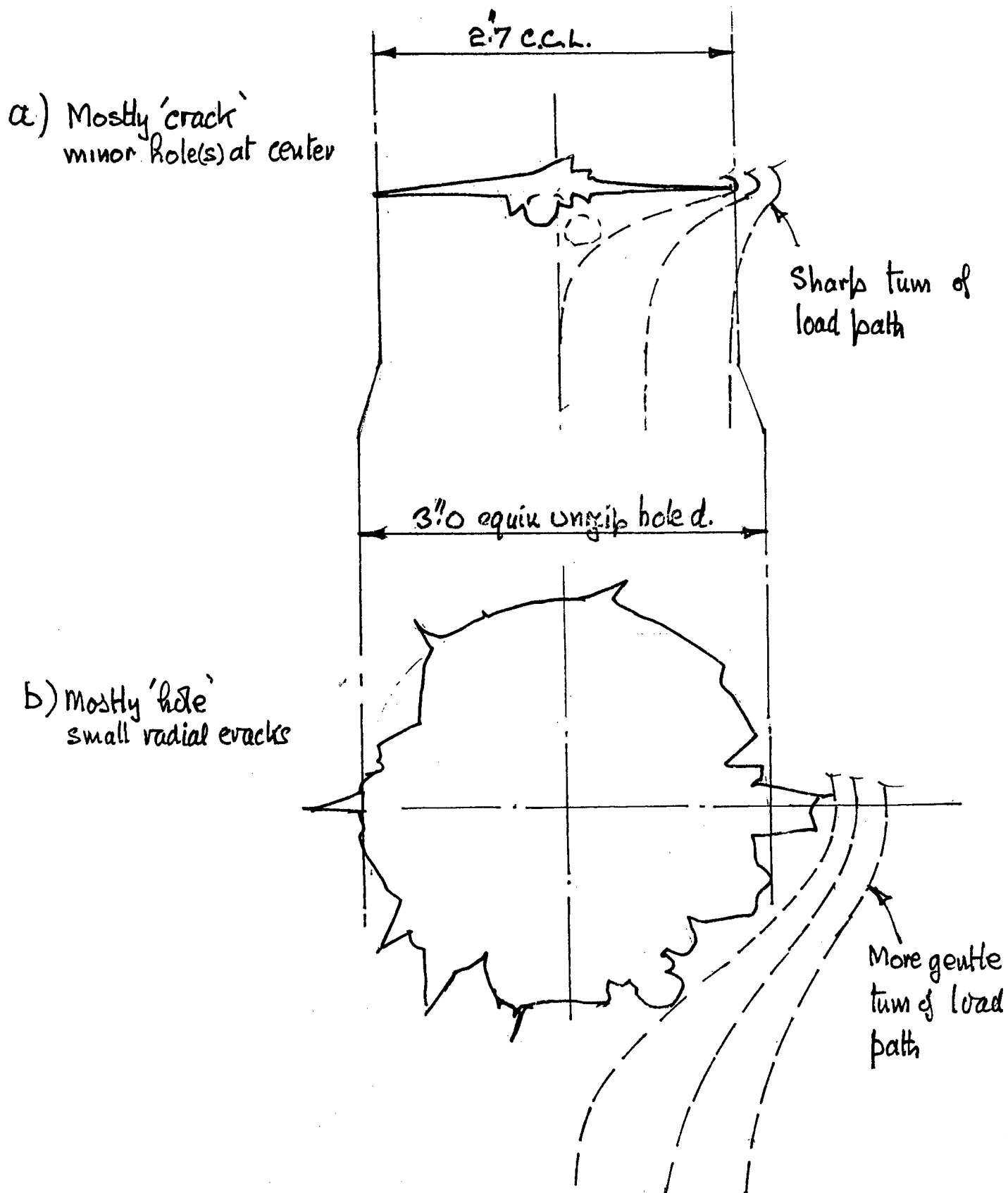


FIGURE B-6 CONCEPT OF CRACK LENGTH/EQUIVALENT HOLE DIA

Legend: — — — Phase bounds A, B, C, ~ BL2 (-10 alum main wall)
 — (X) — Equiv. hole dia in main wall (inches indicated)
 oooooooooo Damage Contours - debris cloud energy triggers UDMH detonation

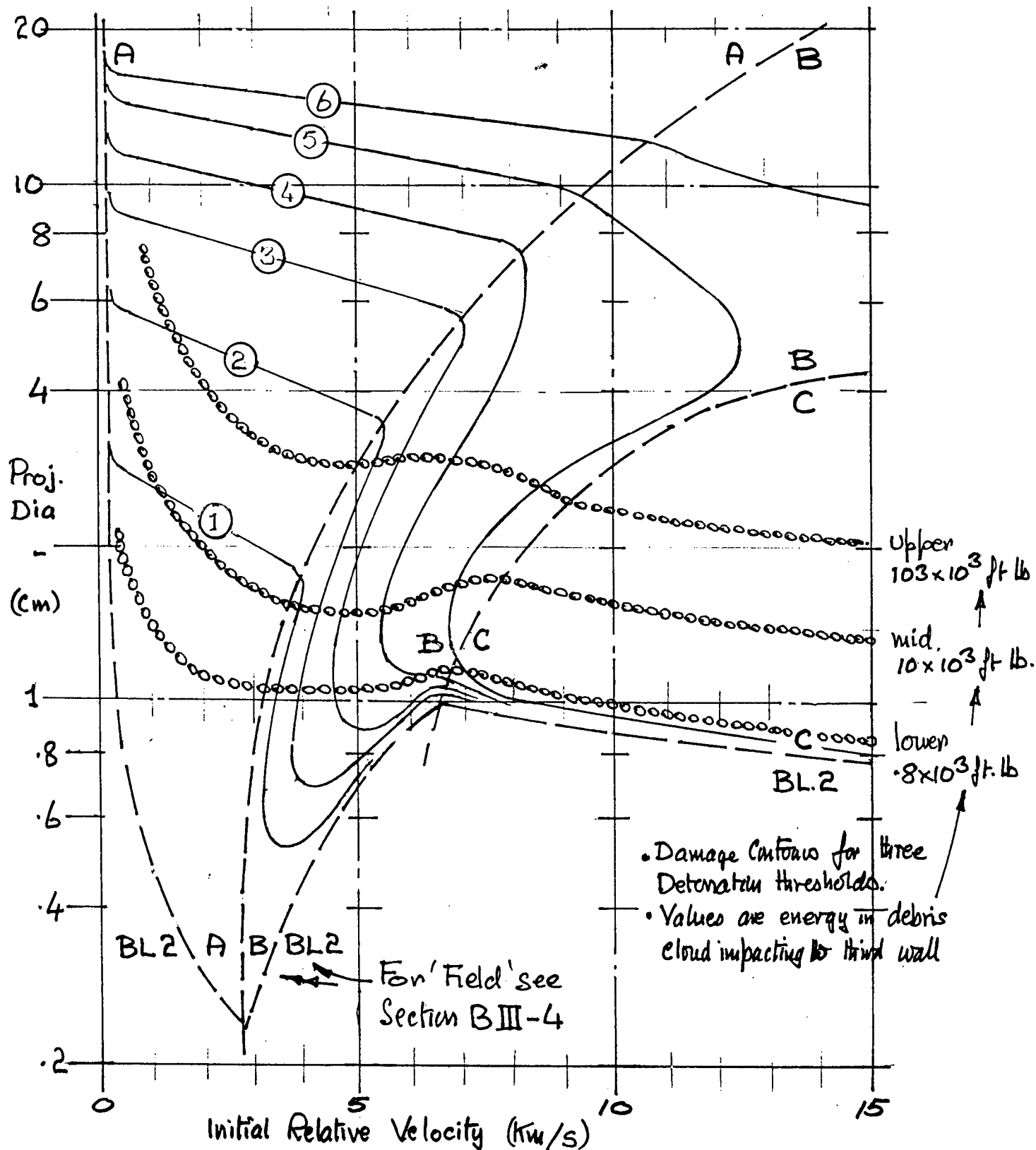


FIGURE B-7. FIELD OF UDMH DETONATION

Legend: — — — Phase bounds A, B, C, ~ BL2 (.10 alum main wall.)

— (X) — Equiv. hole dia. in main wall (inches indicated)

oooooooooooo Damage contour - Venting of Propellant tank GN₂ damages prime structure

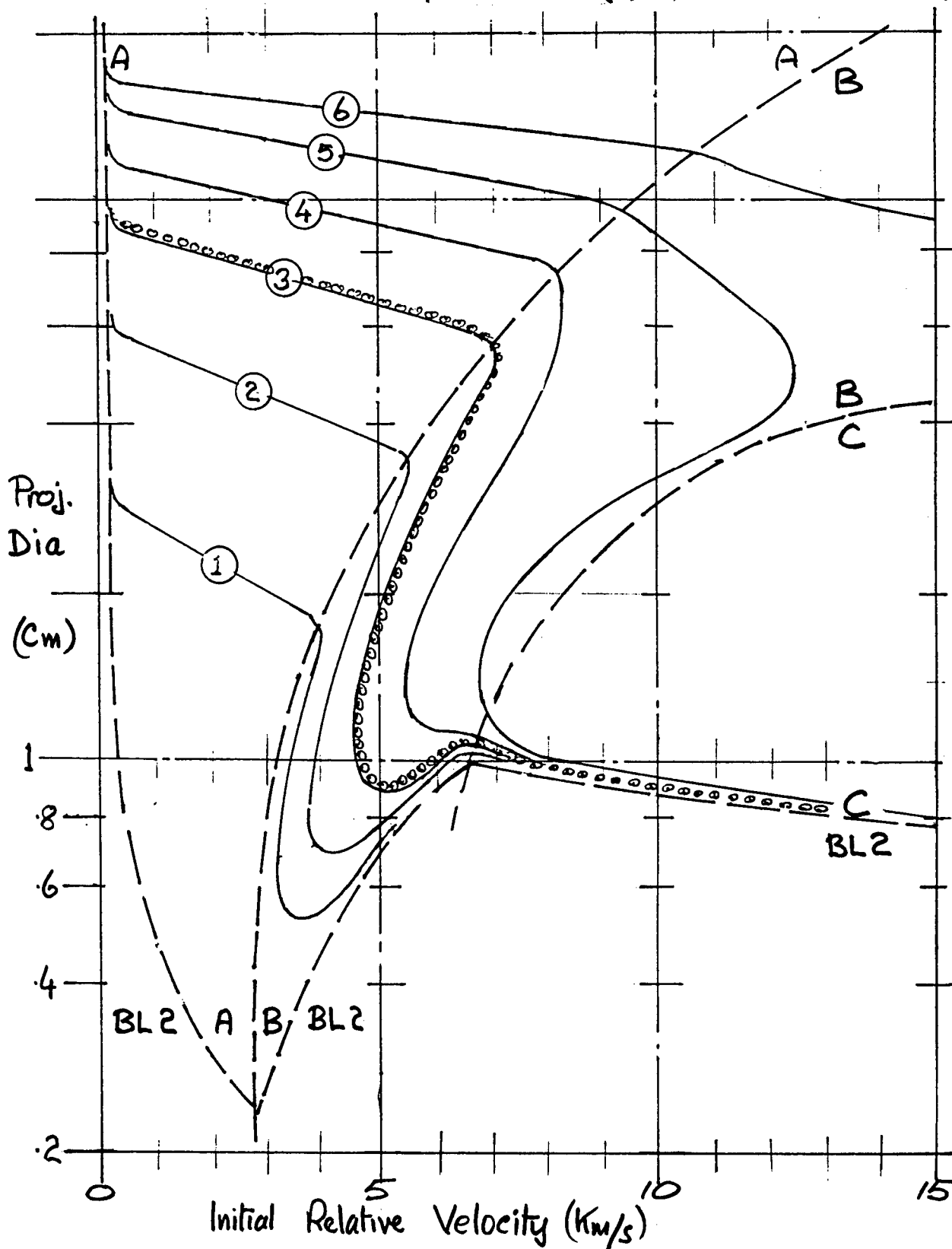


FIGURE B-8 FIELD OF GN₂ VENTING FROM PROPELLANT TANKS

Legend: — — — Phase bounds A.B.C. - BL 2 (.236 titanium main wall)
 — (X) — Equivalent hole dia in main wall - (inches indicated)
 ooooooooooooo Damage Contour - Venting of high pressure bottle GN₂ damages structure

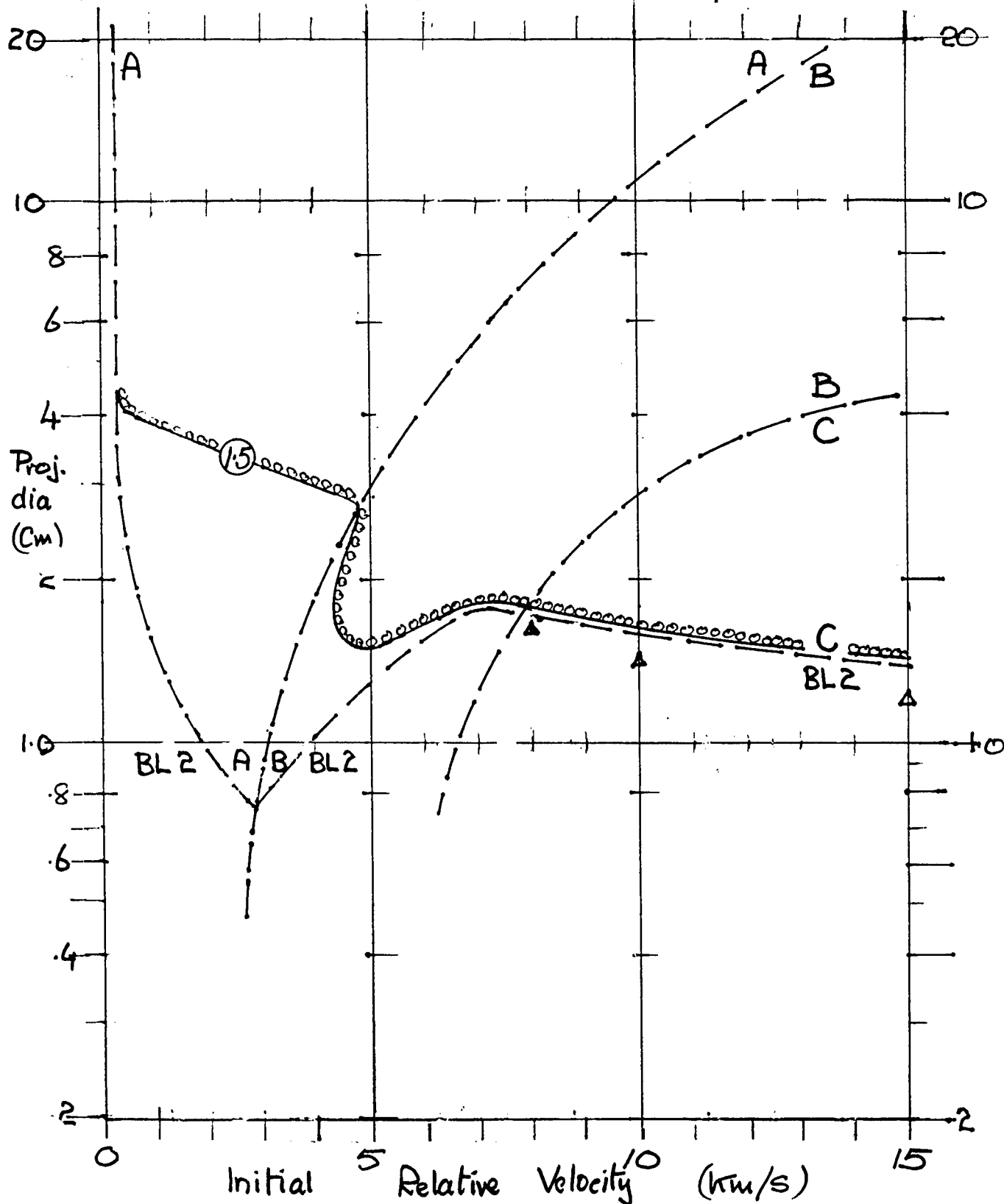


FIGURE B-9 FIELD OF HIGH PRESSURE GN₂ BOTTLE VENTING.

Failure Mechanism	'd'
	$\frac{\text{Flux above Damage Contour}}{\text{Flux above Ballistic Limit}}$
UDMH Detonation	
• Upper Threshold	.13
• Mid Threshold	.22
• Lower Threshold	.41
Prime Structure Damage	
• Vent from Propellant Tank	.48
• Vent from High Press Bottle	.78

TABLE B-3 'd' RATIO VALUE FOR FGB PROPULSION ELEMENTS

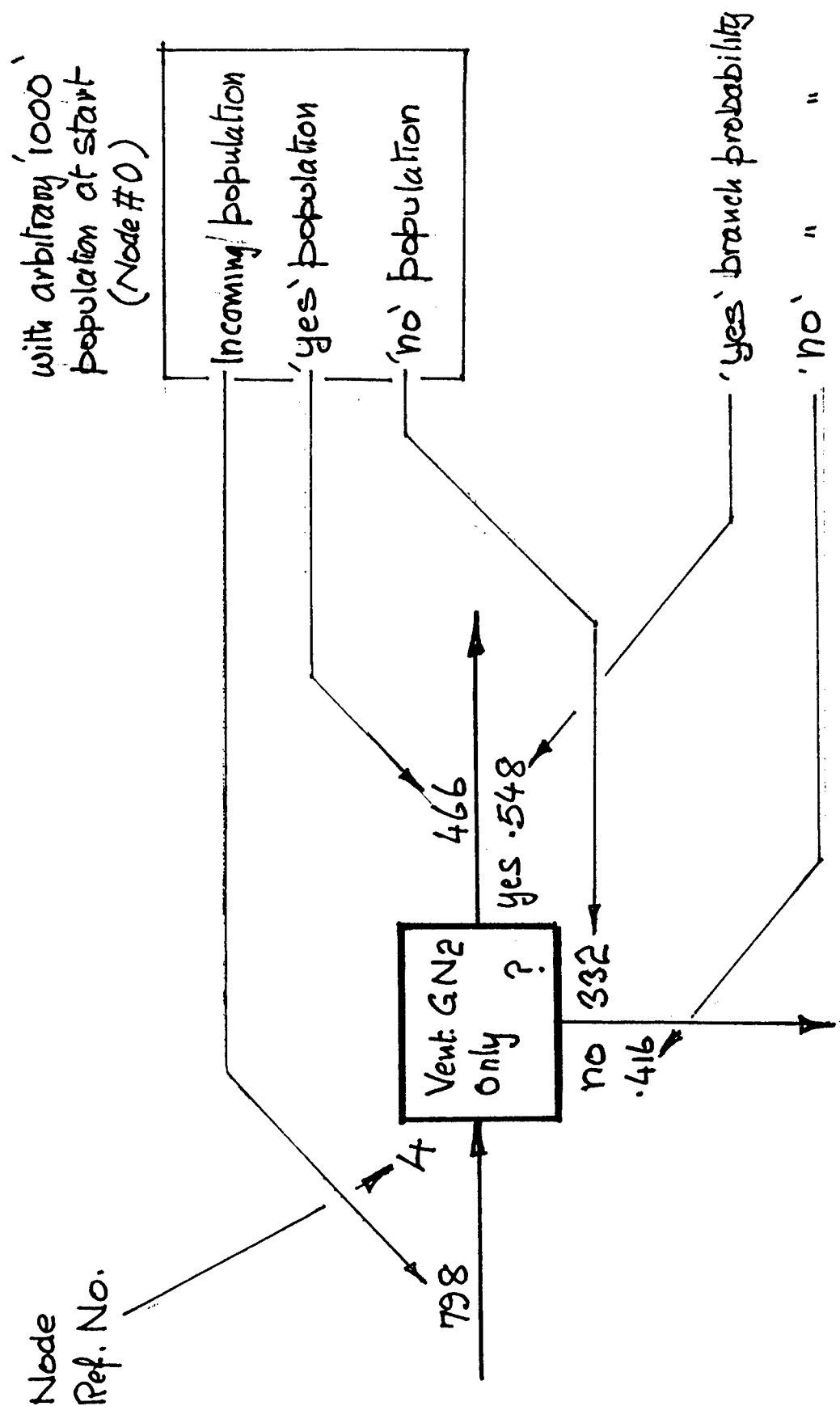


FIGURE B-10 FAULT TREE NUMBERING CONVENTIONS

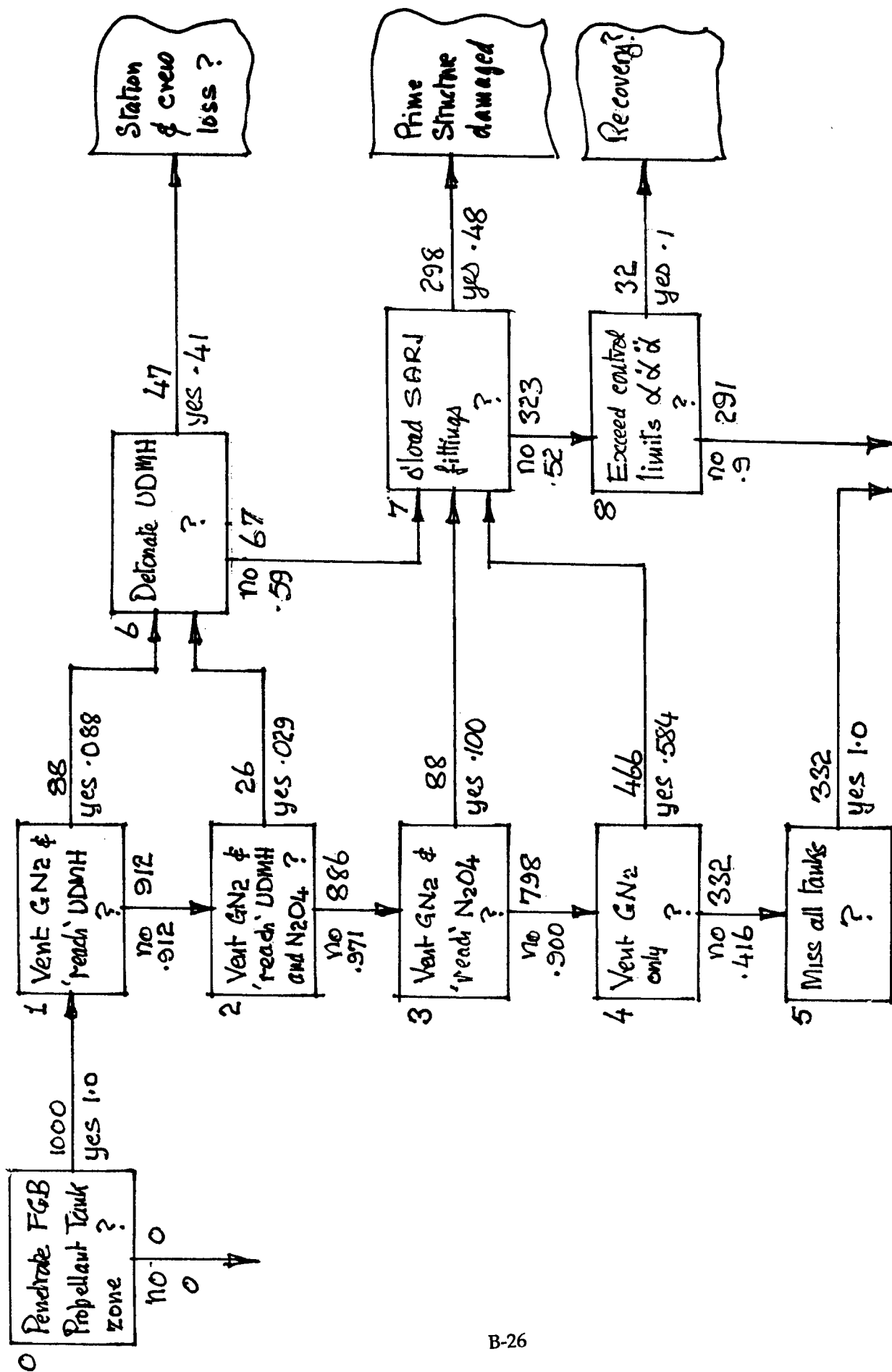


FIGURE B-11 FGB PROPELLANT TANK FAULT TREE

Continued

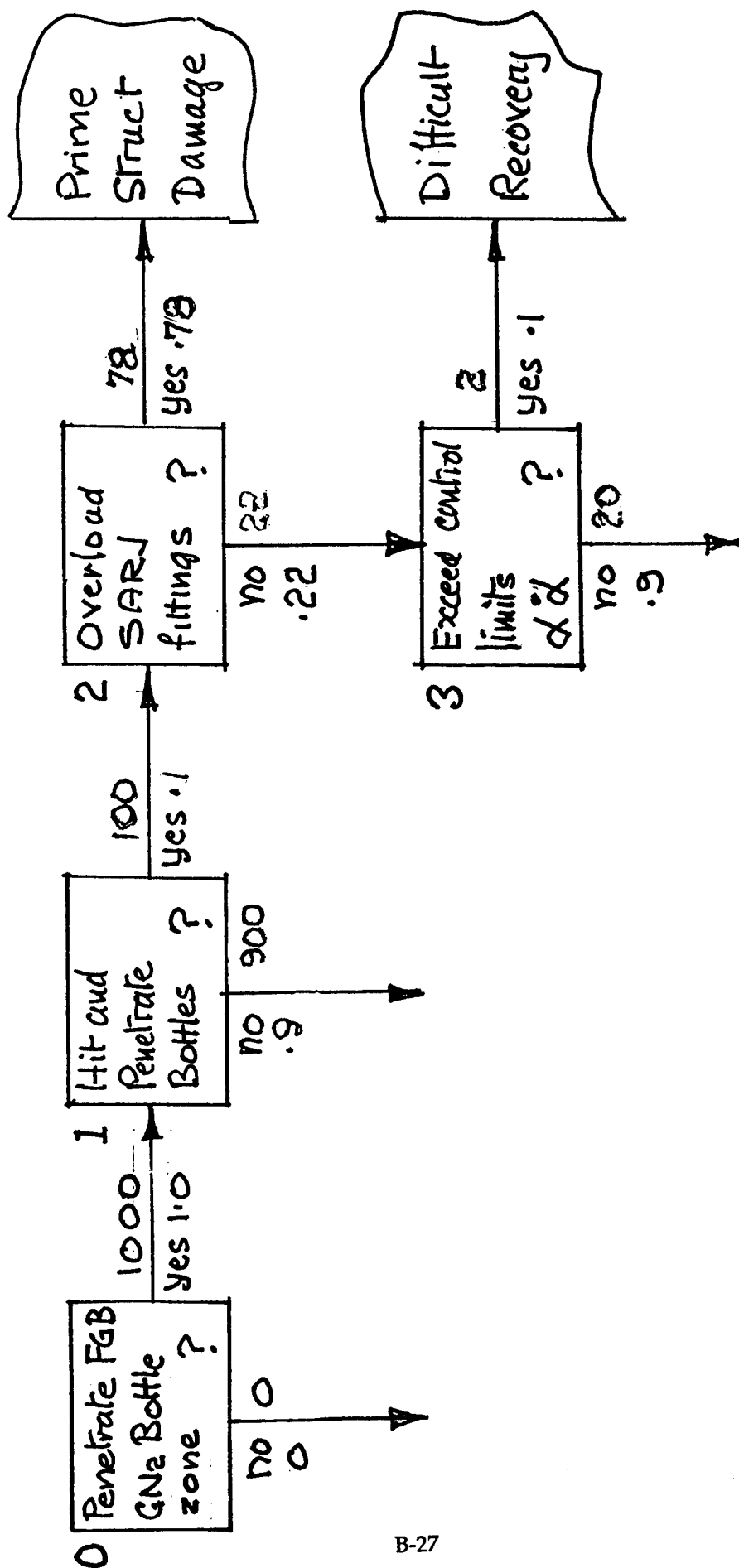


FIGURE B-12. FGB HIGH PRESSURE GN₂ FAULT TREE

B IV Gyrodyne Module Risks

B IV-1 Gyrodyne Module Description

The Russian supplied Gyrodyne module is located in the station plane of symmetry, some 657 in. behind the station complete c.g. Again see Figure B-1. It is mounted on top of the node at the front end of the Russian Service module and its axis points up and down. The module itself, shown in Figure B-13, is a 2200 mm dia. cylinder, pressurized for shirt-sleeves operations, containing six gyrodyne units. Their locations and alignments are defined. Though not immediately apparent, Gyrodynes #1 through #5 form a regular pattern, with #6 having a non standard location and alignment. The main external feature of each gyrodyne unit is a 700 mm dia. vacuum sphere with a spinning rotor inside. Components shown clustered around the sphere are (presumably) controls, instrumentation, motor(s). Figure B-14 shows, on the left, the general appearance of these external items. They are not defined in detail in the material available for this study, so we have in our graphic work simplified the units down to the "icon" shown on the right. This icon shows the assumed line of the rotor shaft and the plane of the rotor itself. Rotor data under nominal conditions includes:

Rotation	6000 rpm.
Angular momentum	2500 n-m-s
Assumed rim centroid dia.	25 inches
Rim mass	87.2 lb
Rim cross section, Steel	3.97 sq.in.
	Titanium 6.94 sq.in.
Hoop stress	Steel 45 ksi
	Titanium 25 ksi

Rotation and Angular Momentum above are given; the key assumption is the rotor rim centroid diameter; the rest of the data follows directly from the given data and the diameter (see Appendix BVI-1) It is worth noting that if the rotor rim is ruptured due to hypervelocity impact, then (good news) the fragments cannot go faster than 200 m /s, but (not such good news) they can be heavy.

From the information available, the Gyrodyne module does not appear to have a general complement of functional and storage racks covering the inside face of the

outer pressure wall. So high energy fragments inside the pressure vessel are more likely than in the case of normal crew modules to impact the main wall, threatening reverse penetration of the pressure vessel (i.e., from the inside out).

B IV-2 Gyrodyne Fault Mechanisms

In our first look at this module, we identified three areas needing numerical analysis before we could construct the fault tree. They are;

- 1) The "Aperture" question; given a penetration of the Gyrodyne module, what is the probability of hitting a Gyrodyne unit?

Then there are two specific risks to the crew and the station that may arise if the attack is severe enough. They are:

- 2) Loss of more than one Gyrodyne unit through fratricide. (It is assumed that loss of one is tolerable).
- 3) Multiple Reverse Penetration of the crew pressure shell, causing hypoxia , thrust or structural separation. Thrust and structural separation have not been considered here.

To simplify the analysis of these three issues it was assumed that the orbital debris attack was coming from a bearing mid way between quadrants III and IV, i.e. 45 deg from the direction of flight (see Figure B-15). It can be shown that there is little or no loss of generality resulting from this. Taking each issue in turn:

The Aperture. Not every penetration of the Gyrodyne module impacts a Gyrodyne unit; and it is the probability of penetrating the module, that "Bumper" (our starting program) gives us. Figure B-15 shows the module looking down the attack vector. Each numbered Gyrodyne is represented by it's vacuum sphere- a solid line- and surrounded by an aperture - a dotted line . Penetrate the main wall of the module within the aperture of a given Gyrodyne and the behind-the -wall-debris will go toward that Gyrodyne; penetrate outside the aperture and it will not. The size of each aperture is driven by the debris cone half angle (here taken as 30 deg.) and by how near or far the Gyrodyne is from the main wall point of penetration. Thus units #4, #3, #5 are "near" the point of penetration and have a small aperture: units #1, #2, #6 are "far"with large apertures (see Appendix BVI-13).

When a main wall penetration occurs within a defined aperture, the question remains, "What is the probability that the Gyrodyne vacuum sphere will be penetrated in its turn?" We have very little knowledge of the state of the debris behind a second wall (fragment and droplet size ranges, velocity ranges, temperature ranges) so we are treating the question parametrically. Figure B-16 has as its output the 'edge and range factor' which answers the question just put. The parameters used are 1) the number of "dangerous" fragments in the cloud behind the main wall: 2) the effect of the air drag within the module in vaporising smaller fragments before they can reach the far Gyrodynes, and 3) the edge effect. This last takes account of the proportion of fragments in a debris cone that will miss a Gyrodyne even though the cone origin lies squarely within the subject aperture. In particular, as the cone origin on the main wall approaches the aperture perimeter, this proportion falls, sinking to zero as it touches the boundary (see Appendix BVI-10 and 11). We have used an edge and range factor of 0.82 for the near Gyrodynes, and 0.65 for the far ones. (For air drag see Appendix BVI-12 and BVI-14 through 17).

Table B-4 multiplies the aperture area for each Gyrodyne by its edge and range factor to obtain an adjusted area, which in its turn is divided by the total projected side area of the module, giving the probability of a penetration of each Gyrodyne following a randomly distributed hit on the main module, not necessarily in an aperture. By this reckoning there is a 0.73 likelihood that a penetration of the main module wall will result in the penetration of one of the six Gyrodynes. This estimate takes no account of the shadowing provided by the Gyrodyne mountings, motors and controls, and as such is conservative.

Gyrodyne Unit Fratricide For this analysis, which is mainly geometric, it is assumed that the rotor of any of the six Gyrodyne units can be ruptured when hit by orbital debris that penetrates the bumper, the Gyrodyne module main wall, and the vacuum sphere shell. Furthermore, once a rotor ruptures, its fragments spread out in its own rotor plane, perhaps disabling or rupturing the rotors of other Gyrodyne(s). Figure B-17 shows typical fratricide features. In the lower left, Gyrodyne #2 (which plays the "Cain" role in this figure) is drawn with its rotor axle in the viewing plane and its rotor datum plane normal to the viewing plane. When the Cain rotor datum plane is extended a couple of diameters it slices through the vacuum sphere, and the rotor

disk, of Gyrodyne #3 ("Abel"). Given the Cain-to-Abel range and the impact diameter (the heavy line cutting the Abel sphere), the probability of a randomly vectored single fragment from Cain hitting Abel is readily found--see the equation at the lower right of Figure B-17. This figure also suggests that the rotor rim width and a modest fragment dispersal angle do not significantly drive the hit probability.

The impact diameter and the range, illustrated in Figure B-17, are determined for each potential Cain / Abel pair using the type of geometry shown in Figure B-18. From these topographies and dimensions, Table B-5 is filled in to show which Cain / Abel pairs are feasible, and what the risk is that a single chunk from a given Cain will hit the subject Abel (see Appendix BVI-2). Note that Gyrodynes 1 through 5 can play either role, depending on which Gyrodyne is first ruptured; and that Gyrodyne #6, due to its unique location and alignment, does not enter into the fratricide game. The risk to Abel of being hit by a single, random, Cain fragment does not vary much from pair to pair. Though the risk from one fragment is not particularly high, we think there may well be a considerable number of them.

Again, this is treated in Figure B-19, using two parameters. Parameter 1 is the number of 'big' fragments that break clear of the Cain spherical vacuum shell. 'Big' in this context means being capable of breaking into the Abel shell, very probably striking obliquely, and at not more than 200 m/s. The rotor rim weighs on the order of 90 lb.; if 'big' means weighing at least one pound, then, allowing for a scatter of fragment size, Abel could be faced with 20 or 30 big ones. We look at the range from 1 to 100 'big' fragments. The rotor rim is remarkably robust: if steel, it has a cross section area of four square inches; if titanium, seven. In either case it is working at less than a quarter of its yield stress. This brings up parameter 2; what percentage of Abel sphere penetrations will end with the rotor ruptured? To get a feel for sensitivity to this, we look at 100% and 80%. In Figure B-19 the output is the Probability of Propagation beyond initial Cain rupture. Its value is sensitive to Parameter 1 when the number of fragments is small, and a bit more sensitive to Parameter 2 when the number of fragments is large. The scrap view on the right is significant. The probability of propagation shown in the main field is the average of six individual values for the six units; but, as already noted, unit #6 never propagates, so the average of all six units cannot rise above 0.833. We have gone forward to the fault analysis with a value of 0.75, which is probably conservative. (For the

derivation of the curves in Figure B-19, see Appendix B VI-2 through 9).

Before leaving the subject of fratricide, it has come to our attention in the last week of this study that the gyrodyne module may be longer than we were originally told. If this has been done, and the gyrodyne units have (perhaps) been moved further apart, then the risk of fratricide will have been significantly reduced: this should be explored.

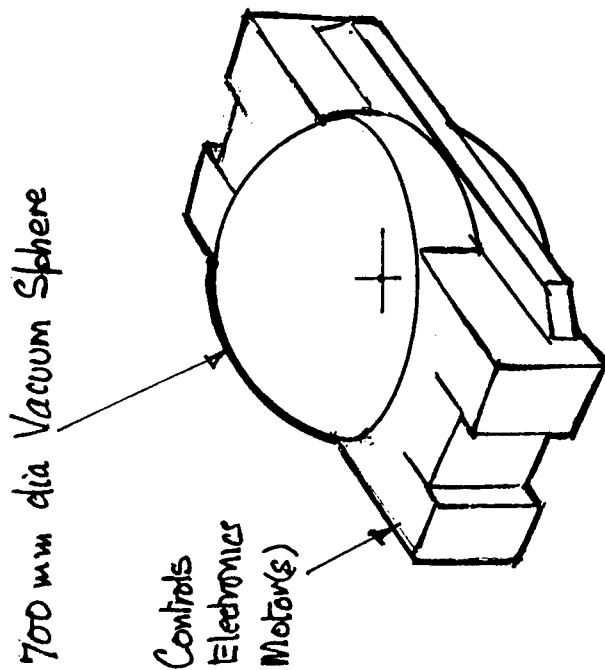
Multiple Reverse Penetration It was not intended that a large part of this contract effort should be spent on this risk, but based on work already done there are three points to make. Firstly, from the fratricide subsection above, if a Cain rotor ruptures, one fragment in thirty six hits an Abel unit, and the other thirty five -- give or take -- hit the main wall. Perhaps these rotor fragments will be dispersed, spreading the rim energy over a wide area, and the main module wall may withstand them. But until this is better understood there appears to be some significant risk of multiple cabin holes. Secondly, the absence of racks, clothing the main walls, makes reverse penetration more likely; including that due to primary, incoming, penetration of the module that does not involve interaction with the Gyrodynes. Thirdly, the hypoxia danger to crew throughout the station is: continuous if the hatch to this module is routinely kept open, and: presumeably, of very short duration if the hatch is closed when the module is not occupied.

B IV-3 Gyrodyne Module Fault Tree.

The Fault Tree for this module uses the sign and numeric conventions previously described, look back to Figure B-10. The Tree itself, Figure B-20, has two dividing points labeled A and B, both of which are 'Ands' not 'Ors', so the absolute population of all the branches increases above the nominal 1000 level as we move from left to right. As on the previous Trees, Node #0 takes it as a given that the Gyrodyne module has been penetrated-- the risk of this was estimated, in late '94, as .XXXXX for the ten years following AC. Immediately following this, the 'And' division point A sets up the two main branches.

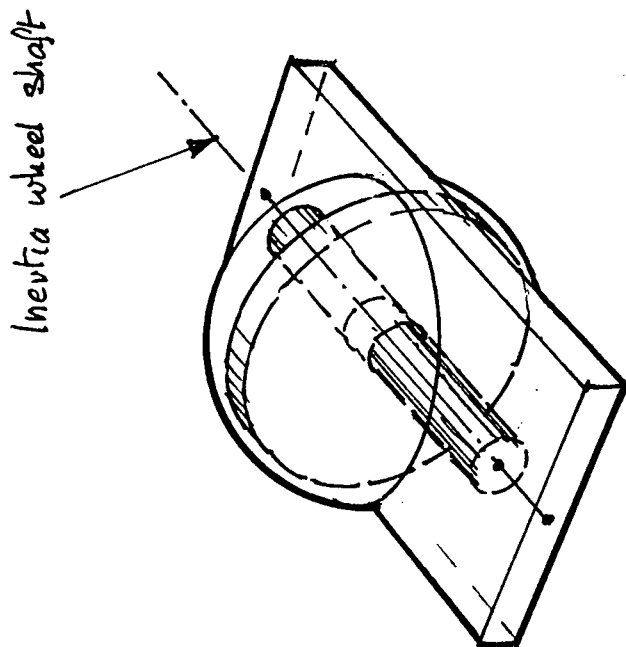
The logic for choosing the 'yes' probability for each Node after #0 is as follows. For Node #1 it is a simple place holder; to refine it would require study of the module penetration internal debris state, the absence of wall racks and, the effects of air drag. For Node #2 it comes from the previous Aperture paragraphs and Table B-4. For Node #3 it is a place holder chosen for conservatism. For Node #4 it comes from the previous Fratricide paragraphs and Figure B-18. For Node #5, the 'yes' probability is again a place holder. Superficially it reads like that for #1, but we have quadrupled the value because, though the rim fragments are slow, they are massive and not in the least softened by fracture heating.

Summarising, the stored energy in the rotor rims, perhaps amplified by fratricide, is potentially a powerful damage agent. The high 'r' values, at about .7 and .5, are also due in part to the fact that debris moving within the module has multiple targets. Of the three place holder 'yes' probabilities used in this tree, the conservative .9 assigned to Node #3 is the most in need of review by people with experience of flywheel rim rupture. In any case, the hatch open or closed protocol is an issue for all the crew on the station, where ever they may be.



Apparent Outer Shape

- few details
- few dimensions
- mounting cantilevered from module wall?



Geometric 'Icon' used

- Shaft alignment assumed
- Controls, electronics, motor(s) not delineated
- mounting not treated

FIGURE B-14 GYRODYNE UNIT ARRANGEMENT & ASSUMPTIONS

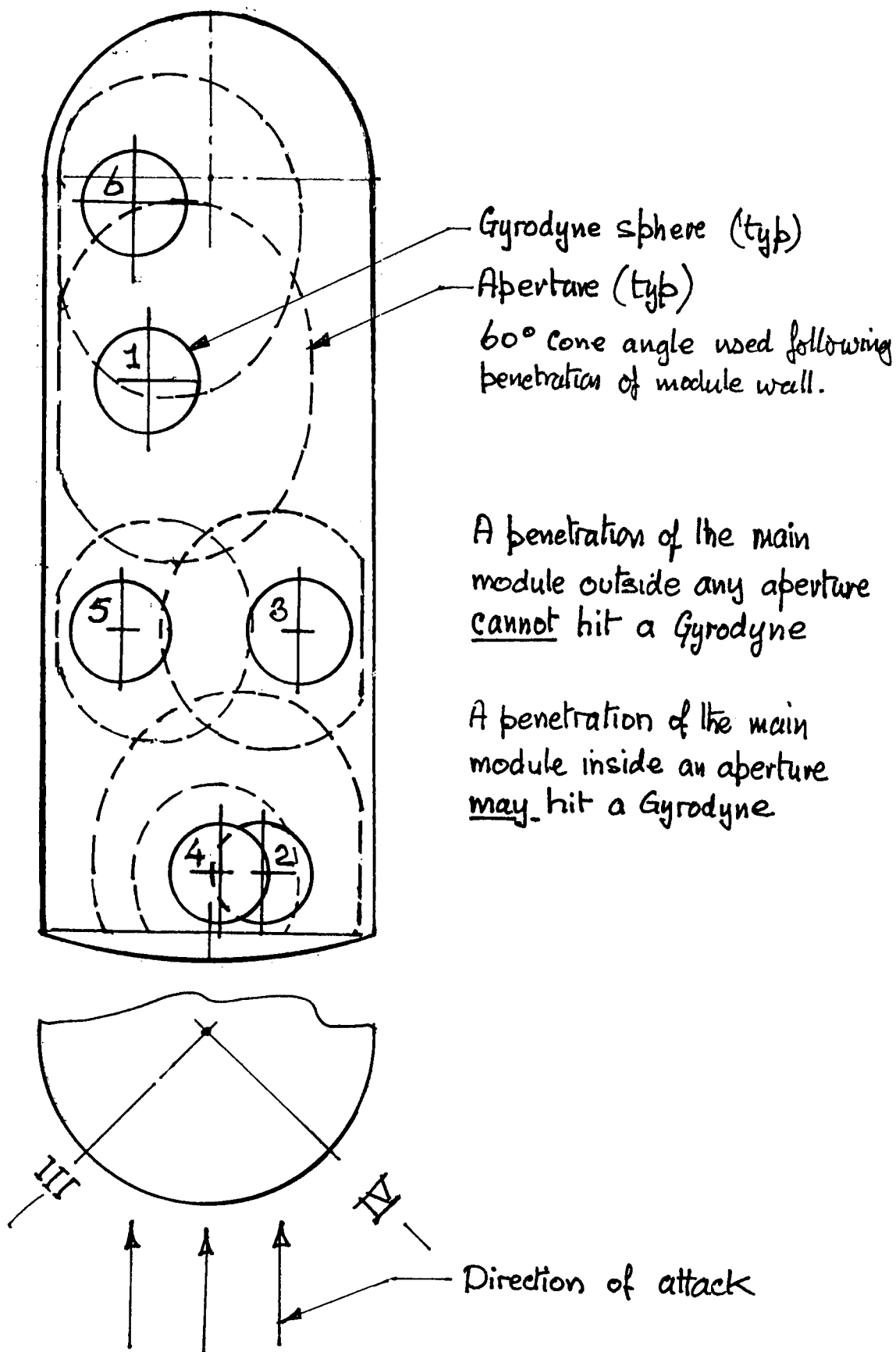


FIGURE B-15

APERTURES

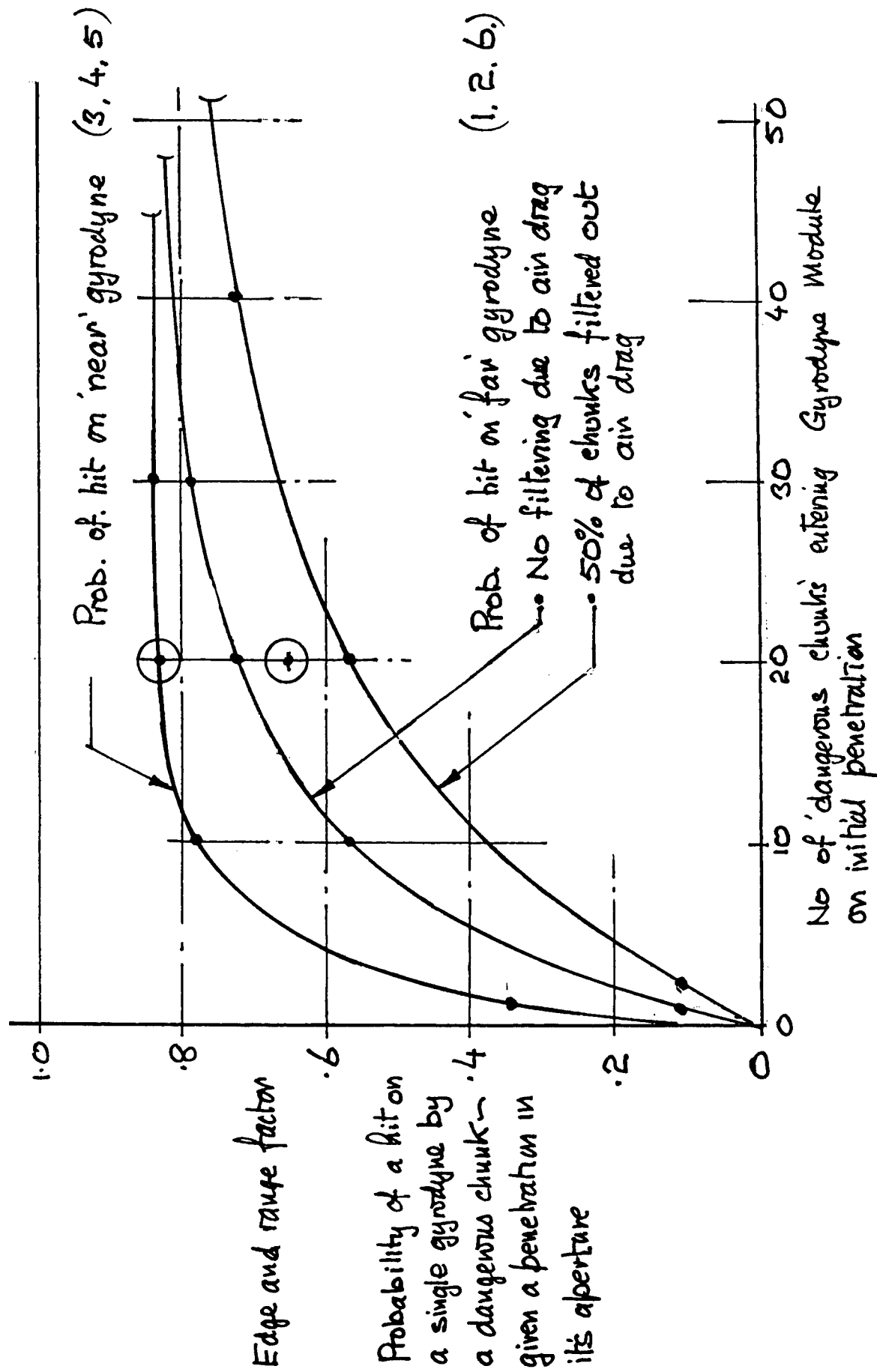


FIGURE B-16 PROBABILITY OF A GYRODYNE HIT FOLLOWING PENETRATION OF THE MODULE IN ITS APERTURE

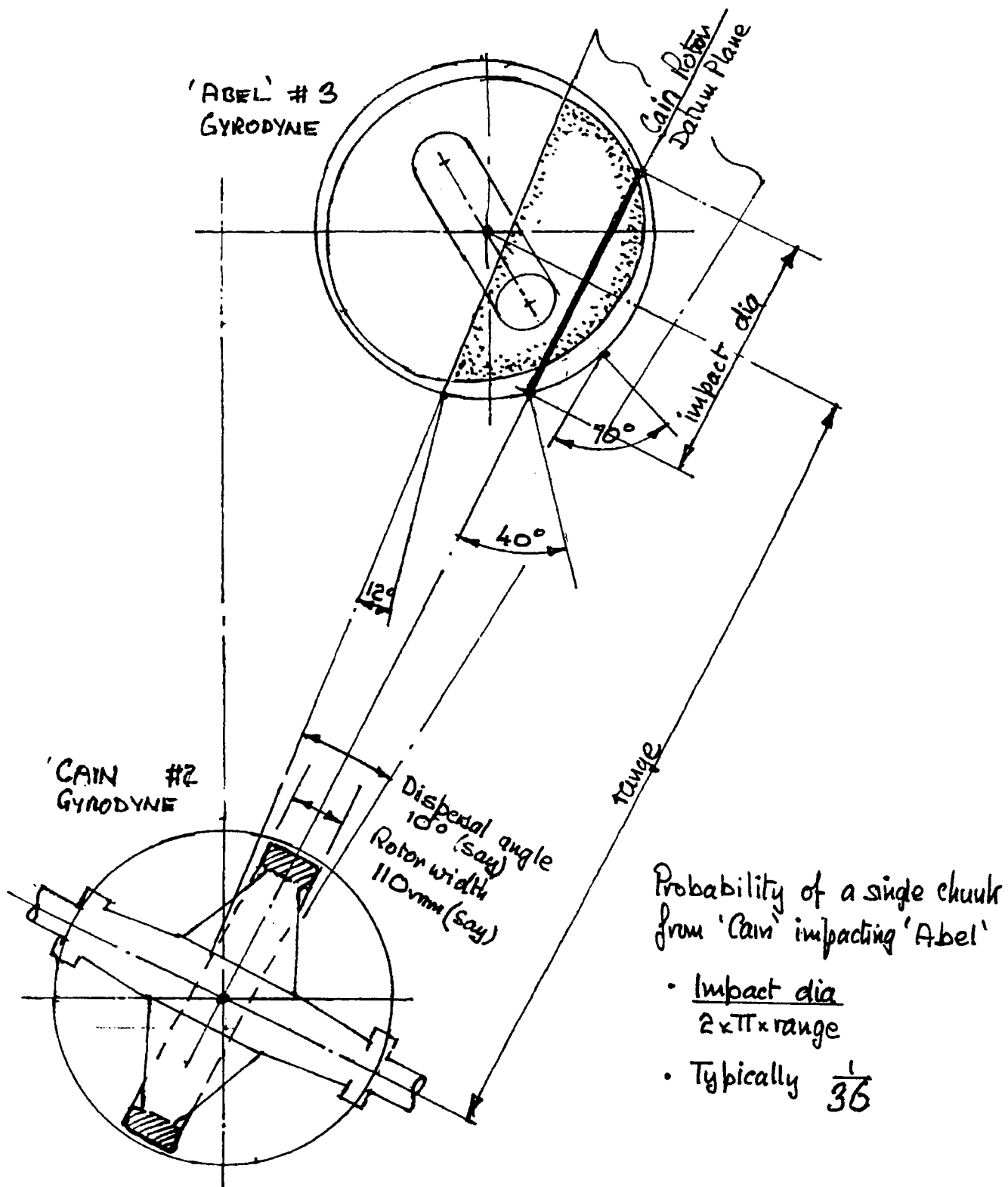


FIGURE B-17 TYPICAL FRATRICIDE GEOMETRY
CAIN-TO-ABEL

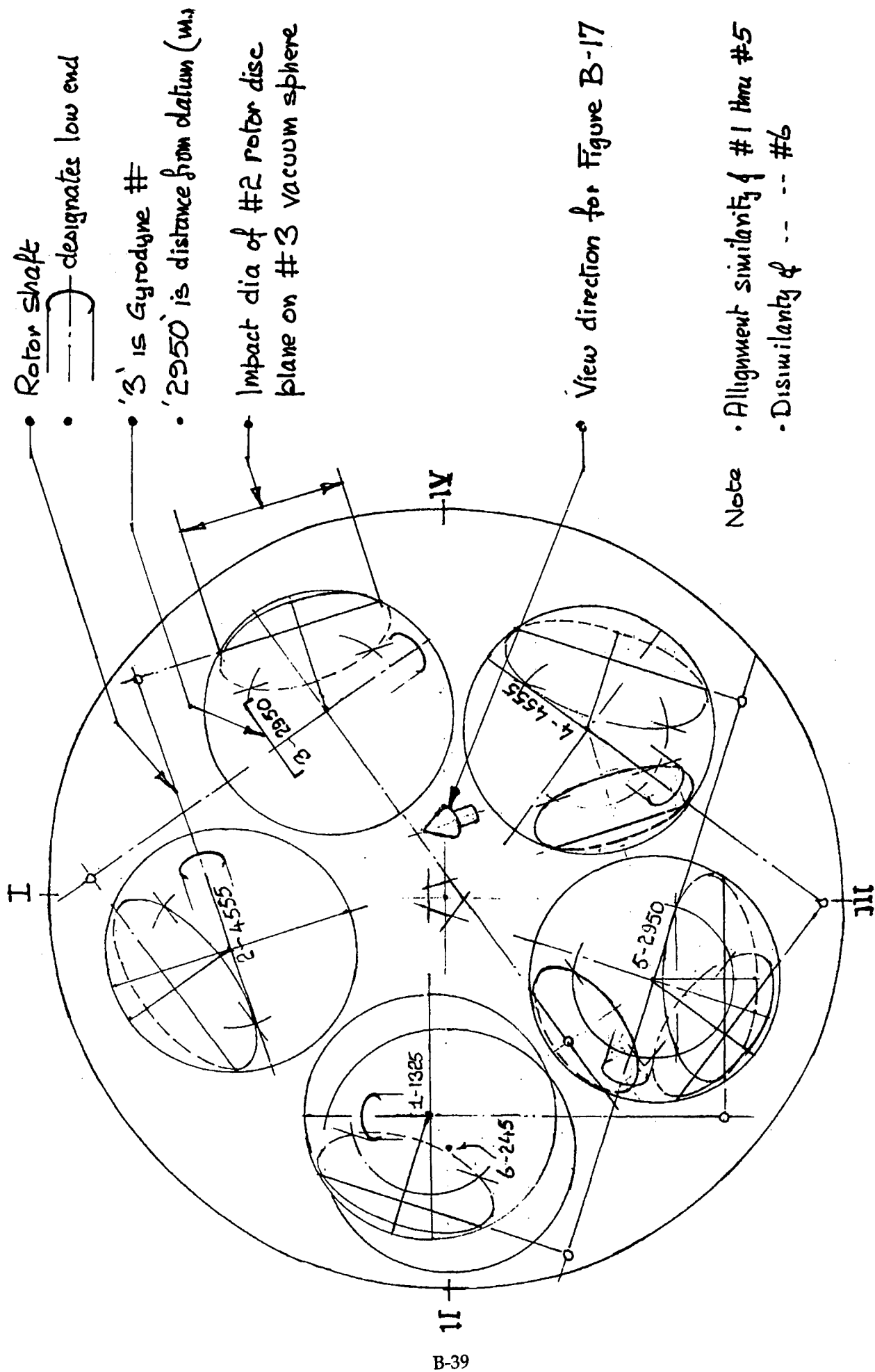


FIGURE B-18 MODULE END VIEW SHOWING GYRODYNE UNIT GEOMETRY

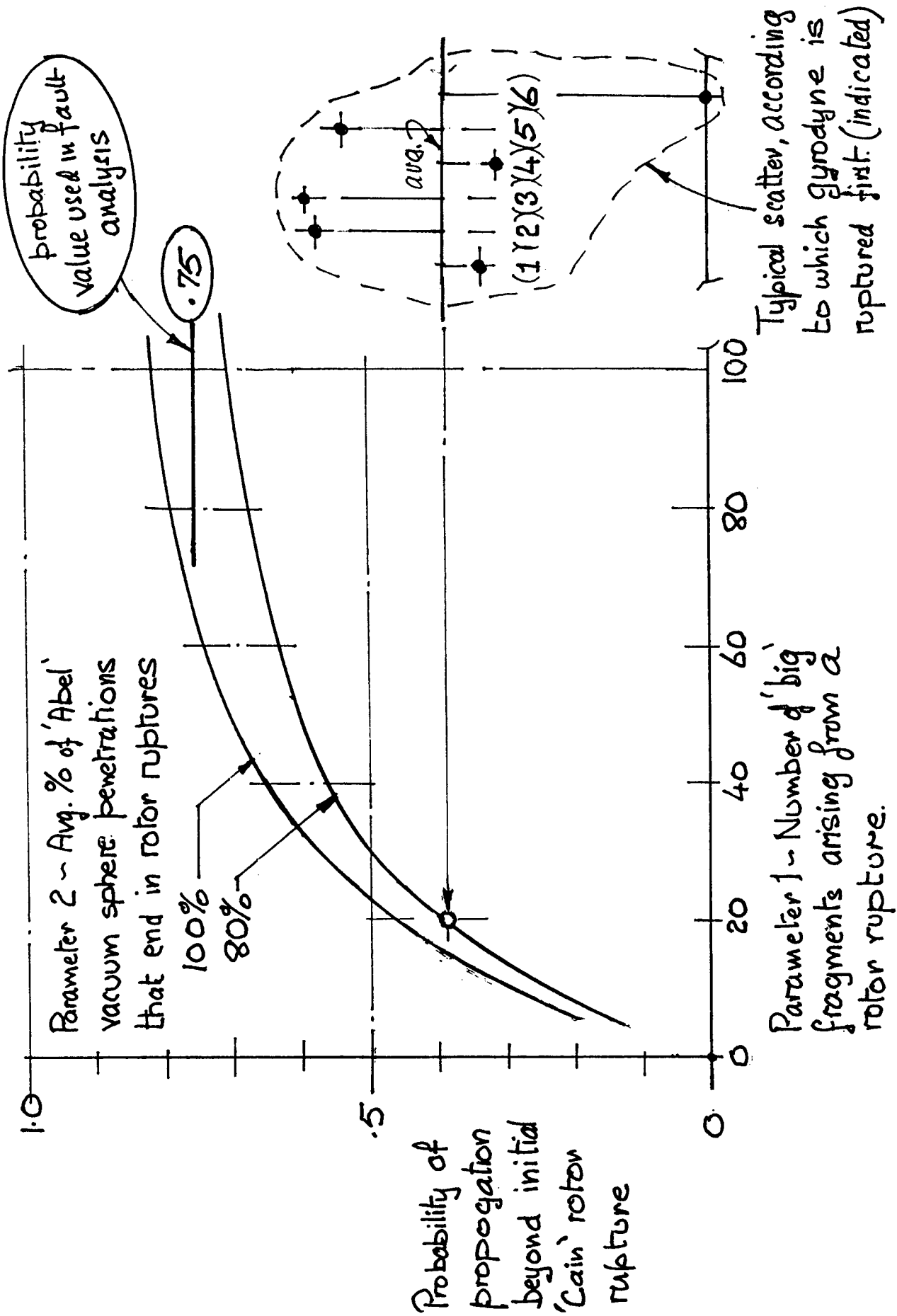


FIGURE B-19. PROBABILITY OF PROPAGATION OF ROTOR RUPTURE

Gyrodyne #	Raw Aperture Area (m ²)	near or far.	edge and range factor	Adjusted Aperture (m ²)	Probability of Gyrodyne Hit
1	3.22	far	.65	2.09	.16
2	2.58	far	.65	1.68	.13
3	2.09	near	.82	1.71	.13
4	1.06	near	.82	.87	.67
5	1.67	near	.82	1.37	.10
6	2.85	far	.65	1.85	.14
					.73

Overall hit probability

TABLE B-4 PROBABILITY OF A GYRODYNE HIT FOLLOWING PENETRATION ANYWHERE ON MAIN MODULE

CAIN ROLE	ABEL ROLE					
	1	2	3	4	5	6
1	—	—	—	—	.0264	—
2	—	—	.0240	.0338	—	—
3	—	.0272	—	—	.0338	—
4	—	—	—	—	.0240	—
5	.0230	—	—	.0272	—	—
6	—	—	—	—	—	—

Risk of ABEL being hit by a single fragment on a random vector from CAIN (typical)

TABLE B-5 FEASIBLE 'CAIN'/'ABEL' PAIRS & THEIR SINGLE FRAGMENT RISKS

B V Findings and Recommendations

We deal with each risk separately, focussing the discussion on the appropriate fault tree.

UDMH detonation (Figure B-11) The Geometric Nodes (#1 and #2) indicate that only just over 10% of the propellant tank bumper Ballistic Limit hits 'reach' the UDMH. This low % age. is due to shadowing, and the fact that, on a time average, UDMH occupies only half the tank length, and that only 8 out the 16 tanks store UDMH. The Danger Node (#6) carries the pessimistic 'detonation yes' probability of 0.41, with a resultant 'r' value of 0.047. This would fall to 0.015 if the optimistic 'detonation yes' probability were used. We recommend that:

- 1) Interest in, and encouragement of, UDMH detonation tests be maintained.
(Are there any relevant Russian tests ?).
- 2) Details of the bellows in the FGB propellant tanks be obtained. (The definition of these is a little thin).
- 3) Thought should be given to to carrying the UDMH always in the inboard tanks. (To exploit shadowing).

Propellant Tank GN2 Venting (Figure B-11) The Geometric Nodes (#3 and #4, with an assist from \$6) result in about 60% of the Ballistic Limit hits on the propellant zone bumper penetrating the GN2 volume of the propellant tanks. The Danger Node (#7) carries a 'yes ' probability of overloading the SARJ fittings of 0.48, hence an overall 'r' value of 0.298. The three main uncertainties in this 'overloading yes' probability , where we recommend further work are:

- 1) That the true tension or compression load on an individual SARJ fitting after which its repair becomes 'Program Scale' expensive, be determined .
- 2) That a deeper attempt be made to estimate initial crack lengths and their resulting unzipped effective hole area.
- 3) That the effect of a range of GN2 pressures be determined.

High Pressure GN2 Venting (Figure B-12) Compared with the previous risk, the Geometric Node (#1) and the Damage Node (#2) both have different 'yes' probabilities and the resultant 'r' value at 0.078 is considerably less; chiefly due to the bottles being better shadowed. Item 1) above would also probably serve to reduce our estimate of this risk, and we recommend:

- 2) and 3) from above, be repeated with the High Pressure Bottle wall and pressure range.
- 4) That the bumper shielding of the High Pressure bottles be more clearly defined.

Overpowering Controls (Figures B-11 and B-12) As previously discussed, this risk was not central to our study, nor do we believe that it would prove catastrophic. Nevertheless, we recommend:

- 1) That venting scenarios, with forces large enough to overcome RCS authority, be run against the control algorithms, and the conditions pertaining when control re-asserts itself, should be estimated. If these (crew vertigo, star tracker, field of view, etc) are not within limits, further planning, and down-stream training, might be indicated.
- 2) Depending on the outcome of recommendation 1) above a review should be made of conditions when the station is lighter and smaller and has lower inertia.

Gyrodyne Unit Fratricide (Figure B-20) The Geometric Node (#2) and the Danger Nodes (#3 and #4) all have fairly high 'yes' probabilities; The resulting 'r' value at 0.493 is high, and we make the following recommendations

- 1) That the Node #3 'rotor-ruptured-yes' value, which is just a conservative place-holder, be investigated in greater depth.
- 2) That control experts define in general terms what the loss, at one time, of two or more Gyrodynes would mean to the station in a programmatic sense.

Multiple Reverse Penetrations of Gyrodyne Module (Figure B-20) For this risk there is only one Geometric Node (#2) and it carries a high, calculated 'hit-and-penetration-yes' probability of 0.73. The other three, (#1, #3, #5), are all Danger Nodes, and all are place-holders, two of them with high 'yes' guesses. The resulting 'r' value of 0.726 is too high for comfort. We recommend therefore that:

- 1) Taking account of this risk, the hatch open-or-closed protocol be defined,

If the hatch is in danger of being open for more than a small % age. of the time, or the hatch protocol cannot be determined, then the folowing further recommendations are made:

- 2) The number, weight range, velocity range, and temperature range, of the initial main wall debris be studied, together with the presence of module air and the absence of module racks, to provide an analytic 'yes' probability for Node #1.
- 3) That the same should be done for Node #5, exepting that the fragments shall be those of a Gyrodyne rotor rim, not those of the module main wall; and the absence of racks will not enter into Node #5.
- 4) We assume that item 1) under Gyrodyne Unit Fratricide above will also be done.

Figure B-21 summarizes the study findings on one page. It gives prominence to the major areas of uncertainty.

ITEM/FAILURE MECHN.	MAJOR INFLUENCES/UNCERTAINTIES	'Y' VALUE
<u>FIG. B.</u> • UDMH Detonation	<ul style="list-style-type: none"> • Shadowed • Tanks half full • Only half the tanks contain UDMH • Big spread of detonation thresholds 	.047/.015
• Gaseous N ₂ Venting from Propellant Tank	<ul style="list-style-type: none"> • Unzipping driven • SARJ fitting strength • Static load analysis 	.48
• Gaseous N ₂ Venting from High Press. Bottle.	<ul style="list-style-type: none"> • Bumper geometry • Thick titanium tank • Unzipping driven • SARJ fitting strength • Static load analysis 	.08
<u>GYRODYNES</u> • Unit-to-Unit Fabricide	<ul style="list-style-type: none"> • Failure of two units assumed dangerous • Unit-to-unit geometry may have been improved • Several place-holders in fault tree 	.49
• Multiple Reverse Penetration of Module	<ul style="list-style-type: none"> • No racks on walls • Air in module • Hatch open/closed protocol 	.73

FIGURE B-21 STUDY FINDINGS SUMMARY.

BVI REFERENCES

1. FGB Tug Propulsion System Description. NASA / JSC / EP4 - J. Sanders.
January 17, 1995.
2. Investigation of Catastrophic Fracturing and Chemical Reactivity of Liquid-Filled Tanks when Impacted by Projectiles of High Velocity. NASA ? LeRCS - F.S. Stepka, R.P. Dengler, and C.R. Morse.
Preprint prepared for Hypervelocity Impact Symposium, Tampa, Florida.
November 17-19, 1964.
3. Fuel Tank Explosion Lethality. Wright Laboratory, Armament Directorate, WL/MN-TR-91-58, SAIC. - C.W. Wilson, D. Warne, and M.D. Chatfield.
January, 1992.
4. Ballistic Limit Equations for SSF Shielding Enhancement Plan. NASA / JSC / SN3. Eric Christiansen, SN3-92-175.
October 13, 1992.
5. FATEPEN2 - NAVSWC-TR-91-399. - J.D. Yatteau, R.H. Zernow, and R.F. Recht.
January, 1991.
6. Multiplate Damage Study - Air Force Armament Laboratory, AFATL-TR-67-116. The Boeing Company - G.T. Burch.
September, 1967.

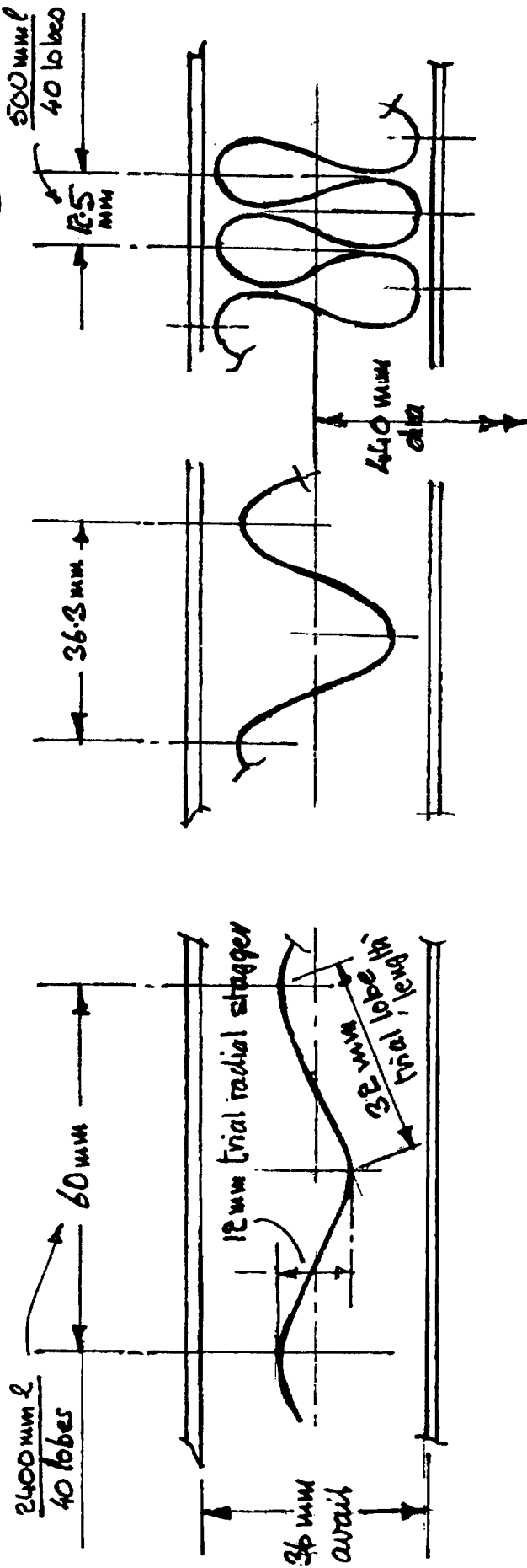
APPENDIX B I FGB MODULE PROPELLANT TANKS

To be read in conjunction with Figures B1-2-3-4
and Table B1 of the main report

- BI-1 FGB Bellows - sanity check
- BI-2 FGB assumed propellant tank wall features
- BI-3 Probability of BL 2 (or greater) hit penetrating to GN₂ or GN₂ plus propellant as a function of fore-and-aft location of strike
- BI-4 Probability of BL 2 (or greater) hit penetrating outboard or inboard tanks as a function of strike height
Aft tanks
- BI-5 FGB bumper-to-wall gap - aft, long tanks
- BI-6 " " " " " - fwd, short tanks
- BI-7 Thoughts on GN₂ pressure and velocity at a propellant tank penetration.

FGB Bellows Sashy Check ~ likely S.S. thickness

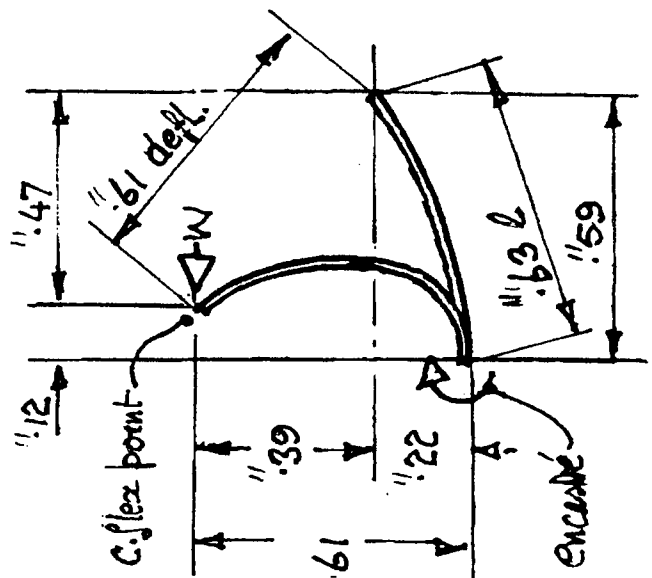
BT-1



Consider unit (1'0) tangential width of bellows ~ sketch at left
Remember that though deflection/shear level are treated as 'one way' at best, both can be halved by starting from a mid way neutral.

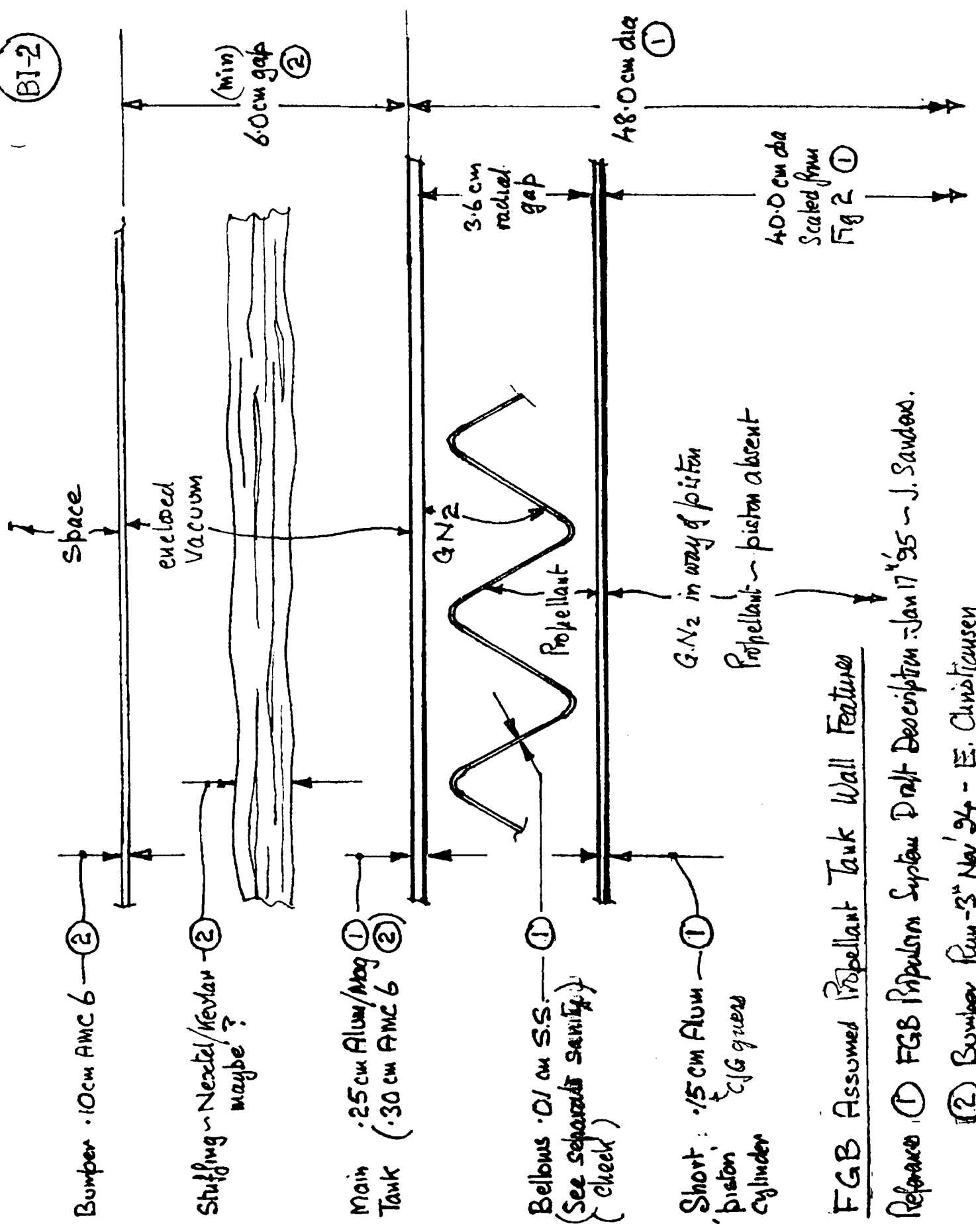
$$\text{defl} = \frac{wL^3}{3EI} \rightarrow w = \frac{\text{defl} \cdot 3EI}{L^3} = \frac{.61 \times 3 \times 10^6 \times \frac{L^3}{12}}{L^3} = 17.1 \times 10^6 \frac{L^3}{L^3}$$

$$fb_{max} = w_{coeff} \times \frac{b}{E^2} = 17.1 \times 10^6 \frac{L^3}{E^2} \times .61 \times \frac{L}{E^2} = 62.5 \times 10^6 \frac{L^3}{E^2}$$



let L (ins)	.020	.010	.008	.006	.004	.002
w (lb/inch)	136.8	17.1	8.76	3.69	1.09	.137
fb (ksi)	1250	625	500	375	250	125
bellows axial (lb)	7500	330	477	200	59	7.5
						feasible

BI-2

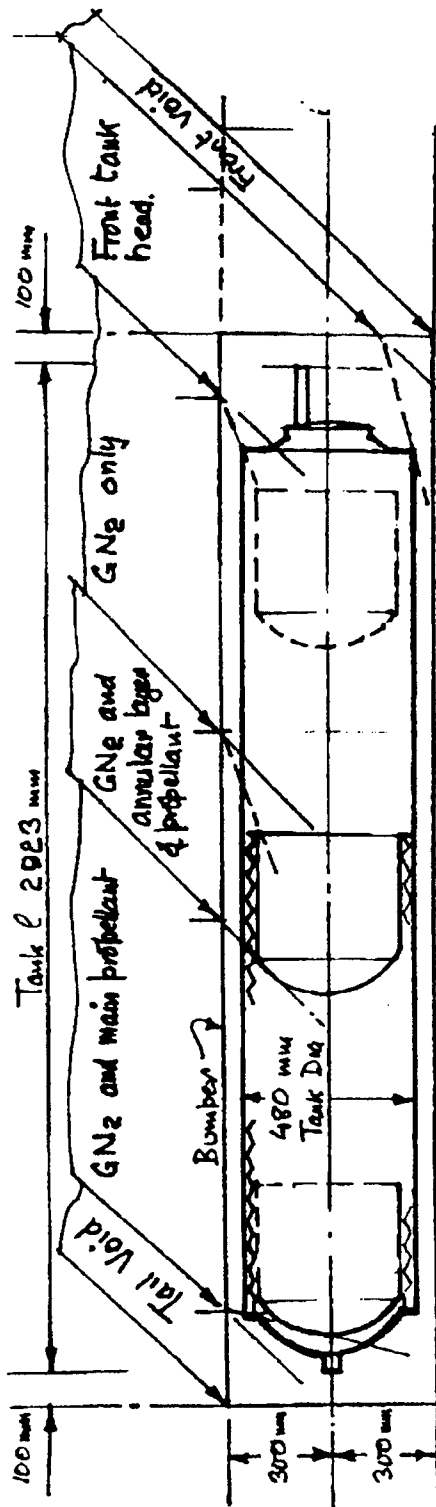


FGB Assumed Propellant Tank Wall Features

Reference 1 FGB Propulsion System Draft Description - Jan 17 '95 - J. Sanders.

2 Bumper Rev-3" Nov '94 - E. Christensen

Probability of a B.L. (or greater) hit penetrating to GN₂ on to GN₂ plus Propellant as a function of fore and aft location of strike



- Short tank
- 50% propellant
- 30° half cone angle
- $\theta = 45^\circ$ wpt. D.O.F.

Length (mm)	280	1149	553	971	627	43	3723
Length normalized	.075	.309	.149	.261	.168	.038	1.000
'Reach' GN ₂ - probability	0	1.0	1.0	1.0	.6	0	.820
• norml. length x probability	0	.309	.149	.261	.101	0	.245
'Reach' GN ₂ + propellant - prob.	0	.6	.4	0	0	0	0
• norml. length x probability	0	.185	.060	0	0	0	0

Equival. long tank figures

Short tank as above

$$\begin{aligned}
 &= .245 \\
 &.820 - .245 = .575 \\
 &1.0 - .820 = .180
 \end{aligned}$$

- Probability of reaching GN₂ and Propellant
- " " " GN₂ only
- " " " no tank penetration.

AFTIC Probability of B.L. (or greater) hits penetrating Outbd/Inbd Tanks as a function of Strike Height

BI-4

ISSUE 2

Penetration Vulnerability vs. Strike Height
 ~all debris assumed to come from the flank

Outbd. tank Inbd. tank GN₂ bottles

56% 34% 13%

F.C.B.



Strike Height band for tank bumper shield

SCRAP SECTION LOOKING AFT ON STARBOARD SIDE

Note:-

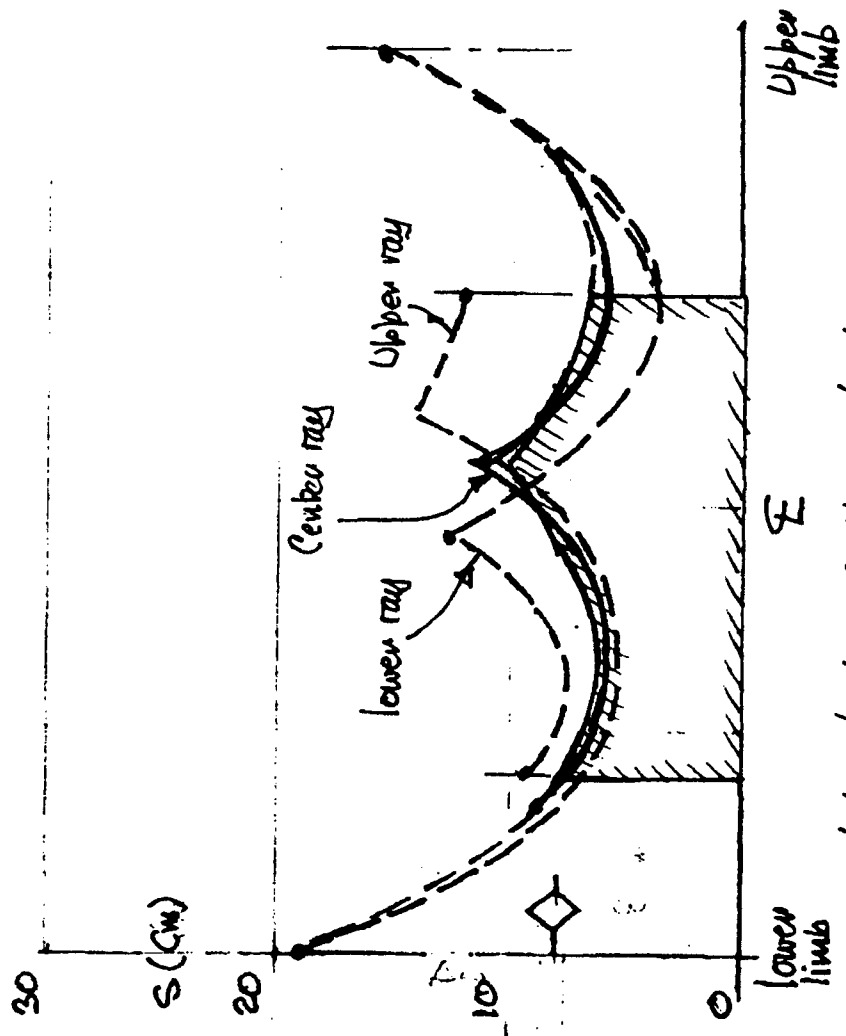
- Shadowing of inbd t. by outbd. t.
- Gap for Outbd tank = 80 mm avg
- " " Inbd " = 130 " "

Ref. FCB Layouts.

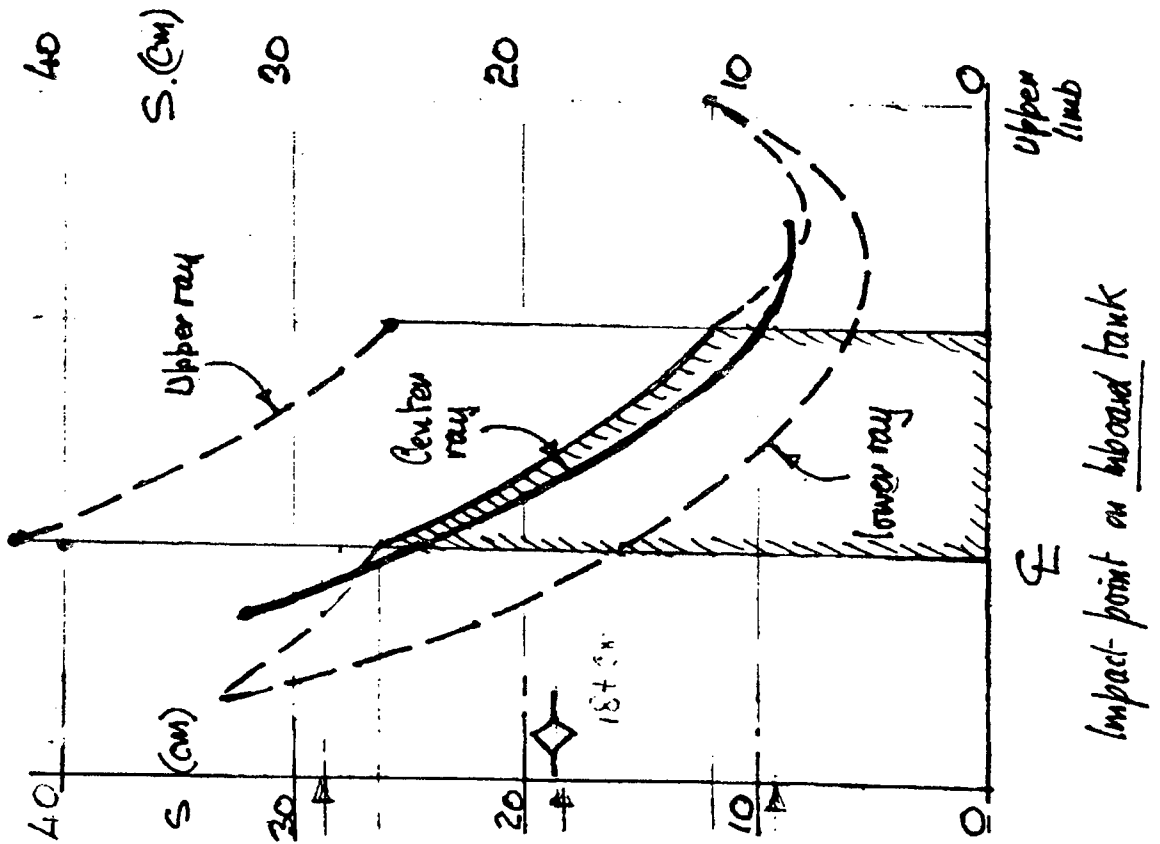
Fig.

FGB Bomber-b-wall gap (S)

Aft-long tanks
Inboard and outboard



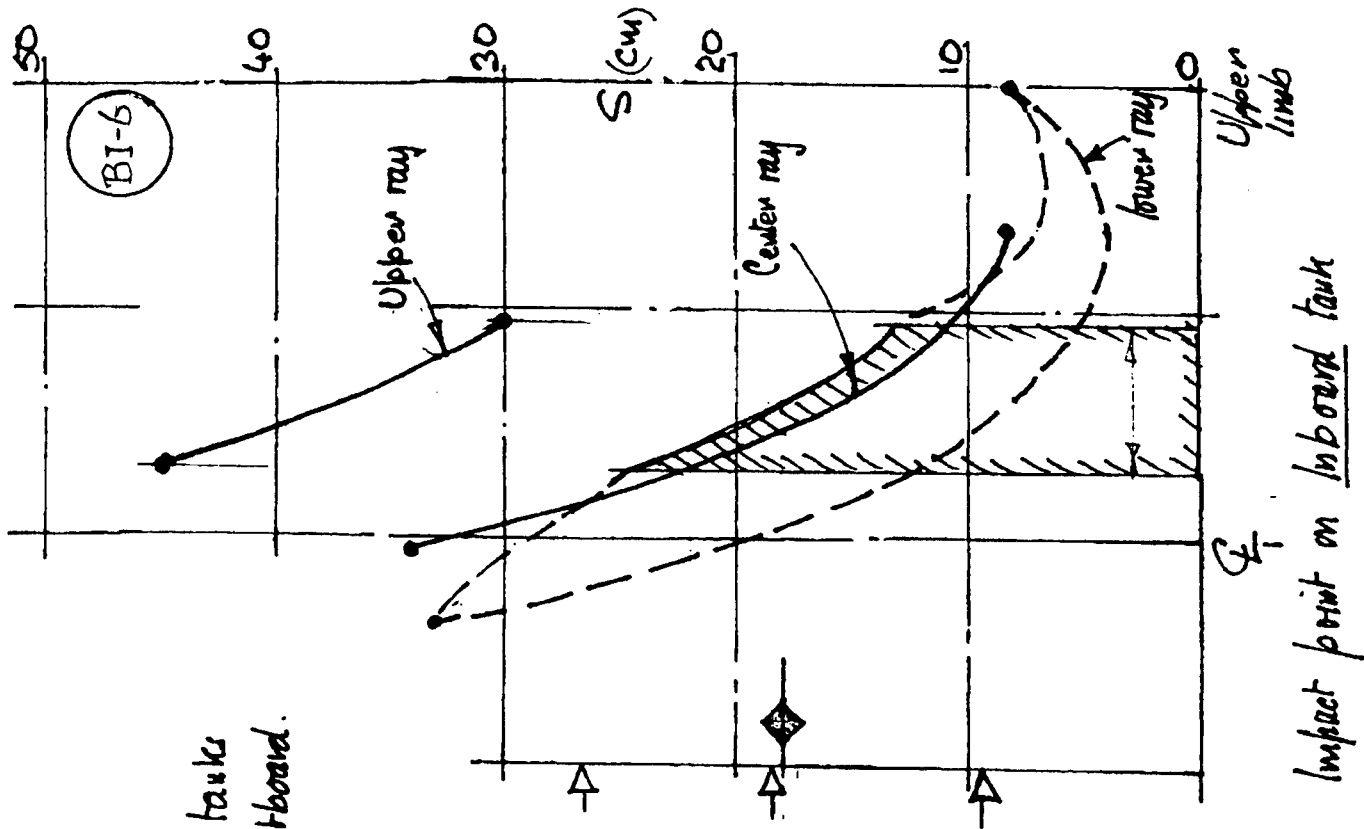
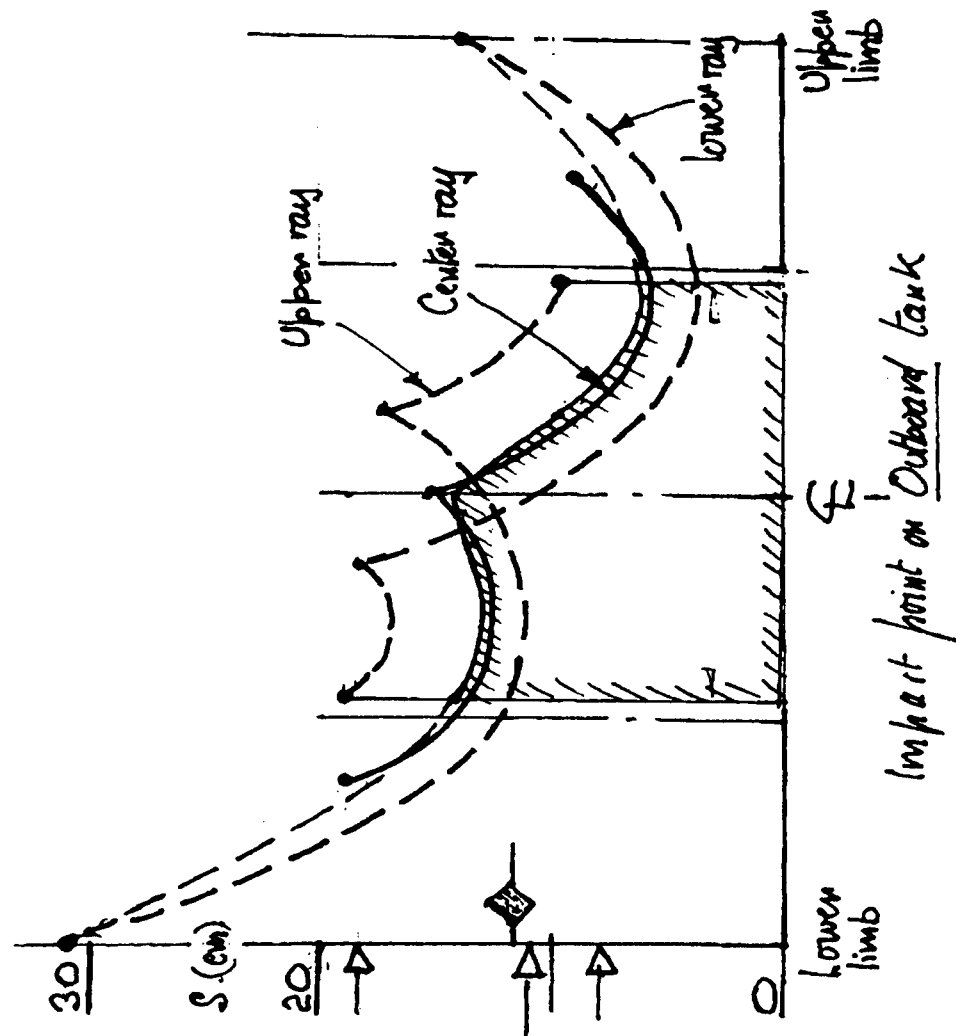
Impact point on Outboard tank

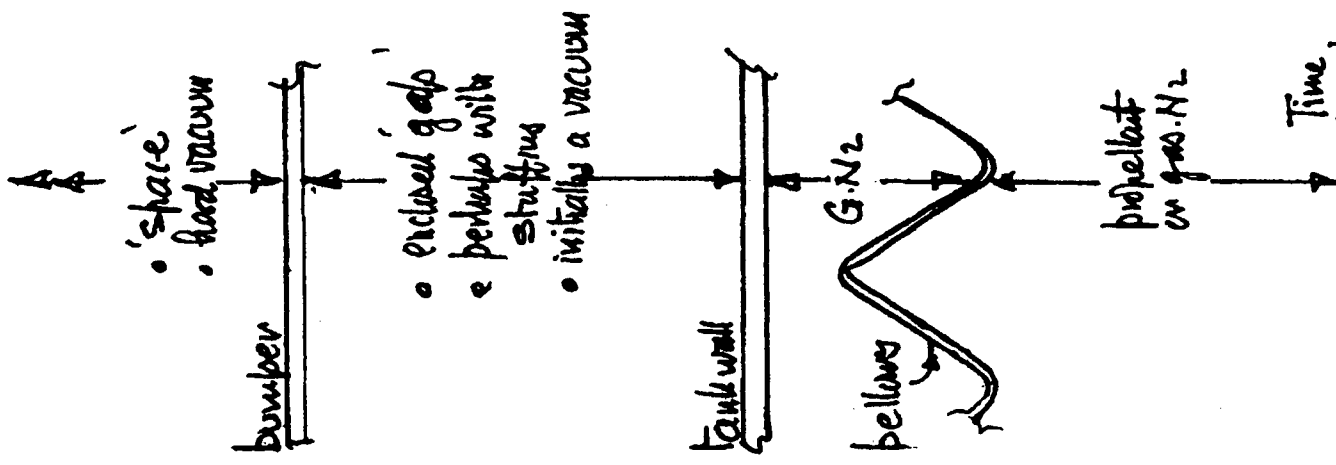


Impact point on inboard tank

Forward / short tanks
Inboard and Outboard.

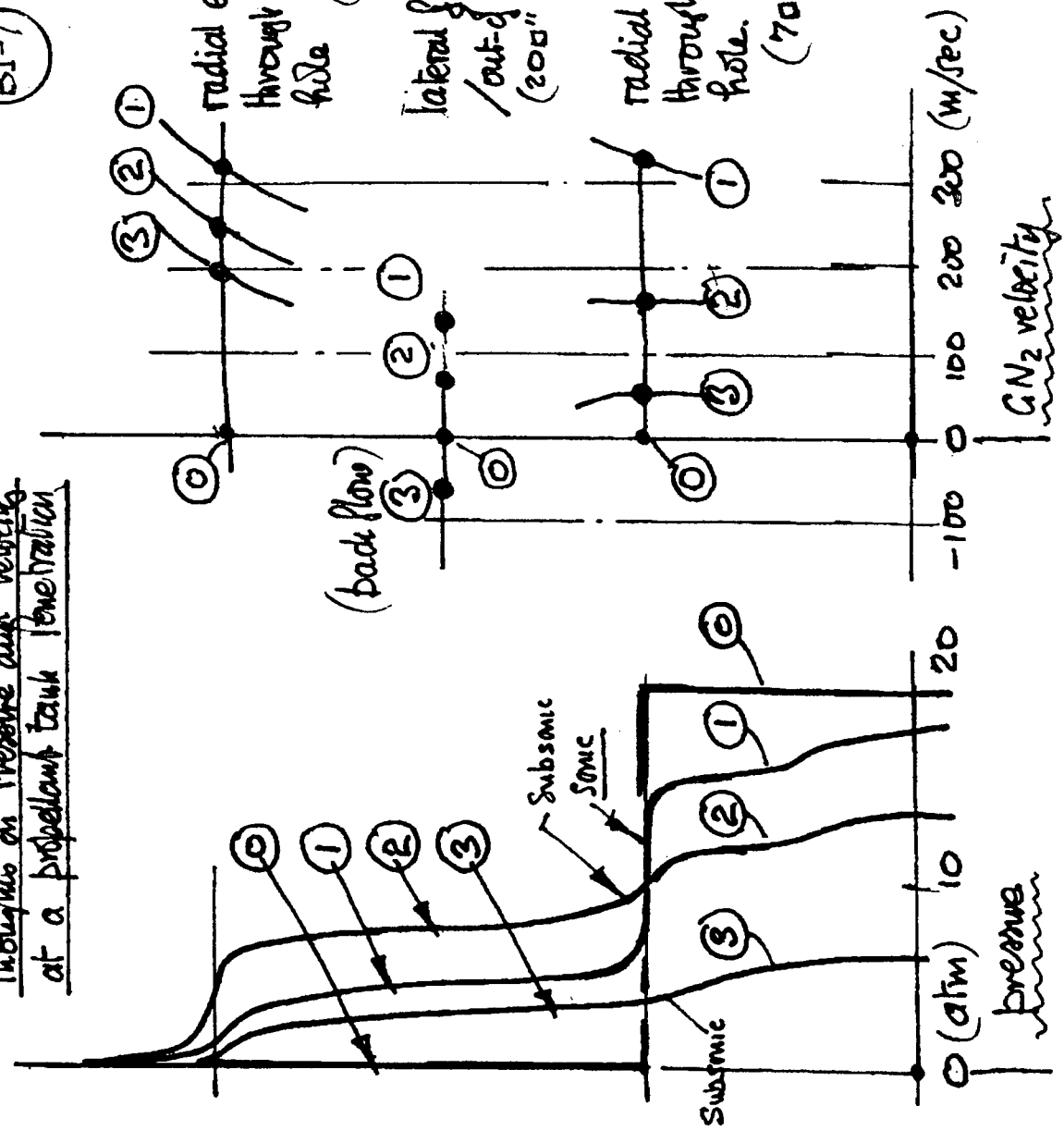
FGB Bumper-to-wall gap (S)





Thoughts on Pressure and Velocity at a propellant tank penetration

(BI-7)



- if propellant is present, what is its velocity?
 - leaks in bumper - exists or caused by rising pressure during tank penetration analysis.
- (1) before strike
 (2) later
 (3) later still
- (1) just after strike
 (2) later
 (3) later still

How 'Big' is the GN₂ supply?

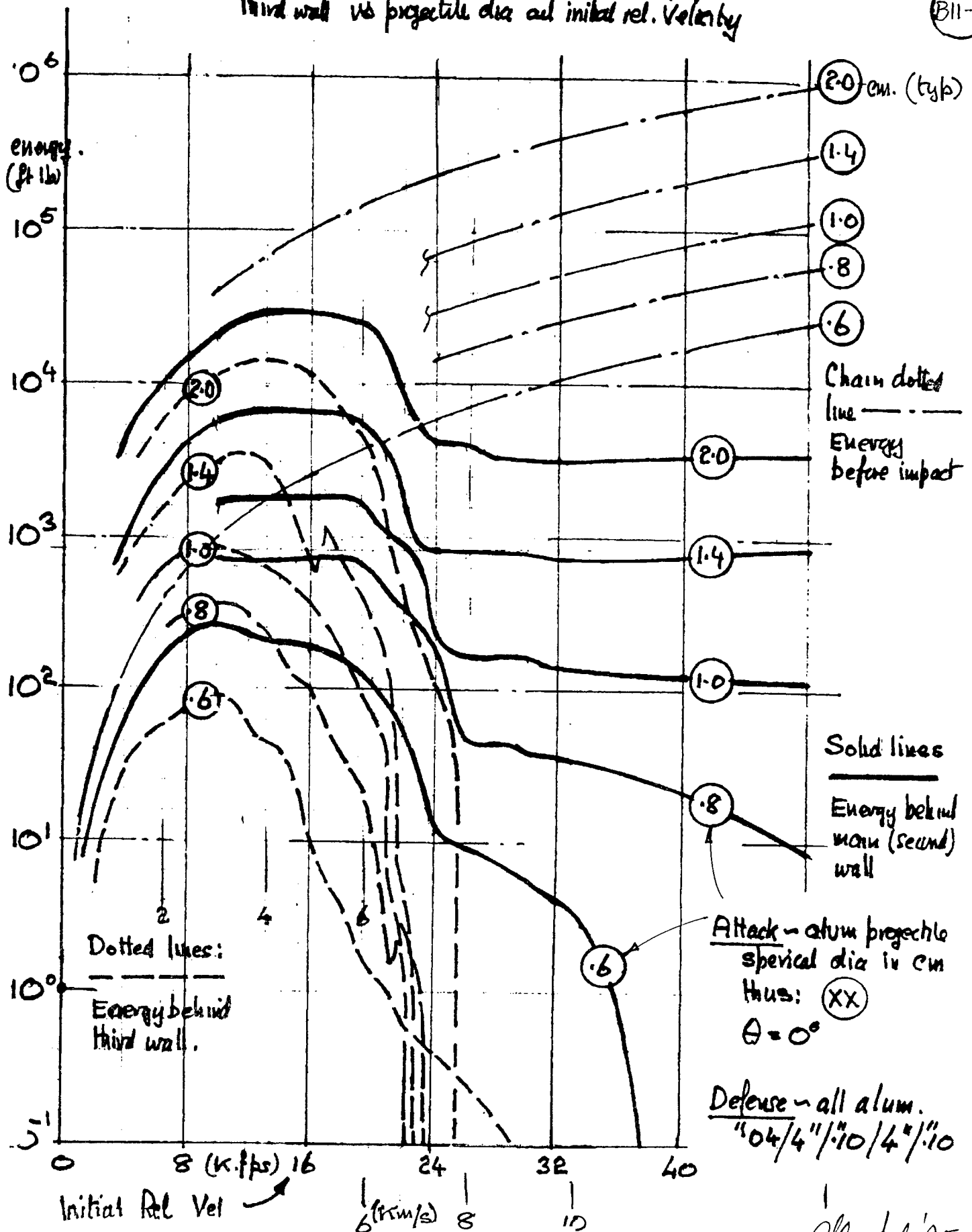
APPENDIX B II UDMH DETONATION THRESHOLD

to be read in conjunction with Figures B-5 and B-7
of the main report

- B II - 1 Fatepen 2 • Energy before impact
 • Energy after second wall
 • Energy after third wall
All plotted against projectile dia. and initial relative velocity
- B II - 2 Debris energy after second wall (reaching third wall - tank -)
plotted against projectile dia. and initial relative velocity - for
two damage prediction methods. Three detonation thresholds
considered - optimistic, midway, pessimistic
- B II - 3 Energy modelling of Wright lab optimistic detonation threshold
encounter
- B II - 4 Fatepen 2 run - sphere of correct weight (test #6583)
- B II - 5 " " - cylinder " " " (")
- B II - 6 " " - sphere " " " (test # 6584)

Fatepen 2 - Energy before impact, after second wall, after third wall vs projectile dia and initial rel. Velocity

B11-1

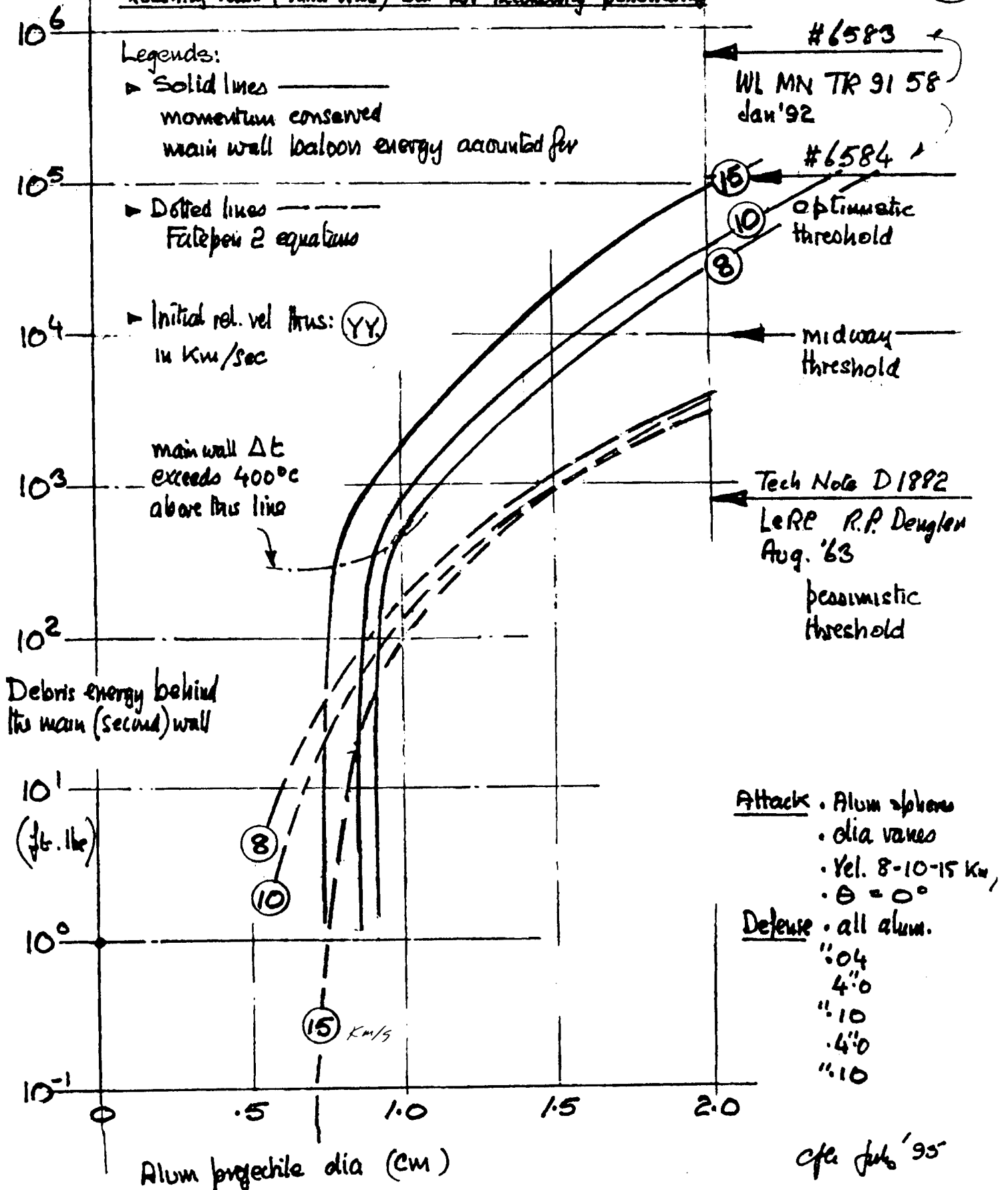


Q.E. Jul. '95

Debris energy behind main wall

Reaching tank (third wall) but not necessarily penetrating

RII-2

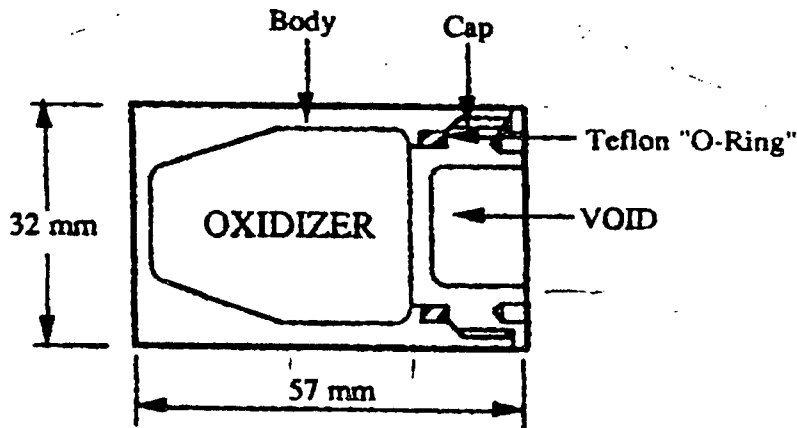


Falpen 2 Modelling of WL/UN-TR-91-58 Test Shots

BII-3

ATTACK

► Test Projectile



► Shape for Falpen 2 calcs

Item modelled Material → dim →	Whole Projectile (#6583)			Cap (#6584)
	Alum equiv vol.	Alum. equiv wt.	"Hexan" equiv vol & weight	Alum equiv wt.
Sphere dia (in)	1.75	1.59	1.75	.92
wt (gn)	1933	1457 .208	1457	290
Cylinder dia (in)	1.25	1.13	1.25	
l. (in)	2.25	2.04	2.25	
wt (gn)	1933	1457	1457	

► Initial Rel. Vel.

4.95 Km/sec ~ 16236 f/s

DEFENSE ~ all aluminum

- bumper 1.6mm .063
- gap 25.4mm 1.0

- main wall .025/.032

$$.20816 \times 16236^2 \text{ ft/s}^2 = 544,000 \text{ ft/s}^2$$

~ 1.1' g

PENETRATOR CHARACTERISTICS

Penetrator Material AL
Penetrator Alloy .000
Weight 1.457E+03 grains
Brinell Hardness 1.200E+02
Shape Sphere
Diameter 1.584E+00 in

6583

B11-4

 Sphere of Correct weight

ENCOUNTER CONDITIONS

Initial Yaw (Y or P) A
Yaw Angle 4.020E+01 deg
Presented Area 1.971E+00 in^2
User Impact Orientation N
Impact Velocity 16236 fps
Impact Momentum 1.050E+02 lb-sec
Impact Energy 8.520E+05 ft-lbs

PLATE ARRAY CHARACTERISTICS

N	Mlt	T	S	Theta	Rhot	Et	Bhnt	Sigmat	Kt	Ut
		in	in	deg	lb/in^3	psi		psi	psi	fps
1	AL	.0630	.00	.000	.100	1.00E+07	120.	6.00E+04	1.0E+07	1.6E+04
2	AL	.0285	1.00	.000	.100	1.00E+07	120.	6.00E+04	1.0E+07	1.6E+04

DAMAGE TO PLATE 1

vtf1=1.85E+00 in Dtf2=0.00E+00 in Dtf3=0.00E+00 in Dtt =0.00E+00 in
zh =1.85E+00 in Npf2=0.00E+00 Npf3=0.00E+00 Npt =0.00E+00
Mlt =1.19E+02 gn Dpf2=0.00E+00 in Dpf3=0.00E+00 in Dpt =0.00E+00 in
It =9.89E+00 lb-sec Dmf =1.85E+00 in Dmt =1.85E+00 in
DEBRIS BEHIND PLATE 1

Mf1 =8.36E+02 gn Df1 =1.15E+00 in
Nf2 =2.04E+00 Mf2 =1.90E+02 gn Df2 =7.01E-01 in Phif=2.80E+01deg
Nf3 =5.98E+00 Mf3 =3.01E+01 gn Df3 =3.80E-01 in Phif=2.80E+01deg
Nt =9.78E+02 Mt =7.73E-02 gn Dt =5.20E-02 in Phit=2.50E+01deg
V1 =1.54E+04 fps P =9.51E+01 lb-sec KE =6.97E+05 ft-lbs
82% of projectile KE

DAMAGE TO PLATE 2

Dtf1=1.47E+00 in Dtf2=8.98E-01 in Dtf3=4.94E-01 in Dtt =5.20E-02 in
Dh =2.92E+00 in Npf2=4.00E-06 Npf3=1.17E-05 Npt =0.00E+00
Mlt =1.33E+02 gn Dpf2=2.92E+00 in Dpf3=2.92E+00 in Dpt =2.78E+00 in
It =6.32E+00 lb-sec Dmf =2.92E+00 in Dmt =2.78E+00 in
DEBRIS BEHIND PLATE 2

Mf1 =8.30E+02 gn Df1 =1.38E+00 in
Nf2 =2.00E+00 Mf2 =1.85E+02 gn Df2 =6.96E-01 in Phif=2.80E+01deg
Nf3 =5.60E+00 Mf3 =2.69E+01 gn Df3 =3.66E-01 in Phif=2.80E+01deg
Nt =1.36E+03 Mt =4.17E-02 gn Dt =4.23E-02 in Phit=2.80E+01deg
l =1.51E+04 fps P =8.87E+01 lb-sec KE =6.39E+05 ft-lbs

BII-5

PENETRATOR CHARACTERISTICS

Penetrator Material AL
Penetrator Alloy .000
Weight 1.457E+03 grains
Brinell Hardness 1.200E+02
Shape Cylinder
Length 2.040E+00 in
Diameter 1.130E+00 in

#6583

Cylinder of correct weight

ENCOUNTER CONDITIONS

Initial Yaw (Y or P) A
Yaw Angle 2.812E+01 deg
Presented Area 1.971E+00 in^2
User Impact Orientation N
Impact Velocity 16236 fps
Impact Momentum 1.050E+02 lb-sec
Impact Energy 8.520E+05 ft-lbs

PLATE ARRAY CHARACTERISTICS

N	Mtlt	T	S	Theta	Rhot	Et	Bhnt	Sigmat	Kt	Ut
		in	in	deg	lb/in^3	psi		psi	psi	fps
1	AL	.0630	.00	.000	.100	1.00E+07	120.	6.00E+04	1.0E+07	1.6E+04
2	AL	.0285	1.00	.000	.100	1.00E+07	120.	6.00E+04	1.0E+07	1.6E+04

DAMAGE TO PLATE 1

Dtf1=1.69E+00 in Dtf2=0.00E+00 in Dtf3=0.00E+00 in Dtt =0.00E+00 in
Dh =1.69E+00 in Npf2=0.00E+00 Npf3=0.00E+00 Npt =0.00E+00
Mlt =9.92E+01 gn Dpf2=0.00E+00 in Dpf3=0.00E+00 in Dpt =0.00E+00 in
It =1.27E+01 lb-sec Dmf =1.69E+00 in Dmt =1.69E+00 in
DEBRIS BEHIND PLATE 1

Nf2 =4.54E+02 Mf1 =7.02E+02 gn Df1 =1.08E+00 in
Nf3 =1.13E+03 Mf2 =1.06E+00 gn Df2 =1.25E-01 in Phif=3.20E+01deg
Nt =5.64E+02 Mf3 =2.00E-01 gn Df3 =7.13E-02 in Phif=3.20E+01deg
V1 =1.57E+04 fps Mt =7.73E-02 gn Dt =5.20E-02 in Phit=2.50E+01deg
P =9.23E+01 lb-sec KE =6.76E+05 ft-lbs
79.3% of projectile KE

DAMAGE TO PLATE 2

Dtf1=1.38E+00 in Dtf2=1.72E-01 in Dtf3=1.05E-01 in Dtt =5.20E-02 in
Dh =2.94E+00 in Npf2=0.00E+00 Npf3=0.00E+00 Npt =0.00E+00
Mlt =1.36E+02 gn Dpf2=2.94E+00 in Dpf3=2.94E+00 in Dpt =2.62E+00 in
It =2.22E+01 lb-sec Dmf =2.94E+00 in Dmt =2.62E+00 in
DEBRIS BEHIND PLATE 2

Nf2 =3.50E+02 Mf1 =6.96E+02 gn Df1 =1.13E+00 in
f3 =6.20E+02 Mf2 =6.64E-01 gn Df2 =1.06E-01 in Phif=3.20E+01deg
t =3.84E+03 Mf3 =8.77E-02 gn Df3 =5.42E-02 in Phif=3.20E+01deg
V1 =1.55E+04 fps Mt =3.54E-02 gn Dt =4.01E-02 in Phit=3.20E+01deg
P =7.01E+01 lb-sec KE =5.11E+05 ft-lbs

PENETRATOR CHARACTERISTICS

Penetrator Material
Penetrator Alloy
Weight
Brinell Hardness
Shape
Diameter

AL
.000
2.900E+02 grains
1.200E+02
Sphere
9.249E-01 in

6584

BT-6

Sphere of correct weight

ENCOUNTER CONDITIONS

Initial Yaw (Y or P)

A

Yaw Angle

4.020E+01 deg

Presented Area

6.719E-01 in^2

User Impact Orientation

N

Impact Velocity

16236 fps

Impact Momentum

2.089E+01 lb-sec

Impact Energy

1.696E+05 ft-lbs

PLATE ARRAY CHARACTERISTICS

N	Mtlt	T	S	Theta	Rhot	Et	Bhnt	Sigmat	Kt	Ut
		in	in	deg	lb/in^3	psi		psi	psi	fps
1	AL	.0630	.00	.000	.100	1.00E+07	120.	6.00E+04	1.0E+07	1.6E+04
2	AL	.0285	1.00	.000	.100	1.00E+07	120.	6.00E+04	1.0E+07	1.6E+04

DAMAGE TO PLATE 1

tfl=1.13E+00 in Dtf2=0.00E+00 in Dtf3=0.00E+00 in Dtt =0.00E+00 in
 1 =1.13E+00 in Npf2=0.00E+00 Npf3=0.00E+00 Npt =0.00E+00
 Mlt =4.41E+01 gn Dpf2=0.00E+00 in Dpf3=0.00E+00 in Dpt =0.00E+00 in
 It =5.13E+00 lb-sec Dmf =1.13E+00 in Dmt =1.13E+00 in
 DEBRIS BEHIND PLATE 1

Nf2 =9.30E+00 Mf1 =4.97E+01 gn Df1 =4.49E-01 in Phif=3.08E+01deg
 Nf3 =2.39E+01 Mf2 =1.49E+01 gn Df2 =3.00E-01 in Phif=3.08E+01deg
 Nt =3.32E+02 Mf3 =2.69E+00 gn Df3 =1.70E-01 in Phit=2.50E+01deg
 V1 =1.47E+04 fps P =1.58E+01 lb-sec KE =1.03E+05 ft-lbs

60.7% of projectile

DAMAGE TO PLATE 2

Dtf1=5.81E-01 in Dtf2=3.93E-01 in Dtf3=2.29E-01 in Dtt =5.20E-02 in
 Dh =2.32E+00 in Npf2=3.82E-06 Npf3=9.85E-06 Npt =0.00E+00
 Mlt =8.42E+01 gn Dpf2=2.32E+00 in Dpf3=2.32E+00 in Dpt =2.06E+00 in
 It =3.98E+00 lb-sec Dmf =2.32E+00 in Dmt =2.06E+00 in
 DEBRIS BEHIND PLATE 2

Nf2 =9.47E+00 Mf1 =1.54E+01 gn Df1 =3.04E-01 in Phif=3.08E+01deg
 Nf3 =2.01E+01 Mf2 =1.50E+01 gn Df2 =3.01E-01 in Phif=3.08E+01deg
 Nt =5.95E+02 Mf3 =1.97E+00 gn Df3 =1.53E-01 in Phit=3.08E+01deg
 1 =1.43E+04 fps P =1.18E+01 lb-sec KE =7.23E+04 ft-lbs

APPENDIX B III ORIGNAL STATION PRIME STRUCTURE /SARJ

To be read in conjunction with table B 2 of the main report

- B III 1 IEA and Solar Arrays out beyond the SARJ.
- inertia and mass
- B III 2 Station complete
- inertia and mass
- B III 3 Limit moment capabilities of SARJ — (on orbit)
- average values for Torque and Overhang moments
- B III 4 Capabilities of SARJ. — Pictorial and dimensional
- B III 5 " " " — On-orbit limit loads.
- B III 6_A Maximum allowable FCB venting forces in various directions and with various offsets. — as governed by Station geometry and inertia, and SARJ limit capabilities
- B III 6_B Second half of B III 6A

BM-1

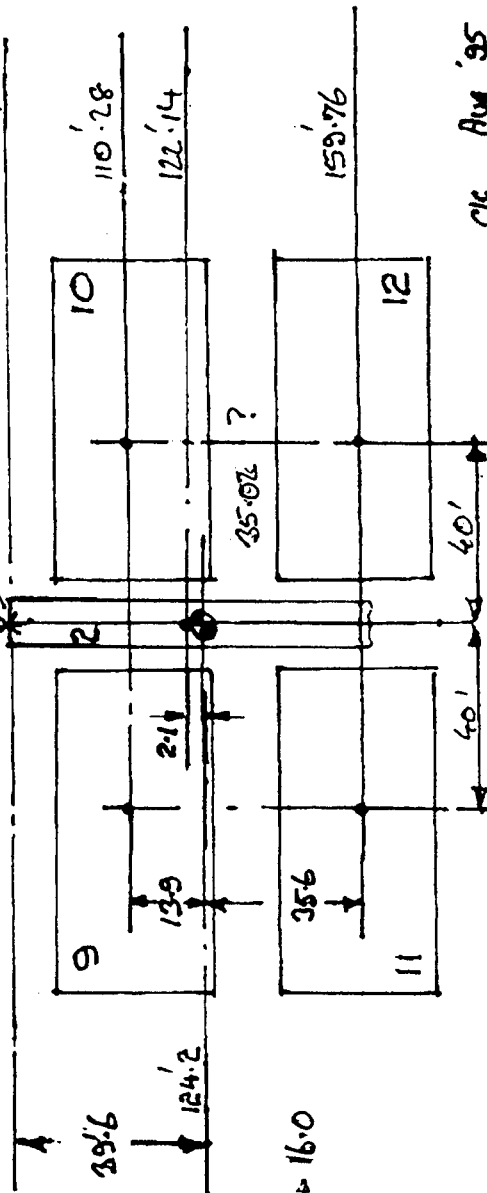
out beyond SARJ. Inertias. / mass

body No	Papa. available	mass lb x 1000	Center of mass x-ft y-ft	2 ft	Inertia Self rotation x-x y-y	inertia (Slugs ft ² x 1000)	xx	yy	zz
2	6'-53	53.0	1.01 122.14	1.11	972 88	904	2.1 -2	7 .2	- 2.1 7
9	6'-78	2.6	-38.71 110.24	1.88	5 196	200	13.9 1	16 1 39.8	128 39.8 139 144
10	6'-78	2.6	41.04 110.28	-2.41	5 196	200	13.9 3.3 16	33 40	130 40 13.9 145
11	6'-78	2.6	-38.71 159.76	1.88	5 196	200	35.6 1	102 1 39.5	128 39.8 35.6 230
12	6'-78	2.6	41.04 159.76	-2.41	5 196	200	35.6 3.3 103	3.3 40	130 40 35.6 232
		63.4	1.04 124.2	.88	992 872 244	1704 758	244	516	758

(45)

SARJ

8464



eq: $\frac{2600}{32.2} \sqrt{\frac{(13.9^2 + 3.3^2)}{1000}} = 16.48 \rightarrow 16.0$

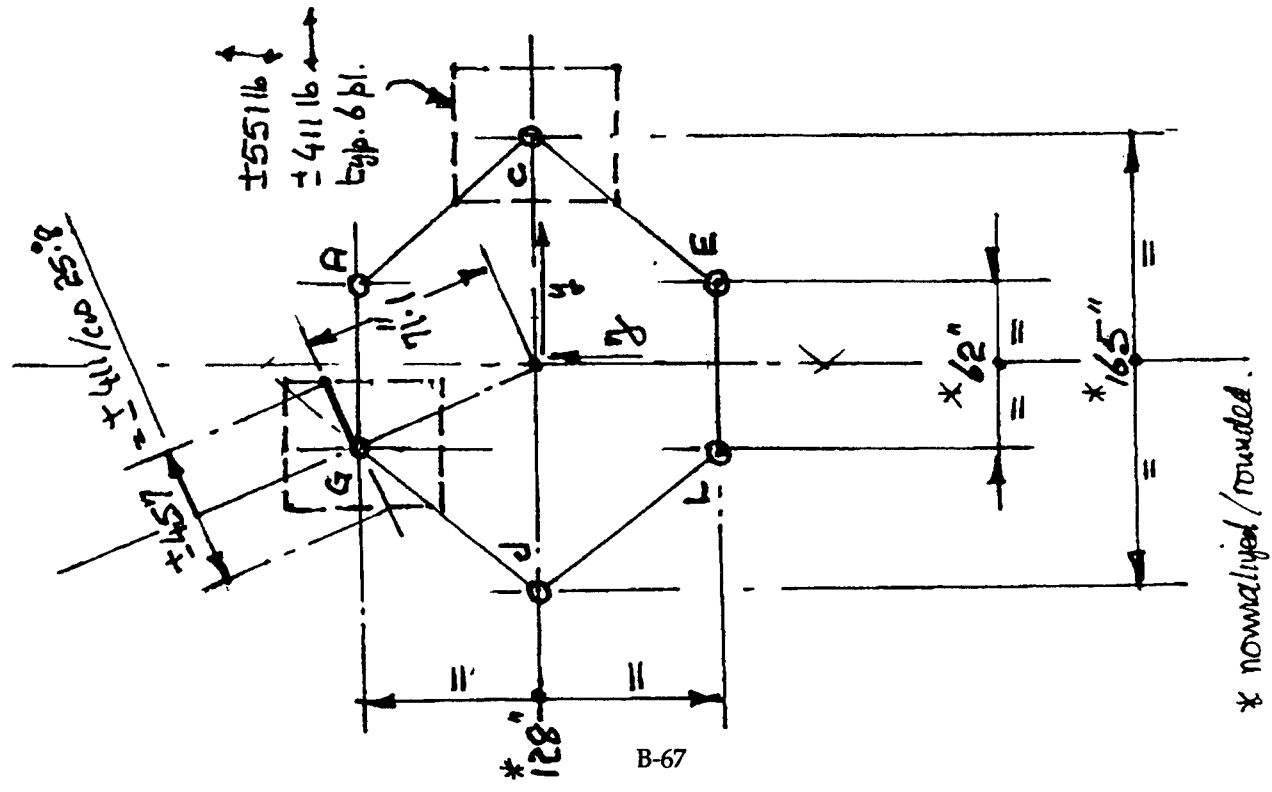
q/c Aug '95

STATION COMPLETE MASS & INERTIAS

body No.	Mass lb x 10 ³	G.C. location			(ft)	Inertia, own C.G. (slugs ft ² x 1000)			Inertia due to offset from Σ C.G.			(slugs ft ² / 1000)	
		x	y	z		xx rot	yy pitch	zz yaw	xx rot	yy pitch	zz yaw	xx	yy
1	6-48	-23.05	-2.64	16.38		18284	53753	58816	.6	3.7	1302	.5	.6
4	6-64	-24.0	48.3	0		35	228	198	48.3	127	49	5	483
5	6-68	-24.0	-48.3	0		35	228	198	"	"	49	"	"
6	6-73	11.6	2.6	-1.7		28	13	26	.6	14.4	595	.6	509
7	6-75	-78.8	19.7	-61.9		84	9	92	19.7	746	758	13.7	430
8	6-77	-77.6	-19.7	-61.9		84	9	92	"	758	1090	"	430
17	6-78	-140.4	0	13.6		10	121	122	2	.9	10908	16.9	2
18	6-79	-50.1	23.5	13.6		2	0	2	23.5	.9	13	286	235
19	6-100	-50.1	-23.5	13.6		2	0	2	"	"	13	"	23
20	6-101	-51.3	26.5	13.6		7	0	7	26.5	.9	186	678	265
21	6-102	-51.3	-26.5	13.6		7	0	7	"	"	186	"	214
2 etc	5 etc	1.0	124.2	.9		1236	1388	2462	124.2	11.5	1456	24	1242
3 etc	5 etc	1.0	-124.2	.9		1236	1388	2462	"	"	1456	"	1242
		-23.5	-2.0	12.7		21750	57137	64486	124.7	272	17393	128.6	17210
						64780	17393	77280					
						86530	74530	141766					

c/a Apr 55

LIMIT MOMENT CAPABILITY OF S.A. ROTARY JOINT.



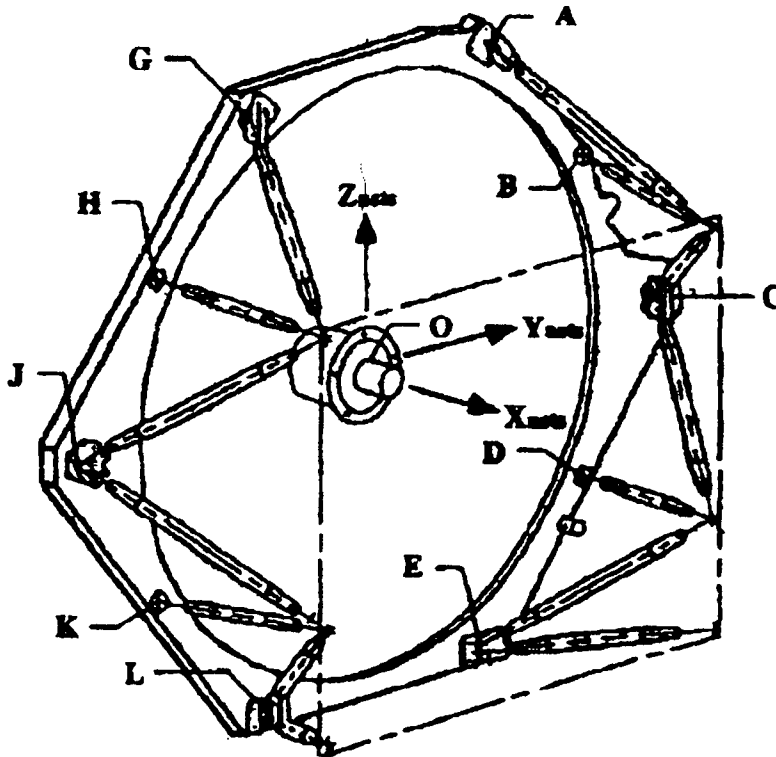
Joint Torque Cap	Shifters gearmed. lb f. K.in.-lb	Sum of strengths lb f. K.in.-lb
C+J	2(530 x 82.5) = 87.5	2(551 x 82.5) = 90.9
A+E+L+G	4(457 x 71.1) = 130.0	4(551 x 31.0) = 68.3
	<u>217.5</u>	4(411 x 64.0) = 105.2
		<u>264.4</u>
avg. (540 x 71.9) / 6		233
Joint yaw cap	station yaw: (on roll if joint clocked 90°)	
C+J	2(731 x 82.5) = 120.6	2(731 x 82.5) = 120.6
A+E+L+G	4(275 x 31.0) = 34.1	4(731 x 31.0) = 90.6
	<u>154.7</u>	<u>211.2</u>
		174
Joint roll cap	station in roll (or yaw if joint clocked 90°)	
A+E+L+G	4(731 x 64) = 187.1	187.1
		<u>187.1</u>
avg. (731 x 41.0) / 6		150, 187
		all avg yaw & roll.

9/1 Aug '95

SSP 44025

September 14, 1994

BIII-4



Interface Launch Limit Loads Application Point Coordinates (For Analysis)

per
data table

Interface Point	Orbiter Coordinates		
	X (in)	Y (in)	Z (in)
C	956.300	82.458	414.000
A	956.300	31.308	478.830
G	956.300	-31.308	478.830
J	956.300	-82.458	414.000
L	956.300	-30.718	350.820
E	956.300	30.718	350.820

0
64.8
64.8
0
-63.2
-63.2

Interface Limit Loads Application Point Coordinates (For Analysis)

Interface Point	Orbiter Coordinates		
	X (in)	Y (in)	Z (in)
B	954.300	58.144	447.819
D	954.300	58.144	380.481
H	954.300	-58.144	447.819
K	954.300	-58.144	380.481

33.8
-33.5
33.8
-33.5

5861-4

Figure 3.2.1.2.1.1-1. P3/P4 Mechanical Interface Launch and On-Orbit Load Limit Application Points

SSP 44025

September 14, 1994

TABLE 3.1.3-1 LINEAR TOLERANCES

English Dimension	Implied Tolerance (inches)
X.XX	± 0.03
X.XXX	± 0.010

3.2 INTERFACE REQUIREMENTS**3.2.1 INTEGRATED TRUSS SEGMENT S3 INTERFACE REQUIREMENTS****3.2.1.1 ENVELOPE REQUIREMENTS**

ITS S3 shall have no obstructions to structural, mechanical and utility interfaces with ITS S4.

3.2.1.2 STRUCTURAL AND MECHANICAL ATTACHMENT

Structural life shall be demonstrated in accordance with SSP 30559, Structural Design and Verification Requirements, paragraph 3.5.7. ITS S3 shall supply structural and mechanical provisions for the structural and mechanical attachment of ITS S3 to ITS S4 during preintegrated assembly.

3.2.1.2.1 STIFFNESS AND LOADS AT THE INTERFACE PLANE**3.2.1.2.1.1 INTERFACE MECHANICAL LOADS**

The on-orbit interface limit loads shall be within the limits shown in Table 3.2.1.2.1.1-1 and Table 3.2.1.2.1.1-2 for the ITS S3 to ITS S4 structural interface. Interface limit loads during launch and landing shall be within the limits shown in Table 3.2.1.2.1.1-3. Load points correspond to Figure 3.2.1.2.1.1-1. These loads shall be applied concurrently in all possible combinations.

TABLE 3.2.1.2.1.1-1 S3/S4 MECHANICAL INTERFACE ON-ORBIT
LIMIT LOADS AT A, C, E, G, J, L

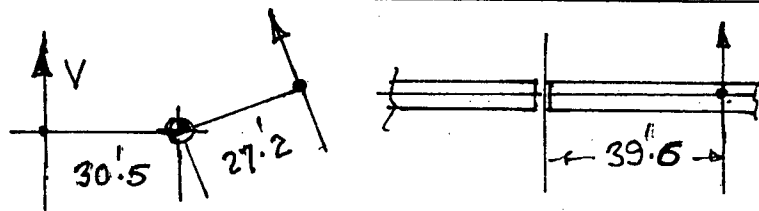
Fx (lb)	Fy (lb)	Fz (lb)	Mx (in-lb)	My (in-lb)	Mz (in-lb)
± 731	± 411	± 551	± 253	± 453	± 955
Note: Load points correspond to Figure 3.2.1.2.1.1-1.					

ROTATION ABOUT STA. CG (ITEM POINT MARK)

ROTATION ABOUT ITEM

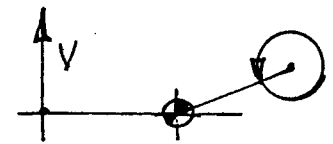
PITCH

IEA 1.39 x 10⁶ slugs ft²
STA 74.5 x 10⁶ "



$$\text{Shear: } \frac{V \times 30.5}{32.2} \frac{63,400 \times 27.2}{74.5 \times 10^6} \frac{\cos \dots}{6} = .0037 V$$

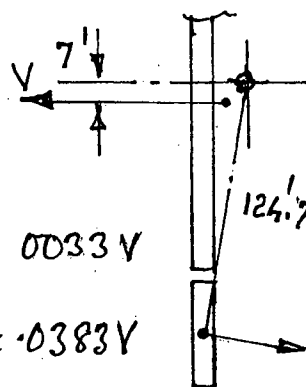
$$\text{Tension: } \frac{39.6}{6 \times 342} = .0422 V$$



$$\frac{V \times 30.5}{74.5} \frac{1.39}{6 \times 6.0} = \dots$$

Roll Added To P.

IEA 1.24 x 10⁶ slugs ft²
STA 86.5 x 10⁶ "



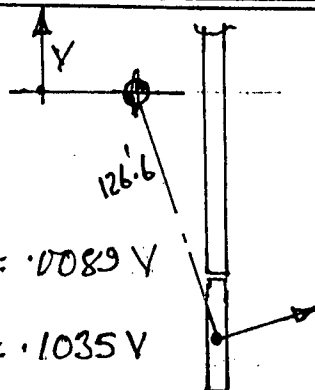
$$\text{Shear: } \frac{V \times 7'}{32.2} \frac{63,400 \times 124.7}{86.5 \times 10^6} \frac{\cos \dots}{6} = .0033 V$$

$$\text{Tension: } \frac{39.6}{6 \times 342} = .0383 V$$

$$\frac{V \times 7' \times 1.24 \times 10^6}{86.5 \times 10^6 \times 6 \times 3.42} = \dots$$

YAW

IEA 2.46 x 10⁶ slugs ft²
STA 141.8 x 10⁶ "



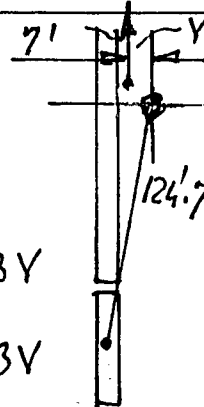
$$\text{Shear: } \frac{V \times 30.5}{32.2} \frac{63,400 \times 126.6}{141.8 \times 10^6} \frac{\cos \dots}{6} = .0089 V$$

$$\text{Tension: } \frac{39.6}{6 \times 344} = .1035 V$$

$$\frac{V \times 30.5 \times 2.46 \times 10^6}{141.8 \times 10^6 \times 6 \times 3.42} = \dots$$

Roll Added To Y.

IEA 1.24 x 10⁶ slugs ft²
STA 86.5 x 10⁶ "



$$\text{Shear: } \frac{V \times 7'}{32.2} \frac{63,400 \times 124.7}{86.5 \times 10^6} \frac{\cos \dots}{6} = .0033 V$$

$$\text{Tension: } \frac{39.6}{6 \times 342} = .0383 V$$

$$\frac{V \times 7' \times 1.24 \times 10^6}{86.5 \times 10^6 \times 6 \times 3.42} = \dots$$

IEA mass 63.4 x 10³ slugs
Sta. mass 894 x 10³ "

Influence Co-efficients for Venting forces --- etc

B-70

BT-6A

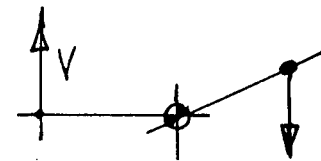
TEM CG (SELF INERTIA)

DIRECT REACTION

Σ Shear

Σ Tension

$$\frac{1}{6'0} = .0158V$$



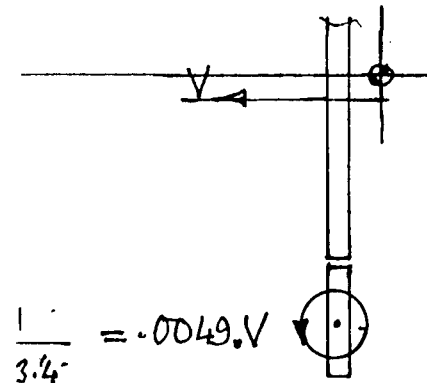
IEA 63,400 lbs
STA 894,000 lbs

$$V \times \frac{63,400}{894,000} \times \frac{1}{6'} = .0118V$$

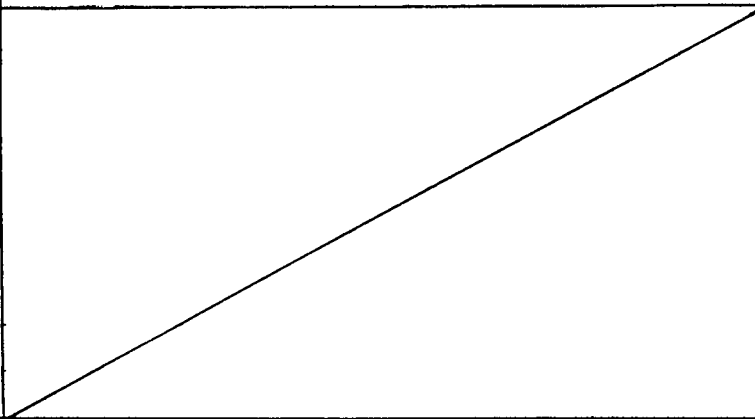
$$\frac{39.6}{6 \times 3'42} = .1369V$$

.0037 R
.0158 ↓
.0118 ↓
.0239

.0422
.1369
.1791

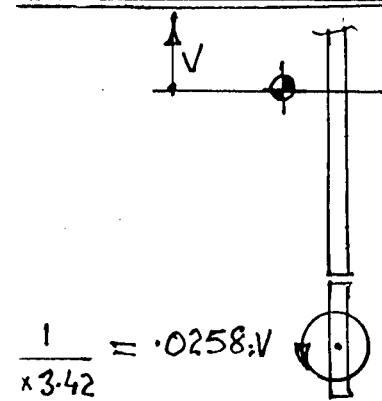


$$\frac{1}{3'4} = .0049V$$

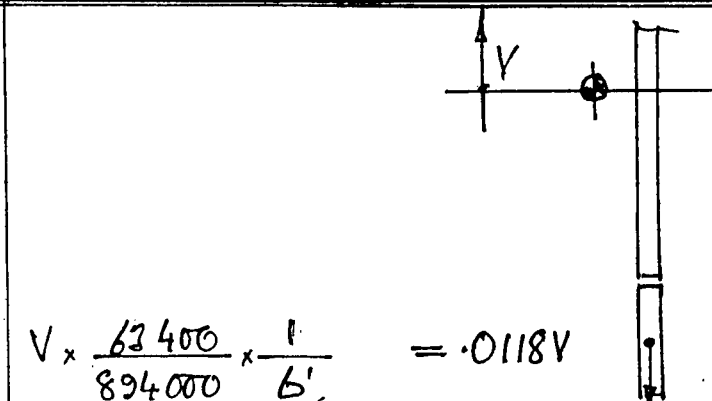


.0033
.0272

.0383
.0049
.2223



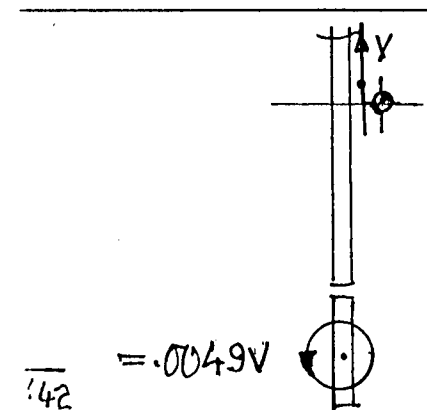
$$\frac{1}{3'42} = .0258V$$



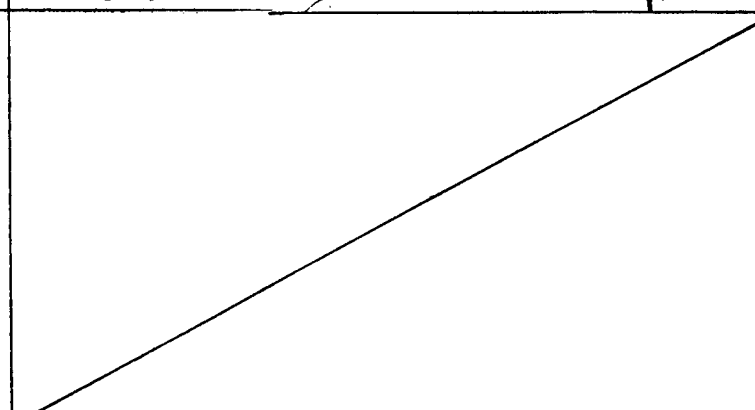
$$V \times \frac{63,400}{894,000} \times \frac{1}{6'} = .0118V$$

.0089

.1035
.0258
.0118
.1411



$$\frac{1}{4'2} = .0049V$$



.0033
.0122

.0383
.0049
.1843

B-71

Influence Coefficients for venting forces with various directions & effects - w.r.t SARI limit loads.

AUG. '95

BM 6-B

APPENDIX. B IV Debris Cloud / Wall Energies in phase C
above and below 1st B.L.
(SSEIC Method)

To be read in conjunction with Figure B-7 in the main report

B IV-1 • Phase C Assumptions Energies, Energy margins, Temperatures

- Energies in Combo (cloud) 3
- Energy margin at wall 3
- Main wall 2 temperature after impulse
- B.L. 3 derived at 8, 10, 15 km/sec initial velocity

B IV-2 • Work Sheet for three wall defense — phase C.

(attack and defense chosen in this example to be)
 (just below Ballistic limit 3 — well above Ballistic limit 2.)

- energy in combo (cloud) 1	=	66 080	ft lb
- " " " (") 2	=	2409	" "
- " " " (") 3	=	1227	" "

- various temperatures / footprints.

- Energy capability of wall 2	=	0	" "
- " " " " 3	=	1255	" "

B IV-3 1" & 3" dia Holes in main wall (2)

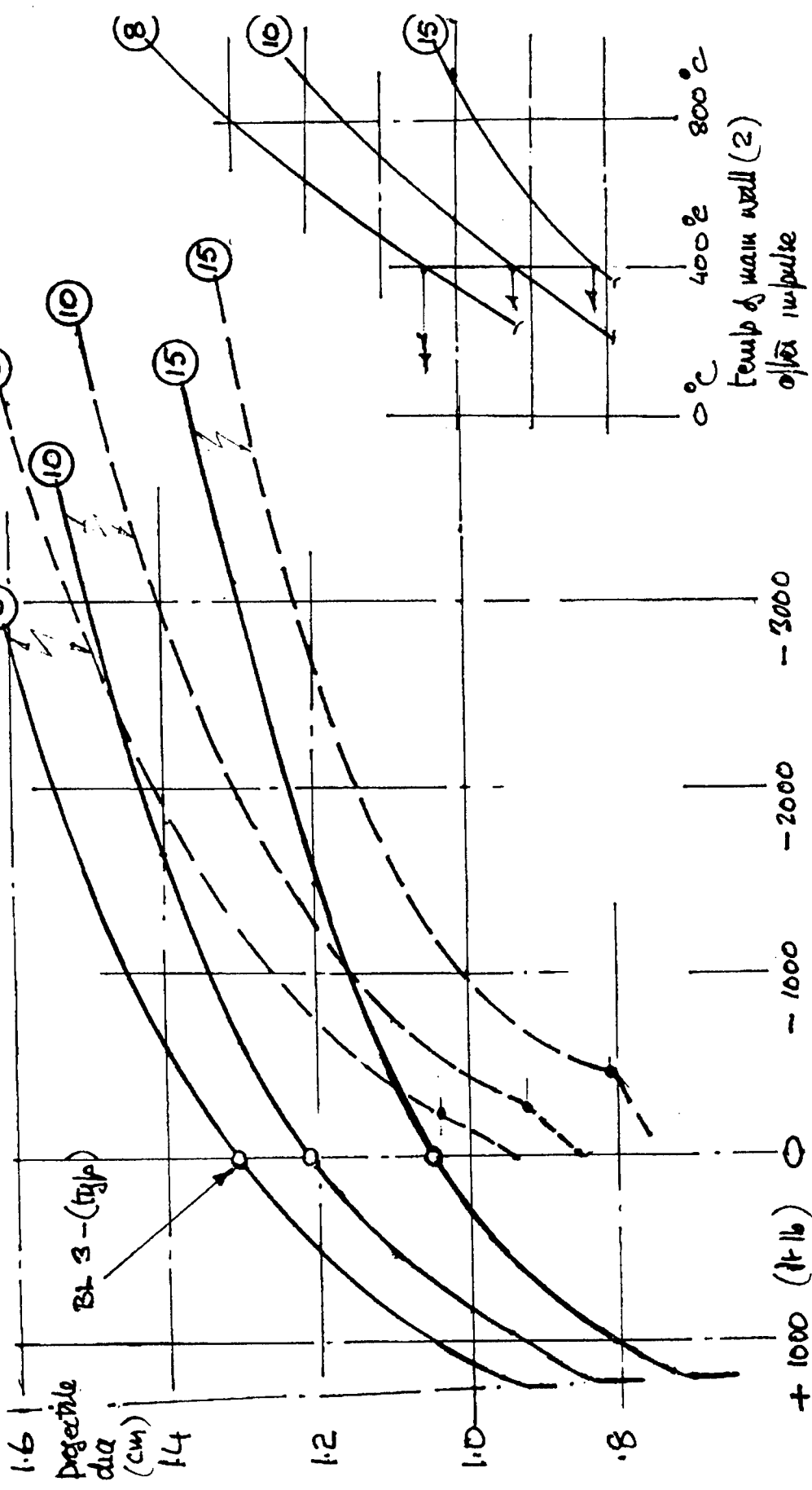
Burch, Fatepen 2, SSEIC estimates compared

PHASE C ASSUMPTIONS ENERGY IN COMBO 3 & MARGIN IN WALLS. —→ B.L. 3.

- Attack alum spheres various diam & initial vel. $\theta = 0^\circ$
- Defense all alum "OK 4"0 "10 4"0 "10

(Typ) Initial Rel. Vel. (km/sec)

- legends: — structural margin in wall 3 — after balancing
- energy in combo 3 — end of impulse



+ 1000 (It 16) ○ — 1000 — 2000 — 3000
 Combo (circled) 3 energy at end of impulse
 Structural margin taking wall 3 into account
 shown —ve
 { —ve above B.L.3
 +ve below B.L.3

Ch. Acc. 95

THREE WALL DEFENSE IN PHASE C

SECOND SERIES

1.2 CM DIA ALUM 10 Knts, $\theta = 0^\circ$

BIV-2

Sequence	dia (in)	mass (lb)	vel. (ft/s)	energy (ft lb)	Δ energy - (ft lbs) new	ΔT (°C) previous	$\Sigma \Delta T$ (°C)
• projectile (alum)	1.2 cm	0.00552	22,872	22,215			
• engaged wall (1)	8.35	0.00219					
• Combo 1 (cloud)		0.00771	23,483	66,020	26,125 .9 0.00771 305		10,000 cloud
• engaged wall (2)	5.09	0.00358					
• Combo 2 end of impulse		0.21129	857	2409	63,611 .9 1.20358 305	6 922	928 wall
• 2nd wall energy cap.				0			0 K.d.f.
• Combo 2 (cloud)		0.21129	857	2409	89,806 .9 2.1129 305		1254 cloud
• engaged wall (3)	5.09	0.00358					
• Combo 3 end of impulse		0.41487	436	1227	1182 .9 2.0258 305	3 17	20 wall
• 3rd wall energy cap.				1295			1.0 K.d.f.
				68			

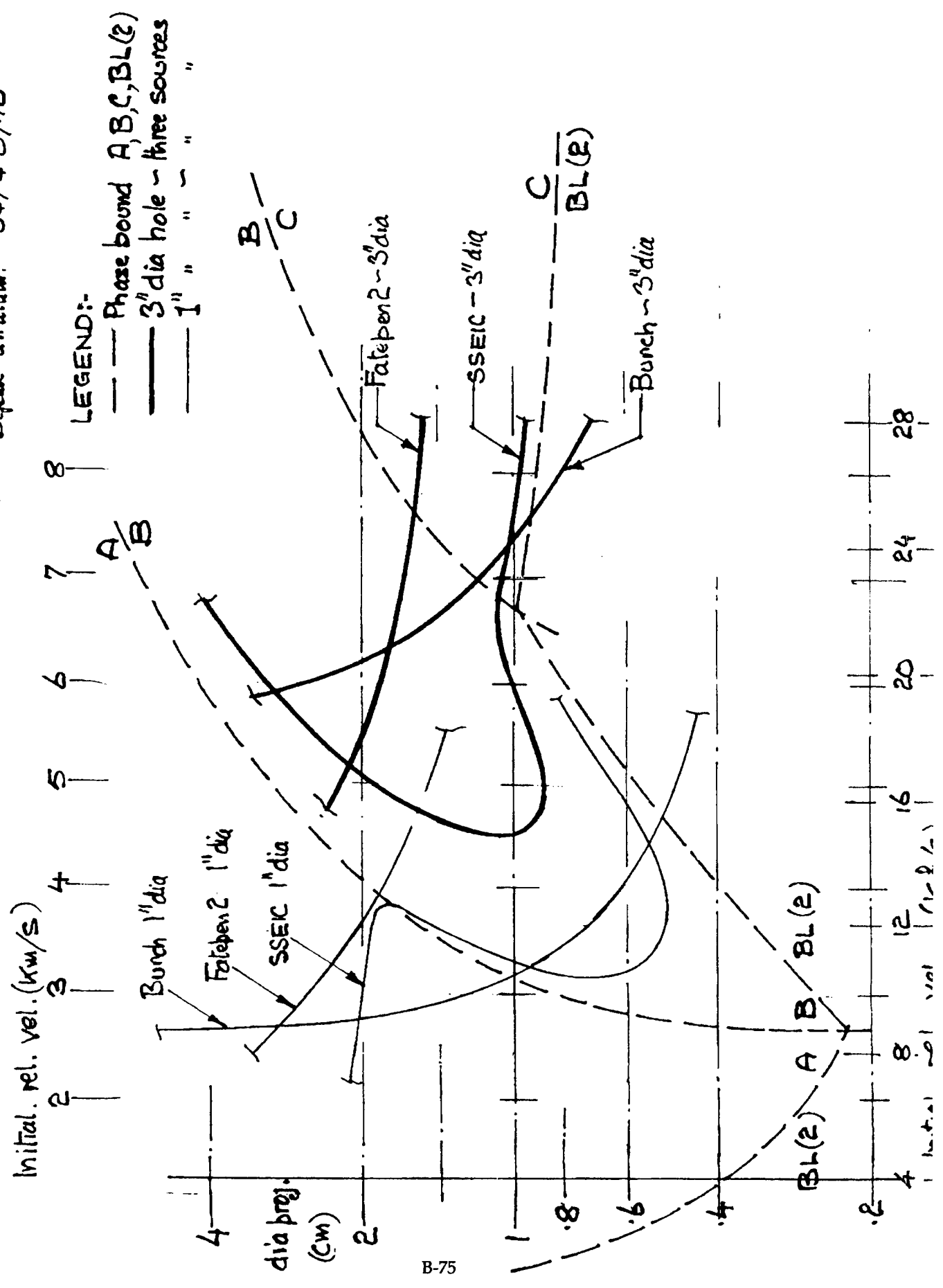
• Structural margin on 3rd wall.

• Defense all alum "04 4.0 "10 4.0 "10

210 Alum

1" & 3" dia. holes in main wall (2) Burr, Fatepen 2, SSEIC estimates Attack - alum spheres $\theta = 0^\circ$
 Defect - all alum. "04/4"0/10

8IV-3



APPENDIX B V DEBRIS FLUX (1989 KESSLER ENVIRONMENT)
 (28.5 INCLINATION)
 (210 N. MILLS ALT)
 (SF = 70)

To be read in conjunction with Table B3 of the main report

BV-1 Flux, Cumulative Flux, Flux in specific velocity bins

BV-2 Debris flux above propellant tank BL2 and above four Damage contours:

- propellant tank venting
- UDMH detonation low threshold
- " " mid "
- " " high "

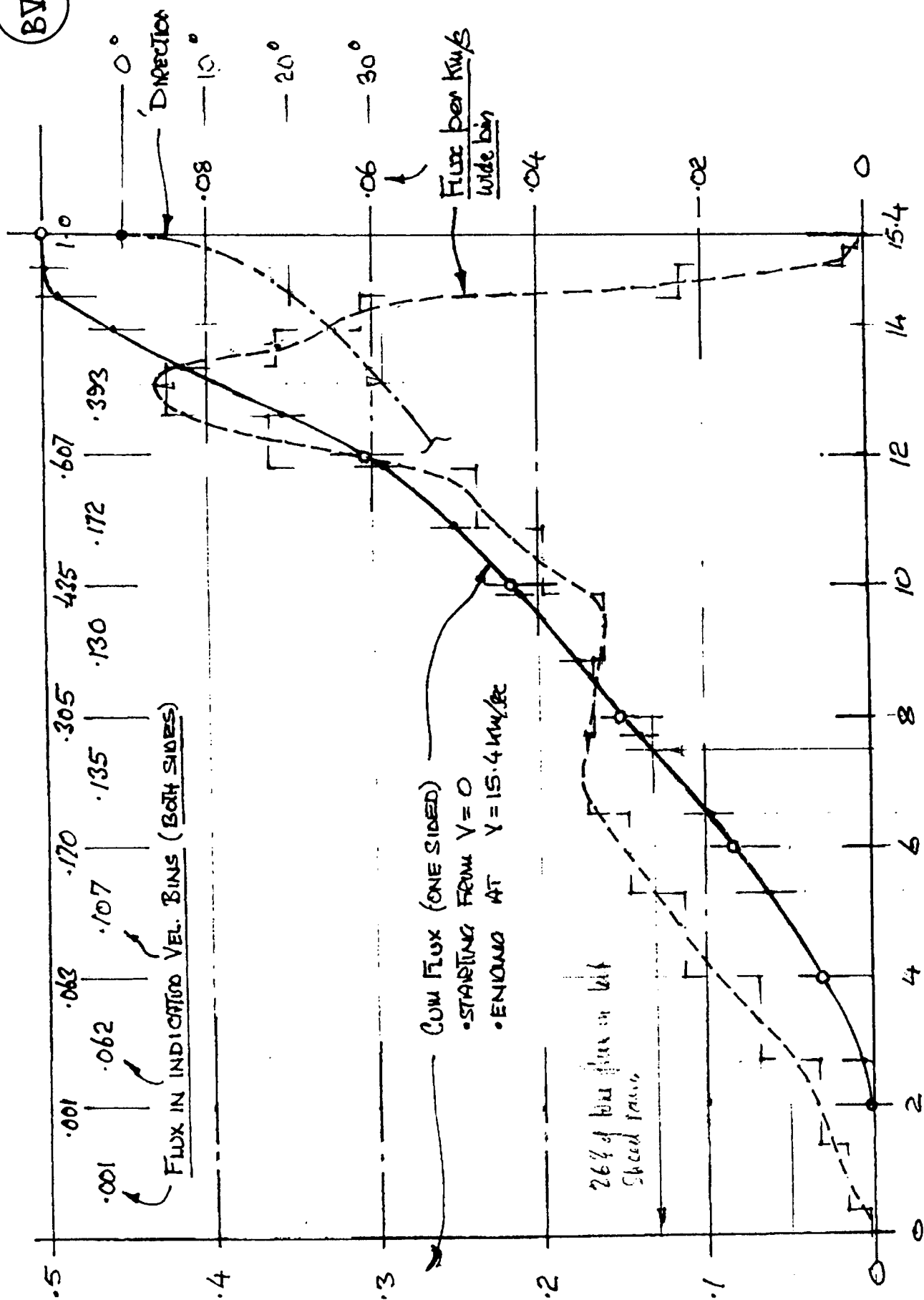
BV-3 Debris flux above CN_2 bottle BL2 and above one Damage Contour:

- High Pressure Bottle venting

BV-4 Example of flux between BL2 and $D_{proj} =$

BV-5 " " " " Venting Damage Contour and $D_{proj} =$

BY-1



Initial Rad. Vel. (km/s)

Mo. 10/11/95

DEBRIS FLUX

ABOVE PROPELLANT TANK B.L. 2 AND VARIOUS DAMAGE CONTOURS

CONTOURS

①	②
Velocity bin (m/s)	normalized share of flux
0-2	.001
2-4	.062
4-6	.107
6-8	.135
8-10	.130
10-12	.172
12-15.4	.393
	1.000

• CASE

• flux above Damage Contour =

flux above B.L.

③	④	⑤
dent B.L. (cm)	flux above dent *	product ②x④
.52	4.3	.004
.30	16.9	1.048
.67	2.3	.246
.96	1.17	.158
.90	1.34	.174
.84	1.50	.258
.89	1.70	.668
↑		2.556
B.L. 2 - Propellant tank		
N.A.		

③	④	⑤
dent Damage (cm)	flux above dent *	product ②x④
8.3	.18	.0
7.3	.19	.012
2.0	.42	.045
1.05	.98	.132
.94	1.23	.160
.88	1.40	.241
.82	1.60	.629
↑		1.219
Propellant tank venting		
$\frac{1.219}{2.556} = .48$		

* flux on tumbling surface / m² gear (multiply by 10⁻⁵)

0-2	.001
2-4	.062
4-6	.107
6-8	.135
8-10	.130
10-12	.172
12-15.4	.393
	1.000

• CASE

• flux above damage contour =

flux above B.L.

③	④	⑤
dent B.L. (cm)	flux above dent *	product ②x④
1.4	.61	.001
1.05	.98	.061
1.05	.98	.105
1.13	.85	.115
1.05	.98	.127
.96	1.17	.221
.88	1.40	.432
↑		1.042
UDMH det. inner threshold		
$\frac{1.042}{2.556} = .41$		

③	④	⑤
dent B.L. (cm)	flux above dent *	product ②x④
2.7	.30	.0
1.7	.49	.030
1.5	.57	.061
1.7	.49	.066
1.6	.57	.066
1.5	.57	.098
1.4	.61	.240
↑		.561
UDMH det. mid threshold		
$\frac{.561}{2.556} = .22$		

③	④	⑤
dent B.L. (cm)	flux above dent *	product ②x④
6.0	.19	.0
3.3	.25	.016
2.8	.28	.030
2.7	.30	.041
2.5	.32	.042
2.3	.35	.060
2.1	.39	.153
↑		.342
UDMH det. outer threshold		
$\frac{.342}{2.556} = .13$		

BY-3

DEBRIS FLUX ABOVE G.N₂ BOTTLE BL.2 AND VENTING DAMAGE CONTOUR

①	②
Velocity bin (km/s)	Nominal size of flux
0-2	.001
2-4	.062
4-6	.107
6-8	.135
8-10	.130
10-12	.172
12-154	.393
	1.000

• CASE

• Flux above damage contour

Flux above B.L.

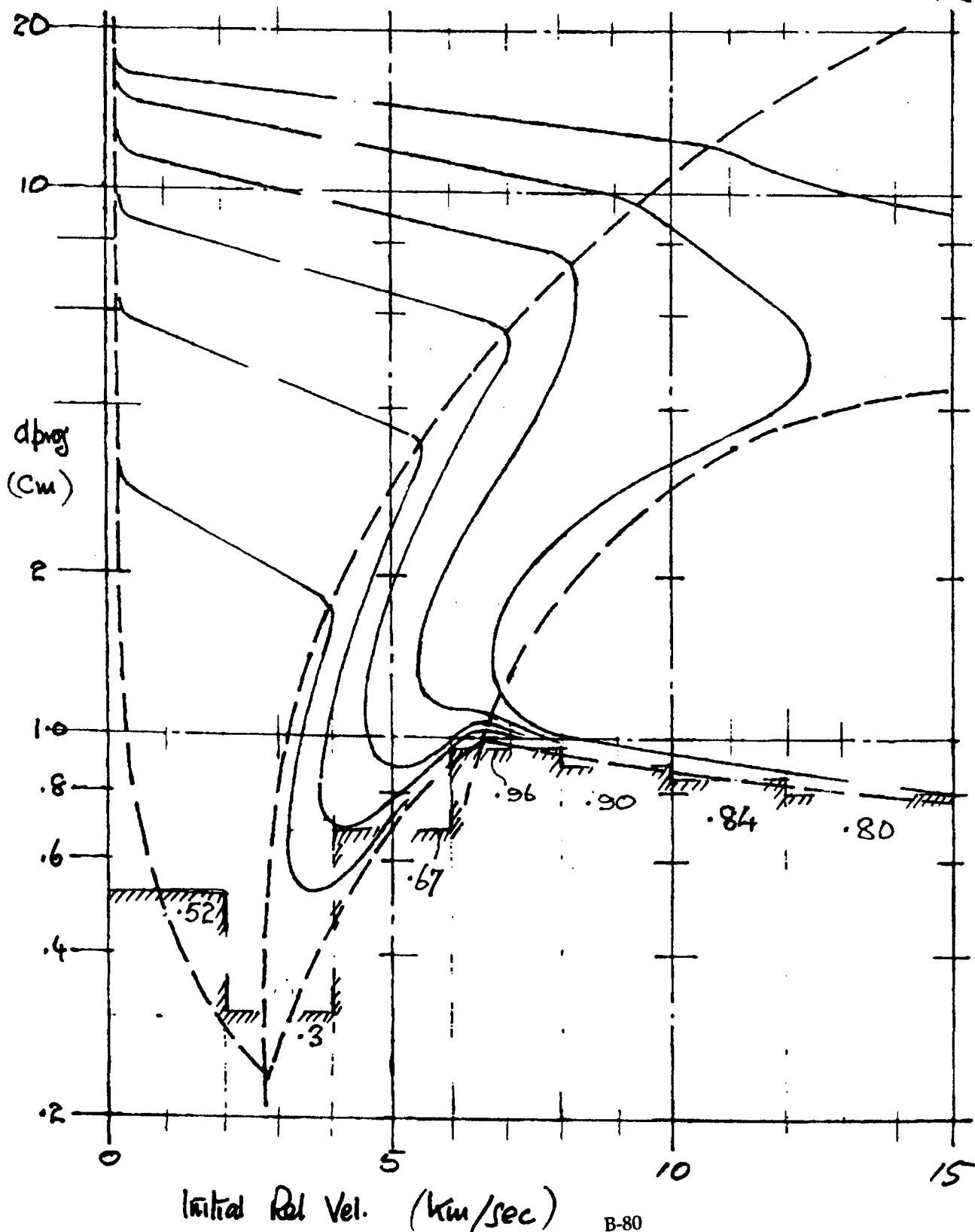
③	④	⑤
d crit B.L. (cm)	flux above d crit *	product ②x④
1.4	.61	.001
.9	.134	.083
1.27	.71	.076
1.70	.49	.066
1.64	.51	.066
1.53	.54	.093
1.40	.61	.240
		.625
↑ B.L.2 - G.N ₂ Bottle		N.A.

③	④	⑤
d crit Damage C. (cm)	flux above d crit *	product ②x④
3.8	.23	.0
3.1	.26	.016
2.0	.42	.045
1.76	.46	.062
1.70	.49	.064
1.58	.52	.089
1.52	.55	.216
		.492
↑ G.N ₂ Bottle venting		$\frac{.492}{.625} = .78$

* flux on tumblers
surface / yr
(multiplied by 10⁻⁵)

BY-4

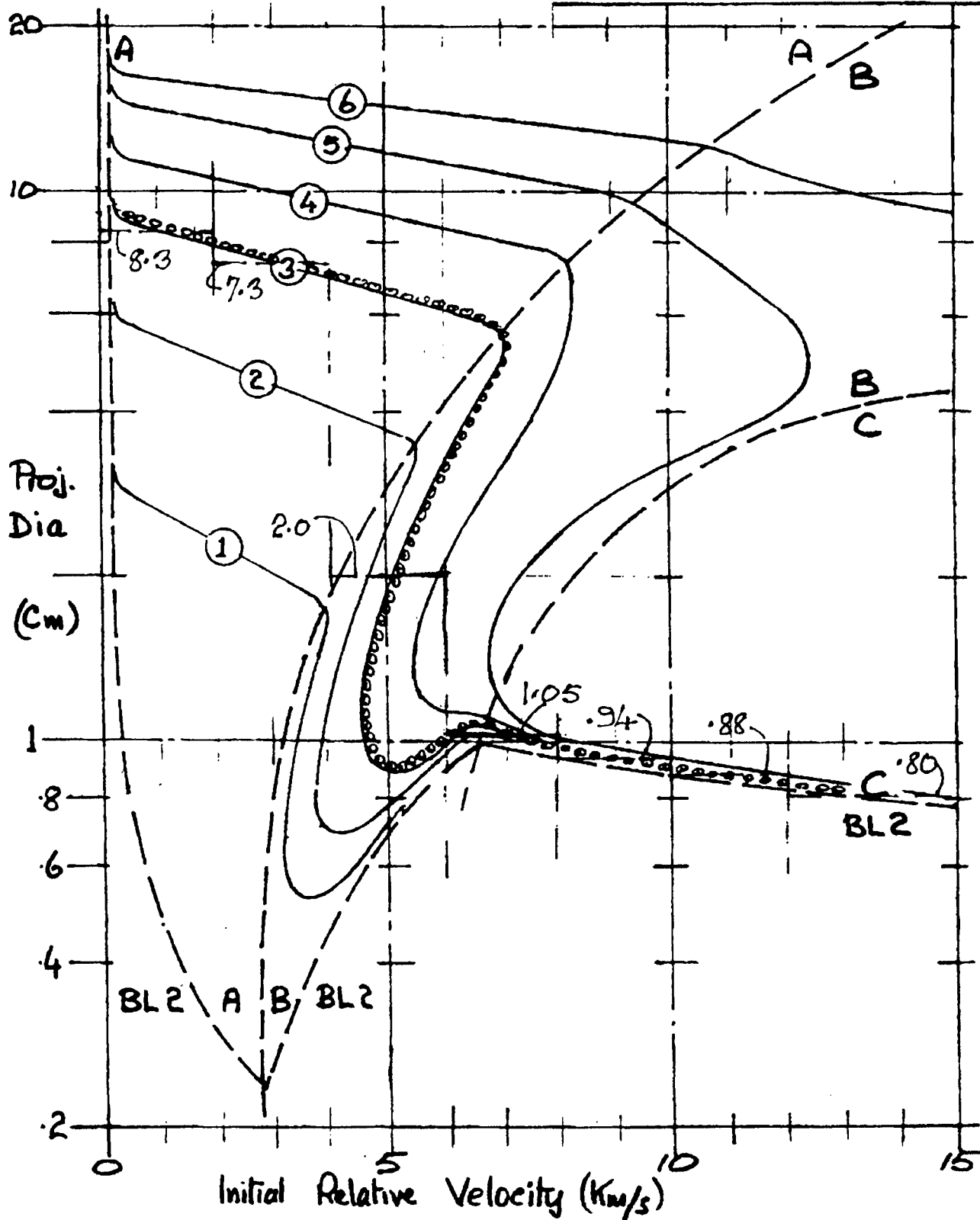
defense all alum. ".04 4"0 "10 FLUX BETWEEN BL2 & $d_{pg} = 20 \text{ cm}$



Legend: — — — Phase bounds A, B, C, ~ BL2 (.10 alum main wall.)

— (X) — Equiv. hole dia. in main wall (inches indicated)

oooooooooooo Damage contour - Venting of Propellant tank GN₂ damage prime structure



Figure

Figure

APPENDIX B VI GYRODYNE MODULE & UNITS

To be read in conjunction with Figures B 13 through 20
and Tables B 4 & B 5.

B VI-1 Conjectural Gyrodynic Features

B VI-2 Risk of a target (Abel) being hit by a single frag. from Cain

B VI-3 Probability of non-propagation of water-vapour in 2 parameters

B VI-4 1-5-4 Fratricide sequence with parameters

B VI-5 Exploration of fragmentation branching - multiple targets

B VI-6 One aggressor with two targets, $2 \subset \frac{3}{4}$ and $3 \subset \frac{2}{5}$

B VI-7 4-5-1 Fratricide sequence with parameters

B VI-8 $5 \subset \frac{1}{4}$ Fratricide sequence with parameters

B VI-9 $5 \subset \frac{1}{4}$ Fratricide sequence with other parameters

B VI-10 'Near' Gyrodynic (# 4, 5, 2) - edge factor calculation

B VI-11 'Far' " (# 1, 2, 6) - " " "

B VI-12 Three wall defense against debris and fragments - general principles

B VI-13 Sanity check on maximum width of apertures

B VI-14 Deceleration effects of air - spherical debris

B VI-15 " " " " - randomly rotating cubic debris

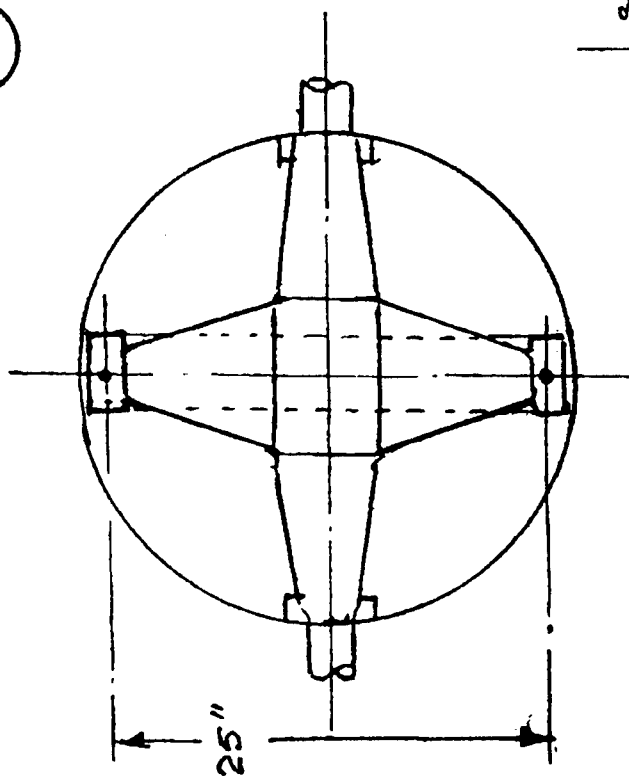
B VI-16 " " " " - continued

B VI-17 Velocity and distance in air to fracture/melt alum debris - various sizes.

CONJECTURAL GYRODYNE FEATURES

- rotor rim centroid dia 25 in
- total rotor mass 150 lbm
- ball-park rim mass ~ 250 lbm
- nominal rotation 100 rps
- nominal rim speed 654 f/s
- nominal angular momentum 2500 N-m-s
- nominal angular momentum 1844 lb-ft-s.

18 kg given



B-83

• Spin-up calc. $1844 \times \frac{24}{25} \times \frac{32.2}{\pi} = \text{rim speed} = 654 \text{ f/s}$ where $\pi = \frac{1844 \times \frac{24}{25} \times 32.2}{654}$

• Assuming titanium rotor ~ rim cross section area

• centrifugal force on one (tangential) inch of rim

• Hoop tension ~ (neglecting spoke/disc restraint)

• Hoop stress ~ (" " " ")

• Rim energy $87.2 \times 654^2 / 64.4$

steel

$$= 87.2 \text{ lb mass}$$

$$= 6.94 \text{ m}^2$$

$$= 14,160 \text{ lb f}$$

$$= 177,000 \text{ lb f}$$

$$= 25,500 \text{ p.s.i.}$$

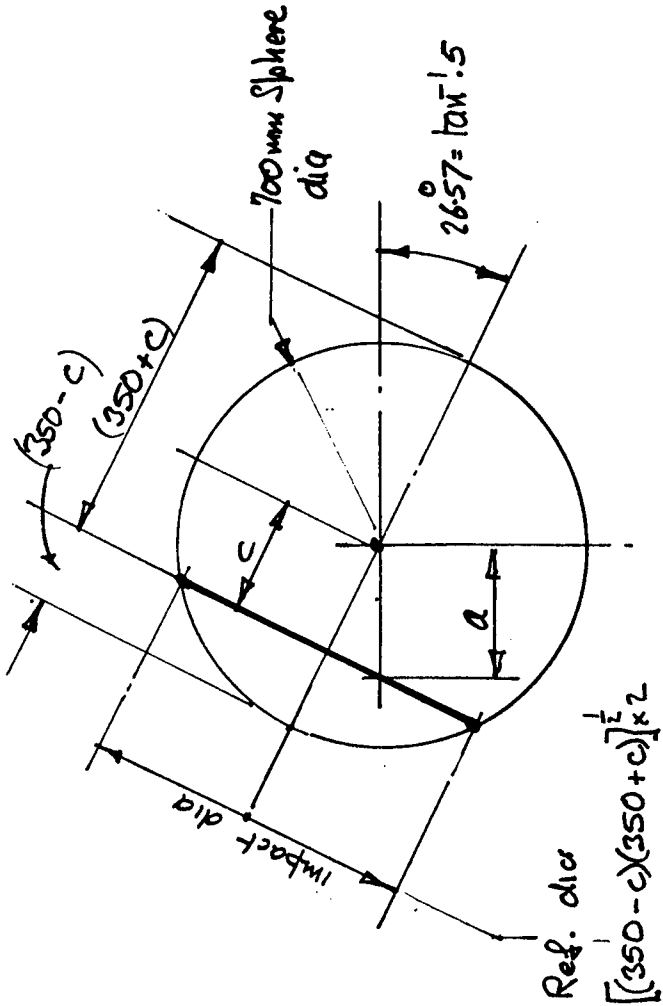
45,000

Abt. 35

RISK OF A TARGET (ABEL) BEING HIT BY A FRAGMENT FROM CANY WAS A FUNCTION

॥

- GEOMETRY OF CAIN/ADLER PAIR
- NO. OF BIG CHANGES COMING FROM CAIN (N)



a (mm)	c (mm)	$(350 - c)$ (mm)	$(350 + c)$ (mm)	Ref dia (mm)	Pair	Range (mm)	$R_{15\%}$ (mm)	$n = 20$	$n = 50$	$n = 100$
199.4	178.3	171.7	528.3	301.2	1-5	1625 / $\cos 26.5^\circ = 1816.9$	0.0264	414	738	931
248.7	222.4	127.6	572.4	270.3	2-3	1605 / $\cos 26.5^\circ = 1794.5$	0.0240	385	703	912
283.0	253.1	96.9	603.1	241.4	2-4	1169.8 / $\cos 14.0^\circ = 1135.1$	0.0338	489	821	968
189.4	169.4	180.6	519.4	306.3	3-2	104.5	0.0272	424	748	937
283.0	253.1			241.4	3-5	1135.1	0.0338	489	821	968
248.7	222.4			270.3	4-5	1794.5	0.0240	385	703	912
258.7	231.4	118.6	581.4	262.6	5-1	1816.9	0.0230	372	688	902
189.4	169.4			306.3	5-4	1794.5	0.0272	424	748	937

average risk for $n=1 \rightarrow .0274$

$$= \frac{1}{36}$$

Ch. A. J. '95-

PROBABILITY OF NON PROPAGATION OF ROTOR RUPTURE BEYOND THE INITIAL CRYSTALLINE UNIT VS 2 PARAMETERS

BVI-3

PARAMETER No. 1 No of big fragments arising from one rotor rupture	20		50		100	
	80	100	80	100	80	100
PARAMETER No. 2. % of Vacuum sphere penetrations that result in a rotor rupture						
Gyrodure Frat. groups						
A 1-5-4	.669	.586	.410	.262	.258	.069
A 2-3-5-1 2-4	.421	.314	.150	.053	.061	.003
A 3-2-4 3-5-1 5-1	.403	.294	.128	.045	.057	.002
A 4-5-1	.692	.615	.438	.297	.270	.088
A 5-1 5-4	.464	.362	.181	.079	.069	.006
Avg non propagation - reject #6	.53	.43	.26	.15	.14	.03
" " " - incl #6	.61	.53	.39	.29	.29	.19

Probability of non-propagation beyond initial rotor-rupture (typ)

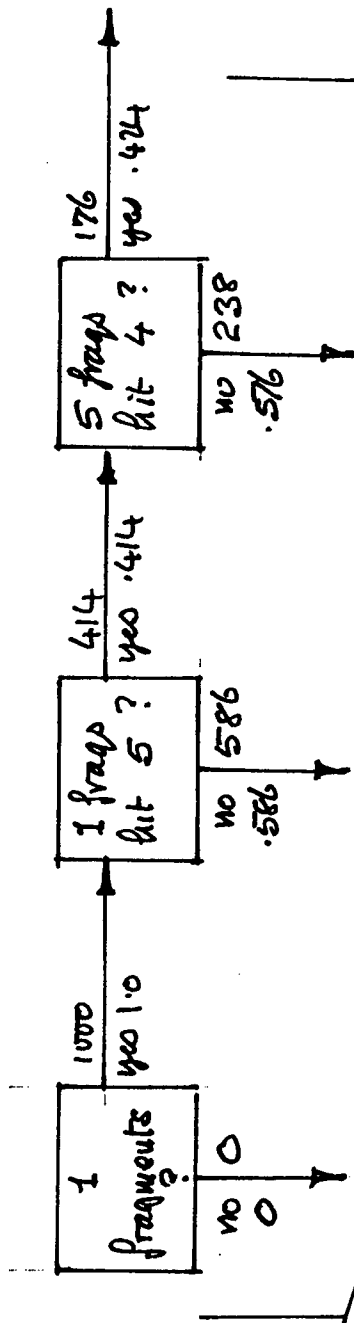
-4
-6
-5
-6
-7
-8
-9

These subsequent checks feed data in to the appropriate rows

Cpl. Alu. 95

1-5-4 FRAGMENT SEQUENCE WITH PARAMETRIC VARIATIONS

BVI-9



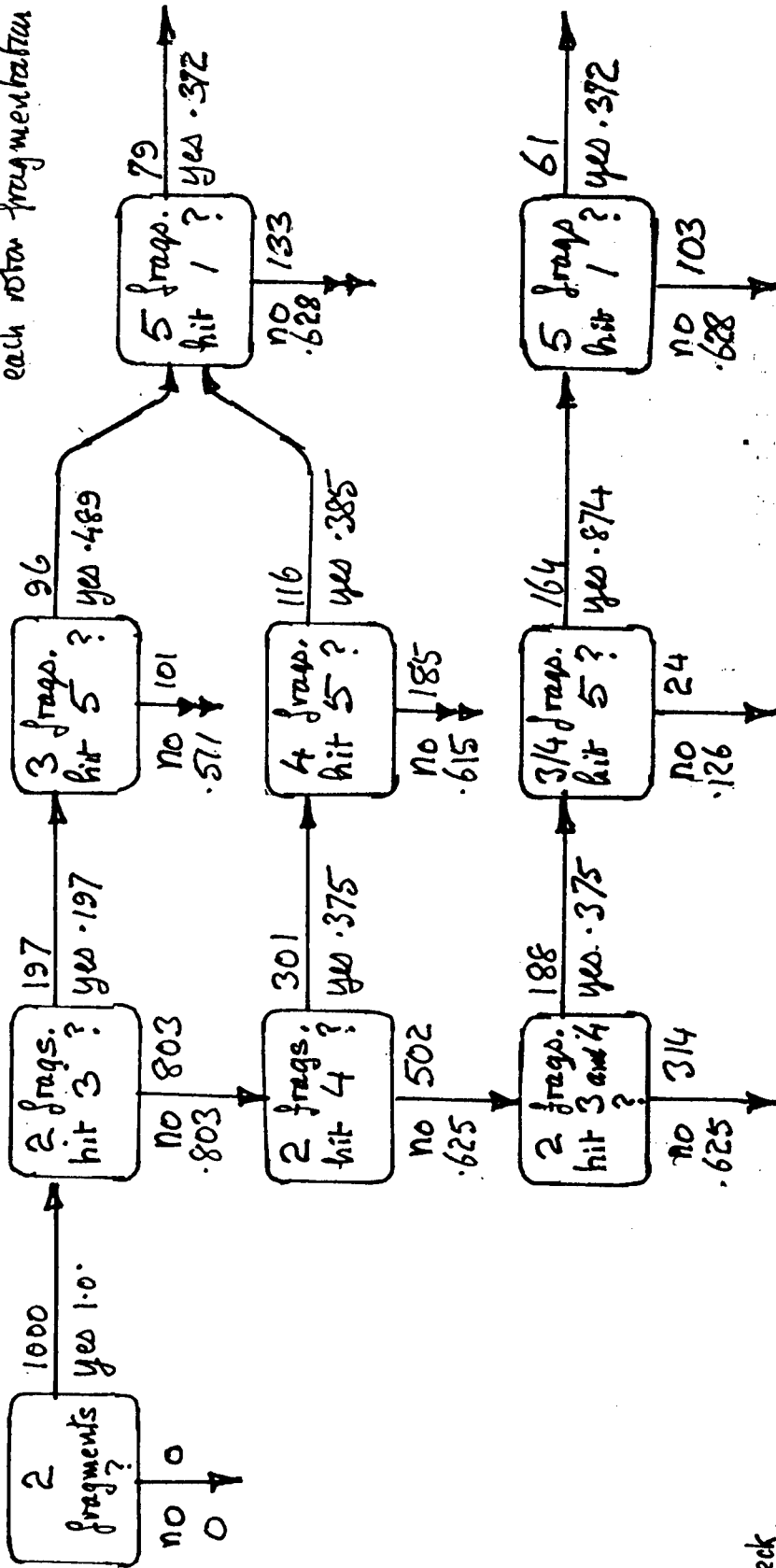
Example

ASSUMPTIONS		20		50		100	
• No. of 'big fragments'		20	80%	20	100%	50	100%
• % of 'big fragments' that break-up after if they hit vacuum sphere.		20	80%	50	100%	100	100%
Proportion of events that destroy:-							
one gyrodyne	1	.665	.586	.410	.262	.258	.065
two "	1+5		.238				
three "	1+5+4		.176				
			1.000				

C/K 11/98

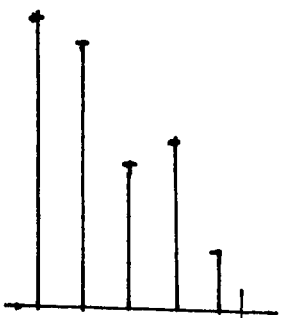
Fragmentation branching after initial break-up of Gyrodyno # 2 Example of one agreeor with two targets - Exploration

- Assumptions**
- Each hit has a 100% probability of rotor fragmentation
 - 20 fatal fragments from each rotor fragmentation

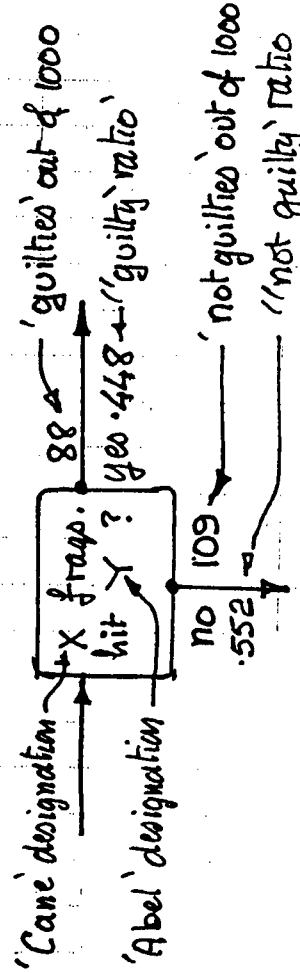


No. check
Gyrodyno fragmented

1	314
2	286
3	157
4	182
5	61
	1000



NODE LEGEND



Ch. 11. 95

9-1A3

Q
"Z

[illegible]
$$N=50$$

179	121	821	4	179	552
2	2	2	2	2	2
3	3	3	3	3	3
703	748	562	438	297	
80%	80%	80%	80%	80%	
657	657	657	657	657	
343	343	343	343	343	
150	150	150	150	150	
179	179	179	179	179	
821	821	821	821	821	
598	598	598	598	598	
407	407	407	407	407	

$$N=100$$

The diagrams illustrate the iterative calculation of the effective interest rate i for a bond. Each diagram shows a timeline with cash flows and the calculation of the effective rate i .

Diagram 1 (Top Left): Shows a timeline with cash flows of 100 at time 0, 100 at time 1, and 100 at time 2. The effective rate i is calculated as 8.0%.

Diagram 2 (Top Right): Shows a timeline with cash flows of 100 at time 0, 100 at time 1, and 100 at time 2. The effective rate i is calculated as 8.0%.

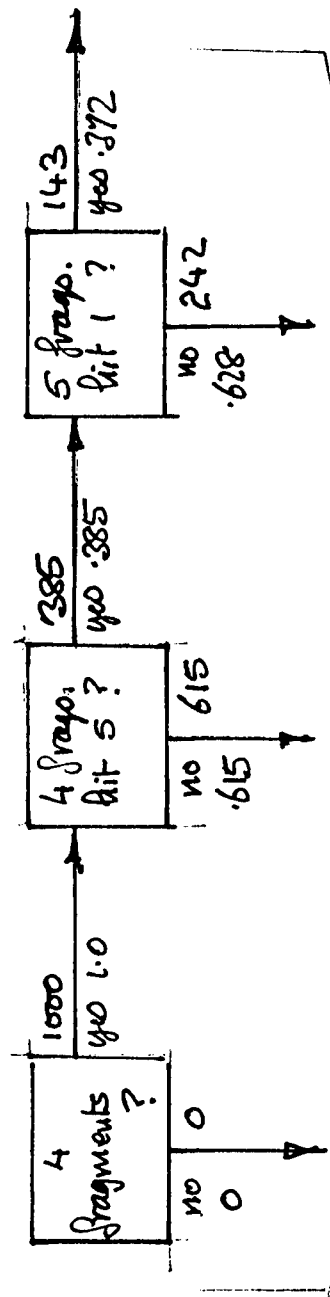
Diagram 3 (Bottom Left): Shows a timeline with cash flows of 100 at time 0, 100 at time 1, and 100 at time 2. The effective rate i is calculated as 8.0%.

Diagram 4 (Bottom Right): Shows a timeline with cash flows of 100 at time 0, 100 at time 1, and 100 at time 2. The effective rate i is calculated as 8.0%.

1956

4-5-1 FRATRICIOUS SEQUENCE WITH PARAMETRIC VARIATIONS

BVI-7

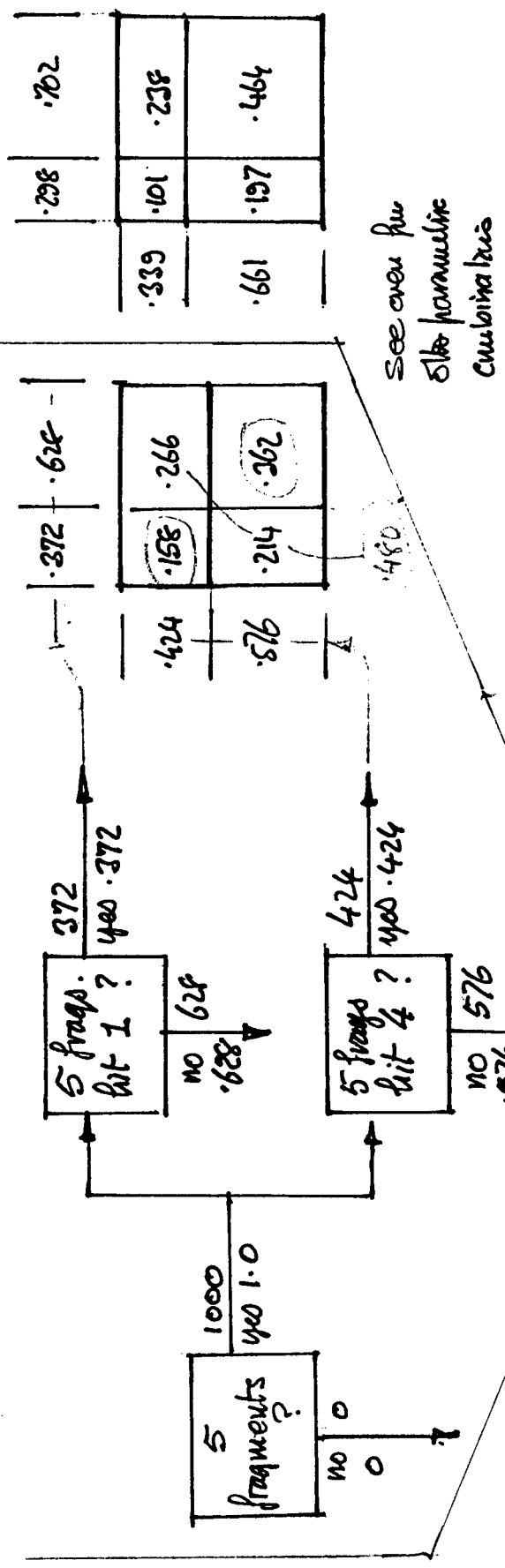


Example

Assumptions	20	20	50	100	100	100
• No. of big fragments						
• % of big fragments that break-up after if they hit vacuum sphere	80%	100%	100%	80%	80%	100%
Proportion of events that destroy:						
one gyrodyn (4)	.692	.615	.438	.297	.270	.088
two " (4+5)		.242				
three " (4+5+1)		.143				
		1.000				

Ch. 11/6/95

5. FRATRICIDE WITH PARAMETRIC VARIATIONS

$$n=20/80\%$$
$$n = 20/100\%$$
[illegible]

BYL-9

$n = 50 / 80\%$

	.550	.450
.598	.329	.269
.402	.221	.181

no propagation - (typ)

$n = 50 / 100\%$

	.688	.312
.748	.575	.233
.252	.173	.079

$n = 100 / 80\%$

	.722	.278
.750	.541	.209
.250	.181	.069

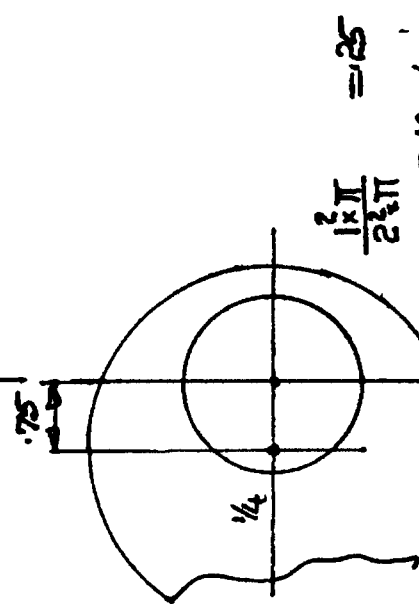
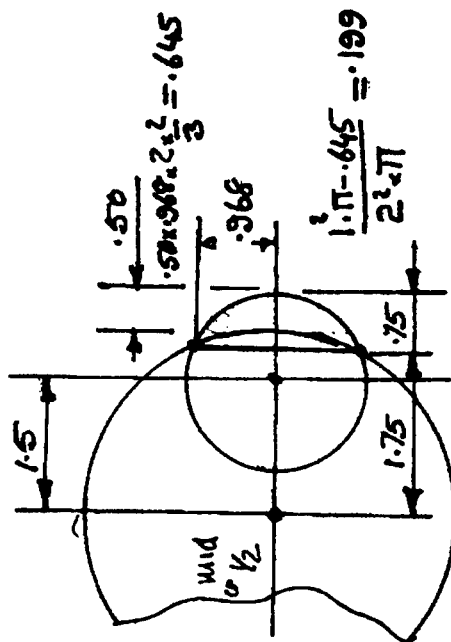
$n = 100 / 100\%$

	.906	.094
.937	.845	.052
.063	.057	.006

5' - 4' FRATRIEUS WITH PARADISES OF THE THAN PREVIOUS CHART.

Diagram showing a circular segment with dimensions and calculations:

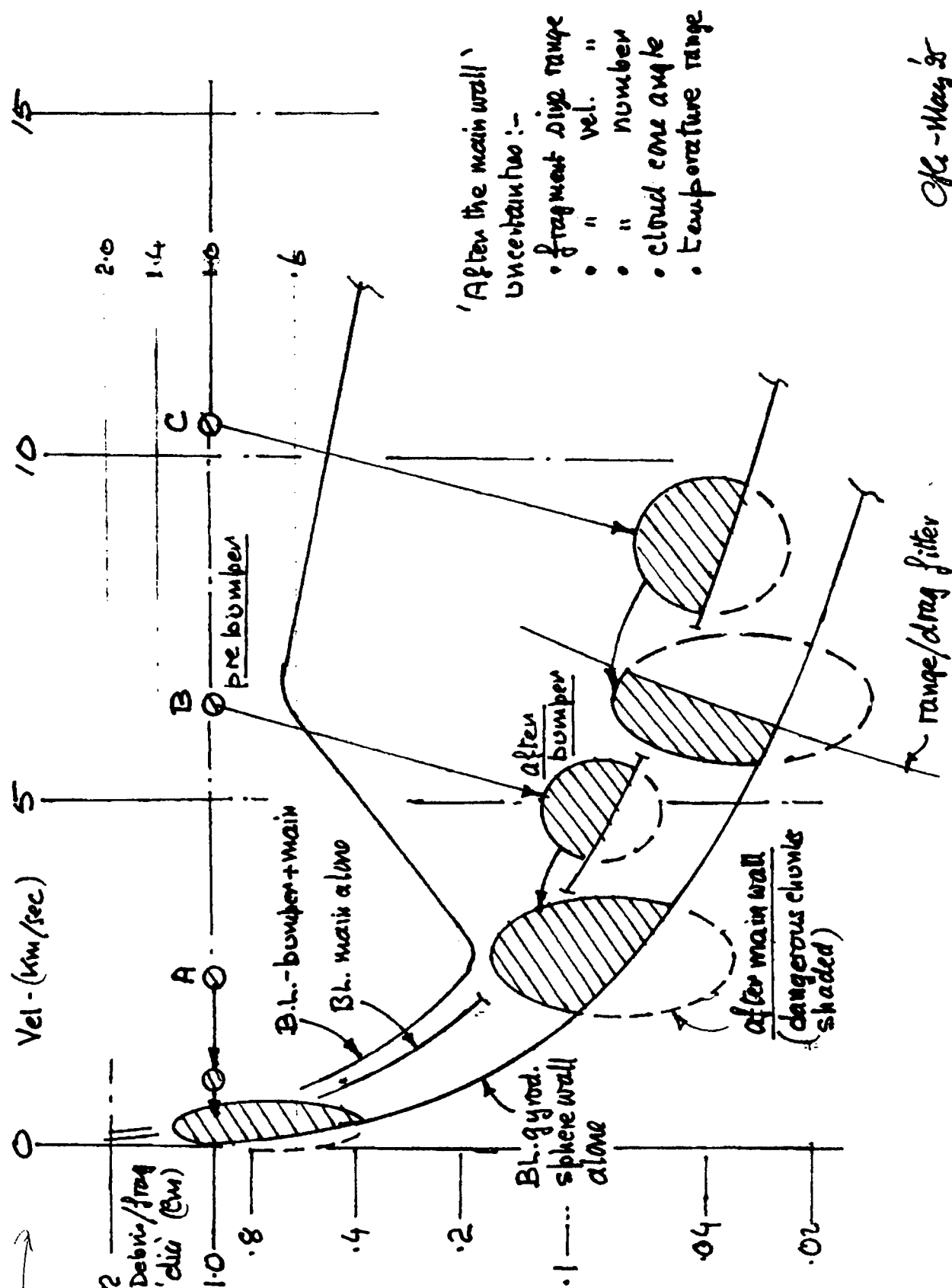
- Radius: $2R$
- Chord length: 1.791
- Segment height: 1.791
- Central angle: $3\frac{3}{4}$
- Area calculation: $.75 \times .889 \times \frac{2}{3} = .859$
- Area calculation: $\frac{.889}{2\frac{1}{2}\pi} = .071$



(Division of Dept. of Haring)

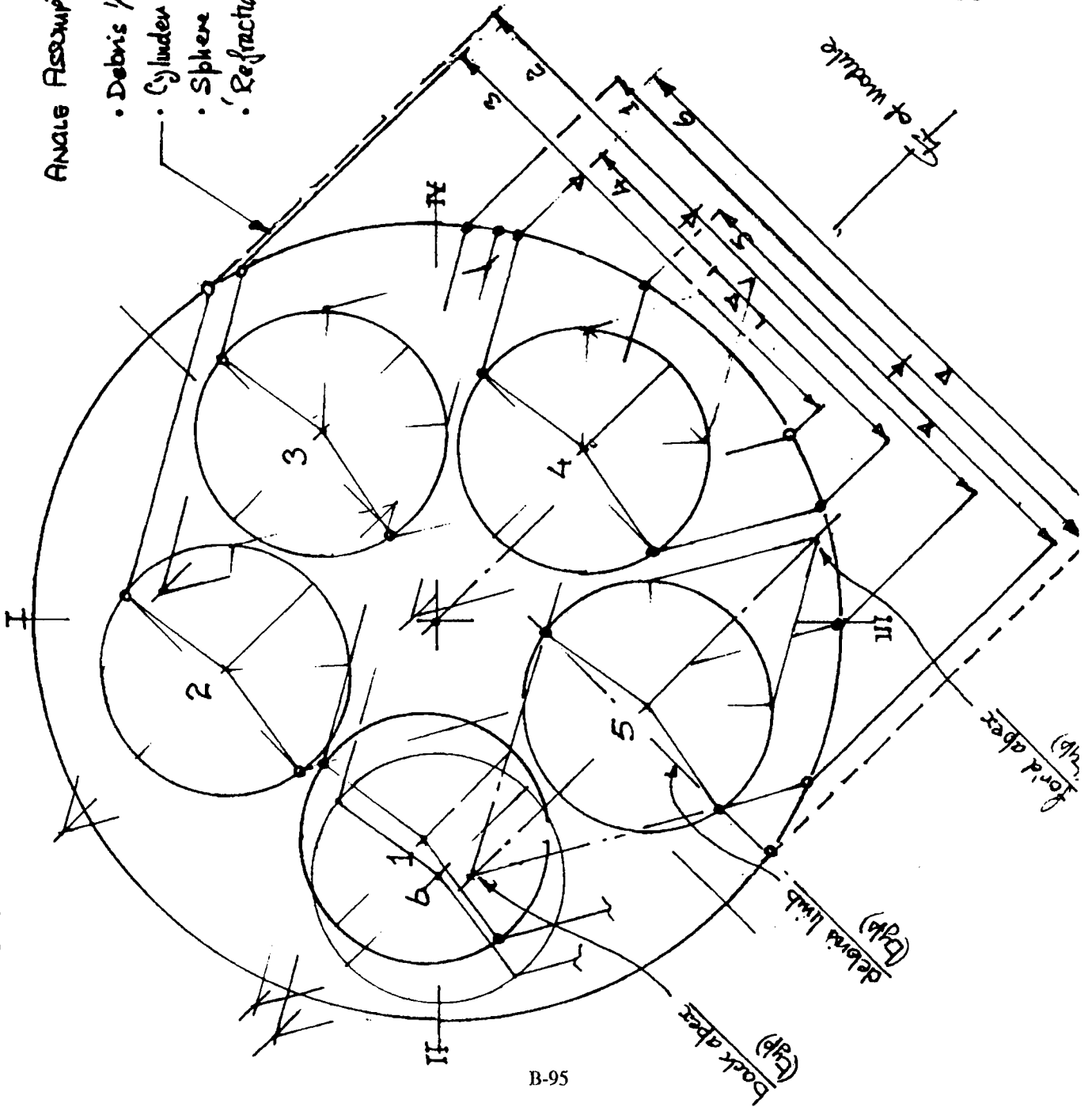
(BII-12)

THREE WALL DEFENSE AGAINST DEBRIS / FRAGMENT SIZE & VELOCITY - GENERAL PRINCIPLES



CPL. May 28

- Debris $\frac{1}{2}$ cone angle 30°
- Cylinder obliquity limit 80°
- Sphere " " 70°
- 'Refraction' not treated



C/Le — Mar '95

DECELERATION STRESS OF AIR AT STOP - ON SIMILAR DEBRIS

Ref: 101 (BIV-114)

Eq: -

let debris dia = d (cm)

debris frontal area (A) = $\left(\frac{d}{25.4}\right)^2 \frac{\pi}{4} \times \frac{1}{12^2}$

debris mass (M) = $\left(\frac{d}{25.4}\right)^3 \cdot \frac{\pi}{6} \times 10$

let debris velocity = V₁ (km/sec) V₁ x 3280

dynamic air pressure (q) = $\frac{\rho V_1^2}{2} (V_1 \times 3280)^2$

Debris deceleration = $\frac{A}{M} \cdot q \cdot C_D \cdot g$

Time to go L cm - (neglecting deceleration)

Speed lost in going L cm (ΔV) = $\frac{V^2}{d} \times 108,900 \times \frac{L}{V \times 100,000}$

Surplus energy made available (in going L cm) = $\frac{M}{2g} \cdot [V_1^2 - (V_1 - \Delta V)^2]$
 $= \frac{d^3 \times 0.003195}{32.2} \times [V_1 \times 3280 \times (V_1 \times 3280)^2]$

Surplus energy per lb of debris in going L cm = $\frac{d^3 V_1^3 L \times 3544}{d^3 \times 0.003195}$

= d² x 0.00845 (ft²)

= d³ x 0.003195 (lbm)

(km/sec) V₁ x 3280 (ft/sec)

= V² x 12,792 (p.s.f.)

= $\frac{d^2 \times 0.00845 \times V^2 \times 12.792 \times 10.322}{d^3 \times 0.003195}$ say 2

= $\frac{V^2}{d} \times 108,900$ (ft/s/s)

= $\frac{L}{V \times 100,000}$ (sec)

= $\frac{V \times L \times 1.089}{d}$ (ft/s)

(ft lb_f)

(ft lb_f)/lb (m)

1.0 cm 394111

0.00845 ft²

0.003195 lbm

6.5 / 21320 ft

541,000.0 psf

(457) lb ft/drag

4.6 x 10⁶ ft/s/s

L = 100 cm / 3.28 ft

0.00154 sec

708 ft/s

shock form true diff two sps

1497 1473

469,000 469,000

etc. Max 95

DECELERATION EFFECTS OF AIR AT STEP - ON RANDOMLY DISTRIBUTED CURVE DESIGN

refers to (BVI-15)

let: alum debris cube side C_1				let	
face area $(A) (\frac{C_1}{2.54})^2 =$				$C_1^2 \cdot .001076$	
mass $(M) (\frac{C_1}{2.54})^3 \times .10$				$C_1^3 \cdot .006102$	
let debris velocity V_1				$C_1 = d \times .886$	
dynamic air press (q)				$V_1^2 \cdot 12.792$	
Debris deceleration $\frac{A}{M} q \cdot C_u g.$				$\frac{C_1^2 \cdot .001076 \cdot V_1^2 \cdot 12.792 \cdot 1.66 \cdot 32.2}{C_1^3 \cdot .006102}$	
time to go C cm (neglects deceleration)				$\frac{V_1^2 \cdot 120600}{C_1}$	
Speed lost gas C cm $(\Delta V) \frac{V_1^2 \cdot 120600 \cdot C}{V_1 \cdot 100000}$				$\frac{C}{V_1 \cdot 100000}$	
Surplus energy must equal (gas C cm)				$\frac{V_1 \cdot C \cdot 1.206}{C_1}$	
Surplus energy must equal $\frac{M}{2g} \cdot [V_1^2 - (V_1 - \Delta V)^2]$				$C_1^2 \cdot V^2 \cdot e \cdot .7496$	
debris energy per lb of debris $\cdot (gas \cdot C$ cm)				$V_1^2 \cdot e \cdot 122.8$	

107

$$V_d^2 \cdot 110.9$$

$$V_1^2 \cdot e \cdot 152.4$$

note: Mass of

DECELERATION EFFECT OF AIR - (CONTD)

ref: 102 3D-16

Assumed 1) Energy needed to fracture, heat to melting, melt, 1lb of aluminum = 360,000 ft-lb

2) a v (Surplus energy due to deceleration) is available for the

3) (1-a) (" " " ") feeds air, disintegrates air, causes light flash, etc

Equation for spherical debris is re-written:-

$$a \cdot \frac{V_1^2}{d} \cdot \ell \times 110.9 = 360,000 \text{ lb ft}^2$$

$$\text{where } V_1 = \left(\frac{d}{\ell} \right)^{\frac{1}{2}} \left(\frac{3646}{a} \right)^{\frac{1}{2}}$$

V_1 to melt sphere w/nt: a, e, d,

a	10	10	30	100	300	1.0	.3	.1	.03	.01
a=10	10	18.0	9.9	5.7	3.1	1.8	1.04	.57	.31	1.8
a=8	10	20.1	11.0	6.4	3.7	2.0	1.16	.64	.35	2.0
a=6	10	22.3	12.7	7.0	4.0	2.2	1.21	.70	.40	2.2

Equation for cubic debris is re-written

$$a \cdot \frac{V_1^2}{\ell} \cdot \ell \times 122.8 = 360,000 \text{ lb ft}^2$$

$$\text{where } V_1 = \left(\frac{\ell}{\ell} \right)^{\frac{1}{2}} \left(\frac{2932}{a} \right)^{\frac{1}{2}}$$

V_1 to melt cubes w/nt: a, e, e,

a	10	10	30	100	300	1.0	.3	.1	.03	.01
a=10	10	17.1	9.4	5.4	3.1	1.7	.94	.54	.31	1.7
a=8	10	19.1	10.5	6.1	3.5	1.9	1.05	.61	.35	1.9
a=6	10	21.1	12.1	7.0	4.0	2.2	1.21	.70	.40	2.2

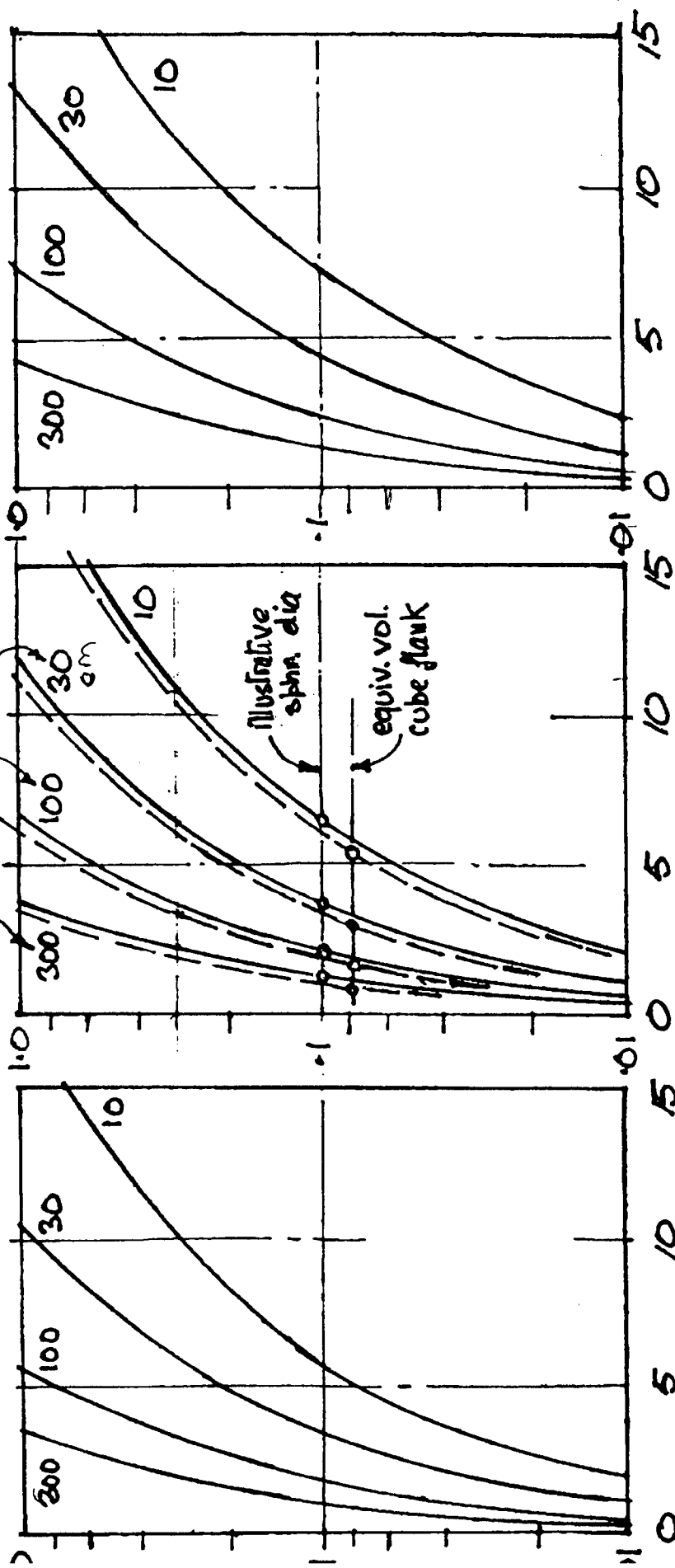
(BD-17)
ref. sec 103

VELOCITY & DISTANCE TRAVELLED IN AIR (AT STP) TO FRACTURE & MELT ALUM FRAGMENTS

Proportion of Deceleration energy going to fracture and melt debris

1.0 → .8 → .6

Alum debris dia or cube flank (cm) Distance to fracture/melt (cm)-hyp.



Initial Vel. in air

Initial Vel in air

Initial Vel. in air (km/s)

- Spheroid fragments —
- Cubic fragments - - -

See 31

c/c May 95

REPORT DOCUMENTATION PAGE			Form Approved OMB No. 0704-0188
Public reporting burden for this collection of information is estimated to average 1 hour per response, including the time for reviewing instructions, searching existing data sources, gathering and maintaining the data needed, and completing and reviewing the collection of information. Send comments regarding this burden estimate or any other aspect of this collection of information, including suggestions for reducing this burden, to Washington Headquarters Services, Directorate for Information Operations and Reports, 1215 Jefferson Davis Highway, Suite 1204, Arlington, Va 22202-4302, and to the Office of Management and Budget, Paperwork Reduction Project (0704-0188), Washington, DC 20503.			
1. AGENCY USE ONLY (Leave Blank)	2. REPORT DATE February 1996	3. REPORT TYPE AND DATES COVERED Contractor Report (Final)	
4. TITLE AND SUBTITLE Catastrophic Failure Modes Assessment of the International Space Station Alpha		5. FUNDING NUMBERS NAS8-37383	
6. AUTHOR(S) B.E.P. Lutz and C.J. Goodwin			
7. PERFORMING ORGANIZATION NAME(S) AND ADDRESS(ES) Meyer Analytics, Inc. 6738 Bridle Path Warrenton, VA 22186-9212		8. PERFORMING ORGANIZATION REPORT NUMBERS M-804	
9. SPONSORING/MONITORING AGENCY NAME(S) AND ADDRESS(ES) George C. Marshall Space Flight Center Marshall Space Flight Center, Alabama 35812		10. SPONSORING/MONITORING AGENCY REPORT NUMBER NASA CR-4720	
11. SUPPLEMENTARY NOTES Technical Monitor: Joel Williamsen, Structures and Dynamics Laboratory, Science and Engineering Directorate			
12a. DISTRIBUTION/AVAILABILITY STATEMENT Unclassified-Unlimited Subject Category 18		12b. DISTRIBUTION CODE	
13. ABSTRACT (Maximum 200 words) This report summarizes a series of analyses to quantify the hazardous effects of meteoroid/debris penetration of Space Station Alpha manned module protective structures. These analyses concentrate on determining (a) the critical crack length associated with six manned module pressure wall designs that, if exceeded, would lead to unstopped crack propagation and rupture of manned modules, and (b) the likelihood of crew or station loss following penetration of unsymmetrical di-methyl hydrazine tanks aboard the proposed Russian FGB ("Tug") propulsion module and critical elements aboard the control moment gyro module (SPP-1). Results from these quantified safety analyses are useful in improving specific design areas, thereby reducing the overall likelihood of crew or station loss following orbital debris penetration.			
14. SUBJECT TERMS hypervelocity impact, orbital debris, fracture mechanics, critical crack propagation		15. NUMBER OF PAGES 232	
		16. PRICE CODE A10	
17. SECURITY CLASSIFICATION Unclassified	18. SECURITY CLASSIFICATION OF THIS PAGE Unclassified	19. SECURITY CLASSIFICATION OF ABSTRACT Unclassified	20. LIMITATION OF ABSTRACT Unlimited

National Aeronautics and
Space Administration
Code JTT
Washington, DC
20546-0001

Official Business
Penalty for Private Use, \$300

Postmaster: If Undeliverable (Section 158 Postal Manual), Do Not Return
